Performance benchmarking of silicon quantum processors

Xue, X.

DOI
10.4233/uuid:20fce6ef-6bb3-42a1-bdd3-53b2a282f0ae

Publication date
2022

Document Version
Final published version

Citation (APA)
Xue, X. (2022). *Performance benchmarking of silicon quantum processors*. [Dissertation (TU Delft), Delft University of Technology]. https://doi.org/10.4233/uuid:20fce6ef-6bb3-42a1-bdd3-53b2a282f0ae

PERFORMANCE BENCHMARKING OF SILICON QUANTUM PROCESSORS

PERFORMANCE BENCHMARKING OF SILICON QUANTUM PROCESSORS

Proefschrift

ter verkrijging van de graad van doctor
aan de Technische Universiteit Delft,
op gezag van de Rector Magnificus prof. dr. ir. T.H.J.J. van der Hagen,
voorzitter van het College voor Promoties,
in het openbaar te verdedigen op dinsdag 31 Mei 2022 om 10:00 uur

door

Xiao XUE

Bachelor of Science in Physics,
University of Science and Technology of China, Hefei, China,
geboren te Zibo, China.

This dissertation has been approved by the promotor:

Prof. dr. ir. L. M. K. Vandersypen

Composition of the doctoral committee:

Rector Magnificus,	chairperson
Prof. dr. ir. L. M. K. Vandersypen	Delft University of Technology, Promotor
Dr. ir. F. Sebastiano	Delft University of Technology, Copromotor
Independent members:	
Prof. dr. S. Tarucha	RIKEN
Prof. dr. G. Burkard	University of Konstanz
Prof. dr. L. DiCarlo	Delft University of Technology
Dr.ir. M. Veldhorst	Delft University of Technology
Reserve member:	
Prof. dr. B. M. Terhal	Delft University of Technology


Keywords: quantum dots, spin qubits, quantum computation, quantum benchmarking

Printed by: Gildeprint

Cover: Designed by Marieke de Lorijn

Casimir PhD Series, Delft-Leiden 2022-16

ISBN 978-90-8593-527-8

An electronic version of this dissertation is available at
`http://repository.tudelft.nl/`.

CONTENTS

SUMMARY

Benchmarking the performance of a quantum computer is of key importance in identifying and reducing the error sources, and therefore in achieving fault-tolerant quantum computation. In the last decade, qubits made of electron spins in silicon emerged as promising candidates for practical quantum computers. To understand their physical properties and the engineering challenges behind, a complete characterization of coupled spin qubits is highly demanded. This dissertation presents extensive studies on performance benchmarking of silicon quantum processors, covering the aspects of quantum logic, quantum measurement, crosstalk and error correlations, and cryogenic quantum control.

The first experiment presented in this dissertation reports the complete characterization of a universal set of quantum gates for silicon spin qubits. As a powerful alternative to conventional Clifford-based single- and two-qubit randomized benchmarking, we introduce a new approach named character randomized benchmarking. We use it to extract a fidelity of 92% for a controlled-Z gate, and show that the crosstalk and error correlations between simultaneous single-qubit gates can be quantified in the same experiment.

The second experiment is focused on the spatial noise correlation between two idling spin qubits. Such correlated noise is critical in quantum error correction. We characterize such correlations by measuring the coherence times of two different two-qubit Bell states with parallel and anti-parallel spins respectively, and find only modest correlations. This is likely due to the existence of uncorrelated nuclear noise arising from ^{29}Si atoms.

In the third experiment, we observe strong nonlinear effects in electric-dipole spin resonance, which is the key mechanism for implementing single-qubit gates in all works presented in this dissertation. Importantly, this induces a novel crosstalk effect between simultaneously driven qubits. The valley-orbit hybridization is investigated and found to give a phenomenological explanation of such nonlinearity. Further studies in material properties and microwave heating effects are needed to explain the discrepancy.

The fourth experiment is about quantum nondemolition measurement of a spin qubit, which is an essential building block of quantum error correction codes. Helped by an ancilla qubit, we can significantly improve the readout fidelity of the data qubit from ~75% to ~95% after 15 repetitive measurements. We experimentally test an improved signal processing method, namely soft decoding, and showcase its advantage when Gaussian noise dominates the readout errors.

In the fifth experiment, we finally break the barrier of 99% for the fidelity of the two-qubit gate for semiconductor spin qubits. Combining isotopically purified silicon, careful Hamiltonian engineering of exchange interactions, and error diagnosis from gate set tomography, we achieve fidelities of all single- and two-qubit gates of over 99.5%, well above the popular surface code error threshold. Powered by the high-fidelity universal

gate set, we are able to execute a variational quantum eigensolver routine for computing the dissociation energy of molecular hydrogen with the silicon quantum processor.

The last experiment steers the focus towards the interface between quantum processor and classical control electronics, known as a major bottleneck in scaling. We propose to solve the problem by utilizing control circuits working at a few Kelvin. A control chip named "Horse Ridge" is therefore tested at 3 Kelvin and demonstrated to match the same control fidelities obtained using bulky commercial instruments working at room temperature, at a cost of only a few hundred milliwatts. The functionality of this control chip is further tested by operating universal two-qubit logic as well as executing a two-qubit Deutsch-Josza algorithm.

At the end of this dissertation, we propose a few possible next-steps to further explore the error sources in spin qubits and approaches for scalable operations.

SAMENVATTING

Het benchmarken van de prestaties van een kwantumcomputer is van cruciaal belang bij het identificeren en verminderen van foutbronnen, en dus voor het bereiken van fouttolerante kwantumberekeningen. In het afgelopen decennium zijn kwantum bits, gebaseerd op elektronenspins in silicium, naar voren gekomen als veelbelovende kandidaten voor praktische kwantumcomputers. Om de fysieke eigenschappen en de technische uitdagingen erachter te begrijpen, is een volledige karakterisering van gekoppelde spin qubits vereist. Dit proefschrift presenteert uitgebreide studies over prestatiebenchmarking van silicium kwantumprocessors, waarbij de aspecten van kwantumlogica, kwantummeting, overspraak, foutcorrelaties en cryogene kwantumcontrole worden behandeld.

Het eerste experiment dat in dit proefschrift wordt beschreven, rapporteert de volledige karakterisering van een universele set kwantumpoorten voor silicium spin qubits. Als een krachtig alternatief voor conventionele, op Clifford gebaseerde enkel- en twee-qubit gerandomiseerde benchmarking, introduceren we een nieuwe benadering genaamd karakter gerandomiseerde benchmarking. We gebruiken het om een betrouwbaarheid van 92% te karakteriseren voor een gecontroleerde-Z-poort en laten zien dat de overspraak- en foutcorrelaties tussen gelijktijdige single-qubit-poorten in hetzelfde experiment kunnen worden gekwantificeerd.

Het tweede experiment is gericht op de ruimtelijke ruiscorrelatie tussen de twee inactieve spinqubits. Dergelijke gecorreleerde ruis is van cruciaal belang bij kwantumfoutcorrectie. We karakteriseren de correlaties door de coherentietijden te meten van twee verschillende Bell-toestanden van twee qubits met respectievelijk parallelle en antiparallelle spins, en vinden slechts bescheiden correlaties. Dit is waarschijnlijk te wijten aan het bestaan van niet-gecorreleerde nucleaire ruis die voortkomt uit ^{29}Si-atomen.

In het derde experiment observeren we sterke niet-lineaire effecten in elektrischedipool spinresonantie, wat het belangrijkste mechanisme is voor het implementeren van single-qubit poorten in alle experimenten die in dit proefschrift worden gepresenteerd. Belangrijk is dat dit een nieuw overspraakeffect induceert tussen gelijktijdig aangestuurde qubits. De vallei-baanhybridisatie is onderzocht en blijkt een fenomenologische verklaring te geven voor dergelijke niet-lineariteit. Verdere studies in materiaaleigenschappen en microgolfverwarmingseffecten zijn nodig om de discrepantie te verklaren.

Het vierde experiment gaat over een kwantum niet-destructieve meting van een spinqubit, een essentiële bouwsteen van kwantumfoutcorrectiecodes. Met behulp van een ancilla-qubit kunnen we de uitleesbetrouwbaarheid van de data qubit aanzienlijk verbeteren van ~75% naar ~95% na 15 herhaalde metingen. We testen experimenteel een verbeterde signaalverwerkingsmethode, namelijk zachte decodering, en demonstreren het voordeel ervan wanneer Gaussische ruis de uitleesfouten domineert.

In het vijfde experiment doorbreken we eindelijk de barrière van 99% voor de betrouwbaarheid van de twee-qubit-poort voor halfgeleider-spinqubits. Door isotopisch gezuiverd silicium te combineren met de zorgvuldige constructie van de Hamiltoniaan van uitwisselingsinteracties en de foutdiagnose van gate-set-tomografie, bereiken we een betrouwbaarheid voor alle enkele- en twee-qubit-poorten van meer dan 99.5%, ruim boven de populaire oppervlaktecode foutendrempel. Door middel van de hoge betrouwbaarheid van de universele poortset zijn we in staat om een variabele kwantum eigensolver-routine uit te voeren voor het berekenen van de dissociatie-energie van moleculaire waterstof met de silicium-kwantumprocessor.

Het laatste experiment focust op de koppeling tussen de kwantumprocessor en klassieke besturingselektronica, bekend als een groot knelpunt voor opschaling. We stellen voor het probleem op te lossen door gebruik te maken van regelcircuits die werken op een temperatuur van een paar Kelvin. Een controle-chip genaamd “Horse Ridge” is getest bij 3 Kelvin en we hebben aangetoond dat de controle-betrouwbaarheid hiervan overeen komt met commerciële instrumenten die op kamertemperatuur werken, tegen een kostprijs van slechts een paar honderd milliwatt. De functionaliteit van deze controle chip wordt verder getest door universele twee-qubit-logica te gebruiken en een twee-qubit Deutsch-Josza-algoritme uit te voeren.

Aan het einde van het proefschrift stellen we een aantal mogelijke vervolgstappen voor om de foutbronnen in spinqubits te onderzoeken en ook mogelijkheden voor schaalbare operaties.

1

INTRODUCTION

1

1.1. IT FROM QUBIT

Since quantum mechanics was established, it has not only brought revolutional developments to both fundamental sciences and industrial technologies, but also has created a bridge between physics and information. In 1990, John Wheeler suggested in his famous "it from bit" doctrine that everything is constructed from simple binary information – bit [1]. It might sound inspiring but the questions behind it are perhaps too metaphysical to be answered by a doctoral student. "No one knows how to derive it from bit... But we can do the next best thing: we can start from the qubit", said David Deutsch [2].

The best effort we can make on examining "it from qubit" is to simulate it using a computer. Such a computer must be made of qubits, meaning quantum bits, which follow the rules of quantum mechanics. Since Richard Feynman unveiled his blueprint "Simulating physics with computers" [3], scientists have been able to encode quantum information into photons, electrons, atoms, molecules... The binary information (0 or 1) is typically encoded into different energy states of these objects. Different from a classical bit, or anything that can be described by classical physics, a qubit can be in a superposition of 0 and 1 at the same time (written as $\alpha|0\rangle + \beta|1\rangle$). This allows a logic operation to process different input information simultaneously, known as "quantum parallelism" (Fig.1.1 b). A very good metaphor for the power of qubits is the "Downhill Skier" by Charles Addams (Fig.1.1 a). Quantum information processing can be seen as the downhill skier – fast and able to go through different paths in parallel, whereas the classical information processing is like the uphill skier – slow and only able to go along a single path. The nature of superposition leads to a straightforward consequence, that is quantum entanglement. In an entangled quantum state, e.g. two-qubit entanglement, the states of the two qubits are maximally correlated $((|00\rangle+|11\rangle)/\sqrt{2}$ or $(|01\rangle+|10\rangle)/\sqrt{2})$. Quantum entanglement has played a critical role in not only accelerating quantum algorithms, but also in building quantum networks and examining quantum foundations [4].

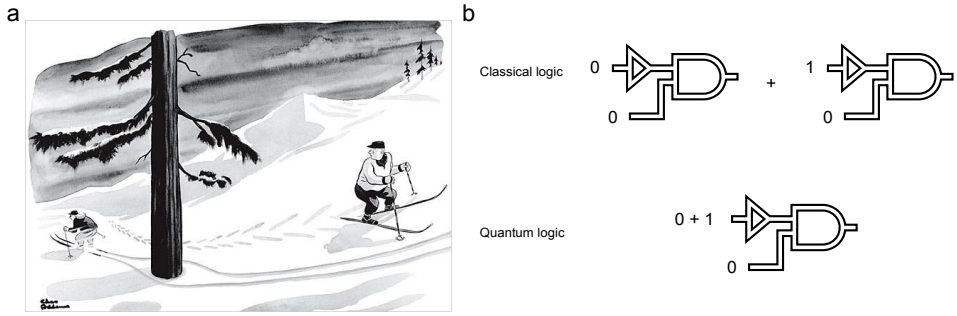

Fig. 1.1: a. The "Downhill Skier" by Charles Addams. **b.** Illustrations of quantum parallelism. A quantum computer logic is capable to process an input of 0 and 1 at the same time, whereas the classical computer logic can only process either 0 or 1 in a single execution.

A qubit is typically a well-defined binary quantum system, or a quantum system consisting of two energy levels. Although there's no fundamental limit on using more than 0 and 1 to store information, it's already known in classical computing that binary digits do have an edge over decimal digits, because of the more natural logic behind – binary

digits answer simple "yes or no" questions, and the robustness against errors such as voltage drift in transistors. Similar arguments also hold for quantum information encoding and thus qubits are generally preferred than other encodings such as "qutrits" and "qudits". While most quantum systems in the real world consist of multiple energy levels, it's mostly possible to select two out of many levels to encode a qubit, as long as they are well distinguishable from other levels.

Quantum states are very fragile and can be easily "killed" by small disturbance in the environment. The qubits need to be relatively coherent so that enough quantum logic operations can be executed before they decohere. Fast quantum operations are highly desired as a consequence. However, implementing quantum operations requires external drives generated by certain control systems, typically microwave signal generators or lasers. These external drives are essentially a special type of disturbance. This means qubits that have longer coherence times are generally more difficult to operate. An example is qubits encoded by atoms or ions in vacuum, which weakly couple to their environment. Their coherence times are typically a few orders of magnitude longer than those of qubits made in solid state environment, but meanwhile logic operation times for ions and atoms are also much longer.

To execute quantum algorithms, it must be possible to initialize and measure the qubits, and to operate them by a universal set of quantum logic gates. Ideally, qubits should be initialized to a known pure state before starting a quantum circuit, and they should be measured with respect to a certain reference pure state. In reality, errors can happen in both the initialization and the measurement. These errors not only will affect the computing efficiency, that is, a larger number of repetition needs to be executed to stabilize the outcomes, but also will cause inaccuracy in diagnosing the performance of quantum gates, as the quantum gates are always characterized in the gauge determined by the initialization and measurement. As for the universal quantum gates, the most commonly referred gate set is the two-qubit Clifford gates plus a single-qubit T gate. Using the universal gate set, a quantum computer can run algorithms that cannot be efficiently executed by a classical computer. In contrast, quantum algorithms compiled by only the Clifford gates, which by themselves are not universal, can be efficiently emulated by a classical computer [5]

In addition, the qubits need to fit in a scalable architecture, and information must be transferable remotely via "flying qubits". So far most solid state qubits show higher promise in scaling, whereas qubits encoded by atoms, ions, and solid state defects can interface a photonic quantum link more easily. A platform with both scalable architecture and remote connectivity still needs to be developed.

These requirements above are also known as the Divincenzo criteria [6]. Following these criteria, scientists and engineers have made great progress in quantum computation, from the first experimental quantum algorithm [7], to the first algorithm that shows the advantage of quantum computing [8]. Although a real useful quantum computer has not yet come true, these requirements and the physical laws behind will instruct us to build it from qubit.

1

1.2. PLENTY OF ROOM ON A CHIP

In the past decades, a few physical systems have been investigated as quantum computer prototypes, including neutral atoms, ions, photons, electrons in quantum dots, and Josephson junctions. Normally these quantum systems have to be placed in extreme environments such as high vacuum or ultra-low temperature, which can already make the setup very complicated. Therefore, it is preferred to have a system that can be scaled up using the least costly additional resources. Atoms and ions are typically trapped in a chunky vacuum chamber, while photonic qubits need large free space and are less programmable. Although these qubits can also be "integrated" on a chip, bulky laser sources and photon detectors are not avoidable so far. In addition, trapped atoms and ions have to be loaded from dedicated atom sources as well. Producing such a setup often requires a lot of manual labor. These features make them less scalable than qubits naturally defined in solid-state environments, such as quantum dots and Josephson junctions.

Pioneered by Feynman's prediction "there's plenty of room at the bottom"[9], nanotechnology has become a major driving force in discovering new physics and creating new tools. The density of computer circuitry is getting higher every year, and billions of transistors can be packed into a microprocessor. These developments directly benefit the solid-state quantum technologies, especially qubits made in semiconductor quantum dots, which is the focus in this dissertation. Although until now qubits are still controlled and readout via bulky cables and instruments at different temperature, advanced semiconductor manufacturing makes there plenty of room on a chip, and thus opens the possibility to highly integrated and multiplexed input/output (I/O) connections [10]. A more ambitious goal is the so-called "quantum integrated circuits", in which the control and readout instrumentation is integrated on the same die/package with the qubit arrays [11]. A good analogy from classical computer technology is the SoC (system on a chip), in which all components including CPU, GPU and DRAMs are integrated on the same chip in order to achieve higher performance for its high bandwidth and low latency, while lowering the power consumption due to the reduced wiring lengths between components (Fig.1.2).

Quantum dots in silicon have shown great promise in large-scale quantum computation for their small footprints and compatibility to advanced lithography technologies [11, 13]. There are a few ways to encode a qubit in quantum dots [14]: the spin state of a single electron in a single quantum dot; the charge state or spin-charge state of a single electron in a double quantum dot; the collective spin state or spin-charge state of a few electrons in a few quantum dots. The choice of encoding can directly impact the qubits' susceptibility to errors. Among all these approaches, we choose the single electron spin state for qubit for various reasons [15, 16]. A single-electron spin qubit has the longest coherence times because it couples the least strongly to charge noise, which is known as the major noise source in the solid state. Another well-know noise source is from the spins of nuclei in the substrate material, which can affect the coherence of spin states via hyperfine interactions. The errors caused by these environmental noise are typically referred to as stochastic errors, which basically describe the decoherence occuting while excuting a quantum circuit. Reducing the stochastic errors mostly require improving the quality of the substrate material, the dielectrics on top, and their interface. Meanwhile, errors can also come from the quantum circuit itself, because the

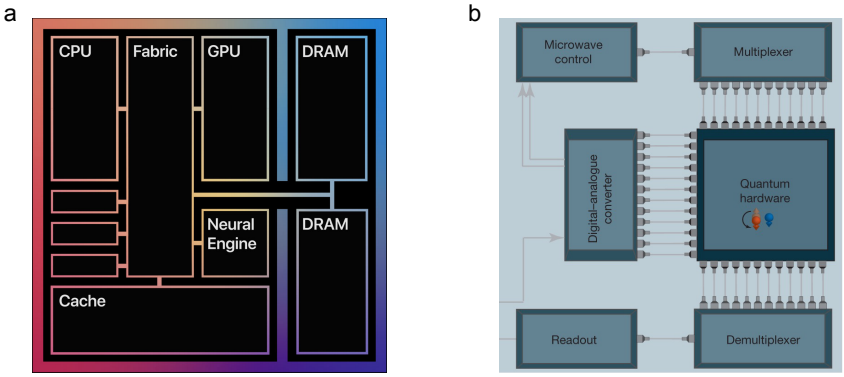

Fig. 1.2: a. A representative SoC architecture: the Apple M1 chip. The compact design and short interconnect allow the chip to process heavy tasks at a lower power consumption. **b.** Architecture of envisioned quantum integrated circuits [12], on which the quantum hardware (qubits) and the modules for control and readout are integrated on the same chip.

control signals from the external instrumentation are never perfect. These errors are called Hamiltonian errors or systematic errors. Hamiltonian errors are typically much larger in systems with more than two levels, with the extra levels forming state leakage channels. On the other hand, single electron spin is naturally a two-level system, which makes it a well defined qubit. Different from stochastic errors, Hamiltonian errors remain constant through the entire run-time of algorithms, and can thus in principle be calibrated and corrected by careful Hamiltonian engineering. This requires a precise description of how qubits respond to the control signals, and an accurate execution of the quantum operations.

Our ultimate goal is to build a fault-tolerant quantum computer using these qubits, which means the errors can be detected and corrected faster than they occur. This requires that the error rate at each step of the computation is below a certain threshold (typically ~1%) [17]. A good starting point for spin qubits is that single spins can be operated at very high fidelity [18, 19]. However, to achieve the grand goal, a few challenges need to be tackled [20]. First, a high-fidelity two-qubit logic must be achieved. A physical system is only credited as a leading quantum computer platform once its two-qubit logic fidelity crosses the 99% threshold. Second, error corrections require a high-fidelity quantum nondemolition measurement scheme that can be executed faster than the decoherence. While high-fidelity readout of spin qubits have been reported, these seemingly nice numbers are typically obtained either under extreme experimental conditions, or in the absence of necessary qubit initialization. Third, these qubits need to be scaled up without increasing the error rate. Therefore it is a demanding task to obtain a deeper understanding of noise correlations and crosstalk errors, which will be crucial in dense qubit arrays. Meanwhile the increasing interconnect complexity of quantum dot devices must be circumvented via novel control architectures.

1

1.3. THESIS OUTLINE

In this dissertation, I present our progress on benchmarking the performance of silicon quantum processors. This covers not only the improvement we have made to boost the performance of spin qubits, but also how we precisely characterize the errors using advanced benchmarking tools.

In **Chapter 2**, I present the theory background and the experiment scheme that support the findings in this dissertation. In the first part of this chapter, I review the theory of quantum logic with single electron spins, and the experimental implementation of spin qubits using gate-defined quantum dots. In the second part, I review the theory of quantum logic fidelities and the methods of precise fidelity characterizations.

In **Chapter 3** I report the first complete benchmarking of single- and two-qubit gate fidelities in silicon spin qubits. We develop a new benchmarking toolbox – character randomized benchmarking, and successfully use it to extract the fidelity of a CPhase gate. I also discuss the limitation of the CPhase gate fidelity.

Keeping high control fidelities while adding more qubits can be challenging, as qubits can "talk" to each other and errors can be passed errors from one to another. In **Chapter 4**, I present the characterization of spatial noise correlations between a pair of spin qubits. And in **Chapter 5**, I discuss our findings of the nonlinear response in single-qubit gates, which is triggered by the discovery of a crosstalk effect between simultaneously driven neighboring qubits.

In addition to high-fidelity quantum logic, another essential ingredient for fault-tolerant quantum computation is high-fidelity quantum nondemolition (QND) measurement. In **Chapter 6**, I present our progress on QND measurement of a spin qubit. We experimentally demonstrate a new decoding method of high efficiency – soft decoding, which can significantly enhance the measurement fidelity under certain noise conditions.

In **Chapter 7**, I present a main achievement in this thesis – a two-qubit system with quantum logic fidelities crossing threshold for surface code. By precisely engineering the exchange interaction between the two spins, and using self-consistent gate set tomography to detect and correct the remaining Hamiltonian errors, we are finally able to achieve a CPhase gate fidelity above 99.5%, addressing a main challenge for spin qubits in semiconductors.

In **Chapter 8**, I present our effort on the co-integration of a quantum processor and a classical controller. We replaced bulky high-frequency instruments by a 2×2 mm^2 control chip, which is operated at 3 K and is designed to meet the requirements for scalable and high-fidelity quantum operations. We experimentally demonstrate the capability of such a cryogenic control chip by using it control real spin qubits. Furthermore, the single-qubit gate fidelity obtained with cryogenic control matches that obtained with the bulky and expensive room-temperature electronics. The work in this chapter forms a bridge to the vision of quantum integrated circuits in Fig.1.2.

Finally I summarize our works in **Chapter 9**, raise a few critical questions, and discuss some possible next-steps.

REFERENCES

[1] J. Wheeler, *Information, physics, quantum: The search for links,* in *Proceedings III International Symposium on Foundations of Quantum Mechanics* (1989) pp. 354–358.

[2] D. Deutsch, *It from qubit,* in *Science and Ultimate Reality: Quantum Theory, Cosmology, and Complexity*.

[3] R. P. Feynman, *Simulating physics with computers,* Int. J. Theor. Phys **21**, 467 (1982).

[4] R. Horodecki, P. Horodecki, M. Horodecki, and K. Horodecki, *Quantum entanglement,* Rev. Mod. Phys. **81**, 865 (2009).

[5] D. Gottesman, *The heisenberg representation of quantum computers,* arXiv:quant-ph/9807006 (1998).

[6] D. P. DiVincenzo, *The physical implementation of quantum computation,* Fortschritte der Physik: Progress of Physics **48**, 771 (2000).

[7] I. L. Chuang, L. M. K. Vandersypen, X. Zhou, D. W. Leung, and S. Lloyd, *Experimental realization of a quantum algorithm,* Nature **393**, 143 (1998).

[8] F. Arute, K. Arya, R. Babbush, D. Bacon, J. C. Bardin, R. Barends, R. Biswas, S. Boixo, F. G. Brandao, D. A. Buell, *et al., Quantum supremacy using a programmable superconducting processor,* Nature **574**, 505 (2019).

[9] R. P. Feynman, *There's plenty of room at the bottom,* Caltech magazine, Engineering and Science **23**, 22 (1960).

[10] D. P. Franke, J. S. Clarke, L. M. Vandersypen, and M. Veldhorst, *Rent's rule and extensibility in quantum computing,* Microprocessors and Microsystems **67**, 1 (2019).

[11] L. M. K. Vandersypen, H. Bluhm, J. S. Clarke, A. S. Dzurak, R. Ishihara, A. Morello, D. J. Reilly, L. R. Schreiber, and M. Veldhorst, *Interfacing spin qubits in quantum dots and donors–hot, dense, and coherent,* npj Quantum Information **3**, 34 (2017).

[12] L. Petit, H. Eenink, M. Russ, W. Lawrie, N. Hendrickx, S. Philips, J. Clarke, L. Vandersypen, and M. Veldhorst, *Universal quantum logic in hot silicon qubits,* Nature **580**, 355 (2020).

[13] A. Zwerver, T. Krähenmann, T. Watson, L. Lampert, H. C. George, R. Pillarisetty, S. Bojarski, P. Amin, S. Amitonov, J. Boter, *et al., Qubits made by advanced semiconductor manufacturing,* Nature Electronics **5**, 184 (2022).

[14] G. Burkard, T. D. Ladd, J. M. Nichol, A. Pan, and J. R. Petta, *Semiconductor spin qubits,* arXiv:2112.08863 (2021).

[15] D. Loss and D. P. DiVincenzo, *Quantum computation with quantum dots,* Phys. Rev. A **57**, 120 (1998).

[16] F. A. Zwanenburg, A. S. Dzurak, A. Morello, M. Y. Simmons, L. C. L. Hollenberg, G. Klimeck, S. Rogge, S. N. Coppersmith, and M. A. Eriksson, *Silicon quantum electronics,* Rev. Mod. Phys. **85**, 961 (2013).

[17] A. G. Fowler, M. Mariantoni, J. M. Martinis, and A. N. Cleland, *Surface codes: Towards practical large-scale quantum computation,* Phys. Rev. A **86**, 032324 (2012).

[18] J. Yoneda, K. Takeda, T. Otsuka, T. Nakajima, M. R. Delbecq, G. Allison, T. Honda, T. Kodera, S. Oda, Y. Hoshi, N. Usami, K. M. Itoh, and S. Tarucha, *A quantum-dot spin qubit with coherence limited by charge noise and fidelity higher than 99.9%,* Nature Nanotechnology **13**, 102 (2018).

[19] C. Yang, K. Chan, R. Harper, W. Huang, T. Evans, J. Hwang, B. Hensen, A. Laucht, T. Tanttu, F. Hudson, *et al.*, *Silicon qubit fidelities approaching incoherent noise limits via pulse engineering,* Nature Electronics **2**, 151 (2019).

[20] M. H. Devoret and R. J. Schoelkopf, *Superconducting circuits for quantum information: an outlook,* Science **339**, 1169 (2013).

2

QUANTUM LOGIC OF SPIN QUBITS AND PERFORMANCE BENCHMARKING PROTOCOLS

This chapter provides the theoretical concepts which support the findings in this dissertation. We start from the basics of quantum dots and spin qubits, followed by the theory of quantum process and fidelity benchmarking methods.

2.1. OPERATIONS OF SPIN QUBITS

A quantum bit (qubit) is defined by a two-level quantum system which interacts with its surrounding environment including external driving signals. A two-level system can be selected from natural objects, such as photons, electrons, atoms, or manufactured in an artificial structure, such as Josephson junctions. The qubit state can be visualized by a vector in a Bloch sphere (Fig.2.1a). As a tradition, the lower energy state is used to encode $|0\rangle$, and the excited state is used as $|1\rangle$. Quantum coherence allows the qubit to be placed into a superposition state, written as $|\Psi\rangle = \cos(\theta/2)|0\rangle + e^{i\phi}\sin(\theta/2)|1\rangle$. θ and ϕ can be controlled using well-defined single-qubit logic, making the quantum state and quantum process "programmable".

The coherence is commonly described by two critical timescales, T_1 and T_2. T_1 is defined as "relaxation time", which describes the timescale of energy damping from the excited state to the ground state. The relaxation process is simply described by an exponential function. T_2 is defined as "dephasing time", which describes the speed of phase randomization caused by the fluctuation of energy splitting between the two states. Dephasing processes can vary from a Gaussian decay to an exponential decay, depending on the noise spectrum. T_1 and T_2 are also called "longitudinal coherence time" and "transverse coherence time". Different types of qubits are susceptible to different types of noise. For spin qubits discussed in this work, relaxation originates from the spin-lattice couplings, or phonons, that absorb energy at the scale of the qubit energy splitting. Dephasing commonly comes from two mechanisms: one is the spin-spin couplings that is, the hyperfine interaction between the electron spins and nuclear spins. Another one is the spin-magnet couplings, whereby charge noise causes fluctuations the position of the electrons in a magnetic field gradient. Note that historically "T_2" is used to describe the temporal and spatial average of the dephasing time of a spin ensemble, which distributes in a slowly evolving inhomogeneous environment. In experiments on individual qubits, "T_2" is sometimes used to describe the coherence time measured with dynamical decoupling protocols. To avoid confusion, we suggest to always specify which measure of T_2 is used. In the context of a single spin, we specifically describe the coherence time measured in a Ramsey interferometry experiment and refer to it as "T_2^*". T_2^* is limited by both the relaxation time and the pure dephasing time T_ϕ. However, the typical T_1 of spin qubits is a few orders of magnitude longer than T_ϕ, so we use "T_2^*" as a good approximation to the dephasing time.

The spin states of a single electron form an ideal two-level quantum system in nature. In an external magnetic field B_{ext}, the energies of spin states are quantized into two eigenvalues, $E_{|\downarrow\rangle} = -g\mu_B B_{ext}/2$ and $E_{|\uparrow\rangle} = +g\mu_B B_{ext}/2$, where g is the Landé g-factor, and μ_B is the Bohr magneton (Fig. 2.1b). As our focus in this thesis is on silicon, which has a positive g-factor, the $|\downarrow\rangle$ state is assumed to be the ground state ($|0\rangle$) from now on. The frequency of the qubit is defined as the precession frequency of the magnetic momentum of the spin about B_{ext}, which is called the Larmor precession. It is quantitatively given by $\omega_0 = g\mu_B B_{ext}/\hbar$, where $\hbar$ is the reduced Planck constant. In materials with positive g-factor such as silicon, the spin-down state ($|\downarrow\rangle$) serves as $|0\rangle$ and the spin-up state ($|\uparrow\rangle$) serves as $|1\rangle$. Unlike most other implementations, where the two energy levels for qubit encoding are often selected from multi-level systems, a single electron spin has only two energy levels, which prevents the quantum information from

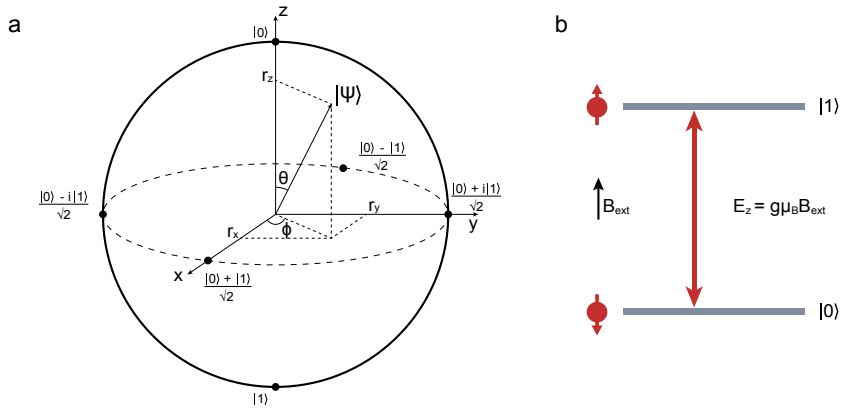

Fig. 2.1: a. Qubit state visualized in the Bloch sphere. **b.** Eigenstates of an electron spin in silicon.

leaking into other states.

In a larger system consisting of multiple qubits, each individual qubit needs to be addressable without affecting other qubits. Thus it is necessary to separate the qubits in their frequency spectrum, if the applied drive cannot be localized. This can be achieved by local modulation of the "effective" g-factor via engineering either the spin-orbit interaction, or by a spatial variation in the external magnetic field. It is worth noting that these approaches do not form discrete areas with different Zeeman energies around each qubit, but instead, it forms a continuous Zeeman energy gradient across the qubits. This means that charge noise can couple to the electron spins and fluctuate their frequencies, which is a main decoherence mechanism in spin qubits.

2.1.1. SINGLE-QUBIT GATES

Single-qubit gates acting on electron spins can be implemented using electron spin resonance (ESR) techniques, where a magnetic field (B_{drive}) linearly oscillating at the qubit frequency ω_0, is applied to the device. B_{drive} needs to oscillate along an axis perpendicular to the external field B_{ext}, in order to perform rotations about the $\hat{x}$ or $\hat{y}$ axis. The linearly oscillating B_{drive} can be seen as a combination of two counter-rotating fields, one of which has the same helicity as the spin precession, thus becoming a static field in the rotating frame which rotates along with the spin. The other component, for its opposite helicity, is at a rotating frequency of $2\omega_0$ seen by the spin. Under the rotating-wave approximation [1], the high-frequency component can be neglected, leaving only a small shift of the qubit frequency, which is called the Bloch-Siegert shift [2].

In the rotating frame, similar as Larmor precession, the spin precesses about the static component of the driving field, which causes a nutation in the laboratory frame [1]. This precession in the rotating frame is called Rabi oscillation, and the rotation frequency around the driving field in the rotating frame is defined as the Rabi frequency, Ω, which linearly depends on the amplitude of the B_{drive}. Moreover, the phase of the B_{drive} determines the relative rotation axis in the $\hat{x}-\hat{y}$ plane. For example, if the rotation axis under a cosinusoidal driving field is defined as the $\hat{x}$ axis, then a sinusoidal

driving field rotates the spin about the $\hat{y}$ axis. It is worth noting that only the relative phase difference between the different driving signals matters. The first operation can be arbitrarily defined to be about any axis, but once it is defined, it also sets a phase reference of the rotating frame for all the subsequent rotations. Rotations around the $\hat{z}$ axis are implemented by changing the reference phase of the rotating frame, which can be easily done in the control software. This essentially changes the definition of the following X and Y gates. Different from the Larmor precession about B_{ext}, the rotation around B_{drive} can be rapidly switch on and off, and its amplitude can be programmed, allowing real-time operations of single spins using short pulses. The accuracy, or fidelity of the operations can be improved by carefully engineering the frequency, phase, and amplitude envelope of these pulses.

In the rotating frame, the Hamiltonian of a single spin under a driving field is directly given by:

$$H_B(t) = \hbar(\omega_{drive} - \omega_0)S_z + \hbar\Omega(t)(S_x \cos\phi(t) - S_y \sin\phi(t)), \tag{2.1}$$

where ω_{drive} is the angular frequency of the driving signal, S_i $(i = x, y, z)$ is related to Pauli operators via $S_i = \sigma_i/2$, and ϕ is the phase of the driving field. The driving speed and the rotation axis are expressed as functions of time, meaning that they can be programmed to rotate via any arbitrary trajectory in the Bloch sphere.

2.1.2. TWO-QUBIT GATES

A universal quantum gate set requires not only single-qubit rotations, but also at least one two-qubit entangling gate [3]. A two-qubit gate requires direct or indirect coherent coupling between the energy levels of the two qubits. A natural result of the coherent coupling is that the energy levels of qubits are shifted, with the shifts conditioned on the joint state of both qubits. For spin qubits in quantum dots, the most straightforward mechanism for two-qubit gate implementations is the direct exchange interaction [4].

The Hamiltonian of two spins with time-dependent exchange interaction is

$$H(t) = 2\pi\hbar J(t)(\mathbf{S^1} \cdot \mathbf{S^2} - 1/4) + \hbar\omega_1 S_z^1 + \hbar\omega_2 S_z^2. \tag{2.2}$$

The first term is the Heisenberg Hamiltonian of coupled spins, where $J(t)$ is the strength of the time-dependent exchange interaction, and $\vec{S^i} = (S_x^i, S_y^i, S_z^i)$ is the spin vector of the i-th qubit. The second and third terms describe the Zeeman energies of individual spins in the external magnetic field, where ω_i is the angular Larmor frequency of the i-th qubit. Without loss of generality, the direction of the external magnetic field is chosen to be along the $\hat{z}$ axis.

Under strong exchange interaction, i.e. the exchange is much larger than the frequency difference between the two qubits $J \gg |f_1 - f_2|$, where $f_i = \omega_i/2\pi$ is the ordinary frequency of the i-th qubit, the eigenstates are approximately spin singlet and triplet states (Fig. 2.2a):

$$\begin{aligned}
&|T_+\rangle = |11\rangle, \\
&|T_0\rangle = (|01\rangle + |10\rangle)/2, \\
&|S\rangle = (|01\rangle - |10\rangle)/2, \\
&|T_-\rangle = |00\rangle.
\end{aligned}$$

On the other hand, if $J \ll |f_1 - f_2|$, the $|01\rangle$ and $|01\rangle$ states will remain the eigenstates (Fig. 2.2b). For non-zero Δf, when the exchange interaction is turned on, the energies of the anti-parallel spin states ($|01\rangle$ and $|10\rangle$) will shift downwards under adiabatic evolution. This is because they contain a spin-singlet component, which is energetically favoured under Fermionic exchange interaction:

$$|01\rangle = (|T_0\rangle - |S\rangle)/\sqrt{2},$$
$$|10\rangle = (|T_0\rangle + |S\rangle)/\sqrt{2},$$

whereas ($|00\rangle$ and $|11\rangle$) are purely spin-triplet states. Consequentially, the system evolves conditioned on the two-qubit joint state, forming the basis of two-qubit gates. The competition between these two sets of eigenstates can be engineered by the design of effective g-factors and the pulsing scheme. This allows not only to implement different types of two-qubit gates [4, 5], but also to encode a qubit into collective states consisting of multiple spins [6].

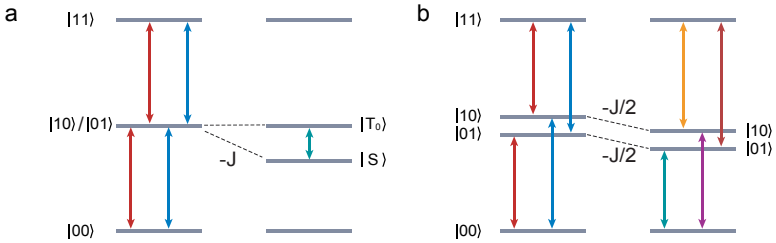

Fig. 2.2: Two-qubit energy diagrams affected by exchange interaction. **a.** When $J \gg |f_1 - f_2| = 0$, the $|T_0\rangle$ and $|S\rangle$ states become the eigenstates. Under the Heisenberg Hamiltonian, this leads to the SWAP-class of two-qubit gates. **b.** When $J \ll |f_1 - f_2|$, $|01\rangle$ and $|10\rangle$ remain the eigenstates. The exchange interaction becomes an Ising Hamiltonian and thus enables the CPhase-class pf two-qubit gates.

In the basis of two qubits ($|00\rangle$, $|01\rangle$, $|10\rangle$, $|11\rangle$), the matrix representation of the Hamiltonian in Eq.2.2 can be written as

$$H(t) = 2\pi\hbar \begin{pmatrix} -(f_1+f_2)/2 & 0 & 0 & 0 \\ 0 & ((f_1-f_2)-J(t))/2 & J(t)/2 & 0 \\ 0 & J(t)/2 & -((f_1-f_2)+J(t))/2 & 0 \\ 0 & 0 & 0 & (f_1+f_2)/2 \end{pmatrix}.$$

When $J = 0$, the Hamiltonian describes two uncoupled spins, and the eigenenergies are the sum of each individual Zeeman energy, meaning the two-qubit gate is turned off. Different types of two-qubit gates can thus be constructed at different exchange coupling strength, with respect to the qubit frequency difference, $|f_1 - f_2|$. We now limit the discussions on the Heisenberg exchange Hamiltonian (H_{exc}) in the two-qubit rotating frame, and thus leave out the Zeemam terms in Eq.2.2

SWAP-CLASS GATES

When $|f_1 - f_2| \ll J$, the exchange interaction dominates the Hamiltonian, and the eigenstates become the singlet and triplet states. For a fixed J in Eq.2.2, the exchange Hamiltonian constantly swaps energy between the two spins, thus swapping the states $|01\rangle$ and $|10\rangle$, at a rate of J. The evolution under H_{exc} is written as a time-dependent operator

$$\begin{aligned} U_{exc}(t) =& \exp\left(-i\frac{H_{exc}t}{\hbar}\right) \\ =& \exp\left(-i\frac{\pi Jt}{2}(X\otimes X + Y\otimes Y + Z\otimes Z - 1)\right) \\ =& \begin{pmatrix} 1 & 0 & 0 & 0 \\ 0 & e^{i\pi Jt}cos(\pi Jt) & -ie^{i\pi Jt}sin(\pi Jt) & 0 \\ 0 & -ie^{i\pi Jt}sin(\pi Jt) & e^{i\pi Jt}cos(\pi Jt) & 0 \\ 0 & 0 & 0 & 1 \end{pmatrix}. \end{aligned}$$

The constant $-1/4$ in Eq. 2.2 commutes with all the operators thus becoming only a global phase to keep the top-left element equal 1. For simplicity, from here we use (I, X, Y, Z) for the Pauli operators $(\sigma_0, \sigma_x, \sigma_y, \sigma_z)$ By controlling the ON-time of the exchange interaction, the operator can be made into an SWAP gate when $t = 1/(2J)$:

$$U_{SWAP} = U_{exc}\left(\frac{1}{2J}\right) = \begin{pmatrix} 1 & 0 & 0 & 0 \\ 0 & 0 & 1 & 0 \\ 0 & 1 & 0 & 0 \\ 0 & 0 & 0 & 1 \end{pmatrix}.$$

Note that in systems where the $Z\otimes Z$ term is absent, this becomes an iSWAP gate [7]. However, the SWAP gate and iSWAP gate are not entangling gates, and thus cannot be used for universal quantum computing. A universal two-qubit gate, $\sqrt{SWAP}$, can be made by setting $t = 1/(4J)$:

$$U_{\sqrt{SWAP}} = U_{exc}(\frac{1}{4J}) = \begin{pmatrix} 1 & 0 & 0 & 0 \\ 0 & \frac{1+i}{2} & \frac{1-i}{2} & 0 \\ 0 & \frac{1-i}{2} & \frac{1+i}{2} & 0 \\ 0 & 0 & 0 & 1 \end{pmatrix},$$

and similarly a $\sqrt{iSWAP}$ gate can be made in absence of the $Z\otimes Z$ term.

CPHASE-CLASS GATES

When $|f_1 - f_2| \gg J$, $|01\rangle$ and $|10\rangle$ remain the eigenstates. In the rotating frame of the $|01\rangle, |10\rangle$ space, the off-diagonal elements in the Hamiltonian, $J(t)/2$, become fast-oscillating terms and can be neglected. The diagonal elements detune the energies of $|01\rangle$ and $|10\rangle$ states by $-J/2$, introducing an extra phase equally to these two states compared to $|00\rangle$ and $|11\rangle$. The time-dependent operator of H_{exc} becomes a controlled-phase (CPHASE)

gate:

$$\begin{aligned} U_{CPHASE}(t) =& exp(-iH_{exc}(t)/\hbar) \\ =& exp(-i\frac{\pi Jt}{2}(Z\otimes Z - I\otimes I)) \\ =& \begin{pmatrix} 1 & 0 & 0 & 0 \\ 0 & e^{i\pi Jt} & 0 & 0 \\ 0 & 0 & e^{i\pi Jt} & 0 \\ 0 & 0 & 0 & 1 \end{pmatrix}. \end{aligned}$$

This can also be intuitively understood as the flip-flop terms ($X\otimes X$ and $Y\otimes Y$) being ineffective when the energy difference between the two qubits is large compared to their coupling strength, and thus it becomes an Ising Hamiltonian. When choosing $t = 1/(2J)$, this operator $diag(1,i,i,1)$ can produce maximally entangled states. A commonly used controlled-Z (CZ) gate can be achieved by applying additional single-qubit $\hat{z}$ rotations:

$$\begin{aligned} U_{CZ} =& Z_1\left(-\frac{\pi}{2}\right) Z_2(-\frac{\pi}{2}) U_{CPHASE}\left(\frac{1}{2J}\right) \\ =& \begin{pmatrix} 1 & 0 & 0 & 0 \\ 0 & 1 & 0 & 0 \\ 0 & 0 & 1 & 0 \\ 0 & 0 & 0 & -1 \end{pmatrix}. \end{aligned}$$

CNOT-CLASS GATES

Controlled-NOT (CNOT) gates are the the most commonly used two-qubit gate in quantum algorithms, especially in quantum error correction circuits. It can be compiled by using a $\sqrt{SWAP}$ gate or a CPHASE gate together with additional single-qubit gates, but it can also be directly implemented with the exchange interaction, in the same regime as the CPHASE gate ($|f_1 - f_2| \gg J$). The two-qubit Hamiltonian in Eq.2.2 yields eigenvalues as follows:

$$\begin{aligned} E_{|00\rangle} =& -2\pi\hbar(f_1+f_2)/2, \\ E_{|01\rangle} =& 2\pi\hbar(-J-\sqrt{J^2+(f_1-f_2)^2})/2 \approx 2\pi\hbar(-J-(f_1-f_2)/2), \\ E_{|10\rangle} =& 2\pi\hbar(-J+\sqrt{J^2+(f_1-f_2)^2})/2 \approx 2\pi\hbar(-J+(f_1-f_2)/2), \\ E_{|11\rangle} =& 2\pi\hbar(f_1+f_2)/2. \end{aligned}$$

Consequentially, the resonance frequency of each qubit becomes dependent on the state of the other qubit:

$$\begin{aligned} f_1(Q_2=|0\rangle) &= (E_{|10\rangle} - E_{|00\rangle})/(2\pi\hbar) = f_1 - J/2, \\ f_1(Q_2=|1\rangle) &= (E_{|11\rangle} - E_{|01\rangle})/(2\pi\hbar) = f_1 + J/2, \\ f_2(Q_1=|0\rangle) &= (E_{|01\rangle} - E_{|00\rangle})/(2\pi\hbar) = f_2 - J/2, \\ f_2(Q_1=|1\rangle) &= (E_{|11\rangle} - E_{|10\rangle})/(2\pi\hbar) = f_2 + J/2, \end{aligned}$$

where Q_i is the i-th qubit. By applying a π-rotation at the frequency of the target qubit when the control qubit is in the $|1\rangle$ state, a controlled-rotation (CROT) gate around the $\hat{x}$ or $\hat{y}$ (CX gate and CY gate) axis can be constructed. Similarly, the CROT gates can also be configured to rotate the target qubit when the control qubit is at $|0\rangle$ state (namely zero-CX and zero-CY). These gates are equivalent to a CNOT (or zero-CNOT) gate up to a single-qubit Z gate. However, a CROT gate requires both the modulation of J and an external driving field for the single-qubit rotation, which imposes more requirements on the control.

2.2. GATE-DEFINED QUANTUM DOTS

To implement programmable quantum circuits in spin qubits, techniques of quantum dots, lattice defects, and donor implants have been utilized to locally confine single electrons in a solid state environment. Spin qubits in defects and donors normally have long coherence times due to their strong localization, making them less susceptible to charge fluctuations [8, 9]. In addition, defect spin qubits have more a complex energy spectrum including transitions at the telecom frequencies, allowing them to directly couple to a photonic quantum network. And the donor atoms that host electron spins typically also carry nuclear spins, which are known for ultra-long coherence times and can therefore serve as local quantum memories. However, so far it remains very difficult to precisely position dopants in the substrate. Further development are still needed to make them scalable.

Quantum dots, known as artificial atoms, can be flexibly designed in their geometry, positions and even energy spectrum. In the past decades, these structures have been successfully applied to achieve high-quality spin qubits in group III/V and group IV semiconductors [8, 10]. There are two major approaches to make quantum dots: a bottom-up approach to grow small islands of a III/V alloy on the surface of another material, e.g. InAs on GaAs, and make them self-assemble to form quantum dots; a top-down approach in which nanofabricated metallic gates are voltage-biased to locally isolate electrons in a nanowire or at at the interface of a two-dimensional quantum well.

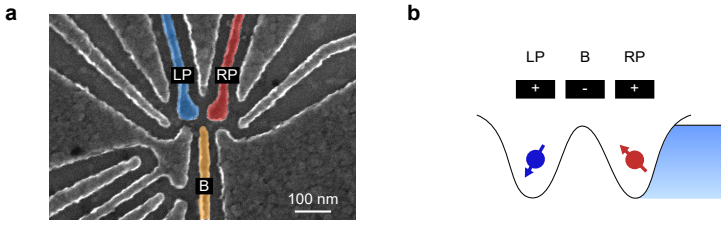

Fig. 2.3: a. Scanning electron microscope image of a double quantum dot device. Quantum dots are formed underneath the tip of LP and RP gates. The tunnel coupling between the dots is controlled by the B gate. **b.** Schematic confinement potentials of a double quantum dot. Typically, the plunger gates are positively biased, whereas the barrier gate is negatively biased.

Nanofabricated quantum dots are credited as scalable platforms for their compatibility with advanced lithography technology used for conventional microprocessors and the capability of all-electrical qubit control [8, 11, 12]. More importantly, this approach

offers great tunability, especially on the couplings between nearest neighbor qubits. Dedicated plunger and barrier gates are used to control the chemical potential of each dot and the tunnel coupling between each neighboring pair respectively (Fig.2.3). By independent control of the voltages applied on the right plunger (V_{RP}) and the left plunger (V_{LP}), the number of electrons in the equilibrium state of a double quantum dot (DQD) can be accurately mapped out in a so-called charge stability diagram (Fig.2.4a). Such a diagram serves as a guidance for the experimental pulsing schemes including the initialization, readout, and single- and two-qubit gates of spin qubits (Fig.2.4b).

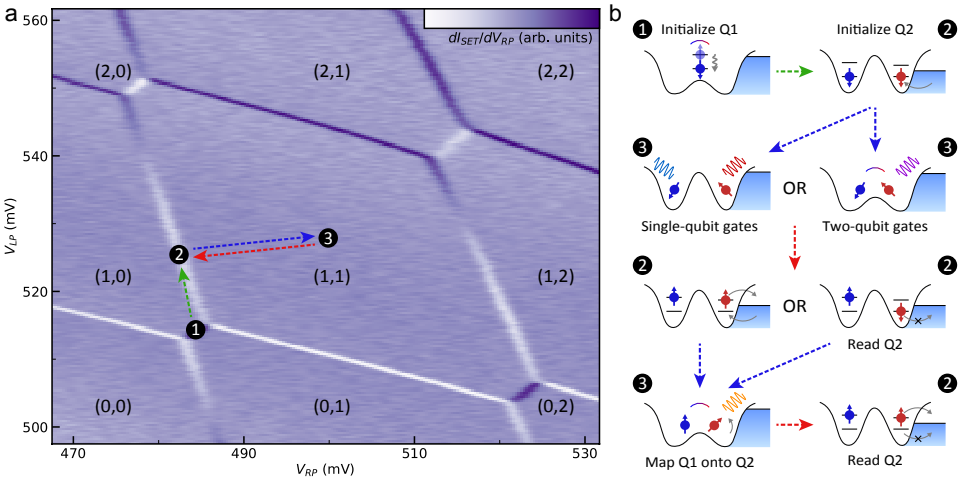

Fig. 2.4: a. Charge stability diagram of the DQD system, showing the differential current signal (dI_{SET}/dV_{RP}) and charge occupation ((M, N), indicating M electrons in the dot below LP and N electrons in the dot below RP) as a function of the voltages applied to gate LP (V_{LP}) and gate RP (V_{RP}). The three main stages of a typical pulse sequence are marked by the numbered circles. **b.** Schematic representations of the DQD system during an experiment cycle. Q_1 is first initialized to its ground state (spin-down) via fast relaxation by pulsing to the charge transition line between (1,0) and (0,1) (stage 1), which is a spin-relaxation hotspot [13]. Then Q_2 is initialized via spin-selective tunneling by pulsing it to the transition line between (1,0) and (1,1) (stage 2). During the qubit operations, the system is pulsed to the middle of the (1,1) region (stage 3) so both electrons are well-confined inside the DQD. The tunnel barrier is independently controlled to turn off the exchange coupling during single-qubit gates and to turn on the coupling for two-qubit logic operations. After the operations, Q_2 state is read out via spin-selective tunneling and reinitialized into the spin-down state (stage 2). The state of Q_1 is read out by mapping its state onto Q_2 via a two-qubit $CROT$ gate (stage 3), followed by readout of Q_2 again (stage 2). The figure and the caption are adapted from ref.[14].

2.2.1. READOUT

As charge signals can be easily detected in electrically controlled quantum dots, spin readout is achieved via spin-to-charge conversion. Two common spin-to-charge conversion modes are spin-selective tunneling [15] and Pauli spin blockade [6, 16].

In spin-selective tunneling, an electron reservoir adjacent to the quantum dots is needed. For the example shown in Fig. 2.4, the spin state is measured at the (1,0) to (1,1) transition line (N = 0 or 1). The voltages need to be precisely configured such that the Fermi level of the electron reservoir lies in between the two spin states. The ground state

($|\downarrow\rangle$) will stay in the dot, whereas the excited state ($|\uparrow\rangle$) will tunnel out to the reservoir, leaving the quantum dot empty of charge until later on an electron in the $|\downarrow\rangle$ tunnels in. A major error source in this type of readout is the thermal broadening of the Fermi level of the reservoir. To overcome this and achieve high readout fidelity, a large magnetic field is needed to achieve a large Zeeman splitting compared to the thermal broadening [17]. However, this sets very high requirements for the external magnet as well as the signal source which generates the driving fields.

Pauli spin blockade (PSB) readout distinguishes singlet and triplet spin states in a tunnel-coupled double quantum dot. It is implemented by detuning the double dot chemical potentials across the (1,1) to (2,0) (or (1,1) to (0,2)) transition line for the readout. If the two spins are in the singlet S(1,1) state, the electron in the right dot can tunnel into the ground orbital state of the left dot and form a singlet S(2,0) state. As for the three triplet spin states T(1,1), due to Pauli's exclusion principle, the electron can only transit to the T(2,0) state which is much higher in energy, and therefore the inter-dot tunneling is blocked in a certain detuning window. Here S(1,1) and T(1,1) describe the singlet and triplet states with one electron in each dot, whereas the S(2,0) and T(2,0) describe the states of two electrons in the left dot. When the detuning exceeds the orbital/valley splitting of the left dot, the T(2,0) state becomes accessible, thus lifting the spin blockade. This sets strong restrictions on the readout window, especially for silicon, where relatively small valley splittings become the bottleneck.

After the spin-to-charge conversion, the charge state can be detected using an adjacent charge sensor such as a quantum point contact (QPC) or a sensing quantum dot (SQD). Typically, the charge sensor is capacitively coupled to one or more quantum dots and the current through the sensor is monitored by external instrumentation. When the sensor is voltage-biased to its sensitive regime, e.g. a transition between two quantized conductance plateaus of a QPC, or a sharp edge of a Coulomb peak of a SQD, a single charge movement in the qubit dots can change the conductance of the sensor drastically. This results in a sudden signal jump, which can then be binarized into 0 or 1 by comparing it to a threshold value [15].

2.2.2. INITIALIZATION

Qubits need to be initialized to known states before executing quantum algorithms, and refreshed in quantum error correction codes. Ideally, we want to initialize them to a pure state such as $|0...00\rangle$. In quantum dots, the initialization can be done in a few different manners: spin-selective tunneling, adiabatic interdot transition, relaxation hotspots, etc.

The first two methods can be seen as the inverse process of the previously introduced readout methods. In spin-selective tunneling, the quantum dot is refilled by an electron in the $|\downarrow\rangle$ state after the readout. Same as the readout, this initialization method is also limited by the thermal broadening of the reservoir. As for the adiabatic interdot transition, the system starts from the S(2,0) state, then is adiabatically moved to the (1,1) configuration, and ends up into one of the two anti-parallel spin states.

The relaxation hotspot in a double dot system is often close to the (1,0) to (0,1) transition line. In this configuration, the T_1 of the spin is significantly reduced due to spin-orbit mixing [13] or spin-valley-orbit mixing [18], and therefore the qubit can be quickly

initialized by equilibration to the ground state. This approach is very efficient and has fewer constraints compared to other methods. However, this method can only initialize one qubit in two quantum dots, the second qubit still needs to be initialized using other methods.

2.2.3. PHYSICAL IMPLEMENTATION OF SINGLE AND TWO-QUBIT GATES

In section 2.1, we have conceptually discussed single-qubit gates using electron spin resonance (ESR) and two-qubit gates using exchange interaction. Here we introduce their implementations in gate-defined quantum dots.

ESR AND EDSR

Single-qubit gates, as mentioned before, require an oscillating magnetic field (B_{drive}) perpendicular to the external magnetic field (B_{ext}). In conventional ESR, microwave bursts on resonance with the qubit are generated by signal sources at room-temperature, and then sent to an antenna fabricated next to the quantum dots on the sample chip. The oscillating magnetic field generated by the current flowing through the antenna directly couples to the spin and executes single-qubit rotations around the $\hat{x}$ or $\hat{y}$ axis. This approach has been widely used for spin qubits in GaAs [19] and silicon [20].

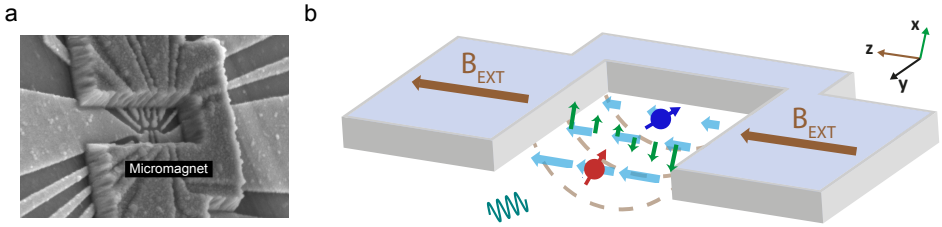

Fig. 2.5: a. Scanning electron microscope images a double quantum dot device and the micromagnet on top. This panel is adapted from ref.[21]. **b.** The magnetic field gradient in the double dot area. The micromagnet is magnetized in parallel to the external magnetic field (in $\hat{z}$ direction) The magnetized micromagnet provides an additional magnetic field (brown dashed lines) which has a longitudinal ($\hat{z}$) component with a field gradient along the double quantum dots. This longitudinal magnetic field gradient (light blue arrows) makes the Zeeman splittings (resonance frequencies) of the two qubits different. Additionally, the micro-magnet also induces a transverse ($\hat{x}$) magnetic field gradient (green arrows). When a microwave pulse is sent to the device through gate MW, the wave functions of the electrons are oscillating in the $\hat{z}$ direction. If the microwave frequency is on resonance with the qubit frequency, the electron is subject to an oscillating magnetic field along the $\hat{x}$ direction, which induces electric-dipole spin resonance (EDSR). This panel is adapted from ref.[14].

Another approach is called electric-dipole spin resonance (EDSR), in which the electric dipole moment of an electron acts as the "mediator" to convert the electric component in the microwave bursts into oscillating magnetic fields. The conversion is engineered by a local magnetic field gradient. The oscillating magnetic field needs to be perpendicular to the external magnetic field (B_{ext}), and thus it is often called "transverse field gradient" (δB_x), in contrast to the "longitudinal field gradient" (δB_z) which separates the qubit frequencies as discussed in the previous section. Several methods have been studied to construct δB_x, including the intrinsic spin-orbit coupling [22] and a Cobalt micromagnet patterned on top of all the metallic gates (Fig.2.5) [23, 24]. When the

electron's wavefunction spatially oscillates in the gradient δB_x at its Larmor frequency, it effectively senses an oscillating magnetic field that implements coherent spin rotations [25]. In both implementations, a separate antenna is not needed and the driving signals can be directly sent to one of the metallic gates used to confine the quantum dot. In materials with very weak spin-orbital coupling, such as silicon, EDSR can only be efficiently implemented using a micromagnet. Micromagnets have shown great success in one-dimensional spin qubit arrays. However, there are a few challenges on its scaling capability, in particular for a two-dimensional array. For example, the micromagnet needs to provide proper magnetic field gradient for each qubit in a dense array, which puts a bar on the design and the tolerance of misalignment in lithography. Importantly, when the qubit is idling, it is preferred to sit at a "sweet spot" where $B_x = 0$, such that the spin quantization axis is along the $\hat{z}$ axis and the rotation axis is perpendicular to it. Although these problems can be mitigated by individual tuning of quantum dots for devices containing only a few qubits, the increased complexity of multi-qubit devices makes it remain a concern.

DETUNING AND BARRIER CONTROL

The key to implementing two-qubit gates in a double quantum dot is to control the exchange interaction, $J = 4t^2U^2/(U^2 - \epsilon^2)$, where t is the interdot tunnel coupling, U is the on-site charging energy of each dot, and ϵ is the detuning of the chemical potentials. In early experiments, the exchange interaction was turned on by pulsing on one or both of the plunger gates, which detunes the chemical potentials of the two dots, e.g. towards the (2,0) charge configuration, thus increasing ϵ [6]. For a large frequency difference between the qubits, $J \ll \left|f_1 - f_2\right|$, the anti-parallel spin states ($|01\rangle$ and $|10\rangle$) are lowered in energy at finite detuning due to the anti-crossing with the S(2,0) state, allowing conditional phase change or frequency selective driving for the CPHASE and CROT gates respectively [26–28]. When the pulse amplitude is large such that $J \gg \left|f_1 - f_2\right|$, the eigenstates $|01\rangle$ and $|10\rangle$ change to $|S\rangle$ and $|T_0\rangle$ and a SWAP/$\sqrt{\text{SWAP}}$ gate can be achieved [29, 30]. The drawback is that the energies of the $|01\rangle$ and $|10\rangle$ states (or the $|S\rangle$ and $|T_0\rangle$) rapidly change with the detuning amplitude. Thus it can be strongly affected by charge noise that causes local chemical potential fluctuations [31], resulting in fast dephasing during the two-qubit gate.

A better way to perform two-qubit gates is via barrier control, or symmetric control [32, 33]. In this scheme, the double dot is operated at the so-called "symmetry point", where the double dot is at zero detuning ($\epsilon = 0$). This is a sweet spot where the charge noise effect is minimized as $\partial J/\partial\epsilon = 0$. The exchange interaction is turned on only by lowering the barrier between the dots, which increases the tunnel coupling t while keeping the chemical potentials symmetric. Compared to the detuning control, symmetric control has been demonstrated to significantly improve the quality of exchange oscillation and gate fidelity [32–35]. Despite the fact that charge noise can still couple to the spins through the tunnel barrier at the symmetry point, a high-fidelity two-qubit gate above 99% can already be achieved (Chapter 7). Further improvement will likely involve dynamical decoupling interleaved in the two-qubit gate [27].

2.2.4. MATERIAL CONSIDERATIONS

Following the pioneering work by Loss and Divincenzo [4], spin qubits were first investigated in quantum dots in GaAs/AlGaAs heterostructures as well as other types of III/V semiconductors. Electrons are accumulated by a p-doped silicon layer at the top and are vertically confined at the interface between GaAs and AlGaAs due to their band offsets, forming a two-dimensional electron gas (2DEG). This type of material has been developed to form ultraclean interface with very high transport mobility, leading to great success in quantum transport experiments. Metallic gates are negatively biased to locally deplete the electrons in the 2DEG to form quantum dots. Quantum dots in GaAs can be confined by only a single layer of lithographically patterned metallic gates due to the small effective electron mass, and they have shown great tunability [36–39]. However, due to the prominent hyperfine interaction between the electron spins and the nuclear spins carried by the Ga and As atoms, the electron's T_2^* has been limited to ~ 10 ns [6, 19].

A big improvement in the T_2^* of spin qubits was made by switching to group IV materials such as silicon [8]. In the three isotopes of silicon, only ^{29}Si carries non-zero nuclear spin, whereas the other two isotopes ^{28}Si and ^{30}Si both have spin-zero nuclei. The natural abundance of ^{29}Si is about only 4.7%. In contrast, Ga and As elements don't have zero nuclear spin isotopes. It has been shown that spin qubits in natural silicon have T_2^* ~ 1 μs [24], which is already about two orders of magnitude longer than that in GaAs. Isotope purification techniques can be used to further reduce the ^{29}Si concentration to ~ 800 ppm as used in most experiments. This leads to another two orders magnitude increase of T_2^*, up to 120 μs [26]. Two popular host materials for spin qubits in silicon are Si/SiO_2 and Si/SiGe heterostructures. The latter one is preferred to be undoped to reduce the disorder and thus improve the stability [40]. Different from the quantum dots formed by depleting a 2DEG in GaAs, quantum dots in undoped silicon are commonly formed via locally accumulating electrons by positively biased plunger gates. Barrier gates are biased with negative voltages to deplete the interdot area.

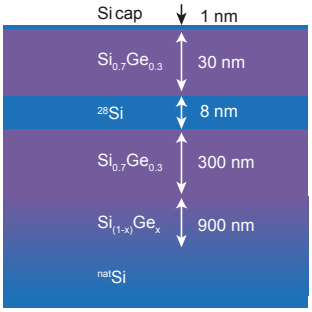

Fig. 2.6: Schematic of ^{28}Si/SiGe heterostructures with corresponding layer thicknesses. This figure is adapted from ref.[14].

In Si/SiGe heterostructure, a thin and strained Si quantum well (typically < 10 nm) is sandwiched by SiGe alloys. Like in GaAs, the low-disorder epitaxial interface gives relatively clean environment for electrons, making it promising to achieve highly uniform qubit arrays. An important challenge in Si/SiGe comes from valley states induced

by indirect band gaps [8]. The valley splitting is affected by the vertical confinement of the electron wafefunction in the quantum well, and it is very sensitive to disorder at the interface. This disorder can form interface steps at atomic scale, which causes a sudden change in the vertical confinement of the electron. The electron's wavefunction can spread across two or more atomic steps at the interface, resulting in a smaller valley splitting on average. This can in principle be solved by making the interface sharper, but it relies on the improvement in growth technique. An alternative solution is using thinner quantum wells. Due to the vertical accumulation, electrons are closer to the top interface of the quantum well, and their wavefunctions partially "penetrate" through the interface into the SiGe alloy. In thinner quantum wells, the electron's wavefunction overlaps more with the SiGe alloy. And tight-binding calculations show that Ge atoms can modulate the band structure and result in a larger valley splitting [41]. However, additional decoherence can be induced by the nuclear spins carried by the ^{29}Si and ^{73}Ge atoms in the SiGe alloy.

Spin qubits can also be made in Si/SiO_2 interface, bearing a resemblance to conventional metal–oxide–semiconductor (MOS) field-effect transistors. In contrast to Si/SiGe, where the Si quantum well is usually 30 - 50 nm below the surface, the thin SiO_2 layer of only a few nanometers makes the electrons much closer to the metallic gates on top, leading to a strong gating effect. Consequentially, the valley splittings in Si-MOS quantum dots can be easily modulated by pulling the electron's wavefunction towards the SiO_2 layer. The abrupt change from Si to SiO_2 causes a large vertical electric field and thus a large valley splitting. On the other hand, the lattice mismatch between Si and SiO_2 results in a lot of interface disorder compared to Si/SiGe. Remarkably, this local disorder could provide additional confinement to electrons and form "spurious" quantum dots in unwanted positions.

2.3. DEVICE AND SETUP

In this section, we briefly introduce a representative quantum dot device and the measurement setup.

2.3.1. DEVICE

The two quantum dot devices used in all experiments included in this thesis are fabricated using a single-layer gate disign, i.e. the plunger gates and the barrier gates are all made in one lithography step. Such a design is chosen for its simplicity in fabrication and thus a high yield, as well as its tunability. In Chapter 3, 4, and 6, we use a device made in natural Si substrate, whereas in Chapter 5, 7, and 8, the device is made in isotopically purified silicon. Here we introduce the details of the purified silicon device as discussed in ref.[14].

The device shown in Fig. 8.1 is fabricated on top of a ^{28}Si/SiGe heterostructure, which is grown on a 100 mm n-type Si(001) substrate (Fig. 2.6). Starting from the Si substrate, the layer sequence comprises a 900 nm linearly graded $Si_{(1-x)}Ge_x$ layer (Ge concentration x varied from 0 to 0.3), followed by a 300 nm strain-relaxed $Si_{0.7}Ge_{0.3}$ buffer layer, a 8 nm tensile strained ^{28}Si quantum well, a 30 nm $Si_{0.7}Ge_{0.3}$ barrier, and a 1 nm sacrificial Si cap. These undoped ^{28}Si/SiGe heterostructures are insulating at low temperature and

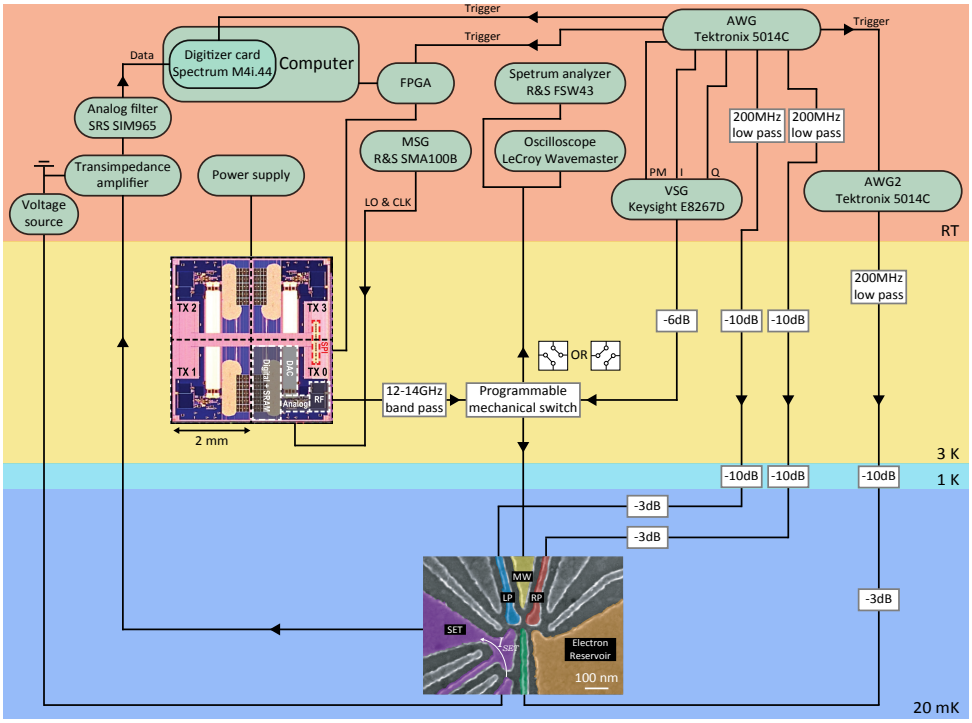

Fig. 2.7: An experimental setup used in the projects presented in Chapter 5, 7, and 8. Different from conventional setups, here a programmable mechanical switch is installed at 4 K, which can switch the input channel of the microwave signals for single-qubit gates. This figure is adapted from ref.[14].

support via gating the accumulation of a two-dimensional electron gas with transport mobility well above 1x10^{5}cm^2/Vs at 55 mK [42, 43].

On top of the heterostructure, a 7 nm AlO_x layer is deposited using atomic-layer deposition (ALD), followed by a 20 nm Al metal film, which is patterned using electron beam lithography in order to define a first gate layer, which shapes the potential landscape. Next another 7 nm AlO_x layer is deposited, followed by a 70 nm Al layer which uniformly covers the quantum dot area. Finally, a 200 nm Co film is deposited and patterned into a micro-magnet (Fig. 2.5).

2.3.2. MEASUREMENT SETUP

Here we show a representative experiment setup that has been used for testing a cryogenic control chip with spin qubits (Chapter 8) and for demonstrating a high-fidelity two-qubit gate (Chapter 7) as well as characterizing nonlinear response and crosstalk effects in EDSR (Chapter 5) using conventional control system at room temperature. In order to flexibly switch between the cryogenic control chip and the room temperature setup, we customized a special measurement setup as shown in Fig. 8.1.

As described in ref. [14], the quantum dot device is wire-bonded onto a printed circuit board (PCB) which is placed at the mixing chamber (~20 mK) of a dilution refrigerator (Bluefors XLD). Voltage pulses onto plunger gates RP and LP (Fig. 2.3) are generated by an arbitrary waveform generator (AWG) at room temperature (RT) (Fig. 8.1), and go through a low-pass filter (Minicircuits) and attenuators before reaching the device. These pulses are used to control the electrochemical potentials of the quantum dots and load/unload electrons from/to the electron reservoir (Fig. 2.4). The voltage pulse onto the barrier gate T is generated by a second AWG (AWG2), which is triggered by and synchronized with the first AWG. A programmable mechanical switch at 3 K is used to connect gate MW either to a vector signal generator (VSG) at RT or to a cryo-controller at 3 K (represented as two boxes next to the switch) through a 12-14 GHz band-pass filter to filter out wide-band noise. The mechanical switch can also be configured to send the output signals from the cryo-controller to the oscilloscope and the spectrum analyzer at RT for electrical characterization in time and frequency domain. The cryo-controller is programmed via an FPGA to generate the microwave bursts using an external local oscillator (LO) signal and a clock (CLK) signal from a microwave signal generator (MSG) at RT. The single electron transistor (SET) next to the quantum dots is voltage biased and the current signal (I_{SET}) through it is converted to a voltage signal through a transimpedance amplifier and digitized by a digitizer card after an analog low-pass filter employed to remove out-of-band (> 10 kHz) noise. I_{SET} is sensitive to the charge occupation of the quantum dots, allowing binary single-shot readout of the qubit states via spin-to-charge conversion (Fig.2.4).

2.4. FIDELITY BENCHMARKING

Errors in a quantum processing task can happen in the initialization, the readout, and the execution of quantum logic. To improve the performance of a quantum processor, these errors must be precisely characterized. To extract the error rates, or the fidelities from a quantum processor, benchmarking protocols have been developed including

quantum state tomography, quantum process tomography, gate set tomography, and randomized benchmarking. The foundation of all benchmarking methods is quantum state tomography, which measures how similar is an experimental quantum state to a target quantum state.

2.4.1. QUANTUM STATE

A phase coherent quantum state can be written as a weighted superposition of different states $|\Psi\rangle = \sum c_i |\psi_i\rangle$, where $\sum |c_i|^2 = 1$. The states are often chosen to be the eigenstates of a system. However, this expression can only describe pure states, which are are visualized as vectors ending at the Bloch sphere. In contrast, the vectors ending at points inside the Bloch sphere represent mixed states, described by a statistical mixture of different pure states. Any quantum state can be described by a density operator (or density matrix) $\rho = \sum |c_i|^2 |\psi_i\rangle\langle\psi_i|$.

Taking a single qubit as an example, its density operator can be conveniently expanded in the Pauli basis:

$$\rho = \frac{1}{2}(I + r_x X + r_y Y + r_z Z).$$

$\vec{r} = (r_x, r_y, r_z)$ is the Bloch vector, with each element being its projection on the corresponding axis (Fig. 2.1a). The diagonal terms in ρ are the probabilities of the system being measured in each eigenbasis, and thus $Tr(\rho) = 1$. The off-diagonal terms represent the phase coherence between different states. An easy metric to distinguish pure states and mixed states is $Tr(\rho^2) = \frac{1}{2}(1 + |\vec{r}|^2)$: a pure state gives $Tr(\rho^2) = 1$, whereas a mixed state gives $Tr(\rho^2) < 1$. Note that in a multi-qubit entangled state, each single qubit is by itself in a mixed state. This can be found by taking the partial trace of an entangled state [44].

The fidelity between an experimental quantum state ρ and a target state ρ_ψ is given by $F(\rho, \rho_\psi) = Tr(\rho\rho_\psi)$. If the target state is a pure state $|\psi\rangle$, this can be simply written as $F(\rho, |\psi\rangle\langle\psi|) = \langle\psi|\rho|\psi\rangle$ [45]. To calculate the state fidelity, ρ must be determined experimentally by quantum state tomography [46, 47], which measures its projections of the density operator on the Pauli operators: $(r_x, r_y, r_z) = (Tr(\rho X), Tr(\rho Y), Tr(\rho Z))$. These projections are directly related to the outcomes in a few projective measurements on the basis states of the Bloch sphere:

$$\begin{aligned} Tr(\rho X) =& Tr(\frac{(|0\rangle + |1\rangle)(\langle 0| + \langle 1|)}{2}\rho) - Tr(\frac{(|0\rangle - |1\rangle)(\langle 0| - \langle 1|)}{2}\rho) \\ =& P_{\frac{|0\rangle+|1\rangle}{\sqrt{2}}} - P_{\frac{|0\rangle-|1\rangle}{\sqrt{2}}} \\ =& 2P_{\frac{|0\rangle+|1\rangle}{\sqrt{2}}} - 1, \end{aligned}$$

and similarly,

$$\begin{aligned} Tr(\rho Y) =& 2P_{\frac{|0\rangle+i|1\rangle}{\sqrt{2}}} - 1, \\ Tr(\rho Z) =& 2P_{|0\rangle} - 1. \end{aligned}$$

Here $P_{|\psi\rangle}$ is the probability of measuring the state in $|\psi\rangle$. The three projective measurements are ideally done by performing an $X_{\pi/2}$, $Y_{\pi/2}$, or identity gate before the measurement. As imperfect readout can cause inaccuracy in the tomography analysis, an additional projective measurement in the $|1\rangle$ basis is often used to calibrate the readout window. Measurements in the $(|0\rangle - |1\rangle)/\sqrt{2}$ basis and in the $(|0\rangle - i\,|1\rangle)/\sqrt{2}$ basis will also be needed if the gates applied before measurements are not perfect.

Multi-qubit quantum state tomography is a straightforward extrapolation of the single-qubit version. A multi-qubit density operator is written in Pauli basis as:

$$\rho = \sum_{i,j,k,l,\ldots}^{4^n} \frac{1}{2^n} Tr(P_i P_j P_k P_l \ldots \rho) P_i P_j P_k P_l \ldots.$$

The state tomography can be similarly implemented by a series of joint projective measurements of all qubits.

2.4.2. QUANTUM MEASUREMENT

A quantum measurement is formulated as a positive operator-valued measure (POVM) E_m, with $\sum E_m = I$. For an ideal POVM, $E_m = |\psi_m\rangle\langle\psi_m|$, with $|\psi_m\rangle$ often chosen to be the eigenstates. To measure a state ρ, the outcome of the POVM E_m is given by probability $P_m = Tr(|\psi\rangle\langle\psi| E_m)$. For a single qubit, an ideal set of POVM is

$$\{E_0 = |0\rangle\langle 0|,\ E_1 = |1\rangle\langle 1|\}.$$

However, the errors in real measurements make a POVM become a statistical mixture of different measurement bases [48]:

$$\{E_0^e = (1-\epsilon_0)\,|0\rangle\langle 0| + \epsilon_1\,|1\rangle\langle 1|,\ E_1^e = \epsilon_0\,|0\rangle\langle 0| + (1-\epsilon_1)\,|1\rangle\langle 1|\},$$

where ϵ_0 and ϵ_1 are the readout errors of $|0\rangle$ and $|1\rangle$ states respectively. Therefore, the measurement fidelity can be calculated as

$$F_0 = Tr(E_0^e E_0) = Tr(E_0^e\,|0\rangle\langle 0|) = 1-\epsilon_0,$$
$$F_1 = Tr(E_1^e E_1) = Tr(E_1^e\,|1\rangle\langle 1|) = 1-\epsilon_1.$$

Ideally, the measurement fidelity can be estimated by perfectly initializing the system to $\rho_0 = |0\rangle\langle 0|$ and $\rho_1 = |1\rangle\langle 1|$ and performing POVM measurements on them. It is worth noting that ϵ_0 and ϵ_1 only describe the errors in the state projection. The projected states, however, can still be wrongly assigned by the readout apparatus, and such "mapping" error is not included in the faulty POVM operators.

The readout apparatus maps the projected states to a classical signal, e.g. amplitude of a current, phase shift of an RF signal, etc. These signals follow certain statistics such as a Gaussian distribution and can be assigned to a binary digit by being compared to a known threshold value [49]. Errors can happen in the readout apparatus if the projected state is mapped to a wrong signal, or the signal is assigned a wrong binary value [50]. We define these errors as the mapping errors: η_0 is the error to map $|0\rangle$ onto $|1\rangle$ and η_1 is the error to map $|1\rangle$ onto $|0\rangle$. A special case to consider here is that errors happen both

in the state projection and in the apparatus mapping. This accidentally gives the correct outcome, although it's not an intended approach. The overall measurement fidelity is therefore calculated as

$$F_0 = (1-\epsilon_0)(1-\eta_0)+\epsilon_0\eta_1,$$
$$F_1 = (1-\epsilon_1)(1-\eta_1)+\epsilon_1\eta_0.$$

In many publications on the topic of spin-qubit readout, the readout fidelities are estimated by performing measurement on a mixed spin state and fitting the distributions of the outcome values, typically under the assumption of Gaussian white noise. The fidelity number is extracted only based on the signal-to-noise ratio of the readout apparatus, and the state projection errors are not accounted for. In the extreme case, the qubit state projection can be completely randomized due to relaxation and excitation effects, resulting in bimodal Gaussian distributions for both states.

2.4.3. QUANTUM OPERATIONS

A quantum operation describes a channel which transfers one density operator to another. The operator needs to be completely positive and trace preserving (CPTP). Complete positivity guarantees non-negative probabilities for a quantum system to be measured in any eigenstate, meaning that the diagonal terms in a state ρ should be non-negative. Trace preservation keeps the total probability preserved, meaning that the $Tr(\rho)$ must always equal one before and after an operation. A straightforward expression of an n-qubit CPTP map is via Kraus operators [44]:

$$\Lambda(\rho) = \sum_{i=1}^{N} K_i \rho {K_i}^{\dagger}.$$

Here $\sum_i K_i {K_i}^{\dagger} = I$, and $N \leq d^2$, where $d = 2^n$ is the dimension of the n-qubit Hilbert space.

DEPOLARIZING AND DEPHASING

The depolarizing channel is a useful quantum process. It describes a noisy channel through which quantum information gets lost equally along all directions [44]. A most important application of the depolarizing channel is the randomized benchmarking protocol and its variants. Moreover, depolarizing noise is widely used as the noise model to analyze the performance of error correction circuits [51]. For a single qubit, the operator that maximally depolarizes the state ρ is

$$\mathcal{K}_{dep_{max}}(\rho) = \frac{\rho + X\rho X + Y\rho Y + Z\rho Z}{4} = I.$$

Any input state will become a completely mixed state, and therefore we say that the state is depolarized. The Kraus operators of the maximum-depolarizing channel $\mathcal{K}_{dep_{max}}$ are $I/2$, $X/2$, $Y/2$, and $Z/2$. The depolarizing process usually happens at a finite error rate. Imagine the state ρ is preserved with probability p, and with probability $1-p$ it is depo-

larized. Such a general depolarizing channel can be written as:

$$\mathcal{K}_{dep}(\rho) = p\rho + (1-p)I \tag{2.3}$$

$$= \frac{1+3p}{4}\rho + \frac{1-p}{4}(X\rho X + Y\rho Y + Z\rho Z). \tag{2.4}$$

Here, the Kraus operators are $\sqrt{1+3p}I/2$, $\sqrt{1-p}X/2$, $\sqrt{1-p}Y/2$, and $\sqrt{1-p}Z/2$. Recurring $\mathcal{K}_{dep}$ will finally fully depolarize the state:

$$\lim_{N\to\infty} {\mathcal{K}_{dep}}^N(\rho) = \mathcal{K}_{dep_{max}}(\rho) = I.$$

This provides an easy way to experimentally extract the depolarizing error rate, which we will further discuss in the randomized benchmarking section [52].

Note that the X and Y operators in the depolarizing channel contain bit-flip errors (Y also contains phase errors), which happen along the longitudes on the Bloch sphere. The Z operator purely describes phase-flip errors, happening along the latitudes. For any state

$$\rho = \begin{pmatrix} a & c^* \\ c & b \end{pmatrix}.$$

The off-diagonal terms, c and c^*, which are related to phase coherence, vanish when the state is maximally dephased:

$$\mathcal{K}_{dephase_{max}}(\rho) = \frac{\rho + Z\rho Z}{2} = a\,|0\rangle\langle 0| + b\,|1\rangle\,|1\rangle\,.$$

The Kraus operators of the maximum-dephasing channel are $I/\sqrt{2}$ and $Z/\sqrt{2}$. A general dephasing channel with an error rate of $1-p$ is written as:

$$\mathcal{K}_{dephase}(\rho) = p\rho + \frac{1-p}{2}(\rho + Z\rho Z) = \frac{1+p}{2}\rho + \frac{1-p}{2}Z\rho Z, \tag{2.5}$$

with the Kraus operators $\sqrt{(1+p)/2}I$ and $\sqrt{(1-p)/2}Z$.

χ-MATRIX

It is convenient to express the Kraus operators in the Pauli basis:

$$\Lambda(\rho) = \sum_{i,j=1}^{N} \chi_{ij} P_i \rho P_j^\dagger,$$

where $N = d^2$, and P_i belongs to the n-qubit Pauli group $\{I, X, Y, Z\}^{\otimes n}$. All coefficients, χ_{ij}, construct a $d^2 \times d^2$ complex-valued matrix, namely χ-matrix or process matrix. It is a Hermitian and positive semidefinite matrix and must satisfy $\sum_{ij}\chi_{ij}P_iP_j = I$. The process fidelity of an experimentally measured matrix χ_{exp} with respect to an ideal matrix χ_{ideal} is given by $F_p = Tr[\chi_{exp}\chi_{ideal}]$. The process fidelity is also called entanglement fidelity [53]. It is directly related to the average gate fidelity F_g [54]:

$$F_g = \frac{dF_p + 1}{d+1}. \tag{2.6}$$

From the Kraus representation in Eq. 2.5, the χ-matrix of a depolarizing channel can be directly written down:

$$\chi_{dep} = \begin{pmatrix} \frac{1+3p}{4} & 0 & 0 & 0 \\ 0 & \frac{1-p}{4} & 0 & 0 \\ 0 & 0 & \frac{1-p}{4} & 0 \\ 0 & 0 & 0 & \frac{1-p}{4} \end{pmatrix}. \tag{2.7}$$

Similarly, from Eq. 2.5, the dephasing channel is written as:

$$\chi_{dephasing} = \begin{pmatrix} p & 0 & 0 & 0 \\ 0 & 0 & 0 & 0 \\ 0 & 0 & 0 & 0 \\ 0 & 0 & 0 & 1-p \end{pmatrix}. \tag{2.8}$$

PAULI TRANSFER MATRIX

A noticeable shortcoming of χ-matrices is that they are not directly multipliable, i.e. the χ-matrix of a quantum circuit cannot be calculated by simple multiplication of the χ-matrices of all individual operations in the circuit. Instead, superoperators, which act on operators, are designed to overcome this issue and conveniently describe quantum operations in circuits. A commonly used representation of superoperators is called the Pauli transfer matrix (PTM), which maps operators to operators in the Pauli basis [55]. The matrix element is written as:

$$\Lambda_{ij}^{\mathcal{K}} = \frac{1}{d} Tr[P_i \mathcal{K}(P_j)]. \tag{2.9}$$

Each matrix element $\Lambda_{ij}^{\mathcal{K}}$ is the coefficient of the map from an input Pauli operator P_j to an output Pauli operator P_i.

The trace preservation constraint forbids any map from a trace-zero operator (any non-identity operator) to the only trace-one operator $I^{\otimes n}$, thus setting $\Lambda_{0j}^{\mathcal{K}} = \delta_{0j}$. Note that the TP constraint is by default used as a fitting condition, and it's therefore always satisfied in practice. On the other hand, in most cases a quantum channel should not increase the coherence of an input operator, meaning that $\Lambda_{i0}^{K} = \delta_{i0}$. An exception is the spontaneous relaxation or the T_1 process, which needs an additional map from I to Z [55].

Following the examples given before, the PTM of the depolarizing channel is:

$$\Lambda_{dep} = \begin{pmatrix} 1 & 0 & 0 & 0 \\ 0 & p & 0 & 0 \\ 0 & 0 & p & 0 \\ 0 & 0 & 0 & p \end{pmatrix}. \tag{2.10}$$

And the PTM of the dephasing channel is:

$$\Lambda_{dephasing} = \begin{pmatrix} 1 & 0 & 0 & 0 \\ 0 & p & 0 & 0 \\ 0 & 0 & p & 0 \\ 0 & 0 & 0 & 1 \end{pmatrix}. \tag{2.11}$$

The average gate fidelity can also be calculated as:

$$F_g = \frac{Tr[\Lambda_{exp}\Lambda_{ideal}^{-1}] + d}{d(d+1)},$$

with Λ_{exp} and Λ_{ideal} the measured PTM and the ideal PTM respectively. The PTM and the χ-matrix are equivalent representations. However, they have the same dimension and are both expressed in the Pauli basis, which can cause confusion. To make a comparison, we use the CPhase gate as an example and plot its PTM and χ-matrix side-by-side in Fig. 2.8.

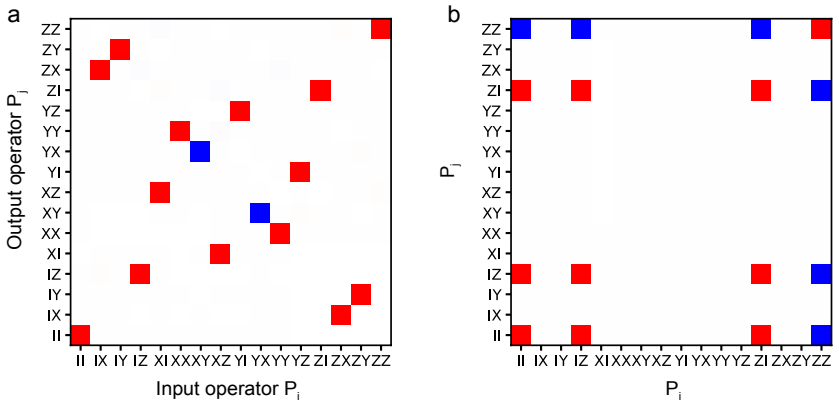

Fig. 2.8: a. The pauli transfer matrix of a CPhase gate. The $\hat{x}$ and $\hat{y}$ axes show the input and output Pauli operators respectively. Red (blue) squares represent coefficients of +1(-1). **b.** The χ-matrix of a CPhase gate. The $\hat{x}$ and $\hat{y}$ axes represent the Kraus operators in the Pauli basis. Red (blue) squares represent coefficients of +1/4(-1/4).

In the superoperator formalism, a density operator ρ is written as a vector in the basis of normalized Pauli operators $\{I/\sqrt{d},\ X/\sqrt{d},\ Y/\sqrt{d},\ Z/\sqrt{d}\}$ [56]. A single-qubit state is represented by

$$|\rho\rangle\!\rangle = \frac{1}{\sqrt{2}}\begin{pmatrix} Tr(\rho I) \\ Tr(\rho X) \\ Tr(\rho Y) \\ Tr(\rho Z) \end{pmatrix} = \frac{1}{\sqrt{2}}\begin{pmatrix} 1 \\ r_x \\ r_y \\ r_z \end{pmatrix},$$

where (r_x, r_y, r_z) is the Bloch vector of ρ. Correspondingly, a single-qubit POVM E is:

$$\langle\!\langle E| = \frac{1}{\sqrt{2}}(1, Tr(EX), Tr(EY), Tr(EZ)),$$

where E, in the ideal case, is the density operator of a pure reference state $|\psi\rangle\langle\psi|$. In practice, a noisy measurement process makes E a mixed reference state as discussed in the previous section. The outcome in a POVM E of a state ρ is $Tr[E\rho] = \langle\!\langle E|\rho\rangle\!\rangle$. Similarly, for the PTM of a quantum gate $\mathcal{G}$, Eq. 2.9 can be rewritten as

$$\mathcal{G}_{ij} = \langle\!\langle P_i|\mathcal{G}|P_j\rangle\!\rangle,$$

and P_i is a normalized n-qubit Pauli operator. The outcome from a quantum circuit consisting of in total N gates can be expressed in a simple format: $p_E = \langle\langle E|\mathcal{G}_N ... \mathcal{G}_2\mathcal{G}_1|\rho\rangle\rangle$, where $\mathcal{G}_i$ is the PTM of the i-th gate.

2.4.4. QUANTUM PROCESS TOMOGRAPHY

Benchmarking a quantum operation is not only about extracting a fidelity number, but about characterizing the type of errors. The most informative way is reconstructing the full process matrix, for which quantum process tomography (QPT) has been the gold standard approach [46]. As the different representations of quantum operations discussed before are essentially equivalent, we use the PTM representation from now on for its convenience in compiling quantum circuits.

This is the superoperator expression of Eq. 2.9. Similar to the discussion in quantum state tomography, the experiment can be implemented by preparing and measuring the state along all the axes in the Bloch sphere. Let's focus on a single-qubit example for simplicity:

$$\begin{aligned}\mathcal{G}_{13} =& \frac{1}{2}\langle\langle X|\mathcal{G}|Z\rangle\rangle \\ =& \frac{1}{2}\langle\langle \rho_{\hat{x}} - \rho_{-\hat{x}}|\mathcal{G}|\rho_0 - \rho_1\rangle\rangle.\end{aligned}$$

Here $\rho_{\pm\hat{x}}$ is the density operator of the $\frac{1}{\sqrt{2}}(|0\rangle \pm |1\rangle)$ state, and $\rho_{0/1}$ is the operator of $|0\rangle / |1\rangle$. Therefore, a PTM $\mathcal{G}$ can be fully reconstructed by preparing and measuring the state in all the basis states $\{\rho_0, \rho_1, \rho_{\hat{x}}, \rho_{-\hat{x}}, \rho_{\hat{y}}, \rho_{-\hat{y}}\}$ before and after the process respectively.

SPAM ERRORS

In both quantum state tomography and quantum process tomography, the errors in state preparation and measurement (SPAM) can cause significant inaccuracy. For a single qubit example, let's prepare the state $\rho_0^{ideal} = |0\rangle\langle 0|$ and perform a POVM as $E_0^{ideal} = |0\rangle\langle 0|$. To implement a QPT protocol, a gate set $\mathcal{F} = \{I_d, X_\pi, X_{\pi/2}, Y_{\pi/2}, -X_{\pi/2}, -Y_{\pi/2}\}$ is utilized to prepare a complete basis of input states and project the output states onto a complete measurement basis, $\{\mathcal{F}_i|\rho_0^{ideal}\rangle\rangle\}$ and $\{\langle\langle E_0^{ideal}|\mathcal{F}_j\}$. Here I_d is the identity operation, and $\pm X/Y_\theta$ rotates the qubit by θ about the $\pm\hat{x}/\hat{y}$ axis. By convention, SPAM errors refer to the errors that make ρ_0^{ideal} and E_0^{ideal} imperfect as

$$\begin{aligned}\rho_0 =& (1-\epsilon)|0\rangle\langle 0| + \epsilon|1\rangle\langle 1|, \\ E_0 =& (1-\eta_0)|0\rangle\langle 0| + \eta_1|1\rangle\langle 1|,\end{aligned}$$

in which ϵ and $\eta_{0/1}$ are the SPAM errors or intrinsic SPAM errors [55]. However, the gates in $\mathcal{F}$ can be also faulty and introduce extra errors in the tomographic input state and projection basis. These errors can be seen as extrinsic SPAM errors [55], but they are essentially gate errors.

In principle, intrinsic SPAM errors can be estimated separately with a priori characterization [27]. However, the fidelity of the measurement cannot be precisely extracted

without knowing the state preparation errors and vice versa. As for the extrinsic SPAM errors, all gates in $\mathcal{F}$ except I_d can have errors and their error syndromes are typically different from each other, meaning that the complete gate set $\mathcal{F}$ needs to be characterized before using them to diagnose any operation in tomography experiments. Therefore, it is necessary to design benchmarking techniques which can characterize the gate errors and the SPAM errors simultaneously, either by self-consistent estimation, or by isolating different types of error.

A self-consistent approach is to design a tomography protocol that can calibrate the target gate $\mathcal{G}_{targ}$, the tomographic gate set $\mathcal{F}$, which might already contain $\mathcal{G}_{targ}$, and the imperfect initial state $|\rho_0\rangle\!\rangle$ and POVM $\langle\!\langle E_0|$ simultaneously and numerically fit all experimental outcomes into a self-consistent error model. This will reconstruct every matrix element in the gate set and the SPAM. The most well-known approach to achieve this is gate set tomography (GST), which has been developed as a do-it-all toolbox [55, 56]. An alternative approach that has been widely used to deal with SPAM errors is randomized benchmarking (RB), which simply isolates SPAM errors from the gate errors, but at a cost of only accessing the average gate fidelities [52]. This is done by amplifying the gate errors in a depolarizing channel, while leaving the SPAM errors constant. In the next two subsections, we will discuss GST and RB.

2.4.5. GATE SET TOMOGRAPHY

The key difference between GST and conventional process tomography is that GST treats the state preparation and measurement as "gates", which means GST characterizes the generally-defined gate set $\{|\rho_0\rangle\!\rangle, \langle\!\langle E_0|, \mathcal{G}_1, \mathcal{G}_2, ..., \mathcal{G}_K\}$, with $\{\mathcal{G}_k\}_{k=1}^K$ the target set of gates. A set of tomographic gates $\{\mathcal{F}_i\}$, which is also referred to as "fiducial" gates [56], is used to prepare the input states $\{|\rho_i\rangle\!\rangle = \mathcal{F}_i|\rho_0\rangle\!\rangle\}$, and project the output states onto different POVMs $\{\langle\!\langle E_i| = \langle\!\langle E_0|\mathcal{F}_i\}$. Normally $\{\mathcal{F}_i\} \subseteq \{\mathcal{G}_k\}$. Let's first write the outcomes of the imperfect tomography experiment:

$$p_{ij}^k = \langle\!\langle E_0|\mathcal{F}_i\mathcal{G}_k\mathcal{F}_j|\rho_0\rangle\!\rangle \tag{2.12}$$

$$= \sum_{rs} \langle\!\langle E_0|\mathcal{F}_i|P_r\rangle\!\rangle\langle\!\langle P_r|\mathcal{G}_k|P_s\rangle\!\rangle\langle\!\langle P_s|\mathcal{F}_j|\rho_0\rangle\!\rangle \tag{2.13}$$

$$= \sum_{rs} A_{ir}(G_k)_{rs}B_{sj}. \tag{2.14}$$

Here, $P_{r/s} \in \{I/\sqrt{2}, X/\sqrt{2}, Y/\sqrt{2}, Z/\sqrt{2}\}^{\otimes n}$. We define the matrices A and B as the SPAM matrices, and they contain both the the intrinsic and extrinsic SPAM errors. Their matrix elements $A_{ir} = \langle\!\langle E_0|\mathcal{F}_i|P_r\rangle\!\rangle$ and $B_{sj} = \langle\!\langle P_s|\mathcal{F}_j|\rho_0\rangle\!\rangle$ are obviously the outcomes from the measurement tomography and the initial state tomography.

Conventional process tomography typically assumes that the SPAM matrices A and B are perfect, and thus $\mathcal{G}_k$ can be simply reconstructed by matrix inversion. In GST, A and B are assumed imperfect and their errors need to be characterized. The direct measurement result p_{ij}^k is an element of the matrix $\tilde{\mathcal{G}}_k = A\mathcal{G}_kB$. When measuring the identity operation I_d, this gives $g = AB$, which is called the state-measurement gram

matrix [57]. Multiplying the inverted gram matrix to $\tilde{\mathcal{G}}_k$ gives an estimation of $\mathcal{G}_k$:

$$\hat{\mathcal{G}}_k = g^{-1}\tilde{\mathcal{G}}_k = B^{-1}\mathcal{G}_k B.$$

Note that A and B can be interpreted as the SPAM basis changes, meaning that they should be invertible. $\hat{\mathcal{G}}_k$ is therefore equivalent to $\mathcal{G}_k$ up to a gauge transformation [56]. Under the gauge transform B, $|\rho_i\rangle\!\rangle$ and $\langle\!\langle E_i|$ become $|\hat{\rho}_i\rangle\!\rangle = g^{-1}|\tilde{\rho}_i\rangle\!\rangle = B^{-1}|\rho_i\rangle\!\rangle$, and $\langle\!\langle \hat{E}_i| = \langle\!\langle \tilde{E}_i| = \langle\!\langle E_i|B$. Notice that $\langle\!\langle E_i|\mathcal{G}_k|\rho_j\rangle\!\rangle = \langle\!\langle \hat{E}_i|\hat{\mathcal{G}}_k|\hat{\rho}_i\rangle\!\rangle$, the gauge transformation is thus not observable without any priori knowledge (Fig. 2.9).

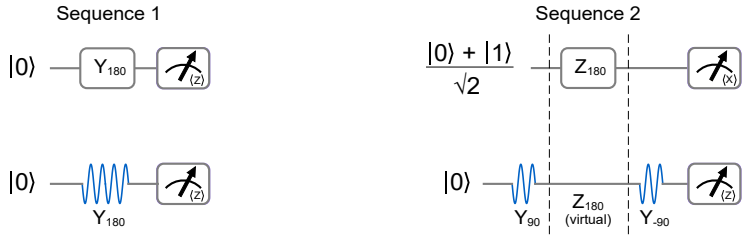

Fig. 2.9: An example of gauge freedom. The Sequence 1 and Sequence 2, although being completely different, cannot be distinguished from the measurement outcomes. The notation ⟨X⟩/⟨Z⟩ in the detector symbols indicates the projection axis in the POVM. The lower circuits show their physical implementations, which are essentially identical.

However, B generally cannot be measured directly, therefore $\{\mathcal{G}_k\}$ cannot fully be reconstructed. The solution to it is finding a gauge matrix $\hat{B}$ that minimizes the discrepancy between $\hat{\mathcal{G}}_k$ and $\mathcal{G}_k$ [55]:

$$\begin{aligned}\sum_{k=1}^{K} &Tr[(\hat{B}\hat{\mathcal{G}}_k\hat{B}^{-1} - \mathcal{G}_k)^T(\hat{B}\hat{\mathcal{G}}_k\hat{\mathcal{B}}^{-1} - \mathcal{G}_k)] \\ &+Tr[(\hat{B}|\hat{\rho}\rangle\!\rangle\langle\!\langle\hat{E}|\hat{B}^{-1} - |\rho\rangle\!\rangle\langle\!\langle E|)^T(\hat{B}|\hat{\rho}\rangle\!\rangle\langle\!\langle\hat{E}|\hat{B}^{-1} - |\rho\rangle\!\rangle\langle\!\langle E|)].\end{aligned}$$

Finally this estimates the gate set to be:

$$\begin{aligned}\mathcal{G}_k^{est} &= \hat{B}\hat{\mathcal{G}}_k\hat{B}^{-1} = \hat{B}B^{-1}\mathcal{G}_k B\hat{B}^{-1}, \\ |\rho\rangle\!\rangle^{est} &= \hat{B}|\hat{\rho}\rangle\!\rangle = \hat{B}B^{-1}|\rho\rangle\!\rangle, \\ \langle\!\langle E|^{est} &= \langle\!\langle\hat{E}|\hat{B}^{-1} = \langle\!\langle E|B\hat{B}^{-1}.\end{aligned}$$

Ideally, $\hat{B} = B$. Now the gauge transform is removed and the gate set is reconstructed in the originally defined gauge.

To achieve a higher accuracy in GST, the tomography experiment is performed not only on a target gates $\mathcal{G}_k$ but also its replications $\mathcal{G}_k^n (n = 1,2,4,...)$, which is called long sequence GST [56]. Thus the errors that commute with G_k can be amplified whereas the SPAM errors remain the same. For example, and amplitude error ϵ_θ in a $X_{\pi/2}$ gate, that leads to an over-rotation (or under-rotation), will accumulate to $n\epsilon_\theta$. This helps to improve the isolation of the SPAM errors from the gate errors. However, some errors can cause the qubit state to refocus after a few repetitions. An example is the rotation axis

error or phase error: if the $X_{\pi/2}$ rotates the qubit about an axis which deviates horizontally from the $\hat{x}$ axis, this error will not be monotonically amplified by repeating the gate, because the state will come back after four repetitions. Such an error has to be amplified by repeating a complex sequence, e.g. $(X_{\pi/2}Y_{\pi/2})^n$. The native gates and the selected complex sequences are together called "germs". In long sequence GST, the selection of germs needs to guarantee that every error can be amplified by some germ [56].

2.4.6. RANDOMIZED BENCHMARKING

The error Λ in the operation $\mathcal{G}$ can be efficiently approximated by a noise channel after the ideal operation $\mathcal{G}^{ideal}$: $\mathcal{G} = \Lambda\mathcal{G}^{ideal}$. If $\mathcal{G}$ is a unitary operation, there is $Tr[\mathcal{G}^{-1}\mathcal{G}^{ideal}] = Tr[\Lambda^{-1}I]$. Therefore, the fidelity of $\mathcal{G}$ is determined by the discrepancy between the noise channel Λ and the identity operator I. The average gate fidelity can be calculated by averaging the state fidelity of the outcome over all pure input states $|\psi\rangle$ [44]:

$$F_g = F_\Lambda = \int d\psi \langle\psi|\Lambda(|\psi\rangle\langle\psi|)|\psi\rangle,$$

which has been demonstrated as an equivalent calculation to 2.6 [54]. Same as $\mathcal{G}$, Λ is in the general superoperator formalism, with $\Lambda(\rho) = \Lambda|\rho\rangle\!\rangle$.

The average fidelity of $\mathcal{G}$, or Λ, equals to the average fidelity of a "twirled" operation of Λ over the unitary group [54, 58]:

$$\Lambda_{twirl}(\psi) = \int dU U^\dagger \Lambda(U|\psi\rangle\langle\psi|U^\dagger)U, \tag{2.15}$$

where U is a unitary operation and $\int dU = I$. The average gate fidelity of Λ_{twirl} is

$$\begin{aligned} F_{\Lambda_{twirl}}(\psi) &= \int d\psi \int dU \langle\psi|U^\dagger\Lambda(U|\psi\rangle\langle\psi|U^\dagger)U|\psi\rangle \\ &= \int dU \int d\psi \langle\psi|U^\dagger\Lambda(U|\psi\rangle\langle\psi|U^\dagger)U|\psi\rangle \\ &= \int dU \int d\psi' \langle\psi'|\Lambda(|\psi'\rangle\langle\psi'|)|\psi'\rangle \\ &= \int dU F_\Lambda \end{aligned}$$

where $|\psi'\rangle = U|\psi\rangle$. Note that F_λ is not a function of U, it results in $F_{\Lambda_{twilr}} = F_\Lambda$. Any quantum channel twirled over the unitary group is a depolarizing channel, thus $\Lambda_{twirl}(\rho) = \Lambda_{dep}(\rho) = p\rho + (1-p)I/d$, with p the depolarizing parameter. The average gate fidelity can be easily calculated as

$$F_g = p + \frac{1-p}{d}, \tag{2.16}$$

and the characterization of the gate fidelity is simplified to a measurement of p.

Naively, the target operator can be twirled by being sandwiched by a randomly sampled U and its complex conjugate $U^\dagger$: $\mathcal{U}^\dagger\Lambda\mathcal{U}$, in which $\mathcal{U}$ is the superoperator of a unitary

operation. The average over the entire unitary group is approximated by averaging the outcome over many such random sequences $\Lambda_{dep} \approx \sum_i \mathcal{U}_i^\dagger \Lambda \mathcal{U}_i$. The depolarizing channel can be concatenated to amplify the noise and also to isolate it from the SPAM error:

$$\begin{aligned}\Lambda_{dep}^m(\rho) &= \Lambda_{dep_m} \ldots \Lambda_{dep_2} \Lambda_{dep_1} |\rho\rangle\!\rangle \\ &= p^m \rho + \frac{1-p^m}{d} I,\end{aligned}$$

where Λ_{dep_i} is the i-th depolarization step. Increasing the total number of depolarization steps m brings the initial state ρ towards a mixed state I. The depolarizing parameter p can be directly fitted from the sequence fidelity as a function of the number of depolarization steps. For an intial state ρ_ψ, which is intended to be prepared into $|\psi\rangle\langle\psi|$, the sequence fidelity is defined as the outcome of a POVM E_ψ:

$$F_{seq}(\rho_\psi) = Tr[E_\psi \Lambda^m(\rho_\psi)] \tag{2.17}$$

$$= Tr[E_\psi(\rho_\psi - \frac{I}{d})]p^m + Tr[E_\psi \frac{I}{d}] \tag{2.18}$$

$$= Ap^m + B. \tag{2.19}$$

The imperfectness of the initial state ρ_ψ and the projective measurement E_ψ are included in the constants A and B, whereas the depolarizing parameter p is completely isolated. By increasing the number of depolarization steps, p, A and B can be easily fitted by such a single exponential decay curve (Fig. 2.10).

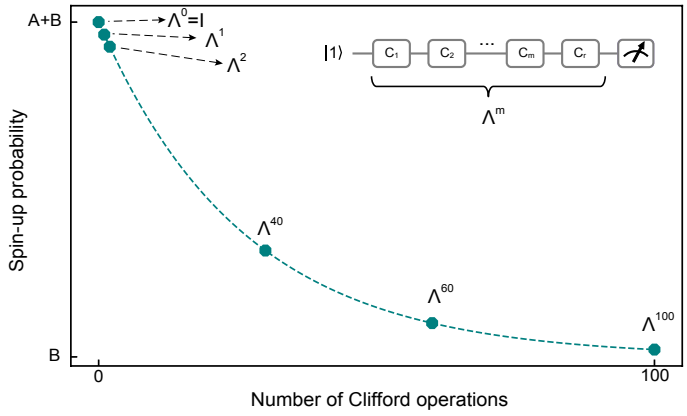

Fig. 2.10: The exponential decay of the sequence fidelity in randomized benchmarking. The SPAM errors are reflected by the visibility window $[B, A+B]$, which should be $[0.5, 1.0]$ if there's no SPAM error. The state of the system evolves towards a mixed state with increasing number of depolarizing steps Λ^m. The visibility window doesn't affect the fitting of the depolarizing parameter p and thus not affecting the estimation of Λ.

However, considering the growing size of the unitary group with increasing number of qubits, it becomes difficult to achieve a good approximation of unitary-twirling by finite randomly sampled unitary operators. On the other hand, the Clifford group, which is a subgroup of the unitary group, has been demonstrated to be a more efficient and

scalable group to approximate the unitary-twirling. In Dankert, *et al.* [59], a unitary-t design is defined as a subset $\{U_k\}_{k=1}^{K}$ of the unitary group, that satisfies

$$\frac{1}{K}\sum_{k=1}^{K} P(t,t)(U_k) = \int dU P(t,t)(U). \tag{2.20}$$

Here $\int dU$ is an integral over the unitary group, and $P(t,t)(U)$ is a polynomial function of a degree equal to or less than t in an operator U, and at a degree equal to or less than t at $U^\dagger$. The Clifford group $\{C_k\}$ is a unitary-2 design, meaning that it can equally twirl any quantum channel into a depolarizing channel:

$$\begin{aligned}\Lambda_{dep}(\rho) &= \int dU U^\dagger \Lambda(U\rho U^\dagger)U \\ &= \frac{1}{K}\sum_{k=1}^{K} C_k^\dagger \Lambda(C_k \rho C_k^\dagger) C_k \\ &= \frac{1}{K}\sum_{k=1}^{K} \mathcal{C}_k^\dagger \Lambda \mathcal{C}_k |\rho\rangle\!\rangle.\end{aligned}$$

$\{\mathcal{C}_k\}$ is the superoperator formalism of $\{C_k\}$. This tells that Λ can be depolarized by randomly applying a Clifford gate C_k and its complex conjugate $C_k^\dagger$ before and after, and averaging over many randomly sampled sequences. Concatenating Clifford-twirling channels gives

$$\Lambda_{dep}^m(\rho) = \int_{k_m,\ldots,k_2,k_1} \frac{1}{K^m} \mathcal{C}_{k_m}^\dagger \Lambda \mathcal{C}_{k_m} \ldots \mathcal{C}_{k_2}^\dagger \Lambda \mathcal{C}_{k_2} \mathcal{C}_{k_1}^\dagger \Lambda \mathcal{C}_{k_1} |\rho\rangle\!\rangle.$$

Here $\mathcal{C}_{k_j}$ is the j-th random Clifford gate in the k-th randomly sampled sequence.

Now let $\mathcal{C}_{l_1} = \mathcal{C}_{k_1}$, $\mathcal{C}_{l_2} = \mathcal{C}_{k_2}\mathcal{C}_{k_1}^\dagger$,..., and $\mathcal{C}_{l_m} = \mathcal{C}_{k_m}\mathcal{C}_{k_{m-1}}^\dagger$, and let $\mathcal{C}_{l_{m+1}} = \mathcal{C}_{k_m}^\dagger = (\mathcal{C}_{l_m}\ldots\mathcal{C}_{l_2}\text{-}\mathcal{C}_{l_1})^\dagger$, the sequence can be written as:

$$\Lambda_{dep}^m(\rho) = \int_{l_m,\ldots,l_2,l_1} \frac{1}{K^m} \mathcal{C}_{l_{m+1}} \Lambda \mathcal{C}_{l_m} \ldots \Lambda \mathcal{C}_{l_2} \Lambda \mathcal{C}_{l_1} |\rho\rangle\!\rangle.$$

Note that $\mathcal{C}_{l_1}$ ... $\mathcal{C}_{l_m}$ are independent from each other, while $\mathcal{C}_{l_{m+1}}$ is determined by inverting the net effect of all previously applied Clifford gates [52].

In experiment, Clifford-based randomized benchmarking is implemented by randomly sampling a sequence of ideal Clifford gates $\mathcal{C}_{l_i}$. Each gate contains an error $\Lambda_{l_i,i}$, which, in reality, is gate-dependent, i.e. it is dependent on its index in the Clifford group l_i, and non-Markovian, i.e. it depends on the position index i inside a sequence [52]. Given an initial state ρ_ψ, we apply a sequence of m random Clifford gates and an additional recovery Clifford gate $\mathcal{C}_{l_{m+1}}$, and perform a POVM measurement E_ψ. The outcome of the l-th random sequence is:

$$Seq_l(\rho_\psi) = \langle\!\langle E_\psi | \Lambda_{l_{m+1},m+1} \mathcal{C}_{l_{m+1}} \Lambda_{l_m,m} \mathcal{C}_{l_m} \ldots \Lambda_{l_2,2} \mathcal{C}_{l_2} \Lambda_{l_1,1} \mathcal{C}_{l_1} |\rho_\psi\rangle\!\rangle.$$

If the error channels are approximately gate-independent and Markovian, there is $\Lambda_{l_i,i} \approx \Lambda$. Averaging the outcome over K random sequences gives:

$$Seq_{ave}(\rho_\psi) = \int_{l_m,\ldots,l_2,l_1} \frac{1}{K^m} Seq_l(\rho_\psi) \approx \langle\!\langle E_\psi | \Lambda \Lambda^m_{dep} | \rho_\psi \rangle\!\rangle.$$

The leftover Λ can be absorbed into the measurement $\langle\!\langle E_\psi|$, and therefore the average Clifford gate fidelity can be extracted from a single exponential decay curve (2.19).

Clifford-based randomized benchmarking is a theoretically valid tool for characterizing multi-qubit gates by using the multi-qubit Clifford groups. However, most Clifford gates are difficult to be directly implemented. They typically require a complex compilation using the native X/Y_π and $X/Y_{\pi/2}$ gates. For a large number of qubits, there can be a huge variation in the compilation complexity across the entire group, and thus the assumption of gate-independent error will no longer be valid.

INTERLEAVED RANDOMIZED BENCHMARKING

The standard randomized benchmarking discussed above can only characterize the average fidelity of the Clifford group. Often it is more demanding to access the fidelity of a particular gate $\mathcal{G}$. This is usually done by interleaving the target gate $\mathcal{G}$ with random Clifford gates [60]. The sequence can be written as:

$$Seq^{int}(\rho_\psi) = \langle\!\langle E_\psi | \Lambda \mathcal{C}_{l_{m+1}} \mathcal{G} \Lambda_\mathcal{G} \Lambda \mathcal{C}_{l_m} \ldots \mathcal{G} \Lambda_\mathcal{G} \Lambda \mathcal{C}_{l_2} \mathcal{G} \Lambda_\mathcal{G} \Lambda \mathcal{C}_{l_1} | \rho_\psi \rangle\!\rangle. \tag{2.21}$$

For simplicity, the error associated to $\mathcal{G}$, $\Lambda_\mathcal{G}$, is expressed as an error happening before the gate. When $\mathcal{G}$ is a Clifford gate, the sequence above can be written as:

$$Seq^{int}(\rho_\psi) = \langle\!\langle E_\psi | \Lambda \mathcal{C}_{l_{m+1}} \Lambda' \mathcal{C}'_{l_m} \ldots \Lambda' \mathcal{C}'_{l_2} \Lambda' \mathcal{C}'_{l_1} | \rho_\psi \rangle\!\rangle, \tag{2.22}$$

with $\mathcal{C}'_{l_m} = \mathcal{G}\mathcal{C}_{l_m}$ and $\Lambda' = \Lambda_\mathcal{G}\Lambda$. This resembles a depolarizing sequence, and the depolarizing parameter $p_\mathcal{G}$ can be fitted from the outcomes, just like the standard RB. To extract the error of $\mathcal{G}$, a reference RB experiment needs to be performed in the standard format, which yields a depolarizing parameter p_{ref}. As demonstrated by Magesan, *et al.* [60], the average gate error in the noise channel $\Lambda_\mathcal{G}$ is estimated by:

$$r_\mathcal{G} = \frac{(1 - p_\mathcal{G}/p_{ref})(d-1)}{d}, \tag{2.23}$$

with d the dimension of the total state space. However, interleaved RB is only valid if the target gate is a Clifford gate. Interleaving a gate outside the Clifford group can break the depolarizing channel and yield a non-exponential decay [61, 62].

SIMULTANEOUS RANDOMIZED BENCHMARKING

Apart from the average fidelities of a gate by itself, it is also useful to estimate the crosstalk errors and correlated errors arising from residual qubit-qubit interactions and environmental fluctuations. A straightforward approach is to simultaneously apply randomized benchmarking sequences on different subsystems [63]. As an example, we look into a

two-qubit system and assume there is no correlation in the initial state and the POVM. When simultaneously performing RB on each qubit, the sequence is

$$Seq^{sim}(\rho) = \langle\langle E|\Lambda\mathcal{C}^1_{l_{m+1}} \otimes \mathcal{C}^2_{l_{m+1}} \Lambda\mathcal{C}^1_{l_m} \otimes \mathcal{C}^2_{l_m} ... \Lambda\mathcal{C}^1_{l_2} \otimes \mathcal{C}^2_{l_2} \Lambda\mathcal{C}^1_{l_1} \otimes \mathcal{C}^2_{l_1} |\rho\rangle\rangle.$$

Here $\rho = \rho^1 \otimes \rho^2$ and $E = E^1 \otimes E^2$ are the two-qubit joint state and the joint POVM respectively. The superscripts indicate the qubit index. Λ is the gate-independent and Markovian error associated to each pair of simultaneous single-qubit Clifford gates $\mathcal{C}^1_{l_i} \otimes \mathcal{C}^2_{l_i}$. Now assuming the errors are not correlated, there is $\Lambda = \Lambda^1 \otimes \Lambda^2$. The two-qubit quantum channel under simultaneous twirling simply becomes a tensor product of two independent single-qubit depolarizing channels:

$$\Lambda^{sim}_{dep}(\rho) = (p_1\rho^1 + \frac{1-p_1}{2} I) \otimes (p_2\rho^2 + \frac{1-p_2}{2} I),$$

where p_1 and p_2 are the depolarizing parameters in the subspaces of Q_1 and Q_2 respectively. This results in a non-uniform depolarization as shown in the PTM below:

$$\Lambda^{sim}_{dep} = \begin{pmatrix} 1 & 0 & 0 & 0 \\ 0 & p_1\mathbf{I}_1 & 0 & 0 \\ 0 & 0 & p_2\mathbf{I}_2 & 0 \\ 0 & 0 & 0 & p_{12}\mathbf{I}_{12} \end{pmatrix}. \tag{2.24}$$

Here $\mathbf{I}_1$, $\mathbf{I}_2$, $\mathbf{I}_{12}$ represent the subspaces of Q_1, Q_2, and the correlation terms between them, spanned by $X/Y/Z \otimes I$, $I \otimes X/Y/Z$, and $X/Y/Z \otimes X/Y/Z$ respectively. This clearly deviates from a two-qubit depolarizing channel in which $p_1 = p_2 = p_{12}$.

In this particular case which contains no correlated errors, there is $p_{12} = p_1 p_2$, so Λ^{sim}_{dep} can be characterized by fitting p_1 and p_2 from the individual single-qubit measurement outcomes. However, more generally, there are correlations between the qubits, meaning that $\Lambda \neq \Lambda^1 \otimes \Lambda^2$, and thus $p_{12} \neq p_1 p_2$. The complete error syndrome cannot be diagnosed by just looking into single-qubit subspaces. The value $|p_{12} - p_1 p_2|$ is usually used as an indicator of the error correlations [63, 64] (also see Chapter 3). When concatenating simultaneous Clifford gates, the three subspaces in the initial state experience different exponential decays. Dividing a POVM E and an initial state ρ into the subspaces:

$$E = \frac{1}{2}(I, E_{\mathbf{I}_1}, E_{\mathbf{I}_2}, E_{\mathbf{I}_{12}}),$$
$$\rho = \frac{1}{2}(I, \rho_{\mathbf{I}_1}, \rho_{\mathbf{I}_2}, \rho_{\mathbf{I}_{12}})^T.$$

The sequence fidelity can now be calculated as

$$\begin{aligned} F_{seq}(\rho) &= Tr[E(\Lambda^{sim}_{dep})^m(\rho)] \\ &= Tr[E_{\mathbf{I}_1}\rho_{\mathbf{I}_1}]p_1^m + Tr[E_{\mathbf{I}_2}\rho_{\mathbf{I}_2}]p_2^m + Tr[E_{\mathbf{I}_{12}}\rho_{\mathbf{I}_{12}}]p_{12}^m + \frac{1}{4} \\ &= A_1 p_1^m + A_2 p_2^m + A_{12} p_{12}^m + B. \end{aligned}$$

The sequence fidelity decays following a combination of three exponential curves. As the fidelity of the simultaneous Clifford gate can be calculated using Λ_{dep}^{sim}:

$$\begin{aligned} F_{C\otimes C} &= \frac{1}{d(d+1)}(Tr[I\Lambda_{dep}^{sim}] + d) \\ &= \frac{1}{20}(5 + 3p_1 + 3p_2 + 9p_{12}). \end{aligned}$$

This shows that the three depolarizing parameters must be individually measured. Comparing this expression to Eq. 2.16, an effective depolarizing parameter can be defined as

$$p^{eff} = \frac{3}{15}p_1 + \frac{3}{15}p_2 + \frac{9}{15}p_{12}.$$

A non-uniform depolarizing channel can also be formed for other reasons, e.g. if there is strong non-Markovian error or state leakage, or if the gate set being used is not the Clifford group. The latter can also happen if the target gate in the interleaved RB does not belong to the Clifford group. More generalized RB protocols, such as character randomized benchmarking, have been developed to solve these problems [62, 64, 65] as we discuss in Chapter 3.

2.5. PROGRESS IN SPIN QUBIT GATE FIDELITIES

To provide a reference for the development of the high-fidelity gates in spin qubits, we collect data from published works and summarize them in the table below, including the benchmarking methods, materials, types of qubit, numbers of qubit, and average single-qubit gate fidelities (F_{1Q}) and two-qubit gate fidelities (F_{2Q}):

Year	Reference	Method	Material	Type	Num	F_{1Q}	F_{2Q}
2014	Veldhorst [20]	RB	$^{28}Si/SiO_2$	spin-1/2	1	99.59%	-
2014	Muhonen [66]	CPMG	P in ^{28}Si	spin-1/2	1	99.6%	-
2014	Kim [67]	QPT	Si/SiGe	hybrid	1	85%	-
2015	Kim [68]	QPT	Si/SiGe	hybrid	1	93-96%	-
2015	Kim [69]	QPT/GST	Si/SiGe	hybrid	1	90%/97%	-
2016	Dehollain [70]	GST/RB	P in ^{28}Si	spin-1/2	1	99.942%	-
2016	Kawakami [24]	RB	Si/SiGe	spin-1/2	1	98.99%	-
2016	Takeda [71]	RB	Si/SiGe	spin-1/2	1	99.59%	-
2016	Nichol [72]	QPT	GaAs	S-T	1	98.6%	90%
2018	Yoneda [73]	RB	$^{28}Si/SiGe$	spin-1/2	1	99.926%	-
2018	Watson [27]	RB	Si/SiGe	spin-1/2	2	98.93-99.36%	-
2018	Zajac [28]	RB	Si/SiGe	spin-1/2	2	99.3-99.7%	-
2018	Takeda [74]	RB	$^{28}Si/SiGe$	spin-1/2	1	99.93%	-
2018	Chan [75]	RB	$^{28}Si/SiO_2$	spin-1/2	1	99.91%	-
2019	Xue [64] (Ch.3)	RB	Si/SiGe	spin-1/2	2	98.79-99.2%	92%
2019	Andrews [65]	RB	$^{28}Si/SiGe$	exchange-only	1	98.65%	-
2019	Huang [76]	RB	$^{28}Si/SiO_2$	spin-1/2	2	98.7-99.9%	98%
2019	Yang [77]	RB	$^{28}Si/SiO_2$	spin-1/2	1	99.954%	-
2020	Hendricx [78]	RB	Ge/SiGe	spin-1/2	2	99.3%	-
2020	Yang [79]	RB	$^{28}Si/SiO_2$	spin-1/2	1	98.6-99.76%	-
2020	Petit [80]	RB	$^{28}Si/SiO_2$	spin-1/2	2	98.7-99.3%	86.1%
2020	Nakajima [81]	RB	GaAs	spin-1/2	1	97.5%	-
2020	Takeda [82]	RB	Si/SiGe	S-T	1	99.6%	-
2020	Cerfontaine [83]	RB	GaAs	S-T	1	99.5%	-
2020	Xue [14] (Ch.8)	RB	$^{28}Si/SiGe$	spin-1/2	1	99.69-99.71%	-
2020	Hendricx [84]	RB	Ge/SiGe	spin-1/2	4	99.3-99.9%	-
2020	Takeda [85]	RB	Si/SiGe	spin-1/2	3	99.43-99.91%	-
2021	Zwerver [12]	RB	$^{28}Si/SiO_2$	spin-1/2	2	99.0-99.1%	-
2021	Mądzik [86]	GST	P in ^{28}Si	spin-1/2	2	99.21-99.93%	99.21%
2021	Xue [21] (Ch.7)	GST	$^{28}Si/SiGe$	spin-1/2	2	99.61-99.87%	99.65%
2021	Nori [87]	RB	$^{28}Si/SiGe$	spin-1/2	2	99.84%	99.51%
2021	Mills [88]	GST/RB	$^{28}Si/SiGe$	spin-1/2	2	99.9%	99.81%
Total	-	-	-	-	46	-	-

Table 2.1: Reported spin qubit gate fidelities.

REFERENCES

[1] L. M. K. Vandersypen and I. L. Chuang, *NMR techniques for quantum control and computation,* Rev. Mod. Phys. **76**, 1037 (2005).

[2] F. Bloch and A. Siegert, *Magnetic resonance for nonrotating fields,* Phys. Rev. **57**, 522 (1940).

[3] D. P. DiVincenzo, *The physical implementation of quantum computation,* Fortschritte der Physik: Progress of Physics **48**, 771 (2000).

[4] D. Loss and D. P. DiVincenzo, *Quantum computation with quantum dots,* Phys. Rev. A **57**, 120 (1998).

[5] T. Meunier, V. E. Calado, and L. M. K. Vandersypen, *Efficient controlled-phase gate for single-spin qubits in quantum dots,* Phys. Rev. B **83**, 121403 (2011).

[6] J. R. Petta, A. C. Johnson, J. M. Taylor, E. A. Laird, A. Yacoby, M. D. Lukin, C. M. Marcus, M. P. Hanson, and A. C. Gossard, *Coherent manipulation of coupled electron spins in semiconductor quantum dots,* Science **309**, 2180 (2005).

[7] R. C. Bialczak, M. Ansmann, M. Hofheinz, E. Lucero, M. Neeley, A. D. O'Connell, D. Sank, H. Wang, J. Wenner, M. Steffen, *et al.*, *Quantum process tomography of a universal entangling gate implemented with Josephson phase qubits,* Nature Physics **6**, 409 (2010).

[8] F. A. Zwanenburg, A. S. Dzurak, A. Morello, M. Y. Simmons, L. C. L. Hollenberg, G. Klimeck, S. Rogge, S. N. Coppersmith, and M. A. Eriksson, *Silicon quantum electronics,* Rev. Mod. Phys. **85**, 961 (2013).

[9] M. Atatüre, D. Englund, N. Vamivakas, S.-Y. Lee, and J. Wrachtrup, *Material platforms for spin-based photonic quantum technologies,* Nature Reviews Materials **3**, 38 (2018).

[10] R. Hanson, L. P. Kouwenhoven, J. R. Petta, S. Tarucha, and L. M. K. Vandersypen, *Spins in few-electron quantum dots,* Rev. Mod. Phys. **79**, 1217 (2007).

[11] L. M. K. Vandersypen, H. Bluhm, J. S. Clarke, A. S. Dzurak, R. Ishihara, A. Morello, D. J. Reilly, L. R. Schreiber, and M. Veldhorst, *Interfacing spin qubits in quantum dots and donors–hot, dense, and coherent,* npj Quantum Information **3**, 34 (2017).

[12] A. Zwerver, T. Krähenmann, T. Watson, L. Lampert, H. C. George, R. Pillarisetty, S. Bojarski, P. Amin, S. Amitonov, J. Boter, *et al.*, *Qubits made by advanced semiconductor manufacturing,* Nature Electronics **5**, 184 (2022).

[13] V. Srinivasa, K. C. Nowack, M. Shafiei, L. M. K. Vandersypen, and J. M. Taylor, *Simultaneous spin-charge relaxation in double quantum dots,* Phys. Rev. Lett. **110**, 196803 (2013).

[14] X. Xue, B. Patra, J. P. van Dijk, N. Samkharadze, S. Subramanian, A. Corna, B. Paquelet Wuetz, C. Jeon, F. Sheikh, E. Juarez-Hernandez, *et al.*, *CMOS-based cryogenic control of silicon quantum circuits,* Nature **593**, 205 (2021).

[15] J. Elzerman, R. Hanson, L. W. Van Beveren, B. Witkamp, L. Vandersypen, and L. P. Kouwenhoven, *Single-shot read-out of an individual electron spin in a quantum dot,* Nature **430**, 431 (2004).

[16] K. Ono, D. Austing, Y. Tokura, and S. Tarucha, *Current rectification by pauli exclusion in a weakly coupled double quantum dot system,* Science **297**, 1313 (2002).

[17] A. Morello, J. J. Pla, F. A. Zwanenburg, K. W. Chan, K. Y. Tan, H. Huebl, M. Möttönen, C. D. Nugroho, C. Yang, J. A. Van Donkelaar, *et al.*, *Single-shot readout of an electron spin in silicon,* Nature **467**, 687 (2010).

[18] C. Yang, A. Rossi, R. Ruskov, N. Lai, F. Mohiyaddin, S. Lee, C. Tahan, G. Klimeck, A. Morello, and A. Dzurak, *Spin-valley lifetimes in a silicon quantum dot with tunable valley splitting,* Nature communications **4**, 1 (2013).

[19] F. H. Koppens, C. Buizert, K.-J. Tielrooij, I. T. Vink, K. C. Nowack, T. Meunier, L. Kouwenhoven, and L. Vandersypen, *Driven coherent oscillations of a single electron spin in a quantum dot,* Nature **442**, 766 (2006).

[20] M. Veldhorst, J. Hwang, C. Yang, A. Leenstra, B. de Ronde, J. Dehollain, J. Muhonen, F. Hudson, K. M. Itoh, A. Morello, *et al.*, *An addressable quantum dot qubit with fault-tolerant control-fidelity,* Nature Nanotechnology **9**, 981 (2014).

[21] X. Xue, M. Russ, N. Samkharadze, B. Undseth, A. Sammak, G. Scappucci, and L. M. Vandersypen, *Quantum logic with spin qubits crossing the surface code threshold,* Nature **601**, 343 (2022).

[22] K. C. Nowack, F. Koppens, Y. V. Nazarov, and L. Vandersypen, *Coherent control of a single electron spin with electric fields,* Science **318**, 1430 (2007).

[23] M. Pioro-Ladrière, T. Obata, Y. Tokura, Y.-S. Shin, T. Kubo, K. Yoshida, T. Taniyama, and S. Tarucha, *Electrically driven single-electron spin resonance in a slanting zeeman field,* Nature Physics **4**, 776 (2008).

[24] E. Kawakami, P. Scarlino, D. R. Ward, F. R. Braakman, D. E. Savage, M. G. Lagally, M. Friesen, S. N. Coppersmith, M. A. Eriksson, and L. M. K. Vandersypen, *Electrical control of a long-lived spin qubit in a si/sige quantum dot,* Nature Nanotechnology **9**, 666 (2014).

[25] Y. Tokura, W. G. van der Wiel, T. Obata, and S. Tarucha, *Coherent single electron spin control in a slanting zeeman field,* Phys. Rev. Lett. **96**, 047202 (2006).

[26] M. Veldhorst, C. Yang, J. Hwang, W. Huang, J. Dehollain, J. Muhonen, S. Simmons, A. Laucht, F. Hudson, K. M. Itoh, *et al.*, *A two-qubit logic gate in silicon,* Nature **526**, 410 (2015).

[27] T. F. Watson, S. G. J. Philips, E. Kawakami, D. R. Ward, P. Scarlino, M. Veldhorst, D. E. Savage, M. G. Lagally, M. Friesen, S. N. Coppersmith, M. A. Eriksson, and L. M. K. Vandersypen, *A programmable two-qubit quantum processor in silicon,* Nature **555**, 633 (2018).

[28] D. M. Zajac, A. J. Sigillito, M. Russ, F. Borjans, J. M. Taylor, G. Burkard, and J. R. Petta, *Resonantly driven cnot gate for electron spins,* Science **359**, 439 (2017).

[29] K. Nowack, M. Shafiei, M. Laforest, G. Prawiroatmodjo, L. Schreiber, C. Reichl, W. Wegscheider, and L. Vandersypen, *Single-shot correlations and two-qubit gate of solid-state spins,* Science **333**, 1269 (2011).

[30] Y. He, S. Gorman, D. Keith, L. Kranz, J. Keizer, and M. Simmons, *A two-qubit gate between phosphorus donor electrons in silicon,* Nature **571**, 371 (2019).

[31] O. E. Dial, M. D. Shulman, S. P. Harvey, H. Bluhm, V. Umansky, and A. Yacoby, *Charge noise spectroscopy using coherent exchange oscillations in a singlet-triplet qubit,* Phys. Rev. Lett. **110**, 146804 (2013).

[32] F. Martins, F. K. Malinowski, P. D. Nissen, E. Barnes, S. Fallahi, G. C. Gardner, M. J. Manfra, C. M. Marcus, and F. Kuemmeth, *Noise suppression using symmetric exchange gates in spin qubits,* Phys. Rev. Lett. **116**, 116801 (2016).

[33] M. Reed, B. Maune, R. Andrews, M. Borselli, K. Eng, M. Jura, A. Kiselev, T. Ladd, S. Merkel, I. Milosavljevic, *et al.*, *Reduced sensitivity to charge noise in semiconductor spin qubits via symmetric operation,* Phys. Rev. Lett. **116**, 110402 (2016).

[34] C. Zhang, R. E. Throckmorton, X.-C. Yang, X. Wang, E. Barnes, and S. D. Sarma, *Randomized benchmarking of barrier versus tilt control of a singlet-triplet qubit,* Phys. Rev. Lett. **118**, 216802 (2017).

[35] Y.-P. Shim and C. Tahan, *Barrier versus tilt exchange gate operations in spin-based quantum computing,* Phys. Rev. B **97**, 155402 (2018).

[36] T. Hensgens, T. Fujita, L. Janssen, X. Li, C. Van Diepen, C. Reichl, W. Wegscheider, S. D. Sarma, and L. M. Vandersypen, *Quantum simulation of a Fermi–Hubbard model using a semiconductor quantum dot array,* Nature **548**, 70 (2017).

[37] C. Volk, A.-M. J. Zwerver, U. Mukhopadhyay, P. T. Eendebak, C. J. van Diepen, J. P. Dehollain, T. Hensgens, T. Fujita, C. Reichl, W. Wegscheider, *et al.*, *Loading a quantum-dot based "Qubyte" register,* npj Quantum Information **5**, 1 (2019).

[38] F. Fedele, A. Chatterjee, S. Fallahi, G. C. Gardner, M. J. Manfra, and F. Kuemmeth, *Simultaneous operations in a two-dimensional array of singlet-triplet qubits,* PRX Quantum **2**, 040306 (2021).

[39] P.-A. Mortemousque, E. Chanrion, B. Jadot, H. Flentje, A. Ludwig, A. D. Wieck, M. Urdampilleta, C. Bäuerle, and T. Meunier, *Coherent control of individual electron spins in a two-dimensional quantum dot array,* Nature Nanotechnology **16**, 296 (2021).

[40] B. M. Maune, M. G. Borselli, B. Huang, T. D. Ladd, P. W. Deelman, K. S. Holabird, A. A. Kiselev, I. Alvarado-Rodriguez, R. S. Ross, A. E. Schmitz, *et al.*, *Coherent singlet-triplet oscillations in a silicon-based double quantum dot,* Nature **481**, 344 (2012).

[41] T. McJunkin, E. MacQuarrie, L. Tom, S. Neyens, J. Dodson, B. Thorgrimsson, J. Corrigan, H. E. Ercan, D. Savage, M. Lagally, *et al.*, *Valley splittings in Si/SiGe quantum dots with a germanium spike in the silicon well,* Phys. Rev. B **104**, 085406 (2021).

[42] W. Lawrie, H. Eenink, N. Hendrickx, J. Boter, L. Petit, S. Amitonov, M. Lodari, B. Paquelet Wuetz, C. Volk, S. Philips, *et al.*, *Quantum dot arrays in silicon and germanium,* Applied Physics Letters **116**, 080501 (2020).

[43] B. Paquelet Wuetz, M. P. Losert, A. Tosato, M. Lodari, P. L. Bavdaz, L. Stehouwer, P. Amin, J. S. Clarke, S. N. Coppersmith, A. Sammak, *et al.*, *Effect of quantum hall edge strips on valley splitting in silicon quantum wells,* Phys. Rev. Lett. **125**, 186801 (2020).

[44] M. A. Nielsen and I. L. Chuang, *Quantum Computation and Quantum Information: 10th Anniversary Edition* (Cambridge University Press, 2011).

[45] R. Jozsa, *Fidelity for mixed quantum states,* Journal of Modern Optics **41**, 2315 (1994).

[46] I. L. Chuang and M. A. Nielsen, *Prescription for experimental determination of the dynamics of a quantum black box,* Journal of Modern Optics **44**, 2455 (1997).

[47] J. B. Altepeter, E. R. Jeffrey, and P. G. Kwiat, *Photonic state tomography,* Advances in Atomic, Molecular, and Optical Physics **52**, 105 (2005).

[48] M. Takahashi, S. D. Bartlett, and A. C. Doherty, *Tomography of a spin qubit in a double quantum dot,* Phys. Rev. A **88**, 022120 (2013).

[49] B. D'Anjou and W. A. Coish, *Soft decoding of a qubit readout apparatus,* Phys. Rev. Lett. **113**, 230402 (2014).

[50] D. Keith, S. Gorman, L. Kranz, Y. He, J. Keizer, M. Broome, and M. Simmons, *Benchmarking high fidelity single-shot readout of semiconductor qubits,* New Journal of Physics **21**, 063011 (2019).

[51] A. G. Fowler, M. Mariantoni, J. M. Martinis, and A. N. Cleland, *Surface codes: Towards practical large-scale quantum computation,* Phys. Rev. A **86**, 032324 (2012).

[52] E. Magesan, J. M. Gambetta, and J. Emerson, *Scalable and robust randomized benchmarking of quantum processes,* Phys. Rev. Lett. **106**, 180504 (2011).

[53] M. A. Nielsen, *The entanglement fidelity and quantum error correction,* arXiv:quant-ph/9606012 (1996).

[54] M. A. Nielsen, *A simple formula for the average gate fidelity of a quantum dynamical operation,* Physics Letters A **303**, 249 (2002).

[55] D. Greenbaum, *Introduction to quantum gate set tomography,* arXiv:1509.02921 (2015).

[56] E. Nielsen, J. K. Gamble, K. Rudinger, T. Scholten, K. Young, and R. Blume-Kohout, *Gate set tomography,* Quantum **5**, 557 (2021).

[57] C. Stark, *Self-consistent tomography of the state-measurement gram matrix,* Phys. Rev. A **89**, 052109 (2014).

[58] J. Emerson, R. Alicki, and K. Życzkowski, *Scalable noise estimation with random unitary operators,* Journal of Optics B: Quantum and Semiclassical Optics **7**, S347 (2005).

[59] C. Dankert, R. Cleve, J. Emerson, and E. Livine, *Exact and approximate unitary 2-designs and their application to fidelity estimation,* Phys. Rev. A **80**, 012304 (2009).

[60] E. Magesan, J. M. Gambetta, B. R. Johnson, C. A. Ryan, J. M. Chow, S. T. Merkel, M. P. Da Silva, G. A. Keefe, M. B. Rothwell, T. A. Ohki, *et al., Efficient measurement of quantum gate error by interleaved randomized benchmarking,* Phys. Rev. Lett. **109**, 080505 (2012).

[61] R. Harper and S. T. Flammia, *Estimating the fidelity of T gates using standard interleaved randomized benchmarking,* Quantum Science and Technology **2**, 015008 (2017).

[62] J. Helsen, X. Xue, L. M. Vandersypen, and S. Wehner, *A new class of efficient randomized benchmarking protocols,* npj Quantum Information **5**, 1 (2019).

[63] J. M. Gambetta, A. D. Córcoles, S. T. Merkel, B. R. Johnson, J. A. Smolin, J. M. Chow, C. A. Ryan, C. Rigetti, S. Poletto, T. A. Ohki, *et al., Characterization of addressability by simultaneous randomized benchmarking,* Phys. Rev. Lett. **109**, 240504 (2012).

[64] X. Xue, T. F. Watson, J. Helsen, D. R. Ward, D. E. Savage, M. G. Lagally, S. N. Coppersmith, M. A. Eriksson, S. Wehner, and L. M. K. Vandersypen, *Benchmarking gate fidelities in a* Si/SiGe *two-qubit device,* Phys. Rev. X **9**, 021011 (2019).

[65] R. W. Andrews, C. Jones, M. D. Reed, A. M. Jones, S. D. Ha, M. P. Jura, J. Kerckhoff, M. Levendorf, S. Meenehan, S. T. Merkel, *et al., Quantifying error and leakage in an encoded Si/SiGe triple-dot qubit,* Nature Nanotechnology **14**, 747 (2019).

[66] J. T. Muhonen, J. P. Dehollain, A. Laucht, F. E. Hudson, R. Kalra, T. Sekiguchi, K. M. Itoh, D. N. Jamieson, J. C. McCallum, A. S. Dzurak, *et al., Storing quantum information for 30 seconds in a nanoelectronic device,* Nature Nanotechnology **9**, 986 (2014).

[67] D. Kim, Z. Shi, C. Simmons, D. Ward, J. Prance, T. S. Koh, J. K. Gamble, D. Savage, M. Lagally, M. Friesen, *et al., Quantum control and process tomography of a semiconductor quantum dot hybrid qubit,* Nature **511**, 70 (2014).

[68] D. Kim, D. R. Ward, C. B. Simmons, D. E. Savage, M. G. Lagally, M. Friesen, S. N. Coppersmith, and M. A. Eriksson, *High-fidelity resonant gating of a silicon-based quantum dot hybrid qubit,* Npj Quantum Information **1**, 1 (2015).

[69] D. Kim, D. Ward, C. Simmons, J. K. Gamble, R. Blume-Kohout, E. Nielsen, D. Savage, M. Lagally, M. Friesen, S. Coppersmith, *et al.*, *Microwave-driven coherent operation of a semiconductor quantum dot charge qubit,* Nature Nanotechnology **10**, 243 (2015).

[70] J. P. Dehollain, J. T. Muhonen, R. Blume-Kohout, K. M. Rudinger, J. K. Gamble, E. Nielsen, A. Laucht, S. Simmons, R. Kalra, A. S. Dzurak, *et al.*, *Optimization of a solid-state electron spin qubit using gate set tomography,* New Journal of Physics **18**, 103018 (2016).

[71] K. Takeda, J. Kamioka, T. Otsuka, J. Yoneda, T. Nakajima, M. R. Delbecq, S. Amaha, G. Allison, T. Kodera, S. Oda, *et al.*, *A fault-tolerant addressable spin qubit in a natural silicon quantum dot,* Science advances **2**, e1600694 (2016).

[72] J. M. Nichol, L. A. Orona, S. P. Harvey, S. Fallahi, G. C. Gardner, M. J. Manfra, and A. Yacoby, *High-fidelity entangling gate for double-quantum-dot spin qubits,* npj Quantum Information **3**, 1 (2017).

[73] J. Yoneda, K. Takeda, T. Otsuka, T. Nakajima, M. R. Delbecq, G. Allison, T. Honda, T. Kodera, S. Oda, Y. Hoshi, N. Usami, K. M. Itoh, and S. Tarucha, *A quantum-dot spin qubit with coherence limited by charge noise and fidelity higher than 99.9%,* Nature Nanotechnology **13**, 102 (2018).

[74] K. Takeda, J. Yoneda, T. Otsuka, T. Nakajima, M. Delbecq, G. Allison, Y. Hoshi, N. Usami, K. Itoh, S. Oda, *et al.*, *Optimized electrical control of a Si/SiGe spin qubit in the presence of an induced frequency shift,* npj Quantum Information **4**, 1 (2018).

[75] K. Chan, W. Huang, C. Yang, J. Hwang, B. Hensen, T. Tanttu, F. Hudson, K. M. Itoh, A. Laucht, A. Morello, *et al.*, *Assessment of a silicon quantum dot spin qubit environment via noise spectroscopy,* Phys. Rev. Applied **10**, 044017 (2018).

[76] W. Huang, C. Yang, K. Chan, T. Tanttu, B. Hensen, R. Leon, M. Fogarty, J. Hwang, F. Hudson, K. M. Itoh, A. Morello, A. Laucht, and A. S. Dzurak, *Fidelity benchmarks for two-qubit gates in silicon,* Nature **569**, 532 (2019).

[77] C. Yang, K. Chan, R. Harper, W. Huang, T. Evans, J. Hwang, B. Hensen, A. Laucht, T. Tanttu, F. Hudson, *et al.*, *Silicon qubit fidelities approaching incoherent noise limits via pulse engineering,* Nature Electronics **2**, 151 (2019).

[78] N. Hendrickx, D. Franke, A. Sammak, G. Scappucci, and M. Veldhorst, *Fast two-qubit logic with holes in germanium,* Nature **577**, 487 (2020).

[79] C. H. Yang, R. Leon, J. Hwang, A. Saraiva, T. Tanttu, W. Huang, J. C. Lemyre, K. W. Chan, K. Tan, F. E. Hudson, *et al.*, *Operation of a silicon quantum processor unit cell above one kelvin,* Nature **580**, 350 (2020).

[80] L. Petit, H. Eenink, M. Russ, W. Lawrie, N. Hendrickx, S. Philips, J. Clarke, L. Vandersypen, and M. Veldhorst, *Universal quantum logic in hot silicon qubits,* Nature **580**, 355 (2020).

[81] T. Nakajima, A. Noiri, K. Kawasaki, J. Yoneda, P. Stano, S. Amaha, T. Otsuka, K. Takeda, M. R. Delbecq, G. Allison, *et al.*, *Coherence of a driven electron spin qubit actively decoupled from quasistatic noise,* Phys. Rev. X **10**, 011060 (2020).

[82] K. Takeda, A. Noiri, J. Yoneda, T. Nakajima, and S. Tarucha, *Resonantly driven singlet-triplet spin qubit in silicon,* Phys. Rev. Lett. **124**, 117701 (2020).

[83] P. Cerfontaine, T. Botzem, J. Ritzmann, S. S. Humpohl, A. Ludwig, D. Schuh, D. Bougeard, A. D. Wieck, and H. Bluhm, *Closed-loop control of a GaAs-based singlet-triplet spin qubit with 99.5% gate fidelity and low leakage,* Nature communications **11**, 1 (2020).

[84] N. W. Hendrickx, W. I. Lawrie, M. Russ, F. van Riggelen, S. L. de Snoo, R. N. Schouten, A. Sammak, G. Scappucci, and M. Veldhorst, *A four-qubit germanium quantum processor,* Nature **591**, 580 (2021).

[85] K. Takeda, A. Noiri, T. Nakajima, J. Yoneda, T. Kobayashi, and S. Tarucha, *Quantum tomography of an entangled three-qubit state in silicon,* Nature Nanotechnology , 1 (2021).

[86] M. T. Mądzik, S. Asaad, A. Youssry, B. Joecker, K. M. Rudinger, E. Nielsen, K. C. Young, T. J. Proctor, A. D. Baczewski, A. Laucht, *et al.*, *Precision tomography of a three-qubit donor quantum processor in silicon,* Nature **601**, 348 (2022).

[87] A. Noiri, K. Takeda, T. Nakajima, T. Kobayashi, A. Sammak, G. Scappucci, and S. Tarucha, *Fast universal quantum gate above the fault-tolerance threshold in silicon,* Nature **601**, 338 (2022).

[88] A. Mills, C. Guinn, M. Gullans, A. Sigillito, M. Feldman, E. Nielsen, and J. Petta, *Two-qubit silicon quantum processor with operation fidelity exceeding 99%,* Science Advances **8**, eabn5130 (2022).

3

BENCHMARKING GATE FIDELITIES OF A SI/SIGE TWO QUBIT DEVICE

We report the first complete characterization of single-qubit and two-qubit gate fidelities in silicon-based spin qubits, including cross-talk and error correlations between the two qubits. To do so, we use a combination of standard randomized benchmarking and a recently introduced method called character randomized benchmarking, which allows for more reliable estimates of the two-qubit fidelity in this system, here giving a 92% fidelity estimate for the controlled-Z gate. Interestingly, with character randomized benchmarking, the two-qubit gate fidelity can be obtained by studying the additional decay induced by interleaving the two-qubit gate in a reference sequence of single-qubit gates only. This work sets the stage for further improvements in all the relevant gate fidelities in silicon spin qubits beyond the error threshold for fault-tolerant quantum computation.

This chapter has been published in Phys. Rev. X **9**, 021011 (2019).

3.1. INTRODUCTION

With steady progress towards practical quantum computers, it becomes increasingly important to efficiently characterize the relevant quantum gates. Quantum process tomography [1–3] provides a way to reconstruct a complete mathematical description of any quantum process, but has several drawbacks. The resources required increase exponentially with qubit number and the procedure cannot distinguish pure gate errors from state preparation and measurement (SPAM) errors, making it difficult to reliably extract small gate error rates. Randomized benchmarking (RB) was introduced as a convenient alternative [4–7]. It estimates the gate fidelity as a concise and relevant metric, requires fewer resources, is more robust against SPAM errors and works well even for low gate error rates.

Various randomized benchmarking methods have been investigated to extract fidelities and errors in different scenarios. In standard randomized benchmarking, sequences of increasing numbers of random Clifford operations are applied to one or more qubits [5, 6] (for a single qubit, the Clifford gates are precisely the gates that rotate states along the $\hat{x}$, $\hat{y}$ or $\hat{z}$ axis on the Bloch sphere to each other). Then, loosely speaking, the average Clifford gate fidelity is extracted from how rapidly the final state diverges from the ideally expected state as a function of the number of random Clifford operations. For multi-qubit systems, the degree of cross-talk can be characterized by simultaneous randomized benchmarking, in which random single-qubit Clifford operations are applied simultaneously to different qubits [8].

In practice we will often be more interested in the fidelity of a particular quantum gate than the average fidelity of a gate set. To characterize this fidelity, we can make use of interleaved randomized benchmarking, in which a sequence of random Clifford gates is interleaved by a particular quantum gate. The fidelity of the interleaved gate can then be estimated by comparing the deviation rate from the ideal state with that obtained from standard randomized benchmarking [9], called the reference fidelity in this context. It must be noted however, that interleaved randomized benchmarking does not provide an exact characterization of the fidelity of the interleaving gate but rather gives an estimate together with upper and lower bounds. These upper and lower bounds, which are essentially due to the fact that the fidelity of the composition of two gates is not necessarily equal to the product of the fidelities of the two gates, grow closer together with increasing reference fidelity [9, 10].

A major drawback of these traditional randomized benchmarking methods is that the number of native gates that needs to be executed in sequence to implement a Clifford operation, can rapidly increase with the qubit number. For example, it takes on average 1.5 controlled-phase (CPhase) gates and 8.25 single-qubit gates to implement a two-qubit Clifford gate [11]. This in turns puts higher demands on the coherence time, which is still a challenge for near-term devices, and leads to rather loose bounds on the gate fidelity inferred from interleaved randomized benchmarking [9, 10]. Therefore, in early work characterizing two-qubit gate fidelities for superconducting qubits, the effect of the two-qubit gate projected in single-qubit space was reported instead of the actual two-qubit gate fidelity [12, 13]. For semiconductor spin qubits, even though two-qubit Bell states have been prepared [14–17] and simple quantum algorithms were implemented on two silicon spin qubits [15], the implementation issues of conventional randomized

benchmarking have long stood in the way of quantifying the two-qubit gate fidelity. These limitations can be overcome by using native gates that compile efficiently [17], which is however not always possible. Another option, which we pursue here, is to use a new method called character randomized benchmarking (CRB), which we developed in [18]. CRB allows us to extract a two-qubit gate fidelity by interleaving the two-qubit gate in a reference sequence consisting of a small number of single-qubit Clifford gates only. This results in lower compilation overhead and thus lower demand on coherence times. Moreover, CRB will generically lead to higher reference fidelities and thus sharper bounds on the fidelity of the interleaved gate. As a final benefit, CRB provides detailed information on separate decay channels and error correlations.

Here we supplement standard randomized benchmarking with character randomized benchmarking for a comprehensive study of all the relevant gate fidelities of two electron spin qubits in silicon quantum dots, including the single-qubit and two-qubit gate fidelity as well as the effect of cross-talk and correlated errors on single-qubit gate fidelities. This work is of strong interest since silicon spin qubits are highly scalable, owing to their compact size (< 100 nm pitch), coherence times up to tens of milliseconds and ability to leverage existing semiconductor technology [19, 20].

3.2. DEVICE AND QUBIT OPERATION

Fig. 3.1 shows a schematic of the device, a double quantum dot defined electrostatically in a 12 nm thick Si/SiGe quantum well, 37 nm below the semiconductor surface. The device is cooled to ~ 20 mK in a dilution refrigerator. By applying positive voltages on the accumulation gate, a two-dimensional electron gas is formed in the quantum well. Negative voltages are applied to the depletion gates in such a way that two single electrons are confined in a double well potential [15]. A 617 mT magnetic field is applied in the plane of the quantum well. Two qubits, Q1 and Q2, are encoded in the Zeeman split states of the two electrons, where spin-up represents $|1\rangle$ and spin-down represents $|0\rangle$.

Single-qubit rotations rely on electric dipole spin resonance (EDSR), making use of the transverse magnetic field gradient from three cobalt micro magnets fabricated on top of the gate stack [21]. The longitudinal magnetic field gradient leads to well-separated spin resonance frequencies of 18.34 GHz and 19.72 GHz for Q1 and Q2 respectively. The rotation axis in the $\hat{x}-\hat{y}$ plane is set by the phase of the on-resonance microwave drive, while rotations around the $\hat{z}$ axis are implemented by changing the rotating reference frame in software [22].

We use the CPhase gate as the native two-qubit gate. An exchange interaction $J(\varepsilon)$ is switched on by pulsing the detuning ε (electrochemical potential difference) between the two quantum dots, such that the respective electron wave functions overlap. Due to the large difference in qubit energy splittings, the flip-flop terms in the exchange Hamiltonian are ineffective and an Ising interaction remains [15, 16, 23, 24]. The resulting time evolution operator in the standard $\{c, |01\rangle, |10\rangle, |11\rangle\}$ basis is given by

$$U_J(t) = \begin{pmatrix} 1 & 0 & 0 & 0 \\ 0 & e^{iJ(\epsilon)t/2\hbar} & 0 & 0 \\ 0 & 0 & e^{iJ(\epsilon)t/2\hbar} & 0 \\ 0 & 0 & 0 & 1 \end{pmatrix}. \tag{3.1}$$

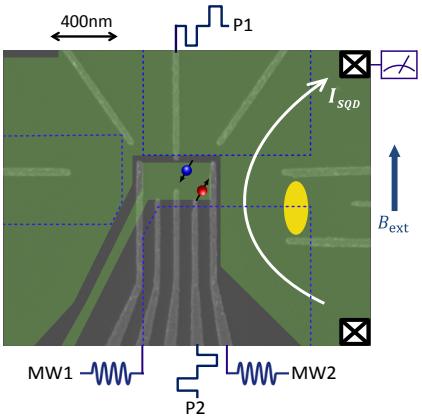

Fig. 3.1: Device Schematic. A double quantum dot is formed in the Si/SiGe quantum well, where two spin qubits Q1 (blue spin) and Q2 (red spin) are defined. The green-shaded areas show the locations of the accumulation gates on top of the double dot and the reservoir. The blue dashed lines indicate the positions of three Co micro-magnets, which form a magnetic field gradient along the qubit region. MW1 and MW2 are connected to two vector microwave sources to perform EDSR for single-qubit gates. The yellow ellipse shows the position of a larger quantum dot which is used as a charge sensor for single-shot readout. Plunger gates P1 and P2 are used to pulse to different positions in the charge stability diagram as needed for initialization, manipulation, and readout, as well as for pulsing the detuning for controlling the two-qubit gate.

Choosing $t = \pi\hbar/J(\epsilon)$ and adding single-qubit $\hat{z}$ rotations on both qubits, we obtain a controlled-Z (CZ) operator

$$Z_1\left(-\frac{\pi}{2}\right)Z_2(-\frac{\pi}{2})U_J\left(\frac{\pi\hbar}{J(\epsilon)}\right)=\begin{pmatrix}1&0&0&0\\0&1&0&0\\0&0&1&0\\0&0&0&-1\end{pmatrix}, \tag{3.2}$$

with $Z_i(\theta)$ a $\hat{z}$ rotation of qubit i over an angle θ.

Spin initialization and single-shot readout of Q2 are realized by energy-selective tunneling [25]. Q1 is initialized to its ground spin state by fast spin relaxation at a hotspot [26]. For read-out, the state of Q1 is mapped onto Q2 using a conditional π rotation [15, 24], which enables extracting the state of Q1 by measuring Q2. Further details on the measurement setup are provided in 3.7.1.

3.3. INDIVIDUAL AND SIMULTANEOUS RANDOMIZED BENCHMARKING

In standard randomized benchmarking, sequences of random multi-qubit Clifford operations are applied to a number of target qubits, followed by a final Clifford operation that, in the absence of errors, maps the qubits' state back to the initial state. A 'survival probability' is then extracted by measuring the system in a basis containing the initial state. Repeating this procedure for many random sequences of Clifford gates and aver-

aging over the resulting survival probabilities yields an average survival probability. This in effect symmetrizes the noise process in the system such that the qubits are effectively subject to a depolarizing channel. The average survival probability P then decays exponentially with the number of Clifford operations m, under broad assumptions [27–29]. By fitting the decay curve to

$$P = A\alpha^m + B, \tag{3.3}$$

where only A and B depend on the state preparation and measurement, the average fidelity of a Clifford operation can be extracted in terms of the depolarizing parameter α as

$$F_{avg} = 1 - (1-\alpha)\frac{d-1}{d}, \tag{3.4}$$

where $d = 2^N$ and N is the number of qubits.

In the present two-qubit system, we first perform standard RB on each individual qubit (filled data points in Fig. 3.2), finding $F_{avg} = 98.50 \pm 0.05\%$ for Q1 and $F_{avg} = 97.72 \pm 0.03\%$ for Q2 (all uncertainties are standard deviations). By dividing the error rate over the average number of single-qubit gates needed for a Clifford operation, we extract average single-qubit gate fidelities of $99.20 \pm 0.03\%$ for Q1 and $98.79 \pm 0.02\%$ for Q2.

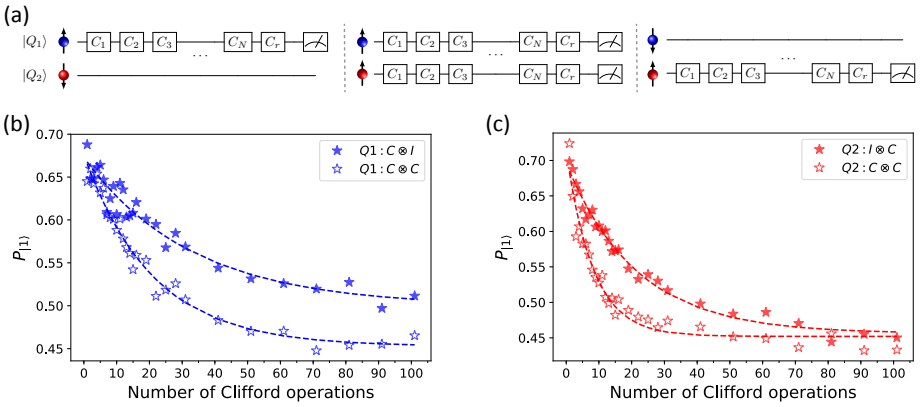

Fig. 3.2: Individual and simultaneous standard randomized benchmarking. (a) Circuit diagrams for individual single-qubit RB on Q1 (left) and Q2 (right), and simultaneous single-qubit RB (middle). (b) Probability for obtaining outcome 1 upon measurement in the $\sigma_z \otimes I$ basis as a function of the number of single-qubit Clifford operations. For the blue solid stars, Q2 is idle while a Clifford operation is applied to Q1 ($C \otimes I$). For the blue open stars, random Clifford operations are applied to Q1 and Q2 simultaneously ($C \otimes C$). For each data point, we sample 32 different random sequences, which are each repeated 100 times. Dashed lines are fit to the data with a single exponential. A constant offset of -0.06 is added to the open data points in order to compensate for a change in read-out fidelities between the two data sets, making comparison of the two traces easier. Without SPAM errors, the datapoints would decay from 1 to 0.5. (c) Analogous single-qubit RB data for Q2, with Q1 idle (red solid stars) and subject to random Clifford operations (red open stars). A constant offset of -0.05 is added to the open data points. Throughout, single-qubit Clifford operations are generated by the native gate set $\{I, X(\pi), Y(\pm\pi), X(\pm\pi/2), Y(\pm\pi/2)\}$.

In practice, single qubit gates are normally applied simultaneously to multiple qubits during quantum computation. Driving one qubit can lead to errors on the other qubit gates due to crosstalk effects such as an undesired excitation, residual qubit coupling, or heating effects. In order to assess the effects of crosstalk, we next perform single-qubit RB while simultaneously applying random Clifford operations to the other qubit (Fig. 3.2 open data points). Following [8], we denote the corresponding depolarizing parameter for qubit i while performing random gates on qubit j as $\alpha_{i|j}$. In contrast to standard RB which is insensitive to SPAM errors, we have to assume here that operations on one qubit do not affect the read-out fidelity of the other qubit [8]. Comparing with individual single-qubit randomized benchmarking results, we find that simultaneous RB decreases the average single-qubit gate fidelity for Q1 by 0.44% to 98.76±0.02% while the fidelity for Q2 decreases by 1.85% to 96.94 ± 0.05%. Since the difference in qubit frequencies of 1.38 GHz is almost three orders of magnitude larger than the Rabi frequencies (∼ 2 MHz), this crosstalk is not due to limited addressability. Furthermore, the cross-talk on Q2 persists when the drive on Q1 is applied off-resonantly, hence it is an effect of the excitation and not a result of performing random gates on Q1. Attempting to understand how the excitation leads to undesired cross-talk, we performed detailed additional studies (see [15] and 3.7.6), ruling out a number of other possible sources of cross-talk, including the AC Stark effect and residual coupling between the qubits. In addition, we observed an anomalous frequency shift on Q2 while driving Q1 [15], although larger frequency shifts did not correlate with a faster Rabi decay of Q2. Increasing the driving power did not yield a higher quality factor of the Rabi oscillations, as reported in [30], which indicates that heating could contribute to their decay. Whether heating from driving Q1 also reduces the fidelity of Q2 needs to be confirmed by further studies. Finally, cross-talk in the experimental setup is likely to be symmetric, so the observed asymmetry indicates that the microscopic details of the quantum dots must also play a role.

3.4. TWO-QUBIT RANDOMIZED BENCHMARKING

To characterize two-qubit gate fidelities, the Clifford group is expanded to a four-dimensional Hilbert space. We first implement standard two-qubit RB, sampling Clifford operations from the 11520 elements in the two-qubit Clifford group. Each two-qubit Clifford operation is compiled from single-qubit rotations and the two-qubit CZ gate, requiring on average 8.25 single-qubit rotations around $\hat{x}$ or $\hat{y}$ and 1.5 CZ gates. The measured probability to successfully recover the initial state is shown in Fig. 3.3. From a fit to the data using Eq. 3.3 and applying Eq. 3.4, we extract an average two-qubit Clifford fidelity F_{avg} of 82.10 ± 2.75%.

The large number of native gates needed to implement a single two-qubit Clifford gate, leads to a fast saturation of the decay, within about eight Clifford operations, leading to a large uncertainty on the two-qubit Clifford fidelity estimate. In addition, this fast saturation makes the randomized benchmarking data vulnerable to deviations from a single exponential decay due to different error processes being associated to each applied gate, possibly biasing the fidelity estimate [29, 31, 32]. Importantly, interleaving a specific gate in a fast decaying reference sequence also yields a rather unreliable estimate of the interleaved gate fidelity. In the present case, interleaving a CZ gate in the reference sequence of two-qubit Clifford operations is not a viable strategy to extract the

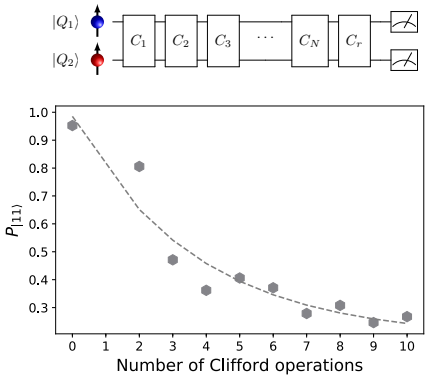

Fig. 3.3: Two-qubit Clifford Randomized Benchmarking. Probability for obtaining outcome 11 upon measurement in the $\sigma_z \otimes \sigma_z$ basis, starting from the initial state $|11\rangle$, as a function of the number of two-qubit Clifford operations. As the native gate set, we use $\{I, X(\pi), Y(\pm\pi), X(\pm\pi/2), Y(\pm\pi/2), \mathrm{CZ}\}$. The elements of the two-qubit Clifford group fall in four classes of operations, the parallel single-qubit Clifford class, the CNOT-like class, the iSWAP-like class and the SWAP-like class. They are compiled by single-qubit gates plus 0, 1, 2 and 3 CZ gates respectively. For each data point, we sample 30 random sequences, which are each repeated 100 times. The dashed line is a fit to the data with a single exponential. The datapoint for a single Clifford operation is missing because we absorb the recovery Clifford gate into the last random Clifford gate, in order to minimize dephasing effects. Here the probability has been normalized to remove initialization and readout errors.

CZ gate fidelity. Furthermore, the compilation of Clifford gates into two different types of native gates – single-qubit gates and the CZ gate – makes it impossible to confidently extract the fidelity of any of the native gates, such as the CZ gate, by itself. This is different from a recent experiment on silicon spin qubits where only a single physical native gate was used, the conditional rotation, in which case the error per Clifford operation can be divided by the average number of conditional rotations per Clifford operation for estimating the error per conditional rotation [17].

As a first step to obtain quantitative information on the CZ gate fidelity, we implement a simplified version of interleaved RB, which provides the fidelities of the two-qubit gate projected in various single-qubit subspaces, as was done earlier for superconducting transmon qubits [12] and hybrid gatemon qubits [13]. In this protocol, the CZ gate is interleaved in a reference sequence of single-qubit Clifford operations. When applying a CZ gate, we can (arbitrarily) consider one qubit the control qubit and the other the target qubit. When the control qubit is $|1\rangle$, the target qubit ideally undergoes a π rotation around the $\hat{z}$ axis. With the control in $|0\rangle$, the target qubit ideally remains fixed (Identity operation). Therefore, projected in the subspace corresponding to the target qubit, this protocol interleaves either a $Z(\pi)$ rotation or the identity operation in a single-qubit RB reference sequence applied to the target qubit. The decay of the return probability for interleaved RB is also expected to follow Eq. 3.3. The fidelity of the interleaved gate is then

found from the depolarizing parameter α for the interleaved and reference sequence, as

$$F_{gate} = 1 - \left(1 - \frac{\alpha_{interleaved}}{\alpha_{reference}}\right)\frac{d-1}{d}. \tag{3.5}$$

From the experimental data, we find CZ fidelities projected in single-qubit space of 91% to 95%, depending on which qubit acts as the control qubit for the CZ, and which eigenstate it is in (see 3.7.5).

3.5. CHARACTER RANDOMIZED BENCHMARKING

In order to properly characterize the two-qubit CZ fidelity, we experimentally demonstrate a new approach to RB called character randomized benchmarking (CRB) [18]. CRB is a powerful generic method that extends randomized benchmarking in a rigorous manner, making it possible to extract average fidelities from groups beyond the multi-qubit Clifford group while keeping the advantages of standard RB such as resistance to SPAM errors. The generality of CRB allows one to start from (a subset of) the natives gates of a particular device and then design an RB experiment tailored to that set. This can strongly reduce compilation overhead and gate-dependent noise, a known nuisance factor in standard RB [29, 31, 32]. Moreover, since the accuracy of interleaved randomized benchmarking depends on the fidelity of the reference gates [9, 10], performing (through CRB) interleaved RB with a reference group generated by high fidelity gates can significantly improve the utility of interleaved RB.

Character randomized benchmarking requires us to average over two groups (the second one usually being a subgroup of the first). The first group is the “benchmark group". It is for the gates in this group that CRB yields the average fidelity. The second group is the “character group". CRB works by performing standard randomized benchmarking using the benchmark group but augments this by adding a random gate from the character group before each RB gate sequence. By averaging over this extra random gate, but weighting the average by a special function known from representation theory as a character function, it guarantees that the average over random sequences can always be fitted to a single exponential decay, even when the benchmark group is not the multi-qubit Clifford group and even in the presence of SPAM errors.

Guided by the need for high reference fidelities, we choose for our implementation of CRB the benchmark group to be the parallel single-qubit Clifford group ($C \otimes C$, the same as in standard simultaneous single-qubit RB) and the two-qubit Pauli group as the character group (see [18] for more information on why this is a good choice for the character group). It is non-trivial that the $C \otimes C$ group allows us to get information on two-qubit gates, since parallel single-qubit Clifford operations cannot fully depolarize the noise in the full two-qubit Hilbert space. In fact, for simultaneous single-qubit RB there are three depolarizing channels, each acting in a different subspace of the Hilbert space of density matrices, spanned by $I \otimes \sigma_i$, $\sigma_i \otimes I$, and $\sigma_i \otimes \sigma_i$, with I the identity operator and σ_i one of the Pauli operators. The three decay channels are reflected in the recovery probability for the final state, which is now described by

$$P_{C\otimes C} = A_1 {\alpha_{1|2}}^m + A_2 {\alpha_{2|1}}^m + A_{12} {\alpha_{12}}^m + B, \tag{3.6}$$

where $\alpha_{i|j}$ is again the depolarizing parameter for qubit i while simultaneously applying random Clifford operations to qubit j, and α_{12} is the depolarizing parameter for the two-qubit parity ($\{|00\rangle, |11\rangle\}$ versus $\{|01\rangle, |10\rangle\}$). We note that if the errors acting on both qubits are uncorrelated, then $\alpha_{12} = \alpha_{1|2}\alpha_{2|1}$ [8]. The question now is how to separate the three decays. Fitting the data using a sum of three exponentials will be very imprecise. Existing approaches combine the decay of specific combinations of the probabilities of obtaining 00, 01, 10 and 11 upon measurement, but suffer from SPAM errors [8]. As discussed above, CRB offers a clean procedure for extracting the individual decay rates that is immune to SPAM errors and does not incur additional overhead.

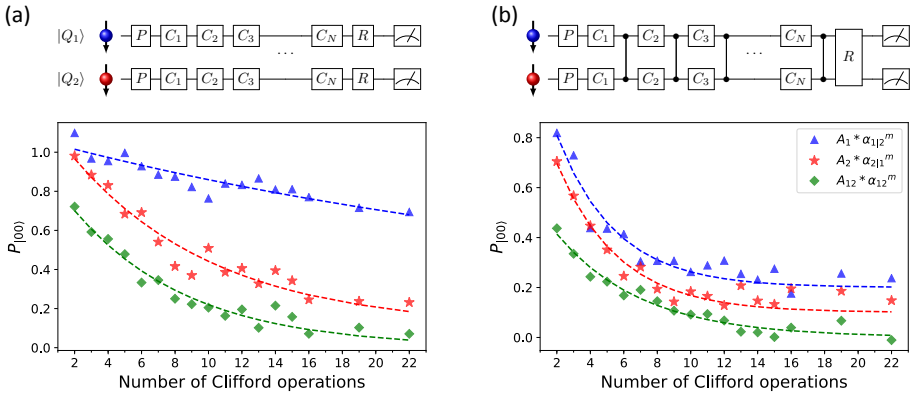

Fig. 3.4: Character randomized benchmarking. (a) Reference CRB experiment. The probabilities P_1 (blue triangles), P_2 (red stars) and P_3 (green diamonds), obtained starting from the initial state $|00\rangle$ followed by a Pauli operation, as a function of the number of subsequent single-qubit Clifford operations simultaneously applied to both qubits (see the schematic of the pulse sequence). As the native gate set, we use $\{I, X(\pi), Z(\pm\pi), X(\pm\pi/2), Z(\pm\pi/2), \mathrm{CZ}\}$. For each of the 16 Pauli operators, we apply 40 different random sequences, each with 20 repetitions. The dashed lines are fits to the data with a single exponential. Without SPAM errors, the datapoints would decay from 1 to 0. (b) Interleaved CRB experiment. This experiment is performed in an analogous way to the reference CRB experiment, but with a two-qubit CZ gate interleaved after each Clifford pair, as seen in the schematic of the pulse sequence. In both figures, the traces are offset by an increment of 0.1 for clarity, and the probabilities have been normalized to remove initialization and readout errors.

Concretely, CRB here proceeds as follows: (1) the two-qubit system is initialized to $|00\rangle$, then (2) one random Pauli operator on each qubit is applied to prepare the system in a state $|\phi_1\phi_2\rangle$ (one of $|00\rangle$, $|01\rangle$, $|10\rangle$, and $|11\rangle$), followed by (3) a random sequence of simultaneously applied single-qubit Clifford operators. In practice, the random Pauli operator is absorbed in the first Clifford operation, making the Pauli gates effectively noise-free. A final Clifford operation is applied which ideally returns the system to the state $|\phi_1\phi_2\rangle$ and finally (4) both qubits are measured. Note that, contrary to standard RB, CRB doesn't always measure the probability of returning to the initial state. Each random sequence is repeated to collect statistics on the probability $P_{\phi_1\phi_2}$ of obtaining measurement outcome 00 when starting from $|\phi_1\phi_2\rangle$ (note that each $P_{\phi_1\phi_2}$ averages over 4 Pauli operations). We combine these probabilities according to their character (see 3.7.2 for

more details) to obtain three fitting parameters,

$$\begin{aligned} P_1 &= P_{00} - P_{01} + P_{10} - P_{11}, \\ P_2 &= P_{00} + P_{01} - P_{10} - P_{11}, \\ P_3 &= P_{00} - P_{01} - P_{10} + P_{11}. \end{aligned} \tag{3.7}$$

Each of these three fitting parameters is expected to decay as a single exponential, isolating one of the decay channels in Eq. 3.6:

$$\begin{aligned} P_1 &= A_1 {\alpha_{1|2}}^m, \\ P_2 &= A_2 {\alpha_{2|1}}^m, \\ P_3 &= A_{12} {\alpha_{12}}^m. \end{aligned} \tag{3.8}$$

Note that there is no constant offset B. This is also a feature of CRB. The three experimentally measured probabilities are shown in Fig. 3.4a. These contain a lot of useful information, including not only the separate depolarizing parameters but also the averaged CRB reference fidelity and information on error correlations. The blue (red) curve shows the decay in the subspace corresponding to Q1 (Q2), spanned by $\sigma_i \otimes I$ ($I \otimes \sigma_i$). The green curve shows the decay in the subspace spanned by $\sigma_i \otimes \sigma_j$. This decay can be interpreted as the parity decay. The fitted depolarizing parameters are $\alpha_{1|2} = 0.9738 \pm 0.0008$, $\alpha_{2|1} = 0.8902 \pm 0.0020$ and $\alpha_{12} = 0.8652 \pm 0.0022$.

The average CRB depolarizing parameter can be found from the separate depolarizing parameters as

$$P = \frac{3}{15}\alpha_{1|2} + \frac{3}{15}\alpha_{2|1} + \frac{9}{15}\alpha_{12}, \tag{3.9}$$

where the weights are proportional to the dimension of the corresponding subspaces of the 16-dimensional Hilbert space of two-qubit density matrices. We obtain a reference CRB fidelity of $91.9 \pm 0.1\%$, which represents the fidelity of two simultaneous single-qubit Clifford operators ($C \otimes C$) in the full two-qubit space.

Finally, from the three depolarizing parameters in Eq. 3.6, we can infer to what extent errors occur independently on each qubit or exhibit correlations between the two qubits. The fact that $\alpha_{12} - \alpha_{1|2}\alpha_{2|1} = -0.0017 \pm 0.0031$ indicates that the errors are essentially independent.

Next we perform the interleaved version of CRB, for which we insert a CZ gate after each single-qubit Clifford pair. Fig. 3.4b shows the three corresponding experimentally measured decays. The fitting parameters we extract now reflect the combined errors from a single-qubit Clifford pair followed by a CZ gate. The fitted depolarizing parameters are $\alpha_{1|2} = 0.7522 \pm 0.0060$, $\alpha_{2|1} = 0.7623 \pm 0.0053$, and $\alpha_{12} = 0.8226 \pm 0.0030$. As can be expected, the three decays lie closer together than those for reference CRB: not only does the additional CZ gate contribute directly to all three decays, it also mixes the three subspaces. From the depolarizing parameters in interleaved and reference CRB measurement, we use Eq. 3.5 to isolate the fidelity of the CZ gate, now in two-qubit space as desired, yielding $92.0 \pm 0.5\%$.

The dominant errors in the CZ gate arise from nuclear spin noise and charge noise. In natural silicon, the abundance of Si^{29} atoms is about 4.7%, and the Si^{29} nuclear spins de-

phase the electron spin states due to the hyperfine interaction [19]. Charge noise modulates the overlap of the two electron wave functions, and thus also the two-qubit coupling strength. In the present device, we could not obtain a sufficiently strong coupling J at the symmetry point where the coupling strength is to first order insensitive to the detuning of the double dot potential [33, 34], hence charge noise directly (to first order) affects the two-qubit coupling strength.

3.6. CONCLUSION

Character randomized benchmarking provides a new method to effectively characterize multi-qubit behavior. It combines the advantages of simultaneous randomized benchmarking and interleaved randomized benchmarking, and gives tighter bounds on the fidelity number than standard interleaved randomized benchmarking due to its simpler compilation. CRB is useful in a wide variety of settings, far beyond the particular case studied here. The general approach to exploiting CRB is to start from a set of native gates that can be implemented easily and with high fidelity, and to construct a suitable reference sequence based on this set. The decay for the reference sequence contains any number of exponentials, which can be separated without suffering from SPAM errors and which provide relevant additional information, in the present case on the fidelity of simultaneously applied gates, cross-talk and on noise correlations. Comparison with interleaved CRB allows one to extract the fidelity of specific gates of interest.

We perform the first comprehensive study of the single-qubit, simultaneous single-qubit and two-qubit gate fidelities for semiconductor qubits, where the use of CRB, which allows for a compact reference sequence, was essential for extracting a reliable two-qubit gate fidelity. Summarizing, independent single-qubit gate fidelities are around 99% in this system, these drop to 98.8% for qubit 1 and to 96.9% for qubit 2 when simultaneously performing random gates on the other qubit, and the two-qubit CZ fidelity is around 92%. We expect that by working in an isotopically purified Si^{28}/SiGe substrate and performing the two-qubit gate at the symmetry point, a CZ gate fidelity above the fault-tolerant threshold (> 99%) can be reached. A recent report on the fidelity of controlled rotations in Si/SiO_2 quantum dots already comes close to this threshold [17]. With further improvements in charge noise levels, two-qubit gate fidelities above 99.9% are in reach.

3.7. APPENDICES

3.7.1. MEASUREMENT SETUP

The measurement setup is the same as the one used in [15]. We summarize here a few key points. The gates P1 and P4 are connected to arbitrary waveform generators (AWG, Tektronix 5014C) via coaxial cables. Applying DC voltage pulses to these two gates moves the system through different positions in the charge stability diagram for initialization, operation and read-out. Voltage pulses applied to these two gates are used to pulse the detuning between the two quantum dots, thereby turning on and off the controlled-phase gate. Gates P2 and P3 are connected to vector microwave sources (Keysight E8267D) for achieving EDSR. Each microwave source has two I/Q input chan-

nels, connected to two channels on the master AWG, which controls the clock of the entire system and triggers all the other instruments. The frequency, phase and duration of the microwave bursts are thus controlled by I/Q modulation. In addition, we use pulse modulation to obtain a larger on/off ratio of the microwave bursts than is possible using I/Q modulation only. A digitizer card (Spectrum M4i.44) installed inside the measurement computer is used to record the current traces of the sensing quantum dot at a sampling rate ~ 60 kHz. Each time trace is converted into a single bit value (0 or 1) by the measurement computer using threshold detection. The average over many repetitions gives us the spin-up and spin-down probabilities (0 and 1).

3.7.2. MATHEMATICAL BACKGROUND OF CRB

Character randomized benchmarking is a generic method for performing randomized benchmarking with finite groups other than the multi-qubit Clifford group. As mentioned in the main text, CRB requires the user to specify two finite groups: the benchmark group and the character group. In this work we chose the benchmark group to be the simultaneous single-qubit Clifford group on two qubits and the character group to be the two-qubit Pauli group. Standard RB and CRB rely on the framework of representation theory. Representation theory gives us powerful tools to interpret averages over group elements, which form a core part of the randomized benchmarking protocol. In particular we can use a result called Schur's lemma. In the context of randomized benchmarking Schur's lemma states that, assuming for simplicity that every gate is subject to an identical noise map $\mathcal{E}$, the average noisy RB operator $\mathcal{M}$ (here the average is taken over the group elements) is of the form

$$\mathcal{M} := \sum_{\substack{G_1,\dots G_m \\ \in C\otimes C}} G_{inv}\mathcal{E}G_m\cdots\mathcal{E}G_1 = \begin{bmatrix} 1 & & & \\ & \alpha_{1|2}\mathbb{I}_{1|2} & & \\ & & \alpha_{2|1}\mathbb{I}_{2|1} & \\ & & & \alpha_{12}\mathbb{I}_{12} \end{bmatrix}^m,$$

where we are describing all quantum channels in the Pauli Transfer Matrix picture, i.e. $\mathcal{M}_{i,j} = \mathrm{Tr}(\sigma_i\mathcal{M}(\sigma_j))/2$ where σ_i, σ_j are Pauli matrices. One can think of the matrix entry $\mathcal{M}_{i,j}$ as describing how much the noise map $\mathcal{M}$ maps the generalized Bloch sphere axis labeled σ_j to the one labeled σ_i. The sub-matrices $\mathbb{I}_{1|2}, \mathbb{I}_{1|2}$ and $\mathbb{I}_{12}$ of the matrix $\mathcal{M}$ are defined as the identity matrix on the sets of 2-qubit Pauli's of the form $\{\sigma_i \otimes I\}, \{I \otimes \sigma_i\}$ and $\{\sigma_i \otimes \sigma_j\}$ respectively. We would like to estimate the numbers $\alpha_{1|2}, \alpha_{2|1}$ and α_{12} individually in a way that does not depend on state preparation and measurement. To do this CRB adds an extra average over another group called the character group, which we choose to be the two-qubit Pauli group. This average is weighted by a so-called character function. This average over the Pauli group projects any initial state onto a single axis of the Bloch sphere. Which axis is projected on depends on the character function used for the weights. By selecting the correct Bloch sphere axes, we can single out the individual blocks of the matrix $\mathcal{M}$. In order to isolate the parameter $\alpha_{1|2}$ we choose to project onto the Bloch sphere axis associated to $\sigma_z \otimes I$. Concretely this means that the character averaged RB operator $\mathcal{M}$ becomes

$$\sum_{\sigma\in P_2} \chi_{\sigma_z I}(\sigma) \sum_{\substack{G_1,\dots G_m \\ \in C\otimes C}} G_{inv}\mathcal{E}G_m\cdots\mathcal{E}G_1\sigma = \mathcal{M}^m\mathcal{P}_{ZI}$$

$\sigma\backslash P$	II	$\sigma_z I$	$I\sigma_z$	$\sigma_z\sigma_z$	$\sigma_x I$	$I\sigma_x$	$\sigma_x\sigma_x$	$\sigma_y I$
$\sigma_z I$	1	1	1	1	−1	1	−1	−1
$I\sigma_z$	1	1	1	1	1	−1	−1	1
$\sigma_z\sigma_z$	1	1	1	1	−1	−1	1	−1
$\sigma\backslash P$	$I\sigma_y$	$\sigma_y\sigma_y$	$\sigma_z\sigma_x$	$\sigma_x\sigma_z$	$\sigma_z\sigma_y$	$\sigma_y\sigma_z$	$\sigma_x\sigma_y$	$\sigma_y\sigma_x$
$\sigma_z I$	1	−1	1	−1	1	−1	−1	−1
$I\sigma_z$	−1	−1	−1	1	−1	1	−1	−1
$\sigma_z\sigma_z$	−1	1	−1	−1	−1	−1	1	1

Table 3.1: Values for the character function $\chi_P(\sigma)$ for $P \in \{(\sigma_z \otimes I), (I \otimes \sigma_z), (\sigma_z \otimes \sigma_z)\}$.

where the function $\chi_{\sigma_z I}(\sigma)$ is given in the first row of Table 3.1 and the matrix $\mathcal{P}_{\sigma_z I}$ has all zero entries except on the diagonal entry corresponding to the Pauli $\sigma_z \otimes I$. By matrix multiplication we see that $\mathcal{M}^m \mathcal{P}_{\sigma_z I} = \alpha_{1|2}^m \mathcal{P}_{\sigma_z I}$. This means that the average measured survival probability in CRB, with input state ρ and measurement operator Q is of the form

$$\sum_{\sigma \in P_2} \chi_{ZI}(\sigma) \sum_{\substack{G_1,\ldots G_m \\ \in C \otimes C}} \mathrm{Tr}(Q G_{inv} \mathcal{E} G_m \cdots \mathcal{E} G_1(\sigma(\rho))) = A \alpha_{1|2}^m$$

where A is a function of Q and ρ. Similarly we can obtain estimates $\alpha_{2|1}$ and α_{12} by constructing projectors onto the Pauli operators $I \otimes \sigma_z$ and $\sigma_z \otimes \sigma_z$ respectively. The character functions for these projectors are given in rows 2 and 3 of Table 3.1 respectively.

As noted in the main text, CRB is a generic procedure, which can be used beyond its application in this manuscript. Another notable example of where we suspect CRB can offer a benefit is when the device native gates are not single-qubit gates but rather two-qubit gates, as happens in [17]. In this case compiling multi-qubit Cliffords is very cumbersome. In the theoretical RB literature benchmarking groups are discussed that are more suitable to this scenario such as the CNOT-dihedral group (for native CNOT gates) [35] and the real Clifford group (for native CPhase gates) [36]. Both of these groups lead to benchmarking data that mixes two exponential decays but using the CRB approach these can be fitted individually in a reliable manner (in both cases the Pauli group is a good choice for character group, see the example in [18] for more information).

3.7.3. EXPERIMENTAL DETAILS FOR CRB

The single-qubit Clifford group is commonly generated by the gate set $\{I, X(\pi), Y(\pm\pi), X(\pm\pi/2), Y(\pm\pi/2)\}$. In our experiment, we perform Z rotations by changing a qubit's reference frame in software [22], which makes Z rotations error-free. To benefit from this, we generate the single-qubit Clifford group by the gate set $\{I, X(\pi), Z(\pm\pi), X(\pm\pi/2), Z(\pm\pi/2)\}$ instead. Furthermore, we keep the Rabi frequency the same for all the X rotations, thus a $X(\pi)$ gate has twice the duration of a $X(\pi/2)$ gate. Combined with using X-Z compilation, we can keep the duration for all the 24 Clifford operations the same as shown below, thereby avoiding any unnecessary idle time which would quickly dephase the qubits.

Class	X/Y generation	X/Z generation
Pauli	I	$X, -X$
	X^2	X^2
	Y^2	$-Z, X^2, Z$
	$Y,^2 X^2$	X, Z^2, X
$2\pi/3$	X, Y	$X, -Z, X, Z$
	$X, -Y$	$X, Z, X, -Z$
	$-X, Y$	$-X, -Z, X, Z$
	$-X, -Y$	$-X, Z, X, -Z$
	Y, X	$-Z, X, Z, X$
	$Y, -X$	$-Z, X, Z, -X$
	$-Y, X$	$Z, X, -Z, X$
	$-Y, -X$	$Z, X, -Z, -X$
$\pi/2$	X	$-Z, X, Z, X, -Z$
	$-X$	$Z, -X, -Z, -X, Z$
	Y	$X, Z, -X$
	$-Y$	$X, -Z, -X$
	$-X, Y, X$	$-X, Z^2, -X, -Z$
	$-X, -Y, X$	$-X, -Z^2, -X, Z$
Hadamard	X^2, Y	$X, -Z, X$
	$X^2, -Y$	X, Z, X
	Y^2, X	$-Z, X, Z, X, Z$
	$Y^2, -X$	$-Z, X, Z, -X, -Z$
	X, Y, X	X^2, Z
	$-X, Y, -X$	$-X^2, -Z$

Table 3.2: Compilation of the single-qubit Clifford group with X/Y rotations and X/Z rotations. Here $(-)K$ and $(-)K^2$ denote $K(\pm\pi/2)$ and $K(\pm\pi)$ gates ($K = X, Y, Z$) respectively.

3.7.4. COMPARISON OF STANDARD AND CHARACTER INTERLEAVED TWO-QUBIT RB

Although it often goes unmentioned, the estimate for the fidelity of an interleaved gate given in Eq. 3.5 is only exact when the qubit noise is exactly depolarizing. In the presence of other types of noise (such as dephasing or calibration errors) this number gives only upper and lower bounds on the fidelity of the interleaved gate. First upper and lower bounds were given in [9] and recently optimal upper and lower bounds were given in [10]. These bounds depend strongly on the fidelity of the gates in the reference sequence, in particular they scale as $O(\sqrt{1-\alpha_{\text{ref}}})$ where α_{ref} is the reference RB decay constant. This means that our implementation of CRB, which uses only single-qubit gates for the reference experiment, has a significant advantage over standard two-qubit interleaved RB also in this respect. We can illustrate this advantage by considering a hypothetical standard two-qubit interleaved experiment with interleaved CZ gate. Recall from Eq. 3.3 that standard two qubit RB (here considered as a reference experiment) yielded a reference fidelity of 82% and thus a depolarizing parameter of $\alpha_{2,\text{ref}} = 0.73$ (suppressing uncertainty for the sake of this exercise). Assuming an interleaved CZ fidelity of 92% (which is what we extracted from the CRB experiment) and assuming that the error on a hypothetical interleaved two qubit RB experiment scales multiplicatively (optimistic given the possibility of calibration errors) we estimate that a hypothetical two qubit interleaved RB experiment would have a depolarizing parameter of $\alpha_{2,\text{int}}$. Using the optimal bounds calculated in [10] this would mean we can only guarantee that the fidelity of the interleaved gate lies in the range $[0.58, 1]$. From the CRB experiment we can however guarantee that the fidelity of the interleaved gate lies in the range $[0.69, 1]$, a significant improvement even in the absolute worst case scenario discussed in [10].

We would also like to note that the bounds given in [9, 10] significantly overestimate the range of possible interleaved gate fidelities if more is known about the noise process. If for instance the noise on the reference gates is assumed to be dominated by stochastic errors (as opposed to coherent errors due to mis-calibration) then the upper and lower bounds can be made significantly tighter. This coincides with experimental consensus that interleaved RB generally gives good estimates of the interleaved gate fidelity. However, since single qubit gates will typically suffer less from calibration errors than compiled two qubit gates we argue that interleaved CRB will yield sharper upper and lower bounds on the interleaved gate fidelity than standard interleaved RB when more is known about the noise process.

3.7.5. INTERLEAVED RB PROJECTED IN SINGLE-QUBIT SPACE

Fig. 3.5 shows experimental results for the experiment discussed in the main text where a CZ gate is interleaved in a standard single-qubit RB sequence applied to one qubit, while the other qubit is in either $|0\rangle$ or $|1\rangle$. This experiment provides the CZ fidelity projected in single-qubit space [12, 13], summarized in the table below for the four possible cases.

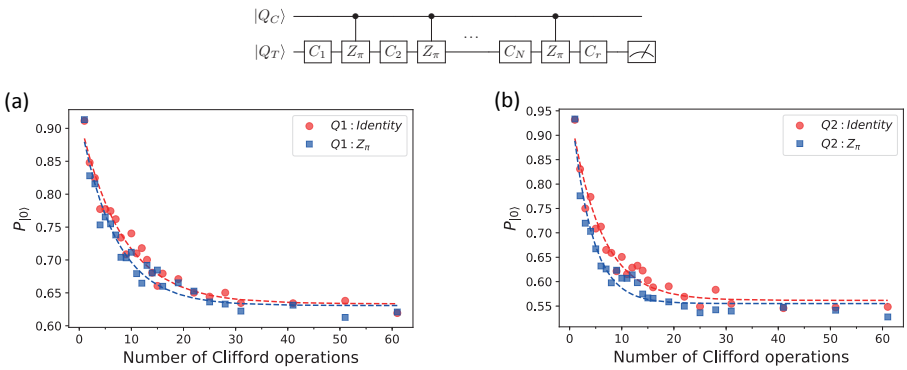

Fig. 3.5: Interleaved Randomized Benchmarking projected in single-qubit space. (a) Probability for obtaining outcome 0 upon measurement in the $\sigma_z \otimes I$ basis as a function of the number of single-qubit Clifford operations, interleaved with the CZ operation. For the red circles (blue squares), Q2 is is in $|0\rangle$ ($|1\rangle$) so Q1 is expected to undergo the identity operation (a $Z(\pi)$ rotation). For each data point, we sample 30 different random sequences for each Clifford number, which are each repeated 100 times. Dashed lines are fits to the data with a single exponential. (b) Analogous data for Q2.

Q_C	Q_C state	Q_T	operation	fidelity
Q_1	$\|0\rangle$	Q_2	I	$94.62 \pm 0.24\%$
Q_1	$\|1\rangle$	Q_2	$Z(\pi)$	$90.79 \pm 0.38\%$
Q_2	$\|0\rangle$	Q_1	I	$95.50 \pm 0.20\%$
Q_2	$\|1\rangle$	Q_1	$Z(\pi)$	$94.38 \pm 0.25\%$

Table 3.3: CZ fidelities for different target-qubits (Q_T), and different states of the control-qubit (Q_C)

3.7.6. CROSSTALK

We here provide more information on the cross-talk effects that occur on one qubit when applying a microwave drive to the other (see also [15] and the supplementary information therein). First, when we perform spectroscopy on Q2 while driving Q1, we find that the frequency of Q2 shifts by of the order of 2 MHz (depending on the power applied to Q1). We compensate for this known frequency shift by shifting the drive frequency applied to Q2 when we simultaneously drive Q1. We note that a frequency shift by a known amount is not expected to contribute to decoherence. However, Fig. 3.6 shows Rabi oscillations for both qubits in the absence and presence of an excitation to the other qubit. Clearly, when simultaneously driving Rabi oscillations on both qubits, we find a faster decay on Q2 comparing to driving Q2 by itself. The effect of simultaneous driving on Q1 is less pronounced. This is consistent with the observed effects of simultaneous driving on the measured single-qubit gate fidelities reported in the main text. The cross-talk effect on Q2 persists when the drive on Q1 is applied off-resonantly or when dot 1 is emptied. We do note that the microwave power used to drive Q1 (~20dBm) is substantially higher than that used for Q2 (~8dbm). This difference is needed to compensate for the tighter confining potential of dot 1 compared to dot 2.

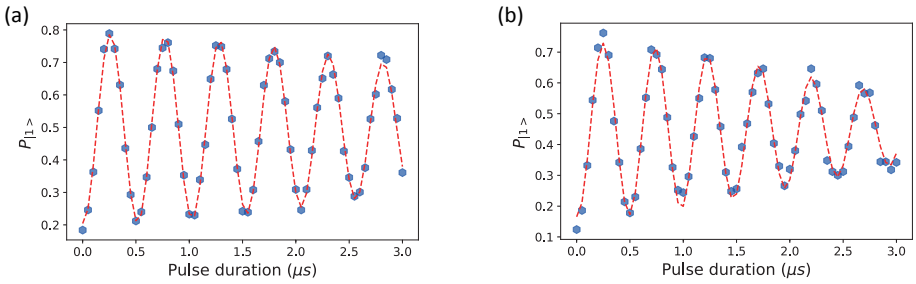

Fig. 3.6: Rabi oscillations of Q2. (a) Probability that measurement of Q2 returns spin up ($|1\rangle$) as a function of the duration of the resonant microwave burst driving the qubit. (b) Analogous data for Q2 when Q1 is simultaneously being driven.

REFERENCES

[1] I. L. Chuang and M. A. Nielsen, *Prescription for experimental determination of the dynamics of a quantum black box,* Journal of Modern Optics **44**, 2455 (1997).

[2] J. L. O'Brien, G. J. Pryde, A. Gilchrist, D. F. V. James, N. K. Langford, T. C. Ralph, and A. G. White, *Quantum process tomography of a controlled-not gate,* Phys. Rev. Lett. **93**, 080502 (2004).

[3] S. T. Merkel, J. M. Gambetta, J. A. Smolin, S. Poletto, A. D. Córcoles, B. R. Johnson, C. A. Ryan, and M. Steffen, *Self-consistent quantum process tomography,* Phys. Rev. A **87**, 062119 (2013).

[4] J. Emerson, M. Silva, O. Moussa, C. Ryan, M. Laforest, J. Baugh, D. G. Cory, and R. Laflamme, *Symmetrized characterization of noisy quantum processes,* Science **317**, 1893 (2007).

[5] E. Knill, D. Leibfried, R. Reichle, J. Britton, R. B. Blakestad, J. D. Jost, C. Langer, R. Ozeri, S. Seidelin, and D. J. Wineland, *Randomized benchmarking of quantum gates,* Phys. Rev. A **77**, 012307 (2008).

[6] J. P. Gaebler, A. M. Meier, T. R. Tan, R. Bowler, Y. Lin, D. Hanneke, J. D. Jost, J. P. Home, E. Knill, D. Leibfried, and D. J. Wineland, *Randomized benchmarking of multiqubit gates,* Phys. Rev. Lett. **108**, 260503 (2012).

[7] J. M. Chow, J. M. Gambetta, L. Tornberg, J. Koch, L. S. Bishop, A. A. Houck, B. R. Johnson, L. Frunzio, S. M. Girvin, and R. J. Schoelkopf, *Randomized benchmarking and process tomography for gate errors in a solid-state qubit,* Phys. Rev. Lett. **102**, 090502 (2009).

[8] J. M. Gambetta, A. D. Córcoles, S. T. Merkel, B. R. Johnson, J. A. Smolin, J. M. Chow, C. A. Ryan, C. Rigetti, S. Poletto, T. A. Ohki, M. B. Ketchen, and M. Steffen, *Characterization of addressability by simultaneous randomized benchmarking,* Phys. Rev. Lett. **109**, 240504 (2012).

[9] E. Magesan, J. M. Gambetta, B. R. Johnson, C. A. Ryan, J. M. Chow, S. T. Merkel, M. P. da Silva, G. A. Keefe, M. B. Rothwell, T. A. Ohki, M. B. Ketchen, and M. Steffen, *Efficient measurement of quantum gate error by interleaved randomized benchmarking,* Phys. Rev. Lett. **109**, 080505 (2012).

[10] A. C. Dugas, J. J. Wallman, and J. Emerson, *Efficiently characterizing the total error in quantum circuits,* arXiv:1610.05296 (2016).

[11] A. D. Córcoles, J. M. Gambetta, J. M. Chow, J. A. Smolin, M. Ware, J. Strand, B. L. T. Plourde, and M. Steffen, *Process verification of two-qubit quantum gates by randomized benchmarking,* Phys. Rev. A **87**, 030301 (2013).

[12] Y. Chen, C. Neill, P. Roushan, N. Leung, M. Fang, R. Barends, J. Kelly, B. Campbell, Z. Chen, B. Chiaro, A. Dunsworth, E. Jeffrey, A. Megrant, J. Y. Mutus, P. J. J. O'Malley, C. M. Quintana, D. Sank, A. Vainsencher, J. Wenner, T. C. White, M. R. Geller, A. N. Cleland, and J. M. Martinis, *Qubit architecture with high coherence and fast tunable coupling,* Phys. Rev. Lett. **113**, 220502 (2014).

[13] L. Casparis, T. W. Larsen, M. S. Olsen, F. Kuemmeth, P. Krogstrup, J. Nygård, K. D. Petersson, and C. M. Marcus, *Gatemon benchmarking and two-qubit operations,* Phys. Rev. Lett. **116**, 150505 (2016).

[14] M. D. Shulman, O. E. Dial, S. P. Harvey, H. Bluhm, V. Umansky, and A. Yacoby, *Demonstration of entanglement of electrostatically coupled singlet-triplet qubits,* Science **336**, 202 (2012).

[15] T. F. Watson, S. G. J. Philips, E. Kawakami, D. R. Ward, P. Scarlino, M. Veldhorst, D. E. Savage, M. G. Lagally, M. Friesen, S. N. Coppersmith, M. A. Eriksson, and L. M. K. Vandersypen, *A programmable two-qubit quantum processor in silicon,* Nature **555**, 633 (2018).

[16] D. M. Zajac, A. J. Sigillito, M. Russ, F. Borjans, J. M. Taylor, G. Burkard, and J. R. Petta, *Resonantly driven cnot gate for electron spins,* Science **359**, 439 (2017).

[17] W. Huang, C. H. Yang, K. W. Chan, T. Tanttu, B. Hensen, R. C. C. Leon, M. A. Fogarty, J. C. C. Hwang, F. E. Hudson, K. M. Itoh, A. Morello, A. Laucht, and A. S. Dzurak, *Fidelity benchmarks for two-qubit gates in silicon,* arXiv:1805.05027 (2018).

[18] J. Helsen, X. Xue, L. M. K. Vandersypen, and S. Wehner, *A new class of efficient randomized benchmarking protocols,* arXiv:1806.02048 (2018).

[19] F. A. Zwanenburg, A. S. Dzurak, A. Morello, M. Y. Simmons, L. C. L. Hollenberg, G. Klimeck, S. Rogge, S. N. Coppersmith, and M. A. Eriksson, *Silicon quantum electronics,* Rev. Mod. Phys. **85**, 961 (2013).

[20] L. M. K. Vandersypen, H. Bluhm, J. S. Clarke, A. S. Dzurak, R. Ishihara, A. Morello, D. J. Reilly, L. R. Schreiber, and M. Veldhorst, *Interfacing spin qubits in quantum dots and donors–hot, dense, and coherent,* npj Quantum Information **3**, 34 (2017).

[21] M. Pioro-Ladrière, T. Obata, Y. Tokura, Y.-S. Shin, T. Kubo, K. Yoshida, T. Taniyama, and S. Tarucha, *Electrically driven single-electron spin resonance in a slanting zeeman field,* Nature Physics **4**, 776 (2008).

[22] L. M. K. Vandersypen and I. L. Chuang, *NMR techniques for quantum control and computation,* Rev. Mod. Phys. **76**, 1037 (2005).

[23] T. Meunier, V. E. Calado, and L. M. K. Vandersypen, *Efficient controlled-phase gate for single-spin qubits in quantum dots,* Phys. Rev. B **83**, 121403 (2011).

[24] M. Veldhorst, C. H. Yang, J. C. C. Hwang, W. Huang, J. P. Dehollain, J. T. Muhonen, S. Simmons, A. Laucht, F. E. Hudson, K. M. Itoh, A. Morello, and A. S. Dzurak, *A two-qubit logic gate in silicon,* Nature **526**, 410 (2015).

[25] J. M. Elzerman, R. Hanson, L. H. Willems van Beveren, B. Witkamp, L. M. K. Vandersypen, and L. P. Kouwenhoven, *Single-shot read-out of an individual electron spin in a quantum dot,* Nature **430**, 431 (2004).

[26] V. Srinivasa, K. C. Nowack, M. Shafiei, L. M. K. Vandersypen, and J. M. Taylor, *Simultaneous spin-charge relaxation in double quantum dots,* Phys. Rev. Lett. **110**, 196803 (2013).

[27] E. Magesan, J. M. Gambetta, and J. Emerson, *Scalable and robust randomized benchmarking of quantum processes,* Phys. Rev. Lett. **106**, 180504 (2011).

[28] E. Magesan, J. M. Gambetta, and J. Emerson, *Characterizing quantum gates via randomized benchmarking,* Phys. Rev. A **85**, 042311 (2012).

[29] J. J. Wallman, *Randomized benchmarking with gate-dependent noise,* Quantum **2**, 47 (2018).

[30] K. Takeda, J. Kamioka, T. Otsuka, J. Yoneda, T. Nakajima, M. R. Delbecq, S. Amaha, G. Allison, T. Kodera, S. Oda, and S. Tarucha, *A fault-tolerant addressable spin qubit in a natural silicon quantum dot,* Science Advances **2** (2016), 10.1126/sciadv.1600694.

[31] A. Carignan-Dugas, K. Boone, J. J. Wallman, and J. Emerson, *From randomized benchmarking experiments to gate-set circuit fidelity: how to interpret randomized benchmarking decay parameters,* New Journal of Physics **20**, 092001 (2018).

[32] T. Proctor, K. Rudinger, K. Young, M. Sarovar, and R. Blume-Kohout, *What randomized benchmarking actually measures,* Phys. Rev. Lett. **119**, 130502 (2017).

[33] F. Martins, F. K. Malinowski, P. D. Nissen, E. Barnes, S. Fallahi, G. C. Gardner, M. J. Manfra, C. M. Marcus, and F. Kuemmeth, *Noise suppression using symmetric exchange gates in spin qubits,* Phys. Rev. Lett. **116**, 116801 (2016).

[34] M. D. Reed, B. M. Maune, R. W. Andrews, M. G. Borselli, K. Eng, M. P. Jura, A. A. Kiselev, T. D. Ladd, S. T. Merkel, I. Milosavljevic, E. J. Pritchett, M. T. Rakher, R. S. Ross, A. E. Schmitz, A. Smith, J. A. Wright, M. F. Gyure, and A. T. Hunter, *Reduced sensitivity to charge noise in semiconductor spin qubits via symmetric operation,* Phys. Rev. Lett. **116**, 110402 (2016).

[35] A. W. Cross, E. Magesan, L. S. Bishop, J. A. Smolin, and J. M. Gambetta, *Scalable randomised benchmarking of non-clifford gates,* npj Quantum Information **2**, 16012 (2016), article.

[36] A. K. Hashagen, S. T. Flammia, D. Gross, and J. J. Wallman, *Real Randomized Benchmarking,* Quantum **2**, 85 (2018).

4

SPATIAL NOISE CORRELATIONS IN A SI/SIGE TWO-QUBIT DEVICE FROM BELL STATE COHERENCES

We study spatial noise correlations in a Si/SiGe two-qubit device with integrated micromagnets. Our method relies on the concept of decoherence-free subspaces, whereby we measure the coherence time for two different Bell states, designed to be sensitive only to either correlated or anticorrelated noise, respectively. From these measurements we find weak correlations in low-frequency noise acting on the two qubits, while no correlations could be detected in high-frequency noise. We expect nuclear spin noise to have an uncorrelated nature. A theoretical model and numerical simulations give further insight into the additive effect of multiple independent (anti)correlated noise sources with an asymmetric effect on the two qubits as can result from charge noise. Such a scenario in combination with nuclear spins is plausible given the data and the known decoherence mechanisms. This work is highly relevant for the design of optimized quantum error correction codes for spin qubits in quantum dot arrays, as well as for optimizing the design of future quantum dot arrays.

This chapter has been published in Phys. Rev. B **101**, 235133 (2020).

4.1. INTRODUCTION

Large-scale quantum computers will need to rely on quantum error correction (QEC) to deal with the inevitable qubit errors caused by interaction with the environment and by imperfect control signals. The noise amplitude can vary from qubit to qubit and furthermore can exhibit correlations or anti-correlations between qubits. Most QEC error thresholds, such as the 1%-threshold for the surface code [1], are derived under the assumption of negligible correlations in qubit errors. Other approaches, such as decoherence-free subspaces (DFSs) [2], are designed under the assumption of correlated noise, taking advantage of symmetry considerations to reduce the qubit sensitivity to external noise. Examples for quantum dot based qubits include the singlet-triplet qubit [3, 4] and the quadrupole qubit [5]. In addition, QEC schemes exist that can deal with short-range correlations in the noise [6]. Spatial noise correlations have therefore been studied extensively, both theoretically [7–14] and experimentally [11, 15, 16].

The most important decoherence sources in natural silicon quantum dots are the hyperfine interaction with nuclear spins and charge noise. Nuclear spin noise is typically uncorrelated between adjacent dots [29]. Charge noise is usually caused by distant fluctuating charges [30–32], which is expected to lead to spatial correlations on the length scale of interdot distances of 100 nm or less. In the presence of a magnetic field gradient, which is commonly used for qubit selectivity and fast qubit control, qubits are sensitive to electric field fluctuations and charge noise will impact spin coherence [21, 33]. However, a quantitative measurement of spatial noise correlations in an actual two-qubit device is lacking.

Here, we study experimentally spatial noise correlations in a Si/SiGe two-qubit device, by preparing Bell states in either the parallel or the anti-parallel subspace, similarly to recent work with NV centers in diamond [34]. Via a Ramsey-style experiment, we find that Bell states in the anti-parallel subspace show a ~30% longer dephasing time than those in the parallel subspace. A Hahn-echo style measurement reveals no detectable difference in the decay time for the respective Bell states. We present a simple model to describe noise correlations on two qubits, including asymmetric noise amplitudes acting on the two qubits, and study numerically the combined effect of multiple (anti-)correlated, asymmetric noise sources. We use these simulations to assess which combinations of noise sources are compatible with the observed coherence times.

4.2. SPIN QUBITS IN DOUBLE QUANTUM DOTS

Figure 4.1(a) shows a schematic of the device used in this work, which is the same as described earlier [23, 25]. It comprises an electrostatically defined double quantum dot (DQD) in a two-dimensional electron gas (2DEG). The 2DEG is confined in a 12-nm-thick silicon quantum well, 37 nm below the surface of an undoped Si/SiGe heterostructure with natural isotope composition. On top of the heterostructure, we fabricate two gate layers with cobalt micromagnets. The device is cooled down to $T \approx 30$ mK and subject to an external magnetic field of $B_{ext} = 617$ mT. Suitable voltages are applied to accumulation and fine gates (in the top and bottom layer, respectively) to form a DQD in the single-electron regime. Single-electron spin states are Zeeman split by the total magnetic field, and used to encode two single-spin qubits. The micromagnets ensure

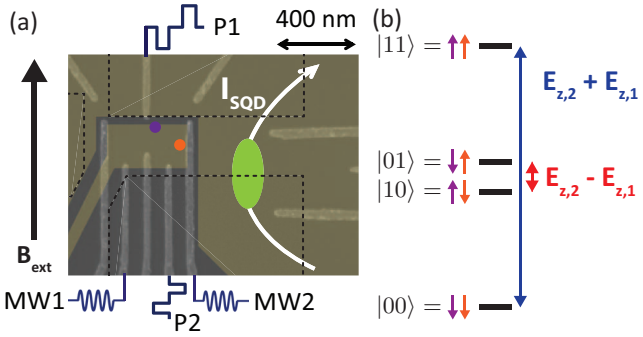

Fig. 4.1: (a) Scanning electron micrograph of a similar Si/SiGe device as used in the measurements, showing the depletion gates used to define the potential landscape in the 2D electron gas accumulated by the yellow shaded gates (drawn digitally). Purple and orange circles indicate the estimated positions of the two dots, occupied by one electron each, and the ellipse indicates a sensing quantum dot. Two-qubit operations are controlled via gate voltage pulses applied to gates P1 and P2, and microwave signals for single-qubit control are applied to gates MW1 and MW2. The contours of cobalt micromagnets are indicated by the dashed black lines. (b) Energy level diagram for two qubits in an inhomogeneous magnetic field, giving rise to a difference in Zeeman energy between the two qubits.

individual qubit addressability by a gradient in the longitudinal magnetic field, resulting in spin resonance frequencies of 18.35 GHz and 19.61 GHz for qubit 1 (Q1) and qubit 2 (Q2), respectively.

Figure 4.1(b) shows the resulting energy level diagram for the two qubits. For perfectly correlated noise, fluctuations in the Zeeman energy for both qubits are the same: $\delta E_{Z,1} = \delta E_{Z,2} = \delta E_Z$. Consequently, the sum of the two qubit energies fluctuates, $\Delta(E_{Z,1} + E_{Z,2}) = 2\delta E_Z$, while their difference is not affected, $\Delta(E_{Z,1} - E_{Z,2}) = 0$. On the other hand, for perfectly anti-correlated noise $\delta E_{Z,1} = -\delta E_{Z,2}$, and the opposite holds for the sum and difference energies. Bell states consist of superpositions of the two-spin eigenstates and allow to study dephasing between these eigenstates. An anti-parallel Bell state, which evolves in time at a rate proportional to the difference of the single-qubit energies, will be affected by anti-correlated noise, but not by correlated noise. A parallel Bell state, which evolves in time at a rate proportional to the sum of the single-qubit energies, is sensitive to correlated noise, but not to anti-correlated noise. Such properties are exploited in DFSs and are used here as a probe for spatial correlations in the noise acting on the qubits.

4.3. SPATIAL NOISE CORRELATIONS

Real systems are often subject to both uncorrelated and (anti-)correlated noise. Furthermore, the noise amplitudes acting on different qubits are generally different, regardless of whether the noise is uncorrelated or (anti-)
correlated. We wish to capture all these scenarios in one unified theoretical formalism. We include pure dephasing only, which is justified by the long T_1 times for spin qubits compared to the experiment and coherence timescales, and assume a quasistatic Gaussian joint probability distribution for the noise acting on the two qubits. We can then

express the two-qubit coherence times for an anti-parallel ($|\Psi\rangle = (|\downarrow\uparrow\rangle - i|\uparrow\downarrow\rangle)/\sqrt{2}$) and a parallel ($|\Phi\rangle = (|\downarrow\downarrow\rangle - i|\uparrow\uparrow\rangle)/\sqrt{2}$) Bell state quantitatively as follows (see 4.7.1):

$$\begin{aligned}\left(\frac{1}{T^*_{2,|\Psi\rangle}}\right)^2 &= 2\pi^2\left(\sigma_1^2+\sigma_2^2-2\rho\sigma_1\sigma_2\right),\\ \left(\frac{1}{T^*_{2,|\Phi\rangle}}\right)^2 &= 2\pi^2\left(\sigma_1^2+\sigma_2^2+2\rho\sigma_1\sigma_2\right),\end{aligned} \tag{4.1}$$

where σ_i^2 is the variance of the noise in the resonance frequency of qubit i (the single-qubit coherence time is given by $\left(\frac{1}{T^*_{2,i}}\right)^2 = 2\pi^2\sigma_i^2$), and ρ is a correlation factor ($-1 \leq \rho \leq 1$). Positive ρ indicates correlations, while negative ρ indicates anti-correlations.

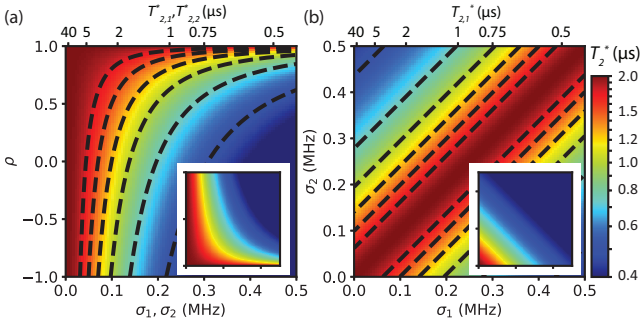

Fig. 4.2: $T^*_{2,|\Psi\rangle}$ extracted from Eq. 4.1 (a) as a function of correlation factor ρ and noise amplitude $\sigma_1 = \sigma_2$, and (b) as a function of σ_1 and σ_2 for $\rho = 1$. Insets show the corresponding images for $T^*_{2,|\Phi\rangle}$. Contours correspond to (0.5, 0.75, 1.0, 1.25, 1.5, 1.75) μs. In all images an uncorrelated noise contribution corresponding to a Bell state coherence time of 2.0 μs is added to prevent singularities.

The effect of the noise amplitudes σ_i and the correlation factor ρ on the coherence time for the anti-parallel Bell state $T^*_{2,|\Psi\rangle}$ is visualized in Fig. 4.2(a). Here $\sigma_1 = \sigma_2$, so for $\rho = 1$, $|\Psi\rangle$ forms a true DFS and the noise has no effect regardless of its amplitude. With decreasing ρ, $T^*_{2,|\Psi\rangle}$ decreases, as the noise becomes initially less correlated ($\rho > 0$), then uncorrelated ($\rho = 0$) and eventually anti-correlated ($\rho < 0$). For $\rho = -1$, $T^*_{2,|\Psi\rangle}$ is only one fourth of the single-qubit coherence times. For $T^*_{2,|\Phi\rangle}$, the corresponding image is mirrored around $\rho = 0$, see the inset of Fig. 4.2a, and the longest coherence time occurs for $\rho = -1$. Figure 4.2(b) shows the effect of asymmetric noise amplitudes on the two qubits for $\rho = 1$. We see that despite the maximal correlation factor, a true DFS only exists for symmetric noise ($\sigma_1 = \sigma_2$) and $|\Psi\rangle$ decoheres when $\sigma_1 \neq \sigma_2$. Clearly, both the asymmetry in the noise and the correlation factor impact the two-qubit coherence.

4.4. BELL STATE COHERENCE TIMES

From Eq. 4.1, we see that, as anticipated, experimental measurement of the decay times for the parallel and anti-parallel Bell states reveals whether (anti-)correlations in the noise acting on the two qubits are present. In order to quantify the correlation factor

ρ, measurements of the single-qubit decay time are needed as well. We now summarize the experimental procedure; for more information on the measurement setup and individual qubit characteristics, see 4.7.3 and Ref. [25]. Q2 is initialized and read out via spin-selective tunneling to a reservoir [36]. Initialization of Q1 to its ground state is done by fast spin relaxation at a hotspot [37], and readout of Q1 is performed by mapping its spin state onto Q2 via a controlled-rotation (CROT) gate followed by spin readout of Q2 [25]. For single-qubit driving we exploit an artificial spin-orbit coupling, induced by cobalt micromagnets, for electric dipole spin resonance (EDSR) [38]. The two-qubit gate relies on the exchange interaction between the two qubits, controlled by gate voltage pulses. We operate in the regime where the Zeeman energy difference between the two qubits exceeds the two-qubit exchange interaction strength, hence the native two-qubit gate is the controlled-phase gate [25, 39, 40].

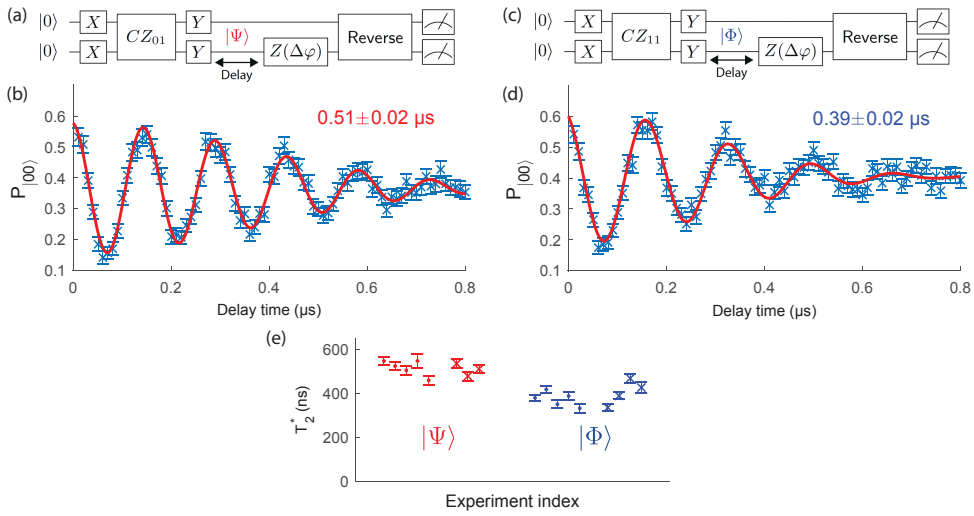

Fig. 4.3: (a,c) Circuit diagrams for two-qubit experiments analogous to the measurement of Ramsey fringes. The gate sequences are designed such that single-qubit rotations are always applied simultaneously to both qubits, avoiding idle times that would lead to faster dephasing. Here $CZ_{ij}|m,n\rangle = (-1)^{\delta(i,m)\delta(j,n)}|m,n\rangle$ for $i,j,m,n \in \{0,1\}$ are the primitive two-qubit gates, constructed from a CZ gate with duration $t = \pi\hbar/J$ and single-qubit rotations [25]. (b,d) Typical $|00\rangle$ return probability as a function of delay time for (b) $|\Psi\rangle$ and (d) $|\Phi\rangle$. The data are fit with a sinusoidal function with Gaussian decay, $P_{|00\rangle} \propto e^{-\left(t/T_2^*\right)^2}$. Error bars are based on a Monte Carlo method by assuming a multinomial distribution for the measured two-spin probabilities and are $\pm 1\sigma$ from the mean [25]. We attribute the slight difference in oscillation frequency between (b) and (d) to crosstalk effects during frequency calibration, as for example observed in Refs. [23, 25, 41]. (e) Scatter plot of decay times for $|\Psi\rangle$ and $|\Phi\rangle$ for two measurement runs separated by ~50 hours (points and crosses). Every data point is averaged over ~100 minutes. The average coherence times are 513 ± 8 ns and 387 ± 6 ns for $|\Psi\rangle$ and $|\Phi\rangle$, respectively. Error bars are $\pm 1\sigma$ from the mean.

Concretely, we perform two-qubit measurements analogous to the measurement of Ramsey fringes to measure the decay of Bell state coherences over time [13]. As shown in the circuits in Figs. 4.3(a,c), we prepare $|\Psi\rangle$ or $|\Phi\rangle$ and after a varying free evolution time we reverse the sequence to ideally return to the $|00\rangle$ state. In every run of the experiment, we measure both spins in single-shot mode and determine the two-spin probabilities

from repeated experiment runs. The two-spin probabilities are normalized and a Gaussian decay is fit to the $|00\rangle$ return probability. To improve the fit of the decay, we add an evolution-time dependent phase to the first microwave pulse applied to Q2 after the delay time (see Z($\Delta\varphi$) in Figs. 4.3(a,c)), so that the measured $|00\rangle$ probability oscillates. We first test the measurement procedure via artificially introduced dephasing from random rotations of each spin around its quantization axis, implemented in software via Pauli frame updates. The decay observed for the anti-parallel (parallel) Bell state is independent of the noise amplitude when the same (opposite) random rotations are applied to both spins, but increases when opposite (the same) random rotations are applied to the two spins, as expected. This validates the measurement protocol.

Figures 4.3(b,d) show typical decay curves for $|\Psi\rangle$ and $|\Phi\rangle$, respectively, when subject to natural noise only. A scatter plot of repeated measurements, Fig. 4.3(e), shows a systematically longer T_2^* for $|\Psi\rangle$ than for $|\Phi\rangle$, indicating correlations in the noise. Using Eq. 4.1, derived for quasistatic noise, we can extract from the decay of $|\Psi\rangle$ and $|\Phi\rangle$ a lower bound for the correlation factor, $\rho \geq 0.27 \pm 0.02$ (see 4.7.8). In order to go beyond a lower bound and determine an estimate of ρ from Eq. 4.1, we also need at least one of the single-qubit dephasing times, which we measured to be $T_{2,1}^* = 0.97 \pm 0.02$ μs and $T_{2,2}^* = 0.59 \pm 0.02$ μs. Using both single-qubit T_2^*s in Eq. 4.1 gives an overdetermined system of equations. We proceed by keeping $T_{2,1}^*/T_{2,2}^*$ equal to the measured ratio, and obtain a modest correlation factor, $\rho = 0.31 \pm 0.03$ (see 4.7.8). The data presented in Figs. 4.3 and 4.4 form a complete dataset with repeated measurements, all performed with very similar gate voltage settings.

We note that in keeping $T_{2,1}^*/T_{2,2}^*$ fixed, Eq. 4.1 returns a value for σ_1 and σ_2 that is ~15% larger than the measured value. The discrepancy may be in part due to the fact that the simple model that leads to Eq. 4.1 assumes quasistatic Gaussian noise. This is a commonly made assumption in simple models of silicon spin qubits, but various experiments showed higher-frequency noise to be relevant as well [20, 22, 25]. However, a more detailed model that accounts for non-quasistatic noise is beyond the scope of this work.

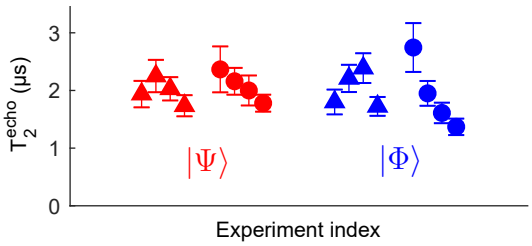

Fig. 4.4: Scatter plot of the two-qubit coherence times obtained in Hahn-echo style measurements for $|\Psi\rangle$ and $|\Phi\rangle$, from a fit to the data with an exponentially decaying sinusoidal function ($P_{|00\rangle} \propto e^{-t/T_2^*}$). Triangles represent data points where the Hahn echo pulses applied to both qubits are rotations around the $\hat{x}$-axis. For the circles, the rotation of Q1 is around $\hat{x}$ and the rotation of Q2 is around $\hat{y}$. Data points are averaged over ~[47, 66, 100, 148] minutes. The average two-qubit Hahn echo coherence times are 2.03 ± 0.09 μs and 1.98 ± 0.09 μs for $|\Psi\rangle$ and $|\Phi\rangle$, respectively. Error bars are $\pm 1\sigma$ from the mean.

In order to gain insight into the frequency dependence of the spatial noise correla-

tions, we perform measurements analogous to Hahn echo measurements. Here the delay times seen in the circuit diagrams of Fig. 4.3(a,c) contain 180 degree rotations around the $\hat{x}$ or $\hat{y}$ axis applied to the two qubits, which reverse the time evolution resulting from static noise contributions (see 4.7.11 for circuit diagrams and details). The results are presented in Fig. 4.4. The echo pulses prolong the two-qubit coherence times by a factor of ~ 4–5. We do not, however, observe a systematic difference in the echo decay times for the parallel versus anti-parallel Bell states, meaning there are no detectable spatial correlations in higher-frequency noise, and the correlations found in the Ramsey-style measurements of Fig. 4.3 are mostly present in the low-frequency part of the spectrum.

4.5. DISCUSSIONS ON NOISE SOURCES

We observe only modest correlations in the noise. In this natural silicon substrate the hyperfine interaction with ^{29}Si nuclear spins, for which little or no spatial correlations are expected [29], is likely to contribute significantly. In the 4.7.9, we estimate the separate contributions to the noise and we estimate the correlation factor in the charge noise only to be $\rho = 0.5 - 0.6$. In order to more reliably assess the spatial noise correlations arising from charge noise only, it would be helpful to repeat the experiments presented here in an isotopically purified ^{28}Si sample.

In addition to noise that is uncorrelated by itself, multiple noise sources that produce correlated noise on the qubits can add up to give rise to noise that is mostly uncorrelated as well. This can be seen from the following observations. Multiple independently fluctuating noise sources each producing perfectly correlated noise ($\rho = 1$) with the same relative amplitude on the two qubits, are equivalent to a single (stronger) source of perfectly correlated noise with this same relative amplitude on the two qubits. However, randomly distributed relative amplitudes with random sign would rapidly render the combined noise indistinguishable from uncorrelated noise.

Different relative amplitudes can occur for charge noise from multiple charge fluctuators close to the dots, which couple to the spin states through the magnetic field gradient. Also remote charge fluctuators can give rise to different noise amplitudes on the two spins, for instance when the tightness of the confining potential, the local magnetic field gradient or the gate screening differs between the dots (indeed Tab. S3 reveals that Q2 is much more sensitive to electric fields than Q1 [35]). In the 4.7.12 we illustrate this effect with an example simulation and describe it mathematically.

Based on this discussion, a picture emerges where the combination of noise from multiple distant charge fluctuators that affect the qubits asymmetrically due to their different confining potentials and nuclear spin noise, is responsible for the (weak) spatial noise correlations at low frequency.

4.6. CONCLUSION

In summary, we have demonstrated a method to quantitatively study spatial noise correlations based on the coherence of Bell states in a Si/SiGe two-qubit device. Experimentally we observe small spatial correlations in low-frequency noise, while for higher-frequency noise correlations appear to be absent. Applying this method to an isotopically purified silicon spin qubit device will yield more quantitative information on corre-

lations present in charge noise only. Our findings on the importance of asymmetric coupling of noise sources to two (or more) qubits can be exploited for reducing or enhancing spatial correlations in the noise in any qubit platform. For the case of spin qubits in quantum dots, this can be done for instance through a device design with engineered differences in confining potential or magnetic field gradient. In this respect, qubits encoded in two-electron spin states in dot-donor systems offer an extreme difference in confining potential [42]. We anticipate that the optimization of future quantum error correction codes will go hand in hand with the design of qubits that either maximize or minimize spatial noise correlations, as has been done in for example Ref. [43].

4.7. APPENDICES

4.7.1. NOISE MODEL

We model the two-qubit system by the Hamiltonian:

$$H = \frac{hf_1}{2}\sigma_1^Z + \frac{hf_2}{2}\sigma_2^Z, \tag{4.2}$$

where h is the Planck constant, $f_i = \frac{g\mu_B B_i}{h}$ is the Larmor frequency for qubit i, g is the electron g-factor, μ_B is the Bohr magneton, B_i is the total magnetic field at the position of qubit i and σ_i^Z is the Pauli Z operator for qubit i. The two qubits are subject to dephasing noise, which we model as a fluctuating qubit frequency f_i. We assume Gaussian distributed noise with zero mean and covariance matrix Σ:

$$\mathbf{f} = (f_1, f_2) \sim \mathcal{N}((0,0), \Sigma); \Sigma = \begin{bmatrix} \sigma_1^2 & \rho\sigma_1\sigma_2 \\ \rho\sigma_1\sigma_2 & \sigma_2^2 \end{bmatrix}, \tag{4.3}$$

where σ_i^2 is the variance of the noise in f_i, and ρ ($-1 \leq \rho \leq 1$) is a correlation factor. Positive ρ indicates correlations, while negative ρ indicates anti-correlations. We obtain the unitary time evolution operator in the $\{|00\rangle, |01\rangle, |10\rangle, |11\rangle\}$ basis by exponentiating the Hamiltonian:

$$U = e^{-iHt/\hbar} = \begin{pmatrix} e^{-i\pi(f_1+f_2)t} & & & \\ & e^{-i\pi(f_1-f_2)t} & & \\ & & e^{i\pi(f_1-f_2)t} & \\ & & & e^{i\pi(f_1+f_2)t} \end{pmatrix}, \tag{4.4}$$

where $\hbar = \frac{h}{2\pi}$. Assuming quasistatic noise, we average over this unitary transformation by integrating over the joint probability distribution function:

$$\rho(t) = \overline{U\rho(0)U^\dagger} = \frac{1}{2\pi\sqrt{\det(\Sigma)}} \int U\rho(0)U^\dagger e^{-\mathbf{f}^T\Sigma^{-1}\mathbf{f}/2} d\mathbf{f}. \tag{4.5}$$

The relevant expressions for anti-parallel ($|\Psi\rangle$) and parallel ($|\Phi\rangle$) Bell states, reflecting dephasing between $|01\rangle$ and $|10\rangle$, and $|00\rangle$ and $|11\rangle$, respectively, are:

$$\begin{aligned} \langle 01|\overline{U\rho(0)U^\dagger}|10\rangle &= \frac{1}{2} \times \frac{1}{2\pi\sqrt{\det(\Sigma)}} \int e^{-i2\pi(f_1-f_2)t} e^{-\mathbf{f}^T\Sigma^{-1}\mathbf{f}/2} d\mathbf{f} = \frac{1}{2}\exp\left[-2\pi^2 t^2(\sigma_1^2+\sigma_2^2-2\rho\sigma_1\sigma_2)\right], \\ \langle 00|\overline{U\rho(0)U^\dagger}|11\rangle &= \frac{1}{2} \times \frac{1}{2\pi\sqrt{\det(\Sigma)}} \int e^{-i2\pi(f_1+f_2)t} e^{-\mathbf{f}^T\Sigma^{-1}\mathbf{f}/2} d\mathbf{f} = \frac{1}{2}\exp\left[-2\pi^2 t^2(\sigma_1^2+\sigma_2^2+2\rho\sigma_1\sigma_2)\right], \end{aligned} \tag{4.6}$$

so the decay for anti-parallel and parallel Bell states is Gaussian with associated time scales (Eq. 1 of the main text):

$$\begin{aligned}\left(\frac{1}{T^*_{2,|\Psi\rangle}}\right)^2 &= 2\pi^2\left(\sigma_1^2+\sigma_2^2-2\rho\sigma_1\sigma_2\right),\\ \left(\frac{1}{T^*_{2,|\Phi\rangle}}\right)^2 &= 2\pi^2\left(\sigma_1^2+\sigma_2^2+2\rho\sigma_1\sigma_2\right).\end{aligned} \tag{4.7}$$

Noting that in the case of Gaussian quasistatic noise for single-qubit decay $\left(\frac{1}{T^*_{2,i}}\right)^2 = 2\pi^2\sigma_i^2$, these expressions can be rewritten in terms of single-qubit coherence times:

$$\left(\frac{1}{T^*_{2,|\Psi\rangle}}\right)^2 = \left(\frac{1}{T^*_{2,1}}\right)^2 + \left(\frac{1}{T^*_{2,2}}\right)^2 - 2\rho\frac{1}{T^*_{2,1}T^*_{2,2}}, \tag{4.8}$$

$$\left(\frac{1}{T^*_{2,|\Phi\rangle}}\right)^2 = \left(\frac{1}{T^*_{2,1}}\right)^2 + \left(\frac{1}{T^*_{2,2}}\right)^2 + 2\rho\frac{1}{T^*_{2,1}T^*_{2,2}}. \tag{4.9}$$

Subtracting Eq. 4.8 from Eq. 4.9, we express the correlation factor ρ in terms of the single- and two-qubit coherence times as:

$$\rho = \frac{T^*_{2,1}T^*_{2,2}}{4}\left[\left(\frac{1}{T^*_{2,|\Phi\rangle}}\right)^2 - \left(\frac{1}{T^*_{2,|\Psi\rangle}}\right)^2\right]. \tag{4.10}$$

4.7.2. MEASUREMENT SETUP

The measurement setup used in this work is the same as the setup used by Watson *et al.* [25] and Xue *et al.* [23]. The measurements were done at a temperature of $T \approx 30$ mK in an external magnetic field of B_{ext} = 617 mT. DC voltages are set via filtered lines from room-temperature digital-to-analog converters. Tektronix 5014C arbitrary waveform generators (AWGs) are connected to gates P1 and P2 via coaxial cables for gate voltage pulses. Keysight E8267D vector microwave sources are connected to gates MW1 and MW2 for EDSR. I/Q input channels of the microwave sources are connected to a master AWG to control frequency, phase and duration of the microwave bursts via I/Q modulation. The phase of the microwave drive signal determines the rotation axis in the $\hat{x}-\hat{y}$ plane of the Bloch sphere, and we update the rotating reference frame in software to perform $\hat{z}$ rotations [45]. Pulse modulation is used to increase the on/off ratio of the microwave bursts. The master AWG also controls the clock of the entire system and triggers all the other instruments. Data acquisition is done by a Spectrum M4i.44 digitizer card that is installed in the measurement computer. This card records the sensing dot current traces at a sampling rate of ~60 kHz after passing through a 12-kHz Bessel low-pass filter (SIM965). Threshold detection is used to convert each trace to a single bit value (0 or 1) by the measurement computer. A schematic of the measurement setup is shown in Extended Data Figure 1 of Ref. [25].

	Q1	Q2
f	18.35 GHz	19.61 GHz
T_1	>50 ms [25]	3.7±0.5 ms [25]
T_2^*	0.97±0.02 μs	0.59±0.02 μs
T_2^{Hahn}	6.8±0.3 μs	2.8±0.2 μs
$F_{\|\Psi^+\rangle}$	0.88±0.02 [25]	
$F_{\|\Psi^-\rangle}$	0.88±0.02 [25]	
$F_{\|\Phi^+\rangle}$	0.85±0.02 [25]	
$F_{\|\Phi^-\rangle}$	0.89±0.02 [25]	

Table 4.1: Relevant single-qubit characteristics for simultaneous driving of both qubits, and Bell state fidelities F for the four Bell states. All errors are $\pm 1\sigma$ from the mean.

4.7.3. QUBIT CHARACTERISTICS

For both qubits the microwave power is tuned to obtain a Rabi frequency of 2 MHz and a CPhase gate is performed in 90 ns. An upper bound on the residual exchange during single-qubit gates and free evolution of 100 kHz is determined from a decoupled CZ experiment with the detuning amplitude set to zero. Maximally a half exchange oscillation is observed in 5 μs.

4.7.4. REMOVING READOUT ERRORS

To remove errors in the measured two-spin probabilities $\mathbf{P}^M = (P^M_{|00\rangle}, P^M_{|01\rangle}, P^M_{|10\rangle}, P^M_{|11\rangle})^T$ caused by the limited readout fidelities $F_{|0\rangle}$ and $F_{|1\rangle}$ we use the relation $\mathbf{P}^M = (\hat{F}_1 \otimes \hat{F}_2)\mathbf{P}$, where

$$\hat{F}_i = \begin{pmatrix} F_{|0\rangle,i} & 1-F_{|1\rangle,i} \\ 1-F_{|0\rangle,i} & F_{|1\rangle,i} \end{pmatrix}, \tag{4.11}$$

to obtain the actual two-spin probabilities $\mathbf{P} = (P_{|00\rangle}, P_{|01\rangle}, P_{|10\rangle}, P_{|11\rangle})^T$. The readout fidelities are estimated from measurements of the spin-up probabilities P_1 and P_2 in experiments where we (1) initialize the qubit in $|0\rangle$ as described in the main text, and (2) initialize the qubit in $|0\rangle$ and perform a π rotation:

$$\begin{aligned} P_{1,i} &= 1 - F_{|0\rangle,i} \\ \frac{P_{2,i}}{P_{\pi,i}} &= F_{|1\rangle,i} \end{aligned} \tag{4.12}$$

where i is the qubit number and $P_{\pi,i}$ is the expected spin-up probability after a π pulse on qubit i. The scripts used for this procedure are included in the Zenodo repository [44].

4.7.5. ERROR ANALYSIS

Error bars on the measured two-spin probabilities, as shown in Figs. 3(b,d) of the main text, are estimated using a Monte Carlo method, that serves to easily account for the propagation of errors, by assuming a binomial and a multinomial distribution for the readout fidelities and two-spin probabilities, respectively. Estimated readout fidelities obtained from an average of the measurements described in the section "Removing readout errors" and the average measured two-spin probabilities are used as input for these

distributions, respectively. For every data point, these distributions are used to obtain samples of the readout fidelities and two-spin probabilities (the number of samples for both distributions is the same as in the experiments), and Eq. 4.11 is used to remove readout errors and obtain actual two-spin probabilities. This procedure is repeated 1000 times to acquire statistics. The mean and standard deviation for every data point are determined from the final distributions.

The error bars on the coherence times, as shown in Fig. 3(e) of the main text, result from the fitting procedure in which the errors of the data points are used as weights. These errors are subsequently propagated to the errors on β, effective single-qubit coherence times and ρ.

4.7.6. IMPROVE FITTING

To improve the fit of the decay, we add an evolution-time dependent phase to the first microwave pulse applied to Q2 after the delay time (see Z($\Delta\varphi$) in Fig. 3(a,c) of the main text). The additional phase $\Delta\varphi$ is increased linearly with the delay time Δt. The added phase shift acting on Q2 affects the phase of the Bell state and consequently the $|00\rangle$ probability oscillates. The proportionality constant between $\Delta\varphi$ and Δt sets the frequency Δf of the oscillation of the $|00\rangle$ probability that results, $\Delta\varphi = \Delta f \cdot \Delta t$. Here we choose Δf = 6 MHz. The additional phase is applied by an update of the rotating reference frame in software in the same way as how we perform $\hat{z}$ rotations.

4.7.7. METHOD VALIDATION

To verify the method used in this work, we inject artificial noise in the experiments by applying random software Z rotations to both qubits and measure the decay curves for $|\Psi\rangle$ and $|\Phi\rangle$. These rotations are implemented by adding an evolution time dependent phase to the first microwave pulse after the waiting time, in addition to the phase to improve the fit of the decay. Adding (anti-)correlated noise is expected to have an effect on $|\Phi\rangle$ ($|\Psi\rangle$), but not on $|\Psi\rangle$ ($|\Phi\rangle$).

Figure 4.5 shows the results of this control experiment. In these measurements, the frequency fluctuations corresponding to the extra phase are sampled from a Gaussian distribution with a standard deviation of 0.4 MHz. However, only a single configuration of artificial noise has been sampled: for every data point on the wait time axis a different artificial noise value has been sampled, but every single-shot measurement for a specific wait time used the same artificial noise value. As a result, there has not been averaging over different artificial noise values in this data. We therefore cannot use this data for a quantitative comparison. Still, we clearly observe the expected behavior that (anti-)correlated noise does not have a noticeable effect on $|\Psi\rangle$ ($|\Phi\rangle$), while the decay curve looks very irregular for $|\Phi\rangle$ ($|\Psi\rangle$), as expected when sampling a different (fixed) noise amplitude for every wait time.

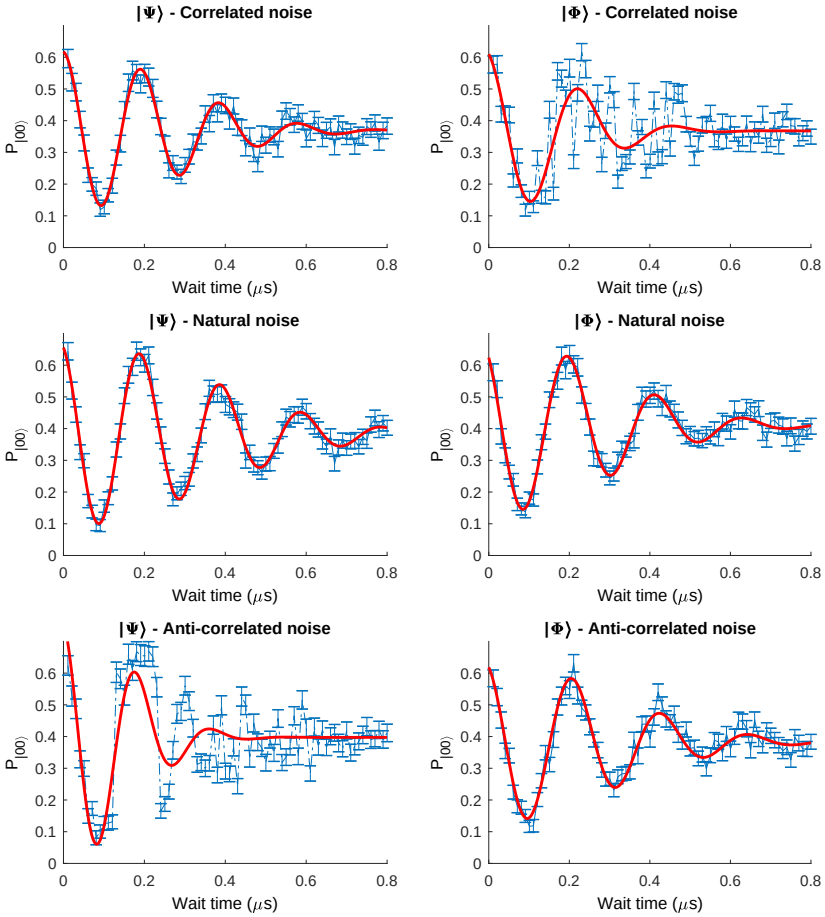

Fig. 4.5: Control experiment in which articial noise has been injected. The left (right) column corresponds to $|\Psi\rangle$ ($|\Phi\rangle$), and in the top, middle and bottom row correlated noise, no noise and anti-correlated noise has been artificially added, respectively. There is no noticeable effect of (anti-)correlated noise on $|\Psi\rangle$ ($|\Phi\rangle$), but the data quality is affected for $|\Phi\rangle$ ($|\Psi\rangle$).

4.7.8. QUANTIFYING CORRELATIONS

Equations 4.8 and 4.9 yield three expressions for ρ. In addition to Eq. 4.10, these expressions are:

$$\rho = \frac{T_{2,1}^* T_{2,2}^*}{2}\left[\left(\frac{1}{T_{2,|\Phi\rangle}^*}\right)^2 - \left(\frac{1}{T_{2,1}^*}\right)^2 - \left(\frac{1}{T_{2,2}^*}\right)^2\right], \tag{4.13}$$

$$\rho = \frac{T_{2,1}^* T_{2,2}^*}{2}\left[\left(\frac{1}{T_{2,1}^*}\right)^2 + \left(\frac{1}{T_{2,2}^*}\right)^2 - \left(\frac{1}{T_{2,|\Psi\rangle}^*}\right)^2\right]. \tag{4.14}$$

Eqs. 4.10, 4.13 and 4.14 yield $\rho = 0.41$, $\rho = 0.79$ and $\rho = 0.037$, respectively, as outcomes by using the measured values for the single- and two-qubit coherence times. Ideally, these expressions give the same outcome, but the different values are the result of the system of equations being overdetermined, deviations from Gaussian decay and experimental uncertainties. Equation 4.10 uses all available coherence times and is symmetric. Equations 4.13 and 4.14 only use three out of four coherence times and are asymmetric, and consequently overestimate (Eq. 4.13) and underestimate (Eq. 4.14) the correlation factor, respectively. Equation 4.10 is the average of Eqs. 4.13 and 4.14. For these reasons, we consider Eq. 4.10 to be more reliable.

In case the experimental data is not fully consistent with the simple quasistatic model, it is still possible to use this model to extract quantitative information on the correlations in the noise acting on the qubits based only on the two-qubit coherence times. From Eqs. 4.8 and 4.9, given the two-qubit coherence times, effective single-qubit coherence times can be calculated as:

$$\left(\frac{1}{T^*_{2,1(2)}}\right)^2 = \frac{\left(\frac{1}{T^*_{2,|\Phi\rangle}}\right)^2 + \left(\frac{1}{T^*_{2,|\Psi\rangle}}\right)^2}{4} \mp \frac{1}{2}\sqrt{\left(\frac{\left(\frac{1}{T^*_{2,|\Phi\rangle}}\right)^2 + \left(\frac{1}{T^*_{2,|\Psi\rangle}}\right)^2}{2}\right)^2 - 4\left(\frac{\left(\frac{1}{T^*_{2,|\Phi\rangle}}\right)^2 - \left(\frac{1}{T^*_{2,|\Psi\rangle}}\right)^2}{4\rho}\right)^2}, \tag{4.15}$$

where the minus (plus) sign corresponds to Q1 (Q2), assuming $T^*_{2,1} \geq T^*_{2,2}$. Solutions only exist if the argument of the square root is equal to or larger than zero, so for

$$|\rho| \geq \rho_{min} = \left| \frac{\left(\frac{1}{T^*_{2,|\Phi\rangle}}\right)^2 - \left(\frac{1}{T^*_{2,|\Psi\rangle}}\right)^2}{\left(\frac{1}{T^*_{2,|\Phi\rangle}}\right)^2 + \left(\frac{1}{T^*_{2,|\Psi\rangle}}\right)^2} \right|. \tag{4.16}$$

Using this simple model, we find a lower bound for the correlation factor $\rho_{min} = 0.27 \pm 0.02$.

Taking into account the experimental single-qubit coherence times and assuming their ratio ($\beta = \frac{T^*_{2,2}}{T^*_{2,1}}$) to be fixed, effective single-qubit coherence times can be obtained by adding Eqs. 4.8 and 4.9, and are given by:

$$\left(\frac{1}{T^*_{2,1}}\right)^2 = \left(\frac{\beta}{T^*_{2,2}}\right)^2 = \frac{\beta^2}{2(1+\beta^2)}\left[\left(\frac{1}{T^*_{2,|\Phi\rangle}}\right)^2 + \left(\frac{1}{T^*_{2,|\Psi\rangle}}\right)^2\right]. \tag{4.17}$$

The correlation factor ρ from Eq. 4.10 in that case is expressed as:

$$\rho = \frac{\beta\left(T^*_{2,1}\right)^2}{4}\left[\left(\frac{1}{T^*_{2,|\Phi\rangle}}\right)^2 - \left(\frac{1}{T^*_{2,|\Psi\rangle}}\right)^2\right]. \tag{4.18}$$

For the experimental value $\beta = 0.61 \pm 0.02$ ($T^*_{2,1} = 0.97 \pm 0.02$ μs and $T^*_{2,2} = 0.59 \pm 0.02$ μs), we find a correlation factor $\rho = 0.31 \pm 0.03$, and effective single-qubit coherence times $T^*_{2,1} = 0.84 \pm 0.03$ μs and $T^*_{2,2} = 0.51 \pm 0.02$ μs. The value obtained in this analysis by fixing β is close to the value obtained through the symmetric expression Eq. 4.10 ($\rho = 0.41$).

4.7.9. SUBTRACTING NUCLEAR SPIN NOISE

In an isotopically purified silicon sample, the contribution from nuclear spin noise would be considerably smaller than in the natural silicon sample in the present experiments. Nuclear spin noise is typically uncorrelated between adjacent dots [29], so it is interesting to obtain insight in the spatial noise correlations arising from charge noise only. Under the assumptions of quasistatic noise, zero correlations in the nuclear spin noise affecting both qubits, and no correlations between the contributions from nuclear spin noise and charge noise, single- and two-qubit coherence times after taking out nuclear spin noise can be found in the following way:

$$\begin{aligned}
\left(\frac{1}{T^*_{2,1,charge}}\right)^2 &= \left(\frac{1}{T^*_{2,1}}\right)^2 - \left(\frac{1}{T^*_{2,1,nuc}}\right)^2 \\
\left(\frac{1}{T^*_{2,2,charge}}\right)^2 &= \left(\frac{1}{T^*_{2,2}}\right)^2 - \left(\frac{1}{T^*_{2,2,nuc}}\right)^2 \\
\left(\frac{1}{T^*_{2,|\Psi\rangle,charge}}\right)^2 &= \left(\frac{1}{T^*_{2,|\Psi\rangle}}\right)^2 - \left(\frac{1}{T^*_{2,1,nuc}}\right)^2 - \left(\frac{1}{T^*_{2,2,nuc}}\right)^2 \\
\left(\frac{1}{T^*_{2,|\Phi\rangle,charge}}\right)^2 &= \left(\frac{1}{T^*_{2,|\Phi\rangle}}\right)^2 - \left(\frac{1}{T^*_{2,1,nuc}}\right)^2 - \left(\frac{1}{T^*_{2,2,nuc}}\right)^2
\end{aligned} \tag{4.19}$$

The correlation factor after removing the effect from nuclear spin noise can then be calculated by using these adjusted coherence times in the procedure outlined in the previous section.

We define the ratio α between between the strengths of the contributions from nuclear spins and charge noise ($\sigma^2_{nuc} = \alpha \cdot \sigma^2_{charge}$ with $\sigma^2_{total} = \sigma^2_{nuc} + \sigma^2_{charge}$), and calculate the resulting correlation factor for several values of α, as listed in Tab. 4.2. As expected, after taking out the effect of nuclear spin noise, we find longer coherence times and an increased correlation factor in all cases. Furthermore, the correlation factor for charge noise (ρ_{charge}) increases when a larger fraction of the total noise is attributed to nuclear spins. Interesting to note is that $T^*_{2,|\Psi\rangle,charge}$ increases more than $T^*_{2,|\Phi\rangle,charge}$, which is expected given that $|\Psi\rangle$ is the decoherence-free subspace for correlated noise.

For illustration purposes, we have also determined the ratio between the contributions from nuclear spin noise and charge noise for which we find a correlation factor of $\rho \approx 1$ with this analysis. We find this requires a ratio of $\alpha \approx 11.4$. Thus only if the noise from nuclear spins is more than an order of magnitude stronger than the charge noise, which we consider an unlikely scenario, we find full correlations in charge noise.

In the Methods of Ref. [25], which made use of the same sample though tuned in a somewhat different configuration, the authors estimate the charge noise and nuclear spin noise contributions to be of the same order of magnitude, with the nuclear spin noise contribution slightly larger ($\alpha = 1.2-1.9$). Assuming this ratio did not change much when retuning the device, we can estimate the correlations in the charge noise to be $\rho = 0.5-0.6$.

α	$T^*_{2,1,charge}$ (μs)	$T^*_{2,2,charge}$ (μs)	$T^*_{2,\|\Psi\rangle,charge}$ (μs)	$T^*_{2,\|\Phi\rangle,charge}$ (μs)	ρ_{charge}
$\frac{1}{1.5}$	1.01	0.61	0.67	0.44	0.44
$\frac{1}{1.25}$	1.03	0.63	0.70	0.45	0.46
1.00	1.06	0.65	0.74	0.46	0.50
1.25	1.10	0.67	0.79	0.47	0.53
1.50	1.13	0.69	0.83	0.48	0.56
1.75	1.16	0.71	0.88	0.49	0.59
2.00	1.19	0.72	0.92	0.50	0.62
11.4	1.51	0.92	2.35	0.57	1.00

Table 4.2

4.7.10. BELL STATE FIDELITIES

The Bell state preparation fidelities can in principle affect the noise correlations extracted from comparing the respective Bell state decays. Imperfect Bell state preparation can result in a finite overlap of the prepared state with Bell states of different symmetry. This will result in a combination of two decays and therefore affect the extracted coherence times and spatial noise correlations. In the present experiments, the Bell states have not been characterized, but for the Bell state density matrices presented in the Supplementary Information of Ref. [25], we determine the overlap of the prepared states with all four Bell states (see Table 4.3). The Bell state fidelities are on the diagonal of this table. The overlap of the prepared states with Bell states of different symmetry is 3–8%, so the contribution of the states with different symmetry is limited. In our experiments we indeed do not see deviations from a single decay and we expect the effect on the extracted spatial noise correlations to be limited.

	$\|\Phi^+\rangle$	$\|\Phi^-\rangle$	$\|\Psi^+\rangle$	$\|\Psi^-\rangle$
$\|\Phi^+\rangle_{exp}$	0.85	0.11	0.02	0.01
$\|\Phi^-\rangle_{exp}$	0.07	0.89	0.02	0.02
$\|\Psi^+\rangle_{exp}$	0.03	0.05	0.88	0.04
$\|\Psi^-\rangle_{exp}$	0.03	0.05	0.04	0.88

Table 4.3: Overlap of the four states experimentally prepared in Ref. [25] (rows) with the four orthogonal Bell states (columns), e.g. the overlap of the prepared $|\Phi^+\rangle_{exp}$ state with $|\Phi^-\rangle$ is 0.11. Only overlap with Bell states of different symmetry (indicated in red) results in a decay with a different timescale.

The main error sources that affect the Bell state preparation fidelities are dephasing due to nuclear spins and charge noise which impact the gate fidelities. Specifically, the two-qubit gate is performed by pulsing the detuning (instead of the tunnel barrier), which renders it first-order sensitive to charge noise.

4.7.11. ECHO EXPERIMENTS

Dynamical decoupling sequences can be used to investigate the frequency dependence of spatial noise correlations, similar to mapping out the frequency spectrum of noise acting on a single qubit [21, 22, 46]. In addition to the measurements analogous to

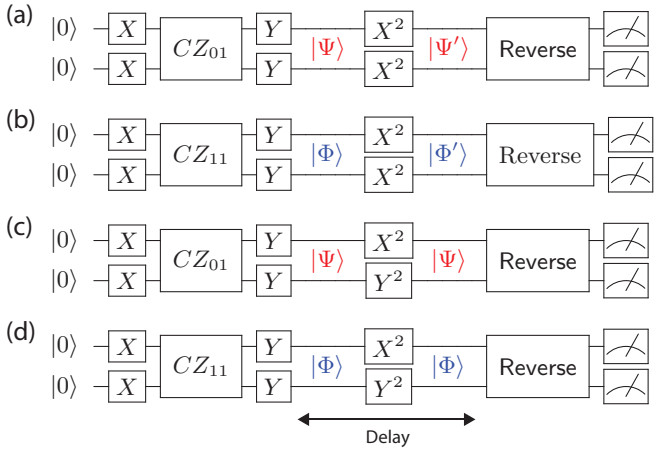

Fig. 4.6: Circuit diagrams for two different versions ((a,b) XX and (c,d) XY) of an experiment analogous to the measurement of a Hahn echo for (a,c) $|\Psi\rangle$ and (b,d) $|\Phi\rangle$.

Ramsey experiments, we performed measurements analogous to a Hahn echo experiment with a single decoupling pulse on each qubit halfway the waiting time. Results are presented in Fig. 4 of the main text. We performed two versions of the echo experiment to which we refer as XX and XY echo, respectively. In the XX echo experiment we apply a π_X pulse on both qubits, which transforms $|\Psi\rangle = (|{\downarrow\uparrow}\rangle - i\,|{\uparrow\downarrow}\rangle)/\sqrt{2}$ into $|\Psi'\rangle = (|{\downarrow\uparrow}\rangle + i\,|{\uparrow\downarrow}\rangle)/\sqrt{2}$, and $|\Phi\rangle = (|{\downarrow\downarrow}\rangle - i\,|{\uparrow\uparrow}\rangle)/\sqrt{2}$ into $|\Phi'\rangle = (|{\downarrow\downarrow}\rangle + i\,|{\uparrow\uparrow}\rangle)/\sqrt{2}$, as shown in the circuits in Figs. 4.6(a,b). The XY echo experiment consists of a π_X pulse on Q1 and a π_Y pulse on Q2, which transforms $|\Psi\rangle$ and $|\Phi\rangle$ to itself, as shown in the circuits in Figs. 4.6(c,d). The difference between the XX and XY sequences is analogous to that between single-qubit echo pulses around $\hat{x}$ versus $\hat{y}$. We do note that for both versions of the two-qubit decoupling used in this work, the two-qubit state is taken out of the logical qubit space during the pulses.

4.7.12. SIMULATION OF MULTIPLE ASYMMETRIC NOISE SOURCES

The result of a simulation of the combined effect of three asymmetric, correlated noise sources is shown in Fig. 4.7. The standard deviations of the distributions of fluctuations in difference and sum frequencies indicate that only modest correlations in the noise remain for their combined effect.

ADDING MULTIPLE INDEPENDENT NOISE SOURCES

Consider a single noise source i with coupling strengths $\alpha_{i,1}$ and $\alpha_{i,2}$ (which can be expressed for instance in units of MHz/mV, if noise source i is expressed in units of mV) to qubit 1 and qubit 2, respectively. The noise source fluctuates with standard deviation σ. The standard deviations of the fluctuations in the difference $(f_1 - f_2)$ and sum $(f_1 + f_2)$ of the frequencies are then given by:

$$\begin{aligned} \sigma_{i,-} &= \sigma|\alpha_{i,1} - \alpha_{i,2}|, \\ \sigma_{i,+} &= \sigma|\alpha_{i,1} + \alpha_{i,2}|. \end{aligned} \tag{4.20}$$

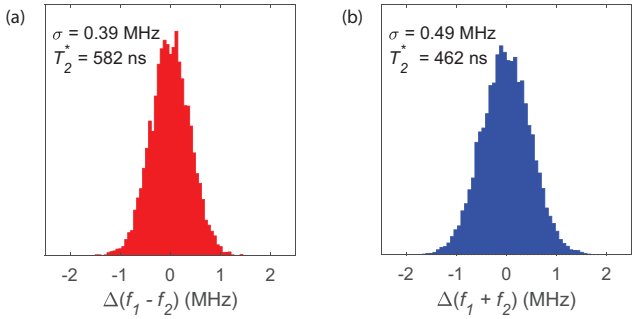

Fig. 4.7: Simulation of three noise sources with coupling factors chosen to correspond to the experimentally measured coupling factors for three of the gate electrodes on the sample, namely P1, P2 and MW2 in Fig. 1(a) of the main text. The coupling factors to the two qubits for these and five other gate electrodes are tabulated in Table 4.4. For all three gate electrodes, voltage fluctuations are sampled from a Gaussian distribution with 50 μV standard deviation. After sampling gate voltage fluctuations, the corresponding total frequency fluctuations for both qubits, and their difference and sum are calculated. The distributions of the fluctuations in (a) difference and (b) sum frequency are plotted.

For N independent noise sources the combined standard deviation is given by:

$$\sigma^2 = \Sigma_i^N \sigma_i^2. \tag{4.21}$$

Combining Eqs. 4.20 and 4.21 gives:

$$\begin{aligned} \sigma_- &= \sqrt{\Sigma_i^N \sigma_{i,-}^2} = \sigma \sqrt{\Sigma_i^N \left(\alpha_{i,1} - \alpha_{i,2}\right)^2}, \\ \sigma_+ &= \sqrt{\Sigma_i^N \sigma_{i,-}^2} = \sigma \sqrt{\Sigma_i^N \left(\alpha_{i,1} + \alpha_{i,2}\right)^2}, \end{aligned} \tag{4.22}$$

where we absorb differences in standard deviations between noise sources in the coupling strengths. Since $T_2^* \propto \frac{1}{\sigma}$, this yields:

$$\frac{T_{2,|\Phi\rangle}^*}{T_{2,|\Psi\rangle}^*} = \frac{\sigma_-}{\sigma_+} \propto \sqrt{\frac{\sum_i (\alpha_{i,1} - \alpha_{i,2})^2}{\sum_i (\alpha_{i,1} + \alpha_{i,2})^2}}. \tag{4.23}$$

This expression mathematically describes the possible effects of a combination of multiple noise sources on qubits that are described in the main text. An extreme example described by this expression, is that perfectly correlated and perfectly anti-correlated noise with equal amplitude combined are equivalent to uncorrelated noise.

Fluctuating background charges in the substrate, interfaces or dielectrics directly affect the qubit splitting because of the magnetic field gradient produced by the micromagnets. When these charges are located close to the dots, they will generally couple differently to the two qubits, introducing asymmetric noise. Specifically for charge fluctuators located in between the two dots, even anti-correlated noise may result. For distant charges, the coupling becomes more symmetric, but several factors can lead to asymmetric noise amplitudes even in this case, for instance a difference in the confining potential between the two dots, a difference in the strength of the local magnetic field

	Q1	Q2
P1	-1	-2
P2	0.175	0.8
MW1	-0.015	0.025
MW2	0.8	8.5
B	0.43	0.36
LD	-0.1	-1.44
accQD	0.9	-1.8
accRes	-0.8	-3.75

Table 4.4: Coupling factors (in MHz/mV) of eight of the surface gate electrodes on our sample to the two qubits.

gradient or different effects of gate screening resulting from the locations of the two dots relative to the gates. We have clear evidence of a pronounced difference in the confining potential of the two dots in this sample, based on the sensitivity of the respective qubit splittings to changes in gate voltages (see Tab. 4.4). Similar considerations apply to the effect of gate voltage noise, which also couples to the qubit splitting through the magnetic field gradient.

REFERENCES

[1] D. S. Wang, A. G. Fowler, and L. C. L. Hollenberg, *Surface code quantum computing with error rates over 1%*, Phys. Rev. A **83**, 020302(R) (2011).

[2] D. A. Lidar, I. L. Chuang, and K. B. Whaley, *Decoherence-Free Subspaces for Quantum Computation*, Phys. Rev. Lett. **81**, 2594 (1998).

[3] J. Levy, *Universal Quantum Computation with Spin*-1/2 *Pairs and Heisenberg Exchange*, Phys. Rev. Lett. **89**, 147902 (2002).

[4] J. R. Petta, A. C. Johnson, J. M. Taylor, E. A. Laird, A. Yacoby, M. D. Lukin, C. M. Marcus, M. P. Hanson, and A. C. Gossard, *Coherent Manipulation of Coupled Electron Spins in Semiconductor Quantum Dots*, Science **309**, 2180 (2005).

[5] M. Friesen, J. Ghosh, M. A. Eriksson, and S. N. Coppersmith, *A decoherence-free subspace in a charge quadrupole qubit*, Nature Communications **8**, 15923 (2017).

[6] J. Preskill, *Sufficient condition on noise correlations for scalable quantum computing*, Quantum Inf. Comput. **13**, 181 (2013).

[7] Á. Rivas and M. Müller, *Quantifying spatial correlations of general quantum dynamics*, New J. Phys. **17**, 062001 (2015).

[8] P. Szańkowski, M. Trippenbach, and Ł. Cywiński, *Spectroscopy of cross correlations of environmental noises with two qubits*, Phys. Rev. A **94**, 012109 (2016).

[9] G. A. Paz-Silva, L. M. Norris, and L. Viola, *Multiqubit spectroscopy of Gaussian quantum noise*, Phys. Rev. A **95**, 022121 (2017).

[10] J. Krzywda, P. Szańkowski, J. Chwedeńczuk, and Ł. Cywiński, *Decoherence-assisted detection of entanglement of two qubit states*, Phys. Rev. A **98**, 022329 (2018).

[11] L. Postler, Á. Rivas, P. Schindler, A. Erhard, R. Stricker, D. Nigg, T. Monz, R. Blatt, and M. Müller, *Experimental quantification of spatial correlations in quantum dynamics*, Quantum **2**, 90 (2018).

[12] D. Kwiatkowski and Ł. Cywiński, *Decoherence of two entangled spin qubits coupled to an interacting sparse nuclear spin bath: Application to nitrogen vacancy centers*, Phys. Rev. B **98**, 155202 (2018).

[13] V. N. Premakumar and R. Joynt, *Error Mitigation in Quantum Computers subject to Spatially Correlated Noise*, arXiv:1812.07076 .

[14] J. Krzywda, P. Szańkowski, and Ł. Cywiński, *The dynamical-decoupling-based spatiotemporal noise spectroscopy*, New J. Phys. **21**, 043034 (2019).

[15] T. Monz, P. Schindler, J. T. Barreiro, M. Chwalla, D. Nigg, W. A. Coish, M. Harlander, W. Hänsel, M. Hennrich, and R. Blatt, *14-Qubit Entanglement: Creation and Coherence*, Phys. Rev. Lett. **106**, 130506 (2011).

[16] A. Ozaeta and P. L. McMahon, *Decoherence of up to 8-qubit entangled states in a 16-qubit superconducting quantum processor*, Quantum Sci. Technol. **4**, 025015 (2019).

[17] D. Loss and D. P. DiVincenzo, *Quantum computation with quantum dots*, Phys. Rev. A **57**, 120 (1998).

[18] F. A. Zwanenburg, A. S. Dzurak, A. Morello, M. Y. Simmons, L. C. L. Hollenberg, G. Klimeck, S. Rogge, S. N. Coppersmith, and M. A. Eriksson, *Silicon quantum electronics*, Rev. Mod. Phys. **85**, 961 (2013).

[19] L. M. K. Vandersypen, H. Bluhm, J. S. Clarke, A. S. Dzurak, R. Ishihara, A. Morello, D. J. Reilly, L. R. Schreiber, and M. Veldhorst, *Interfacing spin qubits in quantum dots and donors—hot, dense, and coherent*, npj Quantum Information **3**, 34 (2017).

[20] M. Veldhorst, J. C. C. Hwang, C. H. Yang, A. W. Leenstra, B. de Ronde, J. P. Dehollain, J. T. Muhonen, F. E. Hudson, K. M. Itoh, A. Morello, and A. S. Dzurak, *An addressable quantum dot qubit with fault-tolerant control-fidelity*, Nature Nanotechnology **9**, 981 (2014).

[21] E. Kawakami, T. Jullien, P. Scarlino, D. R. Ward, D. E. Savage, M. G. Lagally, V. V. Dobrovitski, M. Friesen, S. N. Coppersmith, M. A. Eriksson, and L. M. K. Vandersypen, *Gate fidelity and coherence of an electron spin in an Si/SiGe quantum dot with micromagnet*, PNAS **113**, 11738 (2016).

[22] J. Yoneda, K. Takeda, T. Otsuka, T. Nakajima, M. R. Delbecq, G. Allison, T. Honda, T. Kodera, S. Oda, Y. Hoshi, N. Usami, K. M. Itoh, and S. Tarucha, *A quantum-dot spin qubit with coherence limited by charge noise and fidelity higher than 99.9%*, Nature Nanotechnology **13**, 102 (2018).

[23] X. Xue, T. F. Watson, J. Helsen, D. R. Ward, D. E. Savage, M. G. Lagally, S. N. Coppersmith, M. A. Eriksson, S. Wehner, and L. M. K. Vandersypen, *Benchmarking Gate Fidelities in a Si/SiGe Two-Qubit Device*, Phys. Rev. X **9**, 021011 (2019).

[24] W. Huang, C. H. Yang, K. W. Chan, T. Tanttu, B. Hensen, R. C. C. Leon, M. A. Fogarty, J. C. C. Hwang, F. E. Hudson, K. M. Itoh, A. Morello, A. Laucht, and A. S. Dzurak, *Fidelity benchmarks for two-qubit gates in silicon*, Nature **569**, 532 (2019).

[25] T. F. Watson, S. G. J. Philips, E. Kawakami, D. R. Ward, P. Scarlino, M. Veldhorst, D. E. Savage, M. G. Lagally, M. Friesen, S. N. Coppersmith, M. A. Eriksson, and L. M. K. Vandersypen, *A programmable two-qubit quantum processor in silicon*, Nature **555**, 633 (2018).

[26] N. Samkharadze, G. Zheng, N. Kalhor, D. Brousse, A. Sammak, U. C. Mendes, A. Blais, G. Scappucci, and L. M. K. Vandersypen, *Strong spin-photon coupling in silicon*, Science **359**, 1123 (2018).

[27] X. Mi, M. Benito, S. Putz, D. M. Zajac, J. M. Taylor, G. Burkard, and J. R. Petta, *A coherent spin–photon interface in silicon*, Nature **555**, 599 (2018).

[28] F. Borjans, X. G. Croot, X. Mi, M. J. Gullans, and J. R. Petta, *Long-Range Microwave Mediated Interactions Between Electron Spins*, arXiv:1905.00776 .

[29] E. A. Chekhovich, M. N. Makhonin, A. I. Tartakovskii, A. Yacoby, H. Bluhm, K. C. Nowack, and L. M. K. Vandersypen, *Nuclear spin effects in semiconductor quantum dots*, Nature Materials **12**, 494 (2013).

[30] S. W. Jung, T. Fujisawa, Y. Hirayama, and Y. H. Jeong, *Background charge fluctuation in a GaAs quantum dot device*, Appl. Phys. Lett. **85**, 768 (2004).

[31] E. Paladino, Y. M. Galperin, G. Falci, and B. L. Altshuler, *1/f noise: Implications for solid-state quantum information*, Rev. Mod. Phys. **86**, 361 (2014).

[32] F. Beaudoin and W. A. Coish, *Microscopic models for charge-noise-induced dephasing of solid-state qubits*, Phys. Rev. B **91**, 165432 (2015).

[33] A. Kha, R. Joynt, and D. Culcer, *Do micromagnets expose spin qubits to charge and Johnson noise?*, Appl. Phys. Lett. **107**, 172101 (2015).

[34] C. E. Bradley, J. Randall, M. H. Abobeih, R. C. Berrevoets, M. J. Degen, M. A. Bakker, M. Markham, D. J. Twitchen, and T. H. Taminiau, *A Ten-Qubit Solid-State Spin Register with Quantum Memory up to One Minute*, Phys. Rev. X **9**, 031045 (2019).

[35] See Supplemental Material at [URL will be inserted by publisher], including additional Refs. [45,46], for more details on the noise model, experimental details, method validation, quantification of the observed correlations, notes on the effect of nuclear spin noise and the Bell state fidelity, echo experiments, simulation results and the effect of adding multiple noise sources.

[36] J. M. Elzerman, R. Hanson, L. H. Willems van Beveren, B. Witkamp, L. M. K. Vandersypen, and L. P. Kouwenhoven, *Single-shot read-out of an individual electron spin in a quantum dot*, Nature **430**, 431 (2004).

[37] V. Srinivasa, K. C. Nowack, M. Shafiei, L. M. K. Vandersypen, and J. M. Taylor, *Simultaneous Spin-Charge Relaxation in Double Quantum Dots*, Phys. Rev. Lett. **110**, 196803 (2013).

[38] M. Pioro-Ladrière, Y. Tokura, T. Obata, T. Kubo, and S. Tarucha, *Micromagnets for coherent control of spin-charge qubit in lateral quantum dots*, Appl. Phys. Lett. **90**, 024105 (2007).

[39] T. Meunier, V. E. Calado, and L. M. K. Vandersypen, *Efficient controlled-phase gate for single-spin qubits in quantum dots*, Phys. Rev. B **83**, 121403(R) (2011).

[40] M. Veldhorst, C. H. Yang, J. C. C. Hwang, W. Huang, J. P. Dehollain, J. T. Muhonen, S. Simmons, A. Laucht, F. E. Hudson, K. M. Itoh, A. Morello, and A. S. Dzurak, *A two-qubit logic gate in silicon*, Nature **526**, 410 (2015).

[41] K. Takeda, J. Yoneda, T. Otsuka, T. Nakajima, M. R. Delbecq, G. Allison, Y. Hoshi, N. Usami, K. M. Itoh, S. Oda, T. Kodera, and S. Tarucha, *Optimized electrical control of a Si/SiGe spin qubit in the presence of an induced frequency shift*, npj Quantum Information **4**, 54 (2018).

[42] P. Harvey-Collard, N. T. Jacobson, M. Rudolph, J. Dominguez, G. A. Ten Eyck, J. R. Wendt, T. Pluym, J. K. Gamble, M. P. Lilly, M. Pioro-Ladrière, and M. S. Carroll, *Coherent coupling between a quantum dot and a donor in silicon*, Nature Communications **8**, 1029 (2017).

[43] D. Layden, M. Chen, and P. Cappellaro, *Efficient quantum error correction of dephasing induced by a common fluctuator*, arXiv:1903.01046 .

[44] J. M. Boter *et al.*, Zenodo [Dataset] (2019), 10.5281/zenodo.3524842.

[45] L. M. K. Vandersypen and I. L. Chuang, *NMR techniques for quantum control and computation*, Rev. Mod. Phys. **76**, 1037 (2005).

[46] J. T. Muhonen, J. P. Dehollain, A. Laucht, F. E. Hudson, R. Kalra, T. Sekiguchi, K. M. Itoh, D. N. Jamieson, J. C. McCallum, A. S. Dzurak, and A. Morello, *Storing quantum information for 30 seconds in a nanoelectronic device*, Nature Nanotechnology **9**, 986 (2014).

5

NONLINEAR RESPONSE AND CROSSTALK OF STRONGLY DRIVEN SILICON SPIN QUBITS

Micromagnet-based electric dipole resonance (EDSR) offers an attractive path for the near-term scaling of dense arrays of silicon spin qubits in gate-defined quantum dots while maintaining long coherence times and high control fidelities. However, accurately controlling dense arrays of qubits using a multiplexed drive will require an understanding of the crosstalk mechanisms that may reduce operational fidelity. We identify a novel crosstalk mechanism whereby the Rabi frequency of a driven qubit is drastically changed when the drive of an adjacent qubit is turned on. These observations raise important considerations for scaling single-qubit control.

This chapter have been published in arXiv:2205.04905 (2022).

5.1. INTRODUCTION

Electric dipole spin resonance (EDSR) is a key ingredient for the all-electrical control of single-electron spin qubits in silicon quantum dots [1]. While some approaches are able to utilize the weak intrinsic spin-orbit coupling (SOC) of silicon [2, 3], the placement of an on-chip micromagnet has proven especially effective for gate-based quantum dots in both Si/SiGe [4, 5] and Si-MOS [6] platforms, with single-qubit gate fidelities exceeding 99.9% having been demonstrated [7]. Furthermore, electron spins in dense arrays can be made addressable by engineering an appropriate local magnetic field gradient within a stronger external field [8]. This makes micromagnet-based EDSR attractive for the near-term scaling of spin qubit processors.

In the original description of EDSR, an ac electric field pushes a harmonically confined electron back and forth in a constant magnetic field gradient, such that the spin is effectively acted upon by an ac magnetic field as in conventional electron spin resonance (ESR) [9, 10]. Multiple spectrally-separated spins can ideally be controlled via a single, multiplexed driving field containing a superposition of frequencies addressing individual qubits. Rabi's formula implies that the qubit dynamics are only minorly affected by off-resonance tones in a way such that crosstalk can be systematically accounted for to maintain high fidelity [11].

Substantial effort has been placed on detecting and modelling crosstalk in superconducting and trapped-ion systems [12], but the identification of crosstalk mechanisms in semiconductor quantum dot devices is only beginning to receive attention as these platofmrs mature into the multi-qubit era [13–15]. Given that high qubit density is one of the well-known advantages of semiconductor quantum processors, maintaining high-fidelity operation at small-length scales in the presence of crosstalk is an essential hurdle to overcome.

In this work, we measure the nonlinear Rabi frequency scaling of two single-electron spin qubits controlled via EDSR in a Si/SiGe double-dot device and show how this nonlinearity can phenomenologically give rise to the observed crosstalk during simultaneous single qubit operations. Furthermore, we address the potential physical origin of the observed nonlinearity. While the valley-orbit structure of the silicon quantum dots may give rise to some aspects of the observed nonlinearity, we find that this alone cannot convincingly explain the variety of measured nonlinear Rabi scaling curves. It is therefore possible that other physics not considered in the typical EDSR Hamiltonian, such as device heating, may contribute to crosstalk. The insights made here will help inform the continued development of EDSR-enabled spin qubit devices, as well as raise important considerations for programming spin-based quantum processors in silicon.

5.2. ELECTRIC DIPOLE SPIN RESONANCE

Two quantum dots with single-electron occupancy are electrostatically accumulated in an isotopically purified ^{28}Si/SiGe quantum well (Fig. 5.1(a)). A cobalt micromagnet placed on top of the dot region becomes magnetized in the applied external field, creating local transverse (z'-axis) and longitudinal (x'-axis) magnetic field gradients. The transverse gradient gives rise to a synthetic SOC, and the longitudinal gradient spectrally separates the Larmor frequencies of the two spins. The IQ-modulated electric drive necessary to

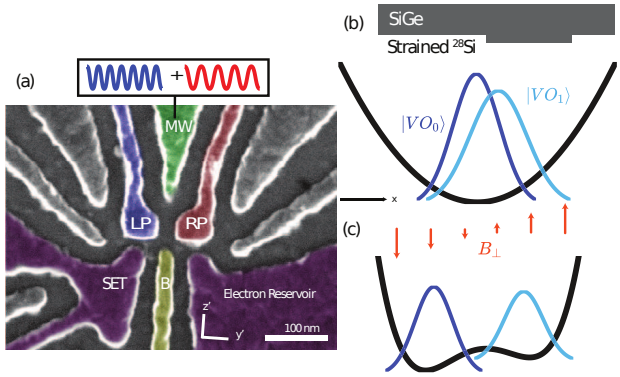

Fig. 5.1: (a) False-coloured SEM of a device nominally equivalent to the one used in the experiment. Single-electron spin qubits Q1 and Q2 are accumulated under plunger gates "LP" and "RP" respectively, while a barrier gate "B" is used to control the tunnel coupling between the dots. Qubit states are read-out using energy-selective tunneling to the electron reservoir, with single-electron transistor (SET) used to measure the corresponding change in charge-occupation. Microwave controls for both qubits are simultaneously applied to either the "MW" or "B" gate. (b) Illustration of the formation of a nonzero matrix element $\langle VO_0|\hat{x}|VO_1\rangle$ between the two lowest-energy valley-orbit states in a strained Si/SiGe quantum well. Such hybridization is highly sensitive depending on the confinement potential and the atomic details of the interface. (c) Illustration of the "double-dot" analogy associated with the two-level valley-orbit subspace. When combined with a synthetic spin-orbit coupling, the anharmonic orbital subspace can lead to nonlinear phenomena in the EDSR response.

control the spin states by EDSR is delivered via the gate "MW" or the gate "B". Further details of the initialisation and readout of the qubits can be found in [16].

A pure-spin resonance facilitated by EDSR is a second-order process whereby one (or more) microwave photons induce a transition in the charge-like state of a confined electron, and spin-orbit coupling mediates an associated spin flip during charge state transition. For single-electron spin qubits in Si/SiGe, the charge states are hybridized valley-orbit states owing to the conduction band degeneracy of strained silicon [17]. The weak intrinsic spin-orbit interaction in silicon often requires the integration of an on-chip micromagnet to generate a slanting magnetic gradient capable of supporting EDSR. These features make EDSR in silicon distinct from that in GaAs or strained germanium quantum wells, where the band structure supports pure orbital charge states, and the intrinsic spin-orbit interactions are sufficiently strong to mediate EDSR without requiring a synthetic micromagnet [18, 19].

To illustrate the difference, consider the following EDSR Hamiltonian:

$$H(t) = H_0 - \frac{E_Z}{2}\sigma_z + \tilde{b}_{SL}\hat{x}\vec{n}\cdot\vec{\sigma} + \tilde{E}_{ac}(t)\hat{x}. \tag{5.1}$$

The first term of Equation 5.1, H_0, is the charge state Hamiltonian. $E_Z = g\mu_B B_{tot}$ is the Zeeman splitting of the spin state, where $g \approx 2$ is the g-factor in silicon, μ_B is the Bohr magneton, and B_{tot} is the total magnetic field along the spin quantization axis. $\tilde{b}_{SL} = \frac{1}{2}g\mu_B|\vec{b}_{SL}|$ gives the strength of the SOC as a function of the magnitude of the magnetic field gradient $|\vec{b}_{SL}|$ along the driving axis (x). $\vec{n} = \begin{pmatrix}0 & \cos\theta & \sin\theta\end{pmatrix}$ characterizes the

nature of the SOC, where θ gives the angle of the gradient with respect to the orthogonal spin axis. The last term describes the electric drive $\tilde{E}_{ac}(t) = e\sum_k E_{ac,k}\sin(\omega_k t)$ oriented along the x-axis.

EDSR is simplest to investigate in the case of harmonic confinement, such that $H_0 = \hbar\omega_0(\hat{a}^\dagger\hat{a}+\frac{1}{2})$. The resulting Hamiltonian H can be analyzed perturbatively to find an on-resonance Rabi frequency of $\Omega_{rabi} \propto \tilde{E}_{ac}$ and a drive-dependent resonance frequency shift of $\hbar\omega_{BSS} \propto -E_{ac}^2$. Linear scaling for small drives has been reported in both GaAs [20, 21] and Si [7]. In this work, we present evidence that the first conclusion about Rabi frequency scaling may not always hold in silicon, even at modest Rabi frequencies on the order of a few MHz. Furthermore, previous work in similar Si/SiGe devices has found frequency shifts of both signs that are not quadratic in driving amplitude [8, 22]. We conclude that a harmonic confinement potential and Eq. 5.1 may not provide a complete model for EDSR in Si/SiGe quantum dots.

Another potential origin of nonlinearity is the anharmonicity of the silicon quantum dot due to hybridization of valley and orbital states. The lowest two valley-orbit states, $|VO_0\rangle$ and $|VO_1\rangle$, are predicted to support a nonzero dipole matrix element $r = \langle VO_0|\hat{x}|VO_1\rangle$ that has been experimentally estimated [23] to be on the order of a few nanometers. Such a dipole element supports EDSR [3, 24, 25], but will vary between quantum dots as the dipole will be sensitive to the atomic details of the quantum well interface [26]. This 2-level subspace can be modelled analogous to a double-quantum-dot charge qubit [27]:

$$H_0 = -\frac{1}{2}(\epsilon\sigma_z + \Delta\sigma_x), \tag{5.2}$$

where ϵ and Δ can be interpreted as "detuning" and "tunnel coupling" parameters respectively. The difference in eigenvalues of H_0 should equal the measured valley splitting $E_V = \sqrt{\epsilon^2+\Delta^2}$. Such an orbital model has been useful for mapping the resonance spectrum of a spin qubit in Si/SiGe and identifying nonlinear phenomena such as second-harmonic driving [28, 29]. We note that other analyses of EDSR in the context of a double-well confinement potential also predict nonlinear Rabi frequency scaling [30, 31].

We verify through numerical simulations of Eq. 5.1 with both an orbital- and valley-like model that a Rabi saturation effect may be expected for moderate Rabi frequencies larger than 10 MHz. However, neither model captures the breadth of nonlinear features we observe in experiment, as will be discussed below. To understand our results, we phenomenologically extend the model of Eq. 5.1 by including a prefactor $f(P_k,\omega_k)$ in the electric driving term such that $\tilde{E}_{ac}(t)\hat{x} \rightarrow f(P_k,\omega_k)\tilde{E}_{ac}(t)\hat{x}$. The prefactor is dependent on the power P_k and frequency ω_k of all applied drives. We will consider the possible physical origins of such a prefactor in our discussion.

To illustrate the consequences of the phenomenological model, consider the prefactor plotted in Fig. 5.2(a). As the total applied electric field increases, the effective driving amplitude no longer rises proportionally. To see the importance of this dependence, Eq. 5.1 is numerically integrated in the time-dependent Schrödinger equation using the prefactor depicted in Fig. 5.2(a). A constant driving tone resonant with Q2 drives Rabi oscillations while the Q1 spin is stationary, as shown in Fig. 5.2(c-d). As a Q1 driving tone is turned on, two distinct effects occur. First, the off-resonant driving dresses the spin

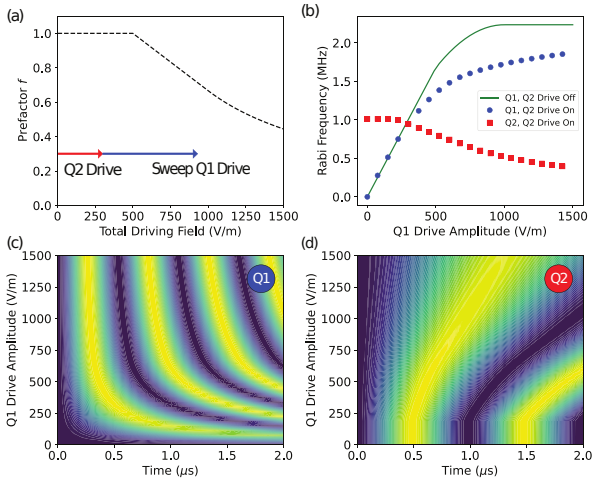

Fig. 5.2: (a) Plot showing one possible instance of the phenomenological prefactor describing the nonlinearity in the EDSR mechanism. To illustrate the emergence of crosstalk, we set the Q2 electric drive to a constant amplitude, and manipulate the amplitude of the Q1 drive. The effective driving term in the Hamiltonian will be unique depending on the sum of both microwave drives. (b) The effect of two microwave drives on the two-spin system is numerically simulated with the nonlinear prefactor in (a). The solid green line gives the modified analytic Rabi frequency, while the discrete points are derived by fitting the numerically solved spin dynamics to a sinusoid. (c-d) The spin dynamics of Q1 and Q2 corresponding to the fits in (b). Light and dark regions indicate the probability of measuring an excited or ground state spin respectively.

and introduces imperfections to the spin flips. Second, the Q2 Rabi frequency decreases markedly as the Q1 Rabi frequency increases.

The fitted Rabi frequencies in Fig. 5.2(b) illustrate the latter effect as a novel crosstalk mechanism, where both the single-qubit logical gate duration and fidelity will be strongly influenced by the presence of the second drive. This effect, which we observe consistently in experiment, has critical implications for simultaneous qubit operation in EDSR-enabled silicon devices.

5.3. EXPERIMENTAL OBSERVATION

We probe this nonlinearity experimentally using the introduced double-dot device by first focusing on the single qubit physics. A standard Ramsey pulse sequence is used to identify the relevant resonance frequencies of the two qubits, which range from 11.89 GHz in a 320 mT external field to 15.91 GHz in 475 mT, and the corresponding drives are applied either to the “MW" or ‘B" gate. The Rabi scaling trends are shown in Fig. 5.3.

In most cases, the linear Rabi frequency-drive amplitude scaling predicted from theory only holds, if at all, for small Rabi frequencies. For each quantum dot, external magnetic field, and driving gate, the associated curve contains unique, but robustly reproducible, nonlinear characteristics. For the smoothest trends, this often takes the form of a “plateau" where the Rabi frequency apparently saturates, or only changes modestly, when the amplitude of the electric drive is adjusted as is described in the phenomeno-

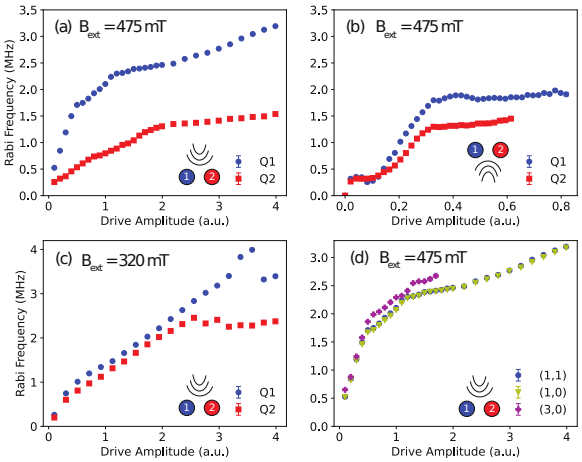

Fig. 5.3: Rabi frequency scalings as a function of the applied resonant ac electric field amplitude. The external field is set to B_{ext} = 475 mT in (a),(b) and (d), and B_{ext} = 320 mT in (c). In (a),(c) and (d),the qubits are driven using the "MW" gate as illustrated. In (b), the qubits are instead driven using the 'B" gate. In (a-c), only a single qubit is driven at once in the (1,1) electron occupation regime, while the undriven qubit is left to idle. In (d), the Q1 Rabi scaling is compared in different charge states of the device. A rectangular pulse window of 3 μs is used, and the measured time-domain spin response is fit to a sinusoidal function $A\cos(2\pi f_{Rabi}t)+C$ to extract the spin Rabi frequency. The horizontal axis is scaled such that 1 unit represents the same nominal drive amplitude delivered to the device by taking into account the vector source power and all nominal attenuations in the signal paths. Impedance mismatches and frequency-dependent cable attenuation make the precise electric field present at the qubits difficult to calculate and compare directly.

logical description of Fig. 5.2. Increasing the driving amplitude greatly does not always yield larger Rabi frequencies, and in the experimental setup considered here will eventually lead to a sudden loss of spin visibility altogether. This may be a result of microwave heating interfering with the energy-selective readout used in the experiment, or may be evidence of photon assisted tunneling of the electron from the quantum dot to the nearest electron reservoir.

In addition to the general Rabi saturation effect observed, each measured Rabi scaling may exhibit distinct local extrema and curvature. Note that the difference in scaling trends between adjacent spins has previously been observed [32] and may be attributed to differences in the local magnetic field gradient at each dot location. However, this does not explain the nonlinearity in the qubit response as the gradient is expected to be nearly constant over the length scale of the dots. From the distinct shapes of the Q1 and Q2 curves, it is apparent that the origin of the nonlinearity is distinct to each qubit frequency and not a global phenomena as could be expected from a uniform distortion in the driving field. We also note that the resonance frequency shift, which has previously been observed in EDSR experiments, is not a plausible cause of the nonlinear scaling since an off-resonant drive will result in faster oscillations, not slower [33].

Next, we consider the possibility that the the nonlinearity is due influence of the second qubit. However, upon removing the Q2 electron, there is no change in the Q1 Rabi scaling as shown in Fig. 5.3(f). Furthermore, the residual exchange interaction between

the two qubits is measured to be well below 50 KHz, indicating a very weak spin-spin interaction taking place. Repeating the experiment in the (3,0) regime produces the same initial linear trend, suggesting that in both the 1-electron and 3-electron modes the same dipole transition element, whether orbit-like or valley-like, is responsible for mediating EDSR here. The nonlinear scaling regime is similarly shaped, but measurably different, suggesting that the root cause of the nonlinearity may be mildly influenced by the quantum dot structure.

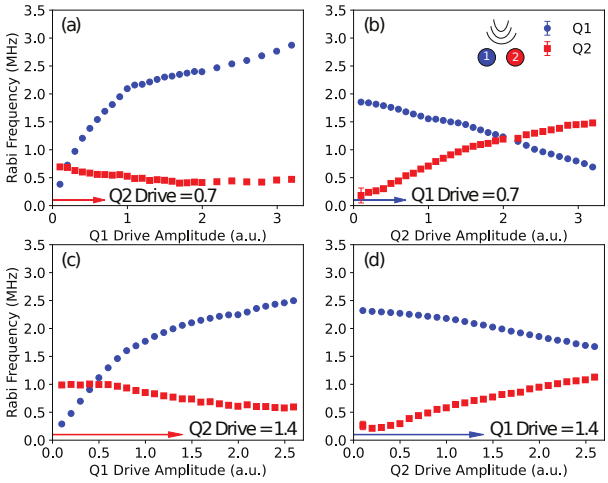

Fig. 5.4: Single-qubit crosstalk. Rabi frequencies of both qubits are shown when a constant driving tone is present (shown in the bottom left of each panel) while a second tone is swept in amplitude. In panels (a) and (b), the initial driving amplitude is half (0.35 a.u.) that in panels (c) and (d) (0.70 a.u.). All experiments are carried out at $B_{ext} = 475$ mT, and the "MW" gate is used in all cases as indicated in the top right illustration.

When both qubit driving tones are simultaneously applied to the same "MW" gate, a strong crosstalk effect occurs (Fig. 5.4) as predicted by the model introduced in Fig. 5.2. As in the model, when a resonantly driven spin is also placed under the influence of an additional off-resonant drive, the additional ac field amplitude modifies the EDSR mechanism as to diminish the resonant spin-flip frequency. This effect has substantial consequences for high-fidelity logic gates which must be calibrated to a ns-precision duration, because even a small unaccounted change in Rabi frequency would result in severe over- or under-rotations of qubit states.

By comparing Fig. 5.4(a-b) with (c-d), it is clear that Rabi frequency is more strongly modified as the resonant tone becomes smaller with respect to the off-resonant pulse. This implies that crosstalk would become more severe as single-qubit operations are more densely multiplexed. Calibrating for this effect directly in larger devices, without more systematic insight, may be unworkable depending on the locality of the nonlinearity. If microwave signals propagate across an entire device, as is most likely, then such an approach would be undermined by a combinatorial explosion. We emphasize again that the crosstalk effect is not a direct consequence of the *existence* of a nearby qubit, but rather is caused by the intention to drive multiple qubits using electrical signals. There-

fore, we anticipate that this crosstalk effect could also arise in sparse qubit arrays.

5.4. CONCLUSION

We now return to the question of the origin of the nonlinearity, which carries implications for both the prospects of efficient calibration and device scalability. Based on the variety of nonlinearities observed from single-qubit measurements, it is clear that at least the microwave power (P_k) and frequency (ω_k) components are important contributing factors. We therefore focus on the time-dependent term of the EDSR Hamiltonian as the encoding source of the nonlinearity and identify two possible physical origins: electric drive distortion and device heating.

Since it is not possible for us to measure the electric field at the dot location (without considering the electron spin as a sensor itself), linear control of the spins depends on a linear relation between the microwave signal generated at room temperature and the signal delivered to the quantum dots. We have verified that the output of the I-Q modulated signal is linear with respect to the output amplitude of the arbitrary waveform generator used. Beyond this element, there are no active electronic components that would normally give rise to nonlinear effects. Furthermore, interference effects caused by cables and attenuators are excluded from the possible sources, as the nonlinear effect is found to be robust against small changes in the qubit frequencies. Although the load, in this case the open-circuited on-chip pin, is not impedance matched to the microwave source, any frequency-dependent reflection would not typically be considered to also be power-dependent, especially at the 26 dBm scale of the current experiments. As transient signals would traverse the entire signal path on the 10 ns timescale, this does not account for the effect seen over the few μs spin lifetime. However, a naive application of microwave circuit theory may not account for possible distorting effects that may occur as the signal couples to neighbouring gates on the nanoscale device. Therefore, we cannot completely rule out the contribution from a classical distortion effect as the origin of the nonlienarity.

Second, we consider the effect of device heating, which has been hypothesized as a possible origin of the anomalous qubit frequency shift observed in semiconductor spin qubits over a 100 ns timescale [22]. Such an effect may manifest in a position rectification of a quantum dot that changes its orbital structure, for example due to device strain. Although a true harmonic confinement potential is robust against this small change, the anharmonicity introduced by the valley degree of freedom is very sensitive to such shifts [26, 27, 34]. We therefore acknowledge the possibility that a nonlinear drive-dependent dipole element $r(E_{tot}) = \langle VO_O(E_{tot})|\hat{x}|VO_1(E_{tot})\rangle$ may occur through a heating mechanism in a way that is consistent with our phenomenology [1].

In conclusion, we have presented experimental evidence of a strong nonlinearity in the fundamental resonance of a single-electron spin qubit controlled by EDSR with a synthetic spin-orbit coupling. To understand both the nonlinear Rabi frequency scaling and crosstalk effects that are observed, we have developed a simple phenomenological model whose accuracy may be probed through further experiments. The novel crosstalk

[1] If this is the case, then it would also be true that the magnitude of the synthetic spin-orbit coupling would be modified in the presence of the drive.

mechanism introduced here poses important questions for the scalability of spin qubit devices relying on multiplexed single-qubit control.

REFERENCES

[1] L. M. K. Vandersypen, H. Bluhm, J. S. Clarke, A. S. Dzurak, R. Ishihara, A. Morello, D. J. Reilly, L. R. Schreiber, and M. Veldhorst, *Interfacing spin qubits in quantum dots and donors—hot, dense, and coherent,* npj Quantum Information **3**, 34 (2017).

[2] A. Corna, L. Bourdet, R. Maurand, A. Crippa, D. Kotekar-Patil, H. Bohuslavskyi, R. Laviéville, L. Hutin, S. Barraud, X. Jehl, and et al., *Electrically driven electron spin resonance mediated by spin–valley–orbit coupling in a silicon quantum dot,* npj Quantum Information **4**, 1 (2018).

[3] W. Huang, M. Veldhorst, N. M. Zimmerman, A. S. Dzurak, and D. Culcer, *Electrically driven spin qubit based on valley mixing,* Phys. Rev. B **95**, 075403 (2017).

[4] E. Kawakami, P. Scarlino, D. R. Ward, F. R. Braakman, D. E. Savage, M. G. Lagally, M. Friesen, S. N. Coppersmith, M. A. Eriksson, and L. M. K. Vandersypen, *Electrical control of a long-lived spin qubit in a si/sige quantum dot,* Nature Nanotechnology **9**, 666 (2014).

[5] X. Croot, X. Mi, S. Putz, M. Benito, F. Borjans, G. Burkard, and J. R. Petta, *Flopping-mode electric dipole spin resonance,* Phys. Rev. Research **2**, 012006 (2020).

[6] R. C. C. Leon, C. H. Yang, J. C. C. Hwang, J. C. Lemyre, T. Tanttu, W. Huang, K. W. Chan, K. Y. Tan, F. E. Hudson, K. M. Itoh, and et al., *Coherent spin control of s-, p-, d- and f-electrons in a silicon quantum dot,* Nature Communications **11**, 1 (2020).

[7] J. Yoneda, K. Takeda, T. Otsuka, T. Nakajima, M. R. Delbecq, G. Allison, T. Honda, T. Kodera, S. Oda, Y. Hoshi, and et al., *A quantum-dot spin qubit with coherence limited by charge noise and fidelity higher than 99.9%,* Nature Nanotechnology **13**, 102 (2018).

[8] T. F. Watson, S. G. J. Philips, E. Kawakami, D. R. Ward, P. Scarlino, M. Veldhorst, D. E. Savage, M. G. Lagally, M. Friesen, S. N. Coppersmith, M. A. Eriksson, and L. M. K. Vandersypen, *A programmable two-qubit quantum processor in silicon,* Nature **555**, 633 (2018).

[9] Y. Tokura, W. G. van der Wiel, T. Obata, and S. Tarucha, *Coherent single electron spin control in a slanting zeeman field,* Phys. Rev. Lett. **96**, 047202 (2006).

[10] M. Pioro-Ladrière, T. Obata, Y. Tokura, Y.-S. Shin, T. Kubo, K. Yoshida, T. Taniyama, and S. Tarucha, *Electrically driven single-electron spin resonance in a slanting zeeman field,* Nature Physics **4**, 776 (2008).

[11] I. Heinz and G. Burkard, *Crosstalk analysis for single-qubit and two-qubit gates in spin qubit arrays,* Phys. Rev. B **104**, 045420 (2021).

[12] M. Sarovar, T. Proctor, K. Rudinger, K. Young, E. Nielsen, and R. Blume-Kohout, *Detecting crosstalk errors in quantum information processors,* Quantum **4**, 321 (2020).

[13] X. Xue, T. F. Watson, J. Helsen, D. R. Ward, D. E. Savage, M. G. Lagally, S. N. Coppersmith, M. A. Eriksson, S. Wehner, and L. M. K. Vandersypen, *Benchmarking gate fidelities in a* Si/SiGe *two-qubit device,* Phys. Rev. X **9**, 021011 (2019).

[14] F. Fedele, A. Chatterjee, S. Fallahi, G. C. Gardner, M. J. Manfra, and F. Kuemmeth, *Simultaneous operations in a two-dimensional array of singlet-triplet qubits,* PRX Quantum **2**, 040306 (2021).

[15] W. I. L. Lawrie, M. Russ, F. van Riggelen, N. W. Hendrickx, S. L. de Snoo, A. Sammak, G. Scappucci, and M. Veldhorst, *Simultaneous driving of semiconductor spin qubits at the fault-tolerant threshold,* (2021), arXiv:2109.07837 .

[16] X. Xue, B. Patra, J. P. van Dijk, N. Samkharadze, S. Subramanian, A. Corna, B. Paquelet Wuetz, C. Jeon, F. Sheikh, E. Juarez-Hernandez, *et al.*, *CMOS-based cryogenic control of silicon quantum circuits,* Nature **593**, 205 (2021).

[17] F. A. Zwanenburg, A. S. Dzurak, A. Morello, M. Y. Simmons, L. C. L. Hollenberg, G. Klimeck, S. Rogge, S. N. Coppersmith, and M. A. Eriksson, *Silicon quantum electronics,* Rev. Mod. Phys. **85**, 961 (2013).

[18] K. C. Nowack, F. Koppens, Y. V. Nazarov, and L. Vandersypen, *Coherent control of a single electron spin with electric fields,* Science **318**, 1430 (2007).

[19] N. W. Hendrickx, W. I. L. Lawrie, L. Petit, A. Sammak, G. Scappucci, and M. Veldhorst, *A single-hole spin qubit,* Nature Communications **11**, 1 (2020).

[20] J. Yoneda, T. Otsuka, T. Nakajima, T. Takakura, T. Obata, M. Pioro-Ladrière, H. Lu, C. J. Palmstrøm, A. C. Gossard, and S. Tarucha, *Fast electrical control of single electron spins in quantum dots with vanishing influence from nuclear spins,* Phys. Rev. Lett. **113**, 267601 (2014).

[21] T. Nakajima, A. Noiri, K. Kawasaki, J. Yoneda, P. Stano, S. Amaha, T. Otsuka, K. Takeda, M. R. Delbecq, G. Allison, A. Ludwig, A. D. Wieck, D. Loss, and S. Tarucha, *Coherence of a driven electron spin qubit actively decoupled from quasistatic noise,* Phys. Rev. X **10**, 011060 (2020).

[22] K. Takeda, J. Yoneda, T. Otsuka, T. Nakajima, M. R. Delbecq, G. Allison, Y. Hoshi, N. Usami, K. M. Itoh, S. Oda, T. Kodera, and S. Tarucha, *Optimized electrical control of a si/sige spin qubit in the presence of an induced frequency shift,* npj Quantum Information **4**, 1 (2018).

[23] C. H. Yang, A. Rossi, R. Ruskov, N. S. Lai, F. A. Mohiyaddin, S. Lee, C. Tahan, G. Klimeck, A. Morello, and A. S. Dzurak, *Spin-valley lifetimes in a silicon quantum dot with tunable valley splitting,* Nature Communications **4**, 1 (2013).

[24] X. Zhang, Y. Zhou, R.-Z. Hu, R.-L. Ma, M. Ni, K. Wang, G. Luo, G. Cao, G.-L. Wang, P. Huang, X. Hu, H.-W. Jiang, H.-O. Li, G.-C. Guo, and G.-P. Guo, *Controlling synthetic spin-orbit coupling in a silicon quantum dot with magnetic field,* Phys. Rev. Applied **15**, 044042 (2021).

[25] P. Huang and X. Hu, *Fast spin-valley-based quantum gates in si with micromagnets,* (2021), arXiv:2010.14844 .

[26] J. K. Gamble, M. A. Eriksson, S. N. Coppersmith, and M. Friesen, *Disorder-induced valley-orbit hybrid states in si quantum dots,* Phys. Rev. B **88**, 035310 (2013).

[27] P. Boross, G. Széchenyi, D. Culcer, and A. Pályi, *Control of valley dynamics in silicon quantum dots in the presence of an interface step,* Phys. Rev. B **94**, 035438 (2016).

[28] P. Scarlino, E. Kawakami, D. R. Ward, D. E. Savage, M. G. Lagally, M. Friesen, S. N. Coppersmith, M. A. Eriksson, and L. M. K. Vandersypen, *Second-harmonic coherent driving of a spin qubit in a Si/SiGe quantum dot,* Phys. Rev. Lett. **115**, 106802 (2015).

[29] P. Scarlino, E. Kawakami, T. Jullien, D. R. Ward, D. E. Savage, M. G. Lagally, M. Friesen, S. N. Coppersmith, M. A. Eriksson, and L. M. K. Vandersypen, *Dressed photon-orbital states in a quantum dot: Intervalley spin resonance,* Phys. Rev. B **95**, 165429 (2017).

[30] D. V. Khomitsky, L. V. Gulyaev, and E. Y. Sherman, *Spin dynamics in a strongly driven system: Very slow rabi oscillations,* Phys. Rev. B **85**, 125312 (2012).

[31] Y. Tokura, T. Kubo, and W. J. Munro, *Power dependence of electric dipole spin resonance,* (2013), arXiv:1308.0071 .

[32] T. Obata, M. Pioro-Ladrière, Y. Tokura, Y.-S. Shin, T. Kubo, K. Yoshida, T. Taniyama, and S. Tarucha, *Coherent manipulation of individual electron spin in a double quantum dot integrated with a micromagnet,* Phys. Rev. B **81**, 085317 (2010).

[33] J. Romhányi, G. Burkard, and A. Pályi, *Subharmonic transitions and Bloch-Siegert shift in electrically driven spin resonance,* Phys. Rev. B **92**, 054422 (2015).

[34] A. Hosseinkhani and G. Burkard, *Electromagnetic control of valley splitting in ideal and disordered si quantum dots,* Phys. Rev. Research **2**, 043180 (2020).

6

REPETITIVE QUANTUM NONDEMOLITION MEASUREMENT AND SOFT DECODING OF A SILICON SPIN QUBIT

Quantum error correction is of crucial importance for fault-tolerant quantum computers. As an essential step towards the implementation of quantum error-correcting codes, quantum non-demolition (QND) measurements are needed to efficiently detect the state of a logical qubit without destroying it. Here we implement QND measurements in a Si/SiGe two-qubit system, with one qubit serving as the logical qubit and the other serving as the ancilla. Making use of a two-qubit controlled-rotation gate, the state of the logical qubit is mapped onto the ancilla, followed by a destructive readout of the ancilla. Repeating this procedure enhances the logical readout fidelity from $75.5 \pm 0.3\%$ to $94.5 \pm 0.2\%$ after 15 ancilla readouts. In addition, we compare the conventional thresholding method with an improved signal processing method called soft decoding that makes use of analog information in the readout signal to better estimate the state of the logical qubit. We demonstrate that soft decoding leads to a significant reduction in the required number of repetitions when the readout errors become limited by Gaussian noise, for instance in the case of readouts with a low signal-to-noise ratio. These results pave the way for the implementation of quantum error correction with spin qubits in silicon.

This chapter has been published in Phys. Rev. X **10**, 021006 (2020).

6.1. INTRODUCTION

A key requirement of quantum error correction is the ability to repeatedly measure multiple physical qubits in a quantum non-demolition (QND) way to identify logical errors [1]. One approach to achieve quantum non-demolition readout of spin qubits is to use a two-qubit gate to map the state of the logical qubit to an ancilla which is then measured. While the readout of the ancilla may be destructive, it leaves the state of the original qubit unperturbed. Consequently, the ancilla may be reinitialized and the logical qubit measurement can be repeated to enhance the signal. Recently, ancilla-based repetitive QND readout has been implemented across several platforms, from trapped ions [2, 3] to electron-nuclear spin systems [4–13] and superconducting qubits [14]. In GaAs quantum dots, repeated non-destructive readout of spin states [15] as well as QND measurement of a spin qubit [16] have been reported. In the latter experiment, however, the information had to be decoded from the evolution of the ancilla qubit under a two-qubit controlled-phase operation with variable interaction time to overcome the fluctuations of the Overhauser field. This makes the cumulative fidelity only slowly increase with the number of QND readouts. In addition, the binary thresholding of individual measurements in these experiments discards valuable information. Furthermore, future experiments on large arrays of spin qubits will likely rely on gate-based dispersive readout, where it is challenging to achieve a high signal-to-noise ratio (SNR) [17–20]. Consequently, both a repetitive QND readout with uniform repetitions and improved decoding methods are highly desirable for quantum error correction. makes full use of the analog information contained in the successive measured detector responses. Such analog information can lead to a more efficient readout of the logical qubit [21].

Here we implement ancilla-based repetitive QND readout of an electron spin qubit hosted in a silicon quantum dot. We study the enhancement in the logical readout fidelity as a function of the number of repetitions, and analyze based on experiment the conditions under which “soft decoding" reduces the number of repetitions needed to achieve a target fidelity.

6.2. SPIN QUBIT OPERATIONS

We use two electron spin qubits in a double quantum dot (DQD) confined in a Si/SiGe heterostructure. The sample and qubit control techniques are described in detail in Ref. [22]. In brief, single-qubit gates are realized by electric-dipole spin resonance (EDSR) enabled by the magnetic field gradient from a nearby micromagnet [23, 24]. The micromagnet gradient also causes the resonance frequencies of the two qubits to be well separated. A two-qubit gate is realized by changing the detuning between the chemical potentials of the two dots, which modifies the strength of the exchange interaction, J, between the two spins. Due to the interplay of the exchange and the energy difference between the qubits, the energies of the $|01\rangle$ and $|10\rangle$ states are shifted down by $J/2$, because of their coupling to the doubly-occupied singlet state, S(0,2) (Fig. 6.1(b)). Consequently, the EDSR resonance frequency of qubit 2 (Q2) depends on the state of qubit 1 (Q1). By applying an EDSR pulse at the resonance frequency of Q2 corresponding to a particular Q1 state, we obtain a controlled-rotation (CROT) gate:

$$U_{CROT}(\alpha|0\rangle_{Q1} + \beta|1\rangle_{Q1})|0\rangle_{Q2} = \alpha|0\rangle_{Q1}|0\rangle_{Q2} + \beta|1\rangle_{Q1}|1\rangle_{Q2} \tag{6.1}$$

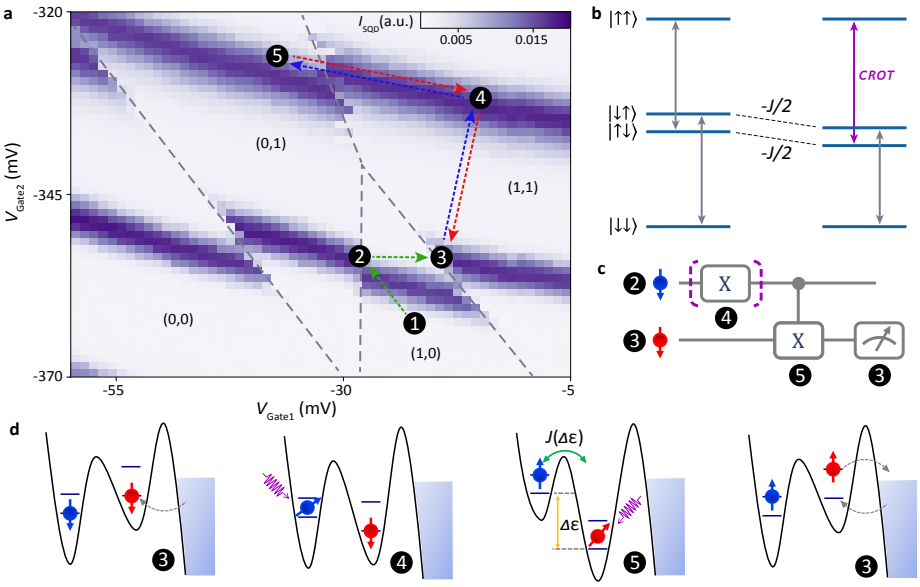

Fig. 6.1: a. Charge stability diagram of the DQD and of the pulsing scheme used in the experiment. The current through a sensing quantum dot is shown in color scale as a function of two gate voltages that control the electrochemical potentials of the two dots. The gate voltages for steps 1 through 5 in the experiment (discussed in the main text) are indicated with black circles, which also appear in panels c and d. We note that the DQD remains in the (1,1) state during step 5 (the CROT gate) because the operation is much faster than the tunneling-out time of Q1. b. Spin states of the two-electron system with and without exchange coupling. The spin state of Q1 is mapped onto the spin state of Q2 via a CROT gate based on frequency-selective spin transitions. c. Quantum circuit for the QND readout procedure. Q1 is used as a logical qubit and as control qubit of the CROT gate, while Q2 is used as ancilla qubit and as target qubit of the CROT gate. An optional X_π pulse is used to prepare Q1 into the spin-up state following initialization to spin-down. d. Schematic representation of the DQD system during the QND measurement protocol. Initialization and readout are implemented by aligning the electrochemical potential of the last electron in dot 2 close to the Fermi energy of the reservoir. The exchange coupling is switched on by detuning the electrochemical potentials of dots 1 and 2. Both electrochemical potentials are varied by applying voltage pulses on the depletion gates that define the DQD confining potential. Spin-flips in single- and two-qubit gates are implemented by EDSR.

Due to the low concentration of nuclear spins in silicon, the mapping from logical qubit to ancilla is close to optimal in every single repetition. In the QND readout experiment, we choose Q1 (shown in blue in the figures) as the logical qubit and Q2 (shown in red) as the ancilla qubit. We do this for two reasons. First, Q1 has a much longer T_1 than Q2 ($T_1 > 50\,\text{ms}$ versus $T_1 \approx 1\,\text{ms}$), allowing multiple readout cycles of Q1 before significant relaxation occurs. Second, Q2 is physically closer to the Fermi reservoir, which makes it easier to perform destructive readout and reinitialization. Here, the readout of Q2 is performed by detecting spin-selective tunneling to the reservoir with the help of a charge sensor [25]. The signature of the spin-up state is the appearance of a step in the charge sensor response as only a spin-up electron tunnels out of the quantum dot. A commonly used [25] and near-optimal [26] strategy to detect such a step is to compare the peak value I_p of the charge sensor signal during the readout time to a fixed threshold (see Fig. 6.3c inset for an example of a charge sensor trace). In the data shown below, we infer the spin states using a readout time that minimizes the average single-repetition

readout error rate (see 6.6.4).

6.3. QUANTUM NONDEMOLITION MEASUREMENT

We test the QND readout through a protocol whereby voltage pulses applied to two of the quantum dot gate electrodes take the system through the following steps (see Figs. 6.1a,c,d). 1) Empty dot 2, 2) initialize Q1 to the spin-down state via spin relaxation at a hotspot [27], 3) initialize Q2 in the spin-down state using spin-selective tunneling, 4) an optional single-qubit π-pulse for initialization of Q1 in the spin-up state, 5) a CROT gate to map the state of Q1 onto the state of Q2 and 6) single-shot readout of Q2. Step 6 occurs at the same gate voltages as step 3), so at the end of the sequence, Q2 is automatically reinitialized through spin-selective tunneling. In successive QND measurements, steps 1, 2 are omitted, and the optional rotation at step 4 is omitted as well (Fig. 6.2(a)). Each readout cycle lasts 3.263 ms. Because the CROT gate does not affect the state of Q1, successive cycles each yield information on the state of Q1 before the first cycle, as long as Q1 has not been flipped due to relaxation or excitation. Therefore, the readout fidelity of the logical qubit Q1 can be significantly enhanced by repeating the readout cycle. In order to obtain directly the visibility from experiment, we prepare Q1 either in state $|0\rangle$ or in state $|1\rangle$. We then perform up to 15 sequential QND measurements.

The simplest way to infer the state of Q1 from the repeated readout of Q2 is to perform a majority vote on the readout outcomes [28]. Ideally, this leads to an exponential suppression of the logical readout error probability $\epsilon^{\log}$ with the number of cycles N, $\epsilon^{\log} \propto \epsilon^N$. Here, ϵ is the single-repetition readout error rate, which includes errors from the CROT mapping and the spin readout of Q2.

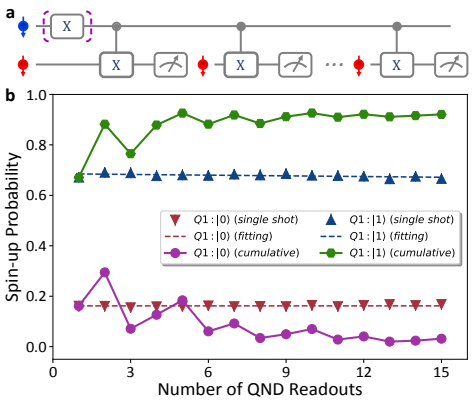

Fig. 6.2: a. Circuit diagram for the repetitive QND readout scheme, using the same labels as in Fig. 6.1c. b. Spin-up probability obtained from individual QND readout cycles (triangles) and from a cumulative weighted majority vote (circles) for preparation of Q1 in state $|1\rangle$ (blue) and in state $|0\rangle$ (red). For the individual readout cycles, the visibility does not improve and in fact slightly decreases due to the finite relaxation time T_1 of Q1. By fitting the measured P_1 for preparation of Q1 in state $|1\rangle$ to an exponential, we estimate $T_1 = 1.8 \pm 0.6$ s. The cumulative weighted majority vote improves the logical readout visibility as more QND readout cycles are performed.

A slightly more sophisticated approach to inferring the state of Q1 is through a weighted

majority vote that accounts for spin relaxation (see 6.6.2 for full details). Intuitively, the later measurement cycles have accumulated more errors from relaxation than the earlier ones, and are thus given less weight. Fig. 6.2(b) shows the estimated spin-up probability of Q1 for each individual QND readout cycle as well as for a cumulative weighted majority vote. The cumulative visibility increases from $51.0 \pm 0.6\%$ after 1 cycle to $88.9 \pm 0.3\%$ after 15 cycles, which corresponds to a cumulative logical fidelity of $94.5 \pm 0.2\%$. Here, the logical fidelity is defined as $F^{\log} = 1 - \epsilon^{\log}$ (see 6.6.2). The oscillation in the cumulative spin-up probabilities is due to an even-odd effect from (weighted) majority voting. Due to spin relaxation of Q1, there is a slow decay of the (single-repetition) spin-up probability when Q1 is prepared in $|1\rangle$. Previous T_1 measurements on the same device shows that there was no observable decay of Q1 up to 50ms [22], consistent with our observations. From the data, it is clear that even higher cumulative fidelities can be achieved using more repetitions (see 6.6.5 for a detailed discussion).

6.4. SOFT DECODING

Further improvements in the readout fidelity for repeated QND readout are possible when taking into account additional information contained in the individual read-out traces. This approach is based on the log-likelihood ratio for the logical state, $\lambda^{\log} = \sum_{i=1}^{N} \lambda(\mathcal{O}_i)$ [3, 29] (in the data analysis below, we use a slightly more sophisticated variant, accounting for relaxation of Q1 during the repeated measurements, see 6.6.2). Here, $\mathcal{O}_i$ is the measurement outcome for the i^{th} repetition and $\lambda(\mathcal{O}_i) = \ln[P(\mathcal{O}_i|1)/P(\mathcal{O}_i|0)]$ is the log-likelihood ratio for that outcome. $P(\mathcal{O}_i|1)$ ($P(\mathcal{O}_i|0)$) is the probability to obtain $\mathcal{O}_i$ when the qubit is prepared in $|1\rangle$ ($|0\rangle$). If $\lambda^{\log} > 0$ ($\lambda^{\log} < 0$), it is decided that the most likely pre-measurement logical state is $|1\rangle$ ($|0\rangle$). When thresholding, the observable $\mathcal{O}_i$ is either a 1 or a 0, an approach we call 'hard decoding'. When considering only a single readout instance, thresholding is optimal. For the repetitive QND readout discussed here, but also for quantum error correction in general, thresholding each individual qubit readout leads to an irreversible loss of information because it discards the level of confidence $\lambda(\mathcal{O}_i)$ that can be assigned to individual readout outcomes [21, 30–35]. A better approach is to take an analog variable as the observable $\mathcal{O}_i$ to calculate $\lambda^{\log}$. For the readout scheme used here, the peak signal is a good choice [26]. We refer to this procedure as 'soft decoding'.

The logical readout error probabilities resulting from hard and soft decoding applied to our raw data are plotted in Fig. 6.3(c) as a function of the number of QND readout cycles. Interestingly, in this instance, the improvement of soft decoding over hard decoding is almost non-existent. This can be understood by examining the empirically measured peak-signal distributions $P(I_p|1)$ and $P(I_p|0)$ at the optimal readout time ($\sim 623\,\mu$s, see 6.6.4) shown in Fig. 6.3(a) along with the log-likelihood ratio $\lambda(I_p)$. Since readout errors caused by noise in the readout traces are small compared to the bit flip errors arising from imperfect CROT operations, ancilla preparation, and spin-to-charge conversion in the readout of the ancilla spin, the peak-signal distributions have clear bimodal features (this is discussed in more detail below). As a result, $\lambda(I_p)$ approximates a step function. This means that all values of I_p on one side of the step are assigned the same level of confidence. It follows that thresholding the values of I_p does not discard much information on the level of confidence in each readout outcome.

For soft decoding to yield an advantage, we must therefore consider situations where $\lambda(I_p)$ is not a step function. One such generic situation occurs in the limit of low SNR for the single-repetition readout. To demonstrate that soft decoding yields an advantage for low SNR, we artificially add Gaussian white noise on top of the experimental readout traces. Fig. 6.3(d) shows the resulting logical error probabilities for both hard and soft decoding. We see that soft decoding achieves the same logical error rate with 10 repetitions instead of 15 repetitions, a reduction by a third in the number of repetitions. Consequently, a significant amount of readout time may be saved. The reason for this advantage is apparent in Fig. 6.3(b), which shows the probability distributions $P(I_p|1)$ and $P(I_p|0)$ and the corresponding $\lambda(I_p)$ after adding the noise (optimal readout time $\sim 475\mu$s). Here, the distributions are close to unimodal Gaussians and strongly overlap. This results in a $\lambda(I_p)$ that varies smoothly with I_p such that values of I_p on a given side of the threshold are given different levels of confidence. This is the additional information that yields the soft decoding advantage.

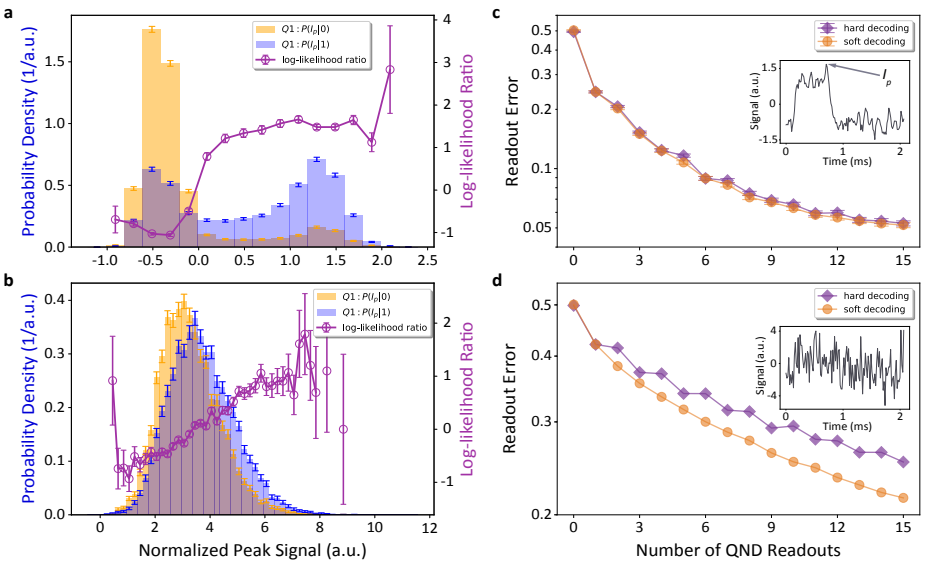

Fig. 6.3: a. Empirically measured distributions $P(I_p|1)$ and $P(I_p|0)$ of the peak sensing dot signal I_p for preparation of Q1 in $|1\rangle$ (blue histograms) and in $|0\rangle$ (yellow histograms), respectively. The distributions are obtained for the readout time that minimizes the single-repetition readout error (see 6.6.4). Due to the bimodal features of the two distributions, the log-likelihood ratio $\lambda(I_p)$ is approximately a step function (magenta curve). b. Same dataset as in panel a but with artificially added Gaussian white noise. Here, the two distributions largely overlap. As a result, the log-likelihood ratio $\lambda(I_p)$ is not a step function and different values of I_p on one side of the threshold acquire different weights. This means that if the values of I_p are thresholded at each cycle, useful information is discarded. c, d. Logical readout error rate without and with artificially added white noise. When the log-likelihood ratio $\lambda(I_p)$ approximates a step function, there is little advantage in using soft decoding. When the log-likelihood ratio $\lambda(I_p)$ strongly deviates from a step function, soft-decoding reduces the number of repetitions required to achieve a given error rate. Insets: example readout traces containing a tunnel event without/with added Gaussian white noise.

It is important to note that the low-SNR readout is not merely of theoretical interest but is also of great practical relevance. One reason is that it might be difficult to achieve

high-SNR in dense qubit arrays where charge sensors, electron reservoirs, or on-chip resonators [19, 20] are not available, and where only gate-based readout [17–20] with SNR limited by a large parasitic capacitance [17, 18] is possible. It also opens the possibilities to improve the fidelity readout at higher operating temperatures [36, 37], in particular when raising the temperature reduces the SNR (e.g. from broadening of the sensing dot Coulomb peaks) while not or only mildly increasing spin-charge conversion errors (e.g. in Pauli spin blockade readout). Operation above 1K is essential to the integration of quantum dots with cryo-electronics [38]. Such situations are precisely the ones where repetitive QND readout may become necessary to achieve low logical readout error rates. Moreover, there are situations where relaxing the constraints on SNR could be beneficial. For instance, it may allow the repetitive readout to operate at lower detector-qubit coupling without loss of fidelity, which could reduce unwanted interference of the detector on the system. Note that these advantages are not limited to the special case of the repetitive QND readout considered here. For instance, quantum error-correcting codes infer error syndromes by using both spatial and temporal redundancy from repeated measurement of ancillas [39–49]. Both our results and recent theoretical work on continuous-variable quantum error correction [50–53] suggest that soft-decoding of quantum codes could help reduce the number of physical qubits and the number of measurements required to achieve a desired logical error rate.

It must also be emphasized that a low SNR is in general not necessary to benefit from soft decoding. Soft decoding helps when errors arising from noise, as small as they may be, are larger than bit flip errors. This ensures that the log-likelihood ratio changes smoothly instead of step-wise [21]. We discuss ways to engineer such conditions for readout of spin qubits in quantum dots in 6.6.6.

6.5. CONCLUSION

In conclusion, we have performed high-fidelity QND readout of a spin qubit in silicon. The readout fidelity is enhanced by repeatedly mapping the qubit state to a nearby ancilla using a two-qubit gate and measuring the ancilla, from $75.5 \pm 0.3\%$ for a single repetition to $94.5 \pm 0.2\%$ for 15 repetitions, and with room for further improvements from additional repetitions (see 6.6.5). We compared two different decoding methods, hard decoding and soft decoding, and discussed the conditions under which soft decoding yields a significant advantage. In the present experiment, hard decoding and soft decoding perform equally well since errors from noise in the readout traces are far less frequent than errors from bit flips. However, with the same rate of bit-flip errors, soft decoding is expected to significantly reduce the number of ancilla measurements required for high-fidelity readout when the SNR is low, as can be the case for gate-based readout in dense qubit arrays, for readout at elevated temperatures, or when SNR must be traded for readout speed.

6.6. APPENDICES

6.6.1. DEVICE AND MEASUREMENT SETUP

The device and measurement setup used in this work have been described by Watson *et al.* [22] and Xue *et al.* [54]. We summarize a few key points. The device is cooled in a dilution refrigerator to ~20 mK. An external magnetic field of 617 mT is applied in the plane of the sample. The longitudinal component of the magnetic field from the micromagnet contributes to the Zeeman splitting and its gradient gives a large separation of the qubit frequencies (Q1: 18.4 GHz; Q2: 19.7 GHz), which facilitates single-qubit addressability. Two confinement gates $P1$ and $P2$ (we use the same labels as in Xue *et al.* [54]) are connected to an arbitrary waveform generator (Tektronix 5014C) via coaxial cables. DC voltage pulses applied to the sample through these two gates allow the system to move into different positions in the charge stability diagram for initialization (Q1: 0.1 ms for fast relaxation; Q2: 4 ms for spin-selective tunneling), operation, and readout (1~2 ms for each qubit). A full cycle of the pulse sequence can be found in Watson *et al.* [22]. Furthermore, during the operation stage, the gates $P1$ and $P2$ are also used to switch on and off the exchange coupling between the two electron spins by controlling the detuning of chemical potentials between them, and thus realize the two-qubit gate. Another two confinement gates $MW1$ and $MW2$ are connected to two vector microwave sources (VSG, Keysight E8267D) for single-qubit gates by microwave-controlled EDSR. We calibrate the VSG powers to achieve Rabi frequencies of both qubits to be 2 MHz, corresponding to a 180 degree rotation (X_π gate) of 250 ns. Readout traces are sampled by a digitizer card (Spectrum M4i.44) after a 20 kHz Bessel low-pass filter (SRS SIM965). Each single readout trace is either converted into a single bit value by comparing the peak signal to a threshold value (hard decoding), or saved for soft decoding analysis.

6.6.2. BAYESIAN INFERENCE

In this section, we give an algorithm to efficiently perform optimal Bayesian inference of the logical qubit state using the empirically determined statistics of the repetitive readout.

REPETITIVE READOUT

Suppose that the logical qubit is repetitively read out N times, with each repetition having a duration δt_{rep}. We may consider the state of the logical qubit at the discrete times:

$$t_k = k\,\delta t_{\text{rep}}, \quad k = 0, 1, ..., N, \tag{6.2}$$

with the k^{th} repetition taking place in the interval $[t_{k-1}, t_k]$. Here, the coherence of the logical qubit in the computational basis plays no role in the statistics of the measurement. For the present purposes, we may therefore model the time evolution of the logical qubit classically. The classical state of the logical qubit at time t_k is labeled x_k. The state evolution of the logical qubit up to $k \leq N$ repetitions follows the stochastic time series:

$$\mathbf{X}_k = \{x_0, x_1, \ldots, x_k\}. \tag{6.3}$$

In reality, each individual readout is noisy. Thus, the state x_k at each repetition is not directly recorded. Instead, a noisy observation $\mathcal{O}_k$ is recorded. This gives the observation sequence:

$$\mathbf{O}_k = \{\mathcal{O}_0, \mathcal{O}_1, \ldots, \mathcal{O}_{k-1}\}. \tag{6.4}$$

Note that in general, the observations $\mathcal{O}_k$ need not be scalar.

MAXIMUM-LIKELIHOOD DECISION

Our goal is to infer the most likely initial state of the logical qubit from the sequence $\mathbf{O}_k$ of noisy repetitive readout outcomes. This is most easily done by calculating the posterior probability ratio:

$$\frac{P(x_0 = 1|\mathbf{O}_k)}{P(x_0 = 0|\mathbf{O}_k)} = \frac{P(\mathbf{O}_k|x_0 = 1)}{P(\mathbf{O}_k|x_0 = 0)} \frac{P(x_0 = 1)}{P(x_0 = 0)}. \tag{6.5}$$

The initial state is most likely 1 if the ratio is larger than unity, and it is most likely 0 if the ratio is smaller than unity. In the absence of prior information on the logical qubit state, $P(x_0 = 0) = P(x_0 = 1) = 1/2$, the above *maximum a posteriori* decision [29] reduces to calculating the log-likelihood ratio:

$$\lambda_k^{\log} = \ln \frac{P(\mathbf{O}_k|x_0 = 1)}{P(\mathbf{O}_k|x_0 = 0)}. \tag{6.6}$$

The initial state is now most likely 1 if $\lambda_k^{\log} > 0$, and it is most likely 0 if $\lambda_k^{\log} < 0$. This results in a maximum-likelihood decision [29].

LOGICAL READOUT ERROR RATE

The average logical readout error rate ϵ is given by

$$\epsilon^{\log} = \frac{1}{2}\left(\epsilon_1^{\log} + \epsilon_0^{\log}\right). \tag{6.7}$$

Here, $\epsilon_1^{\log}$ and $\epsilon_0^{\log}$ are the error rates conditioned on preparation of the logical qubit in states 1 and 0 at time t_0, respectively. These are given by:

$$\begin{aligned} \epsilon_1^{\log} &= P(\lambda_k^{\log} < 0 | x_0 = 1), \\ \epsilon_0^{\log} &= P(\lambda_k^{\log} > 0 | x_0 = 0). \end{aligned} \tag{6.8}$$

An experimental estimate of the logical readout error rate $\epsilon_1^{\log}$ ($\epsilon_0^{\log}$) is obtained by preparing the logical qubit in state $|1\rangle$ ($|0\rangle$) 10^4 times, measuring the record $\mathbf{O}_k$ and calculating $\lambda_k^{\log}$ for each attempt, and counting the number of times where $\lambda_k^{\log} < 0$ ($\lambda_k^{\log} > 0$). Finally, we note that the average readout fidelity quoted in the main text is defined as $F^{\log} = 1 - \epsilon^{\log}$, while the logical visibility is $\mathcal{V}^{\log} = 1 - 2\epsilon^{\log}$.

CALCULATING THE LOG-LIKELIHOOD RATIO

To calculate $\lambda_k^{\log}$, the statistics of the observations $\mathbf{O}_k$ given the initial state of the logical qubit must be known. More precisely, the probability distributions $P(\mathbf{O}_k|x_0 = 1)$ and $P(\mathbf{O}_k|x_0 = 0)$ appearing in Eq. (6.6) must be calculated. In the following, we show how to model and calculate these distributions for the repetitive readout using the theory of hidden Markov models [14, 16, 47, 55, 56]. The hidden Markov model provides a direct connection between the single-repetition probability distributions, $P(\mathcal{O}_k|x_k)$, and the probability distributions for the full measurement record, $P(\mathbf{O}_k|x_0)$, accounting for the dynamics of the logical qubit. From $P(\mathbf{O}_k|x_0)$, the log-likelihood ratio can be evaluated directly using Eq. (6.6). As described in 6.6.3, following Eq. (6.29), here we have determined $P(\mathcal{O}_k|x_k)$ empirically. However, note that these distributions can also be found from an appropriate dynamical model of the readout. See for instance Refs. [26, 57–62] and others, where hidden Markov models are used to determine $P(\mathcal{O}_k|x_k)$ at the level of a single repetition.

Hidden Markov models – As discussed in the main text, the logical qubit state evolves during the measurement via spin relaxation on a time scale T_1. Such a process is Markovian in the sense that the statistics of the state at time t_{k+1} are fully determined by the state at time t_k:

$$P(x_{k+1}|\mathbf{X}_k) = P(x_{k+1}|x_k). \tag{6.9}$$

Because the ancilla qubit is reinitialized after each repetition, the noisy observations $\mathcal{O}_k$ are independent from each other and depend only on the state of the logical qubit at time t_k:

$$P(\mathbf{O}_k|\mathbf{X}_k) = \prod_{l=0}^{k-1} P(\mathcal{O}_l|x_l). \tag{6.10}$$

In other words, the observation noise is white. Finally, prior knowledge about the system state at each time is specified by the prior probability distribution $P(x_k)$ for the state x_k at each time t_k. The set $\{P(x_{k+1}|x_k), P(\mathcal{O}_k|x_k), P(x_k)\}$ defines a 'Hidden Markov Model'.

Forward filtering – For the hidden Markov models discussed above, the log-likelihood ratio may be calculated with the help of an iterative forward filtering algorithm for the logical qubit state. Forward filtering consists in calculating the probability distribution of the logical qubit state x_k at time t_k given all previous observations. We denote this probability distribution as

$$\varrho_k(x_k) = P(x_k|\mathbf{O}_k). \tag{6.11}$$

Using Bayes' rule, the distribution $\varrho_k(x_k)$ may be rewritten as

$$\varrho_k(x_k) = \frac{P(x_k, \mathbf{O}_k)}{P(\mathbf{O}_k)} = \frac{P(x_k, \mathbf{O}_k)}{\sum_y P(y, \mathbf{O}_k)} = \frac{\ell_k(x_k)}{\sum_y \ell_k(y)}. \tag{6.12}$$

Here,

$$\ell_k(x_k) = P(x_k, \mathbf{O}_k) \tag{6.13}$$

is the joint probability distribution of the state x_k and of the previous observations. One advantage of calculating $\ell_k(x_k)$ instead of $\varrho_k(x_k)$ is that $\ell_k(x_k)$ obeys a linear recurrence relation while $\varrho_k(x_k)$ obeys a non-linear recurrence relation (see discussions in "**The filtering equations**").

We note that the denominator in Eq. (6.12) is the likelihood function

$$\mathcal{L}_k = P(\mathbf{O}_k) = \sum_{x_k} \ell_k(x_k). \tag{6.14}$$

Eq. (6.12) now takes the form

$$\ell_k(x_k) = \varrho_k(x_k) \times \mathcal{L}_k. \tag{6.15}$$

It is convenient to introduce the vector notation

$$\left|\varrho_k\right) = \sum_x \varrho_k(x)\,|x), \quad |\ell_k) = \sum_x \ell_k(x)\,|x), \tag{6.16}$$

where $\{|x)\}$ is a set of basis vectors representing the classical logical qubit states x. Eq. (6.15) is then rewritten as

$$|\ell_k) = \mathcal{L}_k \times \left|\varrho_k\right). \tag{6.17}$$

The likelihood function, Eq. (6.14), may compactly be written as

$$\mathcal{L}_k = \mathrm{Tr}\,|\ell_k). \tag{6.18}$$

Here, the trace Tr of a vector is the sum of its elements. Choosing the basis $\{|1), |0)\}$, the likelihood function may be calculated for the initial states $x_0 = 1$ and $x_0 = 0$ of the logical qubit by setting $\left|\varrho_0\right) = |\ell_0) = (1,0)^{\mathrm{T}}$ and $\left|\varrho_0\right) = |\ell_0) = (0,1)^{\mathrm{T}}$, respectively. This enables the maximum-likelihood decision discussed following Eq. (6.6).

The filtering equations – For completeness, we now derive the recurrence relation for forward filtering of hidden Markov models. We note that

$$\begin{aligned} \ell_{k+1}(x_{k+1}) &= P(x_{k+1}, \mathbf{O}_{k+1}) \\ &= \sum_{x_k} P(x_{k+1}, \mathbf{O}_{k+1}|x_k) P(x_k) \\ &= \sum_{x_k} P(\mathbf{O}_{k+1}|x_{k+1}, x_k) P(x_{k+1}|x_k) P(x_k). \end{aligned} \tag{6.19}$$

Next we recall that 1) $\mathbf{O}_{k+1} = \{\mathcal{O}_1, \mathcal{O}_2, \ldots, \mathcal{O}_k\}$ does not depend on x_{k+1} by causality and that 2) the observation noise is white, Eq. (6.10). Thus, we have

$$\begin{aligned} \ell_{k+1}(x_{k+1}) &= \sum_{x_k} P(\mathbf{O}_{k+1}|x_k) P(x_{k+1}|x_k) P(x_k) \\ &= \sum_{x_k} P(\mathcal{O}_k|x_k) P(\mathbf{O}_k|x_k) P(x_{k+1}|x_k) P(x_k) \\ &= \sum_{x_k} P(\mathcal{O}_k|x_k) P(x_{k+1}|x_k) \ell_k(x_k). \end{aligned} \tag{6.20}$$

This recurrence relation may be written in vector form

$$|\ell_{k+1}) = V_k(\mathcal{O}_k)\,|\ell_k)\,. \tag{6.21}$$

Here, we have introduced the matrix $V_k(\mathcal{O}_k)$ with elements

$$(x|\,V_k(\mathcal{O}_k)\,|y) = P(x_{k+1}|y_k)P(\mathcal{O}_k|y_k) = w_k^{xy}\,\mathcal{P}_k^y(\mathcal{O}_k), \tag{6.22}$$

and we have defined

$$\begin{aligned} w_k^{xy} &= P(x_{k+1}|y_k), \\ \mathcal{P}_k^x(\mathcal{O}_k) &= P(\mathcal{O}_k|x_k). \end{aligned} \tag{6.23}$$

The matrix w_k^{xy} describes the transition probabilities for the evolution of the logical qubit state and the vector $\mathcal{P}_k^x(\mathcal{O}_k)$ describes the observation noise for each logical qubit state. Note that there exist corresponding recurrence relations for the state vector $|\varrho_k)$ and for the likelihood function $\mathcal{L}_k$. They take the form

$$|\varrho_{k+1}) = \frac{1}{\mathcal{N}_{k+1}}\,|\tilde{\varrho}_{k+1})\,,\quad \mathcal{L}_{k+1} = \mathcal{N}_{k+1}\times\mathcal{L}_k, \tag{6.24}$$

where

$$|\tilde{\varrho}_{k+1}) = V_k(\mathcal{O}_k)\,|\varrho_k)\,,\quad \mathcal{N}_{k+1} = \mathrm{Tr}\,|\tilde{\varrho}_{k+1})\,. \tag{6.25}$$

Numerical algorithm – We now provide an efficient numerical algorithm for forward filtering. The algorithm simultaneously calculates the probability vector $|\varrho_k)$ and the log-likelihood function $\ln\mathcal{L}_k$ as follows:

1. Set $k = 0$.
2. Calculate the matrix $V_k(\mathcal{O}_k)$.
3. Calculate $|\tilde{\varrho}_{k+1}) = V_k(\mathcal{O}_k)\,|\varrho_k)$.
4. Calculate the norm $\mathcal{N}_{k+1} = \mathrm{Tr}\,|\tilde{\varrho}_{k+1})$.
5. Update the probability distribution $|\varrho_{k+1}) = |\tilde{\varrho}_{k+1})\,/\mathcal{N}_{k+1}$.
6. Update the log-likelihood ratio with $\ln\mathcal{L}_{k+1} = \ln\mathcal{L}_k + \ln\mathcal{N}_{k+1}$.
7. Increase k by one and start again.

Note that we are only interested in estimating the initial state of the logical qubit. Therefore, the matrix $V_k(\mathcal{O}_k)$ may be normalized at each step by any constant factor independent of the qubit state without affecting the maximum-likelihood estimate. In some cases, this may prevent the values of the log-likelihood function from becoming too large.

6.6.3. REPETITIVE READOUT STATISTICS

The hidden Markov model relevant for the repetitive readout discussed in the main text is obtained by specifying the transition matrix w_k and the noise vector $\mathcal{P}_k$ appearing in Eq. (6.23).

As discussed in the main text, the qubit undergoes relaxation to its spin ground state on a time scale T_1. We obtain the value of T_1 by simultaneously fitting the measured single-repetition probabilities P_1 and P_0 shown in Fig. 2b to an expression of the form

$$P_1(t) = A\epsilon^{-t/T_1} + B, \tag{6.26}$$

for the case when Q1 is prepared in $|1\rangle$ before the first measurement cycle, and of the form

$$P_0(t) = B. \tag{6.27}$$

for the case when Q1 is initially prepared in $|0\rangle$. Here, t is the total readout time after the beginning of the repetitive readout and A and B are constants. The fit is shown in Fig. 2b and yields $T_1 = 1.8 \pm 0.6s$. For a relaxation process, the transition matrix w_k^{xy} in the basis $\{|1\rangle, |0\rangle\}$ takes the form:

$$w_k = \exp\left[\begin{pmatrix} -1 & 0 \\ 1 & 0 \end{pmatrix} \frac{\delta t_{\text{rep}}}{T_1}\right]. \tag{6.28}$$

Here, $\delta t_{\text{rep}} = 3.263\,\text{ms}$.

The noise vector $\mathcal{P}_k^y(\mathcal{O}_k)$ describing the distribution of the outcome $\mathcal{O}_k$ for each logical qubit state is given by

$$\mathcal{P}_k(\mathcal{O}_k) = \begin{pmatrix} P(\mathcal{O}_k|x_k = 1) \\ P(\mathcal{O}_k|x_k = 0) \end{pmatrix}. \tag{6.29}$$

Here, $P(\mathcal{O}_k|x_k = 1)$ and $P(\mathcal{O}_k|x_k = 0)$ are the probability distributions of the readout outcome $\mathcal{O}_k$ for preparation of the logical qubit in states 1 and 0, respectively. For the soft decoding procedure discussed in the main text, the readout outcome $\mathcal{O}_k$ is taken to be the peak signal I_p (see 6.6.4). The distributions of outcomes conditioned on the logical qubit state are then simply the empirically observed distributions of the peak signal $P(I_p|x_k = 1)$ and $P(I_p|x_k = 0)$ displayed in Figs. 3a-b of the main text. For the hard decoding procedure, the readout outcome $\mathcal{O}_k$ is taken to be the binary value 1 or 0 obtained by thresholding the peak signal at each repetition. The distributions of outcomes conditioned on the logical qubit state are then given by the conditional single-repetition readout error rates ϵ_1 and ϵ_0:

$$\begin{aligned} &P(1|x_k = 1) = 1 - \epsilon_1, \quad &&P(1|x_k = 0) = \epsilon_0, \\ &P(0|x_k = 1) = \epsilon_1, &&P(0|x_k = 0) = 1 - \epsilon_0. \end{aligned} \tag{6.30}$$

The procedure used to obtain the distributions $P(I_p|x_k = 1)$ and $P(I_p|x_k = 0)$ and the conditional single-repetition readout error rates ϵ_1 and ϵ_0 is detailed in 6.6.4. When $\epsilon_1 = \epsilon_0$ and when $T_1 \to \infty$, the hard decoding procedure reduces to a simple majority vote on the binary outcomes [21].

6.6.4. SINGLE-REPETITION READOUT CALIBRATION

Since all repetitions are identical, we use the first repetition to calibrate the single-repetition readout. At $t_0 = 0$, the logical qubit is prepared 10^4 times in state $x_0 = 1$ and 10^4 times in state $x_0 = 0$. For each preparation, a readout trace $I(t)$ is recorded for a total time of 2.01 ms in steps of $\delta t = 16.38\,\mu$s. For all readout times $t_R \leq 2.01$ ms, we extract the peak signal $I_p = \max_t I(t)$ [25] and construct the probability distributions of I_p conditioned on the logical qubit state, $P(I_p|x_0 = 1)$ and $P(I_p|x_0 = 0)$. For a given readout time t_R, single-repetition readout is performed by calculating the single-repetition log-likelihood ratio

$$\lambda(I_p) = \ln \frac{P(I_p|x_0 = 1)}{P(I_p|x_0 = 0)}. \tag{6.31}$$

If $\lambda(I_p) > 0$ [$\lambda(I_p) < 0$], we decide that the qubit state is most likely $|1\rangle$ [$|0\rangle$]. Therefore, the single-repetition readout error rates ϵ_1 and ϵ_0 for each state are obtained from marginals of the distributions $P(I_p|x_0 = 1)$ and $P(I_p|x_0 = 0)$ as follows:

$$\begin{aligned} \epsilon_1 &= P(\lambda^{\log} < 0|x_0 = 1) = \sum_{\{I_p|\lambda(I_p)<0\}} P(I_p|x_0 = 1), \\ \epsilon_0 &= P(\lambda^{\log} > 0|x_0 = 0) = \sum_{\{I_p|\lambda(I_p)>0\}} P(I_p|x_0 = 0), \end{aligned} \tag{6.32}$$

and the average single-repetition readout error rate is given by:

$$\epsilon = \frac{1}{2}(\epsilon_1 + \epsilon_0). \tag{6.33}$$

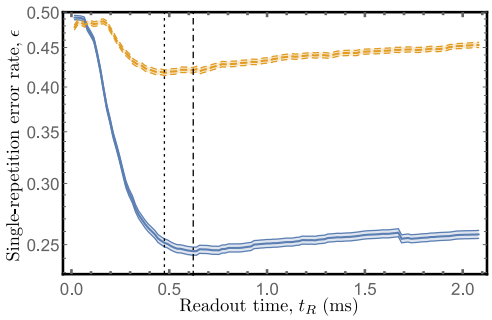

Fig. 6.4: Average single-repetition readout error rate ϵ as a function of readout time t_R in the absence of added noise (solid blue line) and in the presence of added noise (dashed yellow line). The optimal readout time in the absence (presence) of added noise is indicated by the dot-dashed (dotted) line. In both cases, the shaded areas give the statistical uncertainty (see text). Finally, we note that the small discontinuity in the blue curve at $t_R \approx 1.7$ ms is a consequence of the finite histogram bin size and has no particular physical significance.

The value of ϵ is plotted in Fig. 6.4 as a function of readout time in the absence and in the presence of artificially added noise. We choose the value of t_R that minimizes ϵ. The histograms $P(I_p|x_0 = 1)$ and $P(I_p|x_0 = 0)$ and the error rates ϵ_1 and ϵ_0 corresponding to that optimal value of t_R are those used throughout the main text. In particular, they

are used to perform the Bayesian analysis detailed in 6.6.3. Without adding artifical noise to the readout traces, we find $\epsilon_1 = 32.9 \pm 0.5\%$ and $\epsilon_0 = 16.2 \pm 0.4\%$ at an optimal readout time $t_R = 623\,\mu$s. After adding noise, we find $\epsilon_1 = 41.1 \pm 0.5\%$ and $\epsilon_0 = 42.3 \pm 0.5\%$ at an optimal readout time $t_R = 475\,\mu$s. The error bars on ϵ_1 and ϵ_0 are given by the standard deviation of the corresponding binomial error process with $N = 10^4$ samples, $\delta\epsilon_1 = \sqrt{\epsilon_1(1-\epsilon_1)/N}$ and $\delta\epsilon_0 = \sqrt{\epsilon_0(1-\epsilon_0)/N}$.

Note that we have assumed perfect preparation of the logical qubit state throughout. For this device, preparation errors have been reported [22] to be ~ 1%, smaller than the single-repetition readout errors reported in 6.6.4. In 6.6.5, we argue that the average preparation error is in fact around $2-3\%$ ($4-5\%$ for state $|1\rangle$ and $< 1\%$ for state $|0\rangle$) for this run of the experiment. Therefore, the empirically measured single-repetition readout distributions in Figs. 3a-b are close to what they would be without preparation errors and lead to decoding procedures (hard and soft) that are close to optimal. In 6.6.5, we give rough estimates for the expected logical readout fidelity that would be measured in the absence of preparation errors.

6.6.5. THEORETICAL SIMULATION

To explore the full potential of the repetitive readout discussed in the main text, we perform a numerical simulation. For each qubit state, we randomly sample 10^4 outcome sequences according to the hidden Markov model described in 6.6.3. We use the experimentally extracted value of T_1 and the empirically measured peak-signal distributions of Fig. 3a as input parameters. A Monte-Carlo estimate of the average logical readout error rate $\epsilon^{\log}$ is obtained by thresholding the simulated outcome sequences as described in 6.6.4 and then applying the hard decoding procedure detailed in 6.6.2.

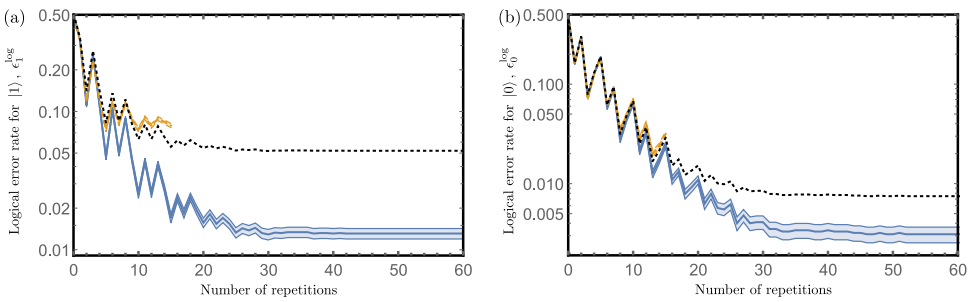

Fig. 6.5: Simulated logical readout error rate (solid blue line) as a function of the number of repetitions for (a) state $|1\rangle$ and (b) state $|0\rangle$. In both cases, the experimentally measured logical readout error rate is shown for comparison (dashed yellow line). The bands give the statistical error associated with the binomial statistics of the sampled errors as explained in 6.6.4. Moreover, the dotted black curves give the simulated curves corrected to fit the experimental curves accounting for finite preparation errors using Eq. (6.34). The best fit values for the preparation errors are $\eta_1 = 4\%$ for state $|1\rangle$ and $\eta_0 = 0.44\%$ for state $|0\rangle$, resulting in an average preparation error of $\eta = 2.2\%$.

The conditional logical readout error rates $\epsilon_1^{\log}$ and $\epsilon_0^{\log}$ are plotted in Fig. 6.5 as a function of the number of repetitions. The experimental results of Fig. 3c are shown for comparison. It is clear from Fig. 6.5 that the simulated logical readout error rate under-

estimates the experimentally measured readout error rate as the number of repetitions increases. We believe that this is due to the logical readout error rate becoming comparable to preparation errors for Q1. This assumption is consistent with the simulation and experiment agreeing at low repetition number, where the logical readout error rate is much larger than the expected preparation error (of the order of 1% [22]). In fact, it is possible to estimate the preparation error η by fitting the simulated error rate ϵ^{sim} to the experimentally measured error rate $\epsilon^{\log}$ using the error composition relation

$$\epsilon^{\log} = (1-2\eta)\epsilon^{\text{sim}} + \eta. \tag{6.34}$$

We find that the simulation and experiment agree for a preparation error of $\eta_1 \approx 4-5\%$ for state $|1\rangle$ and of $\eta_0 < 1\%$ for state $|0\rangle$, giving an average preparation error of approximately $\eta \approx 2-3\%$. The simulation results suggest that in the absence of preparation errors, the measured fidelity could reach $\sim 98\%$ after 15 repetitions and saturate at $> 99\%$ for more than 30 repetitions.

6.6.6. ENGINEERING GAUSSIAN DISTRIBUTIONS

It is known that if $P(I_p|1)$ and $P(I_p|0)$ are unimodal Gaussian distributions, soft decoding can reduce the number of readout cycles by up to a factor of two for arbitrarily large readout SNR. For this advantage to exist, the 'bit-flip' conversion errors creating the bimodal features of the measured probability distributions must be small enough that the errors are dominated by the Gaussian noise [21]. Understanding the origin of the conversion errors is thus of great importance. Here, the 'bit-flip' conversion errors may arise from an imperfect CROT gate, imperfect ancilla preparation, or imperfect spin-to-charge conversion in the readout of Q2. The CROT and preparation errors will be generically suppressed as the control and preparation fidelities are improved. The imperfect spin-to-charge conversion in the readout of Q2 may be the most challenging to overcome. In what follows, we discuss avenues to suppress the spin-to-charge conversion errors.

For initialization of Q2 in state $|1\rangle$, the dot should ideally remain empty at all times. Thus, imperfect spin-to-charge conversion arises either from

1) the finite time scales for an electron to leave or re-enter the dot. The conversion errors caused by these charge transitions could be suppressed by, e.g., engineering the density of states [63] of the reservoir so that a spin-up electron tunnels out of the quantum dot very rapidly, and so that a spin-down electron tunnels back in the quantum dot very slowly [26]. If that were the case, the dot would remain empty at nearly all times and the bimodality of $P(I_p|1)$ would be suppressed.

2) spin relaxation of Q2 before the electron is able to leave the dot. Indeed, the spin relaxation time of Q2 is of order 1 ms, which is only an order of magnitude longer than the observed time scale $\sim 100\,\mu$s for an electron to escape to the reservoir. The strategy to suppress spin relaxation of Q2 during readout depends strongly its physical origin. However, there is *a priori* no fundamental reason why the spin relaxation time of Q2 cannot be as large as that of Q1 (although it must be noted that increasing the dot-reservoir coupling as suggested in point 1) may negatively affect the spin relaxation time via cotunneling processes).

For initialization of Q2 in state $|0\rangle$, the dot should ideally remain occupied at all times. The probability of an electron leaving the dot should in principle be exponentially suppressed in the ratio of the thermal energy to the Zeeman splitting. However, the observed probability of transitioning to the reservoir is too large to be explained by such thermal suppression. Instead, a measurement of the transition probability as a function of the plunger gate voltage of Q2 suggests that the electron escapes the $|0\rangle$ state via an excited quantum dot state. The value of the plunger voltage at which the transitions are suppressed is consistent with an excited state with energy tens of μeVs above the ground state. We conjecture that this state is an excited valley state with the same spin (spin-down) as the ground state. Therefore, a likely explanation for the dominant transition mechanism is excitation to a higher valley state (via, e.g., absorption of energy from the biased charge sensor) followed by a transition from the excited valley state to the reservoir. The bimodality of $P(I_p|0)$ could therefore be suppressed by engineering valley splitting much larger than the charge sensor bias.

The above discussion highlights the importance of understanding the underlying physics for optimization of qubit readout.

REFERENCES

[1] A. G. Fowler, M. Mariantoni, J. M. Martinis, and A. N. Cleland, *Surface codes: Towards practical large-scale quantum computation,* Phys. Rev. A **86**, 032324 (2012).

[2] T. Schaetz, M. D. Barrett, D. Leibfried, J. Britton, J. Chiaverini, W. M. Itano, J. D. Jost, E. Knill, C. Langer, and D. J. Wineland, *Enhanced quantum state detection efficiency through quantum information processing,* Phys. Rev. Lett. **94**, 010501 (2005).

[3] D. Hume, T. Rosenband, and D. J. Wineland, *High-fidelity adaptive qubit detection through repetitive quantum nondemolition measurements,* Phys. Rev. Lett. **99**, 120502 (2007).

[4] L. Jiang, J. S. Hodges, J. R. Maze, P. Maurer, J. M. Taylor, D. G. Cory, P. R. Hemmer, R. L. Walsworth, A. Yacoby, A. S. Zibrov, and M. D. Lukin, *Repetitive readout of a single electronic spin via quantum logic with nuclear spin ancillae,* Science **326**, 267 (2009).

[5] P. Neumann, J. Beck, M. Steiner, F. Rempp, H. Fedder, P. R. Hemmer, J. Wrachtrup, and F. Jelezko, *Single-shot readout of a single nuclear spin,* Science **329**, 542 (2010).

[6] L. Robledo, L. Childress, H. Bernien, B. Hensen, P. F. Alkemade, and R. Hanson, *High-fidelity projective read-out of a solid-state spin quantum register,* Nature **477**, 574 (2011).

[7] G. Waldherr, J. Beck, M. Steiner, P. Neumann, A. Gali, T. Frauenheim, F. Jelezko, and J. Wrachtrup, *Dark states of single nitrogen-vacancy centers in diamond unraveled by single shot NMR,* Phys. Rev. Lett. **106**, 157601 (2011).

[8] P. C. Maurer, G. Kucsko, C. Latta, L. Jiang, N. Y. Yao, S. D. Bennett, F. Pastawski, D. Hunger, N. Chisholm, M. Markham, D. J. Twitchen, J. I. Cirac, and M. D. Lukin,

Room-temperature quantum bit memory exceeding one second, Science **336**, 1283 (2012).

[9] A. Dréau, P. Spinicelli, J. Maze, J.-F. Roch, and V. Jacques, *Single-shot readout of multiple nuclear spin qubits in diamond under ambient conditions,* Phys. Rev. Lett. **110**, 060502 (2013).

[10] J. J. Pla, K. Y. Tan, J. P. Dehollain, W. H. Lim, J. J. Morton, F. A. Zwanenburg, D. N. Jamieson, A. S. Dzurak, and A. Morello, *High-fidelity readout and control of a nuclear spin qubit in silicon,* Nature **496**, 334 (2013).

[11] I. Lovchinsky, A. O. Sushkov, E. Urbach, N. P. de Leon, S. Choi, K. De Greve, R. Evans, R. Gertner, E. Bersin, C. Müller, L. McGuinness, F. Jelezko, R. L. Walsworth, H. Park, and M. D. Lukin, *Nuclear magnetic resonance detection and spectroscopy of single proteins using quantum logic,* Science **351**, 836 (2016).

[12] J. M. Boss, K. S. Cujia, J. Zopes, and C. L. Degen, *Quantum sensing with arbitrary frequency resolution,* Science **356**, 837 (2017).

[13] J. Holzgrafe, J. Beitner, D. Kara, H. S. Knowles, and M. Atatüre, *Error corrected spin-state readout in a nanodiamond,* npj Quantum Information **5**, 13 (2019).

[14] S. S. Elder, C. S. Wang, P. Reinhold, C. T. Hann, K. S. Chou, B. J. Lester, S. Rosenblum, L. Frunzio, L. Jiang, and R. J. Schoelkopf, *High-fidelity measurement of qubits encoded in multilevel superconducting circuits,* Phys. Rev. X **10**, 011001 (2020).

[15] T. Meunier, I. Vink, L. W. Van Beveren, F. Koppens, H.-P. Tranitz, W. Wegscheider, L. Kouwenhoven, and L. Vandersypen, *Nondestructive measurement of electron spins in a quantum dot,* Phys. Rev. B **74**, 195303 (2006).

[16] T. Nakajima, A. Noiri, J. Yoneda, M. R. Delbecq, P. Stano, T. Otsuka, K. Takeda, S. Amaha, G. Allison, K. Kawasaki, A. Ludwig, A. D. Wieck, D. Loss, and S. Tarucha, *Quantum non-demolition measurement of an electron spin qubit,* Nature Nanotechnology **14**, 555 (2019).

[17] P. Pakkiam, A. V. Timofeev, M. G. House, M. R. Hogg, T. Kobayashi, M. Koch, S. Rogge, and M. Y. Simmons, *Single-shot single-gate rf spin readout in silicon,* Phys. Rev. X **8**, 041032 (2018).

[18] A. West, B. Hensen, A. Jouan, T. Tanttu, C.-H. Yang, A. Rossi, M. F. Gonzalez-Zalba, F. Hudson, A. Morello, D. J. Reilly, and A. S. Dzurak, *Gate-based single-shot readout of spins in silicon,* Nature Nanotechnology **14**, 437 (2019).

[19] M. Urdampilleta, D. Niegemann, E. Chanrion, B. Jadot, C. Spence, P. Mortemousque, C. Bäuerle, L. Hutin, B. Bertrand, S. Barraud, R. Maurand, M. Sanquer, X. Jehl, S. De Franceschi, M. Vinet, and T. Meunier, *Gate-based high fidelity spin readout in a cmos device.* Nature Nanotechnology **14**, 737 (2019).

[20] G. Zheng, N. Samkharadze, M. L. Noordam, N. Kalhor, D. Brousse, A. Sammak, G. Scappucci, and L. M. K. Vandersypen, *Rapid gate-based spin read-out in silicon using an on-chip resonator,* Nature Nanotechnology **14**, 742 (2019).

[21] B. D'Anjou and W. A. Coish, *Soft decoding of a qubit readout apparatus,* Phys. Rev. Lett. **113**, 230402 (2014).

[22] T. F. Watson, S. G. J. Philips, E. Kawakami, D. R. Ward, P. Scarlino, M. Veldhorst, D. E. Savage, M. G. Lagally, M. Friesen, S. N. Coppersmith, M. A. Eriksson, and L. M. K. Vandersypen, *A programmable two-qubit quantum processor in silicon,* Nature **555**, 633 (2018).

[23] M. Pioro-Ladrière, T. Obata, Y. Tokura, Y.-S. Shin, T. Kubo, K. Yoshida, T. Taniyama, and S. Tarucha, *Electrically driven single-electron spin resonance in a slanting zeeman field,* Nature Physics **4**, 776 (2008).

[24] E. Kawakami, P. Scarlino, D. R. Ward, F. R. Braakman, D. E. Savage, M. G. Lagally, M. Friesen, S. N. Coppersmith, M. A. Eriksson, and L. M. K. Vandersypen, *Electrical control of a long-lived spin qubit in a si/sige quantum dot,* Nature Nanotechnology **9**, 666 (2014).

[25] J. M. Elzerman, R. Hanson, L. H. Willems van Beveren, B. Witkamp, L. M. K. Vandersypen, and L. P. Kouwenhoven, *Single-shot read-out of an individual electron spin in a quantum dot,* Nature **430**, 431 (2004).

[26] B. D'Anjou and W. A. Coish, *Optimal post-processing for a generic single-shot qubit readout,* Phys. Rev. A **89**, 012313 (2014).

[27] V. Srinivasa, K. C. Nowack, M. Shafiei, L. M. K. Vandersypen, and J. M. Taylor, *Simultaneous spin-charge relaxation in double quantum dots,* Phys. Rev. Lett. **110**, 196803 (2013).

[28] H.-A. Engel, V. N. Golovach, D. Loss, L. Vandersypen, J. Elzerman, R. Hanson, and L. Kouwenhoven, *Measurement efficiency and n-shot readout of spin qubits,* Phys. Rev. Lett. **93**, 106804 (2004).

[29] S. M. Kay, *Fundamentals of Statistical Signal Processing, Vol. II: Detection Theory*, Vol. II (Prentice Hall, New Jersey, U.S.A., 1998).

[30] D. Chase, *A class of algorithms for decoding block codes with channel measurement information,* IEEE Trans. Inform. Theory **vol IT-18** (1972).

[31] I. Bari, M. T. Delgado, M. Mondin, and F. Daneshgaran, *Soft-metric based decoding for photon counting receivers,* in *Multitopic Conference (INMIC), 2012 15th International* (2012) pp. 159–164.

[32] C. A. Ryan, B. R. Johnson, J. M. Gambetta, J. M. Chow, M. P. da Silva, O. E. Dial, and T. A. Ohki, *Tomography via correlation of noisy measurement records,* Phys. Rev. A **91**, 022118 (2015).

[33] H. T. Dinani, D. W. Berry, R. Gonzalez, R. Maze, Jeronimo, and C. Bonato, *Bayesian estimation for quantum sensing in the absence of single-shot detection,* Phys. Rev. B **99**, 152413 (2019).

[34] G. Liu, M. Chen, Y.-X. Liu, D. Layden, and P. Cappellaro, *Repetitive readout enhanced by machine learning,* Mach. Learn.: Sci. Technol. **1**, 015003 (2020).

[35] J. H. Xu, A. X. Chen, W. Yang, and G. R. Jin, *Data processing over single-port homodyne detection to realize super-resolution and super-sensitivity,* arXiv:1911.12912 (2019).

[36] C. Yang, R. Leon, J. Hwang, A. Saraiva, T. Tanttu, W. Huang, J. C. Lemyre, K. Chan, K. Tan, F. Hudson, K. M. Itoh, A. Morello, M. Pioro-Ladrière, A. Laucht, and A. S. Dzurak, *Silicon quantum processor unit cell operation above one kelvin,* arXiv:1902.09126 (2019).

[37] L. Petit, H. Eenink, M. Russ, W. Lawrie, N. Hendrickx, J. Clarke, L. Vandersypen, and M. Veldhorst, *Universal quantum logic in hot silicon qubits,* arXiv:1910.05289 (2019).

[38] E. Charbon, F. Sebastiano, A. Vladimirescu, H. Homulle, S. Visser, L. Song, and R. M. Incandela, *Cryo-CMOS for quantum computing,* in *2016 IEEE International Electron Devices Meeting (IEDM)* (IEEE, 2016) pp. 13–5.

[39] L. Sun, A. Petrenko, Z. Leghtas, B. Vlastakis, G. Kirchmair, K. Sliwa, A. Narla, M. Hatridge, S. Shankar, J. Blumoff, L. Frunzio, M. Mirrahimi, M. H. Devoret, and R. J. Schoelkopf, *Tracking photon jumps with repeated quantum non-demolition parity measurements,* Nature **511**, 444 (2014).

[40] J. Kelly, R. Barends, A. Fowler, A. Megrant, E. Jeffrey, T. White, D. Sank, J. Mutus, B. Campbell, Y. Chen, Z. Chen, B. Chiaro, A. Dunsworth, I.-C. Hoi, C. Neill, O. P. J. J, C. Quintana, P. Roushan, A. Vainsencher, J. Wenner, A. N. Cleland, and J. M. Martinis, *State preservation by repetitive error detection in a superconducting quantum circuit,* Nature **519**, 66 (2015).

[41] J. Cramer, N. Kalb, M. A. Rol, B. Hensen, M. S. Blok, M. Markham, D. J. Twitchen, R. Hanson, and T. H. Taminiau, *Repeated quantum error correction on a continuously encoded qubit by real-time feedback,* Nature communications **7**, 11526 (2016).

[42] N. Ofek, A. Petrenko, R. Heeres, P. Reinhold, Z. Leghtas, B. Vlastakis, Y. Liu, L. Frunzio, S. M. Girvin, L. Jiang, M. Mirrahimi, M. H. Devoret, and R. J. Schoelkopf, *Extending the lifetime of a quantum bit with error correction in superconducting circuits,* Nature **536**, 441 (2016).

[43] S. Rosenblum, P. Reinhold, M. Mirrahimi, L. Jiang, L. Frunzio, and R. J. Schoelkopf, *Fault-tolerant detection of a quantum error,* Science **20**, 266 (2018).

[44] V. Negnevitsky, M. Marinelli, K. K. Mehta, H.-Y. Lo, C. Flühmann, and J. P. Home, *Repeated multi-qubit readout and feedback with a mixed-species trapped-ion register,* Nature **563**, 527 (2018).

[45] L. Hu, Y. Ma, W. Cai, X. Mu, Y. Xu, W. Wang, Y. Wu, H. Wang, Y. P. Song, C.-L. Zou, S. M. Girvin, L.-M. Duan, and L. Sun, *Quantum error correction and universal gate set operation on a binomial bosonic logical qubit,* Nature Physics **15**, 503 (2019).

[46] C. K. Andersen, A. Remm, S. Lazar, S. Krinner, J. Heinsoo, J.-C. Besse, M. Gabureac, A. Wallraff, and C. Eichler, *Entanglement stabilization using ancilla-based parity detection and real-time feedback in superconducting circuits,* npj Quantum Information **5**, 69 (2019).

[47] C. C. Bultink, T. E. O'Brien, R. Vollmer, N. Muthusubramanian, M. W. Beekman, M. A. Rol, X. Fu, B. Tarasinski, V. Ostroukh, B. Varbanov, A. Bruno, and L. DiCarlo, *Protecting quantum entanglement from qubit errors and leakage via repetitive parity measurements,* arXiv:1905.12731 (2019).

[48] D. Ristè, L. C. G. Govia, B. Donovan, S. D. Fallek, W. D. Kalfus, M. Brink, T. Bronn, Nicholas, and T. A. Ohki, *Real-time decoding of stabilizer measurements in a bit-flip code,* arXiv:1911.12280 (2019).

[49] C. K. Andersen, A. Remm, S. Lazar, S. Krinner, N. Lacroix, G. J. Norris, M. Gabureac, C. Eichler, and A. Wallraff, *Repeated quantum error detection in a surface code,* arXiv:1912.09410 (2019).

[50] K. Fukui, A. Tomita, and A. Okamoto, *Analog quantum error correction with encoding a qubit into an oscillator,* Phys. Rev. Lett. **119**, 180507 (2017).

[51] C. Vuillot, H. Asasi, Y. Wang, L. P. Pryadko, and B. M. Terhal, *Quantum error correction with the toric Gottesman-Kitaev-Preskill codes,* Phys. Rev. A **99**, 032344 (2019).

[52] K. Noh, S. Girvin, and L. Jiang, *Encoding an oscillator into many oscillators,* arXiv:1903.12615 (2019).

[53] K. Noh and C. Chamberland, *Fault-tolerant bosonic quantum error correction with the surface–Gottesman-Kitaev-Preskill code,* Phys. Rev. A **101**, 012316 (2020).

[54] X. Xue, T. F. Watson, J. Helsen, D. R. Ward, D. E. Savage, M. G. Lagally, S. N. Coppersmith, M. A. Eriksson, S. Wehner, and L. M. K. Vandersypen, *Benchmarking gate fidelities in a* Si/SiGe *two-qubit device,* Phys. Rev. X **9**, 021011 (2019).

[55] C. T. Hann, S. S. Elder, C. S. Wang, K. Chou, R. J. Schoelkopf, and L. Jiang, *Robust readout of bosonic qubits in the dispersive coupling regime,* Phys. Rev. A **98**, 022305 (2018).

[56] J. Yoneda, K. Takeda, A. Noiri, T. Nakajima, S. Li, J. Kamioka, T. Kodera, and S. Tarucha, *Repetitive single electron spin readout in silicon,* arXiv preprint arXiv:1910.11963 (2019).

[57] J. Gambetta, W. A. Braff, A. Wallraff, S. M. Girvin, and R. J. Schoelkopf, *Protocols for optimal readout of qubits using a continuous quantum nondemolition measurement,* Phys. Rev. A **76**, 012325 (2007).

[58] A. H. Myerson, D. J. Szwer, S. C. Webster, D. T. C. Allcock, M. J. Curtis, G. Imreh, J. A. Sherman, D. N. Stacey, A. M. Steane, and D. M. Lucas, *High-fidelity readout of trapped-ion qubits,* Phys. Rev. Lett. **100**, 200502 (2008).

[59] T. P. Harty, D. T. C. Allcock, C. J. Ballance, L. Guidoni, H. A. Janacek, N. M. Linke, D. N. Stacey, and D. M. Lucas, *High-fidelity preparation, gates, memory, and readout of a trapped-ion quantum bit,* Phys. Rev. Lett. **113**, 220501 (2014).

[60] S. Gammelmark, K. Mølmer, W. Alt, T. Kampschulte, and D. Meschede, *Hidden markov model of atomic quantum jump dynamics in an optically probed cavity,* Phys. Rev. A **89**, 043839 (2014).

[61] S. Ng and M. Tsang, *Optimal signal processing for continuous qubit readout,* Phys. Rev. A **90**, 022325 (2014).

[62] B. D'Anjou, L. Kuret, L. Childress, and W. A. Coish, *Maximal adaptive-decision speedups in quantum-state readout,* Phys. Rev. X **6**, 011017 (2016).

[63] M. Möttönen, K. Y. Tan, K. W. Chan, F. A. Zwanenburg, W. H. Lim, C. C. Escott, J.-M. Pirkkalainen, A. Morello, C. Yang, J. A. van Donkelaar, A. D. C. Alves, D. N. Jamieson, L. C. L. Hollenberg, and A. S. Dzurak, *Probe and control of the reservoir density of states in single-electron devices,* Phys. Rev. B **81**, 161304(R) (2010).

7

QUANTUM LOGIC WITH SPIN QUBITS CROSSING THE SURFACE CODE THRESHOLD

High-fidelity control of quantum bits is paramount for the reliable execution of quantum algorithms and for achieving fault-tolerance, the ability to correct errors faster than they occur. The central requirement for fault-tolerance is expressed in terms of an error threshold. Whereas the actual threshold depends on many details, a common target is the ~ 1% error threshold of the well-known surface code. Reaching two-qubit gate fidelities above 99% has been a long-standing major goal for semiconductor spin qubits. These qubits are promising for scaling as they can leverage advanced semiconductor technology. Here we report a spin-based quantum processor in silicon with single- and two-qubit gate fidelities all above 99.5%, extracted from gate set tomography. The average single-qubit gate fidelities remain above 99% when including crosstalk and idling errors on the neighboring qubit. Utilizing this high-fidelity gate set, we execute the demanding task of calculating molecular ground state energies using a variational quantum eigensolver algorithm. Having surpassed the 99% barrier for the two-qubit gate fidelity, semiconductor qubits are well positioned on the path to fault-tolerance and to possible applications in the era of noisy intermediate-scale quantum (NISQ) devices.

This chapter has been published in Nature **601**, 343–347 (2022).

7.1. INTRODUCTION

Quantum computation involves the execution of a large number of elementary operations that take a qubit register through the steps of a quantum algorithm [1]. A major challenge is to implement these operations with sufficient accuracy to arrive at a reliable outcome, even in the presence of decoherence and other error sources. The higher the accuracy, or fidelity, of the operations, the higher the likelihood that near-term applications for quantum computers come in reach [2]. Furthermore, for most presently known algorithms, the number of operations that must be concatenated will unavoidably lead to excessive accumulation of errors, and these errors must be removed using quantum error correction [3]. Correcting quantum errors faster than they occur is possible when the error probability per operation is below a threshold, the fault-tolerance threshold. For the widely considered surface code, for instance, the fault-tolerance threshold is between 0.6% and 1%, under certain assumptions, albeit at the cost of a large redundancy in the number of physical qubits [4, 5].

In this work, using a precisely engineered two-qubit interaction Hamiltonian, we report the demonstration of single- and two-qubit gates with fidelities above 99.5%. We use gate set tomography not only to characterize the gates and to quantify the fidelity, but also to improve on the gate calibration. The high-fidelity gates allow us to compute the dissociation energy of molecular hydrogen with a variational quantum eigensolver algorithm, reaching an accuracy for the dissociation energy of around 20 milliHartree, limited by readout errors.

7.2. QUANTUM DOT DEVICE

We use a gate-defined double quantum dot in an isotopically enriched ^{28}Si/SiGe heterostructure (Fig. 7.1a) [6], with each dot occupied by one single electron. The spin states of the electrons serve as qubits. The spin states are measured with the help of a sensing quantum dot (SQD), which is capacitively coupled to the qubit dots [7]. A micromagnet on top of the device provides a magnetic field gradient enabling electric-dipole spin resonance (EDSR) [8], and separates the resonance frequencies of the qubits in the presence of an external magnetic field (~320 mT) to 11.993 GHz (Q1) and 11.890 GHz (Q2). Single-qubit X and Y gates are implemented by frequency-multiplexed microwave signals applied to gate MW, and virtual Z gates are implemented by a phase update of the reference frame [9]. The plunger gates (LP and RP) control the chemical potentials of the quantum dots.

The native two-qubit gate for spin qubits utilizes the exchange interaction [10, 11], originating from the wave-function overlap of electrons in neighbouring dots. This selectively shifts the energy of the anti-parallel spin states and thus allows for an electrically pulsed adiabatic CZ gate [12–14]. The barrier gate (B) controls the tunnel coupling between the dots, allowing to precisely tune the exchange coupling from < 100 kHz to 20 MHz. In order to minimize the sensitivity to charge noise, we activate the exchange coupling while avoiding a tilt in the double dot potential [15, 16] (Fig. 7.1a). This symmetric condition can be determined accurately by decoupled adiabatic exchange pulses inside a Ramsey sequence (Fig. 7.1c-d). The tunnel barrier is controlled by simultaneously pulsing gate B and compensating on LP and RP to avoid shifts of the electrochem-

ical potentials [15], constituting a virtual barrier gate. The detuning between quantum dots is controlled by additional offsets on the LP and RP pulses in opposite directions. As the decoupling pulses remove additional single-qubit phase accumulation from electron movement in the magnetic field gradient, the spin-up probability of Q1 results in a symmetric Chevron pattern, with the symmetry point at the center (Fig. 7.1d).

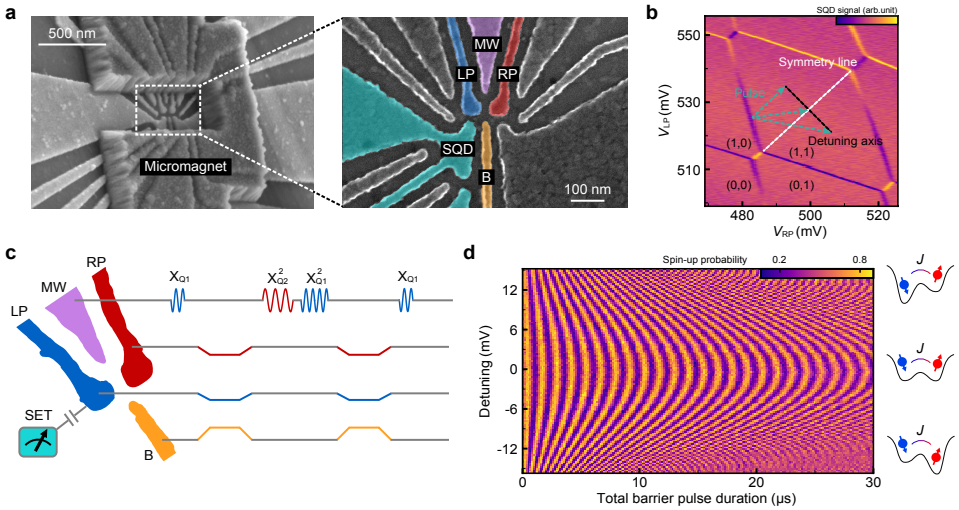

Fig. 7.1: Two-qubit device and symmetry operating point. a. Scanning electron microscope images of a similar device to that used here showing the quantum dot gate pattern and the micromagnet on top (the device used in the experiment has an additional screening gate above the fine gates [6]). **b.** Control paths for determining the symmetry operation point in the charge stability diagram. (M,N) represent the number of electrons in the dots underneath the tip of LP and RP respectively. **c.** Pulse sequence schematic of a decoupled controlled-phase operation interleaved in a Ramsey interference sequence on Q1. **d.** Spin-up probability of Q1 after the Ramsey sequence in **c**, as a function of the detuning in the double dot potential and the total duration of the barrier voltage pulses.

7.3. GATE SET TOMOGRAPHY AND SINGLE-QUBIT GATE FIDELITIES

Among the various quantum benchmarking techniques, quantum process tomography (QPT) is designed to reconstruct all details in a target process [1]. However, due to the susceptibility of QPT to state preparation and measurement (SPAM) errors, self-consistent benchmarking techniques such as gate set tomography (GST) [17] and alternative techniques such as randomized benchmarking (RB) [18] have been developed. Different than RB, GST inherits the advantage of QPT in that it reports the detailed process, which allows us to isolate Hamiltonian errors from stochastic errors and to correct for such errors in the control signals (7.7.2). In addition, GST accounts for gate-dependent errors. We benchmark the fidelities of a universal gate set using GST [17, 19] (Fig. 7.2a). The gate set we choose contains an idle gate (I), sequentially operated single-qubit $\pi/2$ rotations about the $\hat{x}$ and $\hat{y}$ axes for each qubit (X_{Q1}, Y_{Q1}, X_{Q2}, and Y_{Q2}),

and a two-qubit controlled-phase (CZ) gate. A total of 36 fiducial sequences containing $\{null, (X_{Qi})^{n=1,2,3}, Y_{Qj}{}^{n=1,3}\}$ on each qubit, where $null$ unlike the idle gate has no waiting time, are used to tomographically measure the two-qubit state. These fiducials are interleaved by germ sequences and their powers up to a sequence depth of 16. Germs are short sequences of gates taken from the universal gate set (see 7.7.7). They are repetitively executed to amplify different types of gate errors in the gate set, such that SPAM errors can be isolated. GST allows using a maximum-likelihood estimator to compute completely positive and trace preserving (CPTP) process matrices for each element of the gate set [1]. The gate fidelity can be calculated by comparing the measured process using the Pauli transfer matrix (PTM) $\mathcal{M}_{\text{exp}}$, with the ideal PTM $\mathcal{M}_{\text{ideal}}$, $F_{\text{gate}} = (\text{Tr}(\mathcal{M}_{\text{exp}}^{-1}\mathcal{M}_{\text{ideal}}) + d)/[d(d+1)]$, where d is the dimension of the Hilbert space. These process matrices provide a detailed error diagnosis of the gate set allowing for efficient feedback calibration (Fig. 7.2a) [20]. Analyzing the error generator $\mathcal{L} = \log(\mathcal{M}_{\text{exp}}\mathcal{M}_{\text{ideal}}^{-1})$ provides easy access to information. For example, coherent Hamiltonian errors can be isolated from incoherent stochastic errors, and single-qubit errors can be isolated from each other and from two-qubit errors [21].

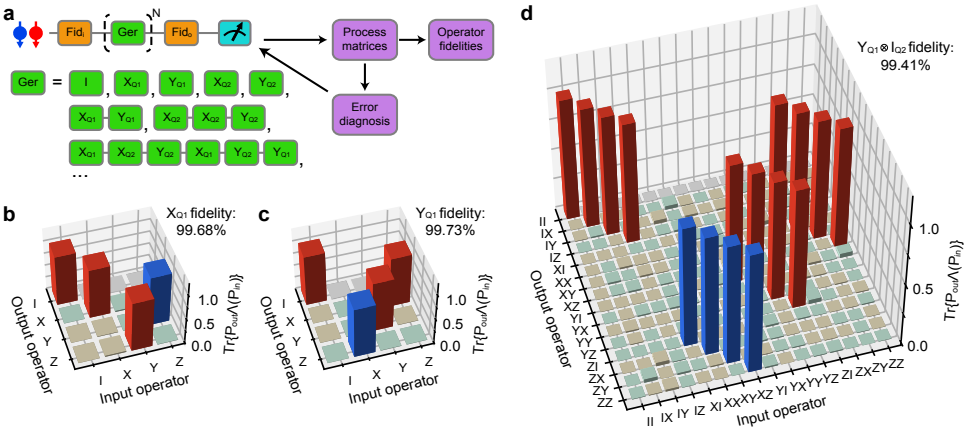

Fig. 7.2: Gate set tomography and single-qubit gate. a. Workflow of the GST experiment. Colored blocks show the input and output fiducial sequences (Fid_i and Fid_o, orange) and the germ sequences (green). A few examples of single-qubit germ sequences are listed. The outcome is used to adjust pulse parameters in the next run. **b-c.** PTMs of X_{Q1} and Y_{Q1} in the subspace of Q1. The red (blue) bars are theoretically +1 (-1), and are measured to be positive (negative). The brown (green) bars are theoretically 0 (0) but measured to be positive (negative). P_{in} and P_{out} are the input and output operators. **d.** Experimentally measured PTM of $Y_{Q1} \otimes I_{Q2}$ in the complete two-qubit space. The color code is the same as in **b-c**.

Figs. 7.2b-c show the reduced PTMs of X_{Q1} and Y_{Q1} operations in the Q1 subspace, and Fig. 7.2d shows the full PTM of Y_{Q1} in two-qubit space ($Y_{Q1} \otimes I_{Q2}$) containing additional errors from decoherence and crosstalk on Q2 while operating Q1 (see 7.7.7 for other PTMs), and from unintentional entanglement due to a residual exchange interaction. The average single-qubit gate fidelity is 99.72% in the single-qubit subspace (X_{Q1}: 99.68%; Y_{Q1}: 99.73%; X_{Q2}: 99.61%; Y_{Q2}: 99.87%, see the 7.7.7 for all error bars). A metric that is rarely reported is the single-qubit gate fidelity in the full two-qubit space, here 99.16% on average (see 7.7.7). These results highlight that single-qubit bench-

marking is not sufficient to identify all errors occurring during single-qubit operations. By analysing the error generators, we find that errors from uncorrelated dephasing of the idling qubit dominate the drop in single-qubit gate fidelity when characterized in the two-qubit space. Coherent microwave-induced phase shifts, the main source of crosstalk errors, have been corrected by applying a compensating phase gate on the idling qubit (7.7.2). The elimination of idling errors and other crosstalk errors from the microwave drive, such as through heating effects, will be a crucial step in improving the quality of the single-qubit operations further.

7.4. HIGH-FIDELITY TWO-QUBIT GATE

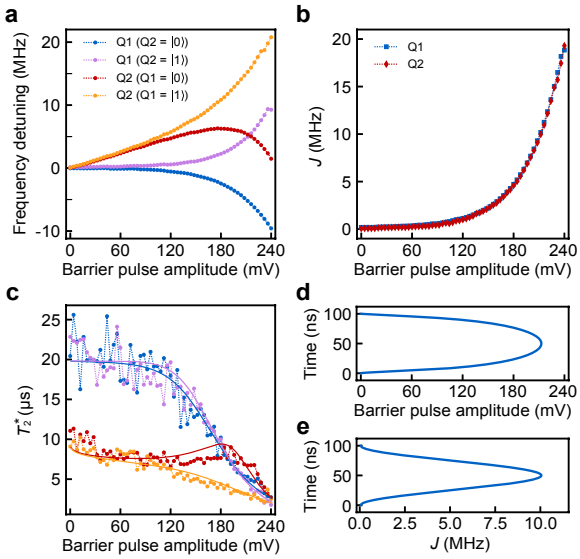

Fig. 7.3: Hamiltonian engineering of exchange interaction. a. Frequency detuning of each qubit conditional on the state of the other qubit as a function of barrier pulse amplitude. The horizontal axis shows the real voltage applied on gate B. **b.** Exchange strength as a function of barrier pulse amplitude. The data is extracted directly from **a**. **c.** T_2^* of each qubit conditional on the state of the other qubit as a function of barrier pulse amplitude (same color code as in **a**). Each data point is averaged for about 8 minutes. Fitting the T_2^* values to a quasistatic noise model (solid lines, see 7.7.4), the low-frequency amplitudes of the fluctuations are estimated as $\delta f_{Q1} = 11\,\text{kHz}$, $\delta f_{Q2} = 24\,\text{kHz}$, $\delta v_B = 0.4\,\text{mV}$. **d.** Shape of the barrier pulse, designed to achieve a high-fidelity CZ gate. **e.** The cosine-shaped J envelope seen by the qubits during the pulse shown in **d**.

For a high-fidelity adiabatic CZ gate, precise control of the exchange coupling, J, between the two qubits is required. Specifically, in order to avoid unintended state transitions due to non-adiabatic dynamics, we must be able to carefully shape the envelope of J. We characterize J over a wide range using a Ramsey sequence interleaved by a virtual barrier pulse with incremental amplitude v_B. Fig. 7.3a shows the measured frequency shift of each qubit as functions of the barrier pulse amplitude and the state of the other qubit. The exchange interaction is modeled to be exponentially dependent on the barrier pulse amplitude $J(v_B) \propto e^{\alpha v_B}$ [22, 23]. The micromagnet-induced single-qubit

frequency shifts are approximated by linear functions within the voltage window of the CZ gate in the numerical simulations. By fitting the measured data sets simultaneously to theoretical models (see 7.7.4), J can be extracted very precisely as the difference between the two conditional frequencies of each qubit [14, 24] (Fig. 7.3b).

The barrier pulse $v_B \propto \log\left(A_{v_B}(1-\cos(2\pi t/t_{\text{gate}}))/2\right)$ (Fig. 7.3d) compensates the exponential dependence such that $J \propto (1-\cos(2\pi t/t_{\text{gate}}))$ follows a cosine window function, which ensures good adiabaticity [25] (Fig. 7.3e). In addition, the virtual gates are calibrated such that the symmetric operation point is maintained for each barrier setting, minimizing the influence of charge noise via the double dot detuning. The most relevant remaining noise sources include charge noise affecting J through fluctuations in the virtual barrier gate δv_B, and fluctuating qubit frequencies $\delta f_{Q1}, \delta f_{Q2}$ from charge noise entering through artificial spin-orbit coupling from the micromagnet and residual nuclear spin noise coupling through the hyperfine interaction. By analysing the decay of the Ramsey oscillations at each transition frequency, individual dephasing times T_2^* can be extracted, and from there also δv_B, δf_{Q1} and δf_{Q2} (Fig. 7.3c).

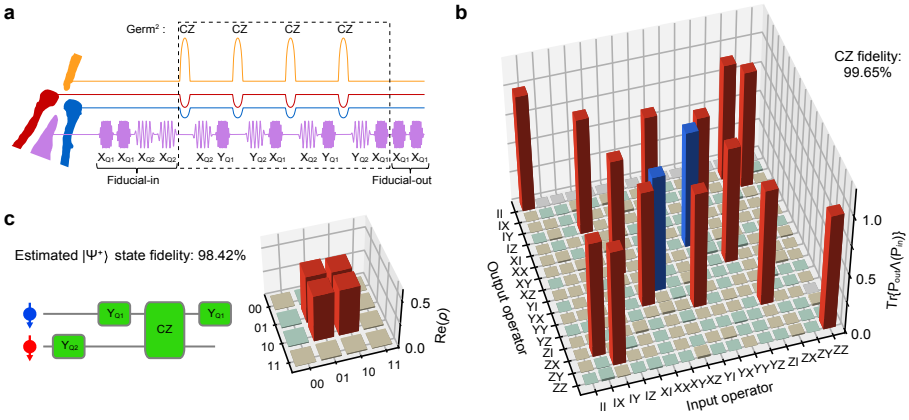

Fig. 7.4: High-fidelity two-qubit gate. a. A sequence of pulses generated by the AWGs in an example GST sequence. The purple waveforms show the in-phase component of X/Y gates. The CZ gate is indicated by the orange pulse on gate B with the blue and red compensation pulses on gate LP and gate RP. **b.** Experimentally determined PTM of a CZ gate. The color code is the same as in Fig. 7.2. **c** Left is the quantum circuit used to reconstruct the Bell state $|\Psi^+\rangle = (|01\rangle + |10\rangle)/\sqrt{2}$ based on the corresponding PTMs. Right is the real part of the reconstructed density matrix of the $|\Psi^+\rangle$ state. The color code is the same as in Fig.7.2 except that red (blue) bars here are theoretically +0.5 (-0.5).

Fig. 7.4a shows an example GST pulse sequence that contains twice in a row the germ $[\text{CZ}, X_{Q2}, Y_{Q1}, \text{CZ}, Y_{Q2}, X_{Q1}]$. The PTM of the CZ gate obtained from GST is shown in Fig. 7.4b. Using the detailed information from the error generator to fine tune the calibration parameters, we can achieve a CZ fidelity of $99.65 \pm 0.15\%$ (see 7.7.2). Error bars displayed here and elsewhere show the $2\sigma \approx 95\%$ confidence intervals computed using the Hessian of the loglikelihood function [26]. The CZ error generator reveals that at this point incoherent errors dominate. The virtual barrier gate technique used here efficiently suppresses crosstalk errors during two-qubit gates. Therefore, we expect the CZ fidelity to be mostly affected by dephasing errors of idling qubits in a larger space which

can be corrected for with decoupling pulses. From the obtained PTMs we can numerically estimate Bell state fidelities by multiplications of the PTMs necessary to construct the corresponding state, giving an estimate of 97.75% - 98.42%, neglecting SPAM errors, for the four Bell states (Fig. 7.4c and 7.7.7).

7.5. VARIATIONAL QUANTUM EIGENSOLVER

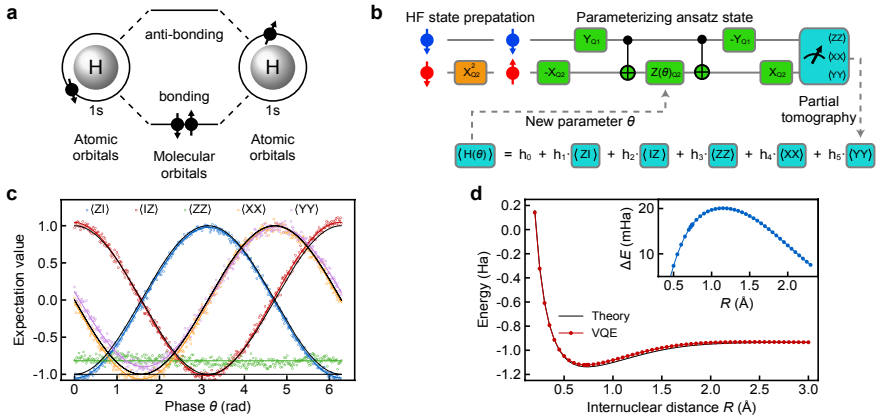

Fig. 7.5: Variational quantum eigensolver. a. Lowest two molecular orbitals of a H_2 molecule, formed by the $1s$ orbitals of two hydrogen atoms. **b.** The quantum circuit to implement the VQE algorithm for a H_2 molecule. The orange block prepares the HF initial state by flipping Q2. The circuit in green blocks creates the parametrized ansatz state. $-X_{Qi}$ and $-Y_{Qj}$ include virtual Z gates. CNOT gates are compiled as $[-Y_{Q2}, \text{CZ}, Y_{Q2}]$. To make use of the high-fidelity CZ gate, such compilation is preferred instead of using a single controlled-phase gate with incremental length for creating the parametrized ansatz state. **c.** Expectation values of the operators in the two-qubit Hamiltonian under BK transformation as a function of θ. Black solid lines show the predicted values. The colored solid lines are sinusoidal fits to the data (and a constant fit for the case of ZZ). **d.** Potential energy of the H_2 molecule at varying R. The VQE data is normalized to the theoretical energy at large R to directly compare the dissociation energy with the theoretical value. The inset shows the error in the normalized experimental data.

We next employ the high-fidelity gate set in the context of an actual application, in order to provide a quantitative benchmark for future work under realistic conditions. Specifically, we implement a variational quantum eigensolver (VQE) algorithm to compute the ground state energy of molecular hydrogen (H_2) (Fig. 7.5a). In a VQE algorithm, a quantum processor is utilized to implement a classically inefficient subroutine (see 7.7.8). The second quantized H_2 Hamiltonian can be mapped onto two qubits under the Bravyi-Kitaev (BK) transformation $H = h_0 II + h_1 ZI + h_2 IZ + h_3 ZZ + h_4 XX + h_5 YY$. Here I, X, Y and Z are Pauli operators, for example ZI is shorthand for $Z \otimes I$, and the coefficients h_0-h_5 are classically computable functions of the internuclear distance, R. Fig. 7.5b shows the schematic of the VQE algorithm and its circuit implementation for a H_2 molecule. The qubit is initialized in $|01\rangle$, which represents double-occupation of the lowest molecular orbital, corresponding to the Hartree-Fock ground state. A parametrized ansatz state is then prepared by considering single- and double-excitation, which after the BK transformation yields $\left|\psi(\theta)\right\rangle = e^{-i\theta XY}|01\rangle$, with θ the parameter to variationally optimize. By performing partial tomography on the ansatz state

with an initial guess θ_0, the expectation value of the Hamiltonian for $|\psi(\theta_0)\rangle$ can be calculated. A classical computer can efficiently compute the next guess θ_1 as the new input for the quantum computer. This loop is iterated until the result converges. For a H_2 molecule, there is only one parameter θ to optimize, thus a scan of the entire parameter range of 2π with finite samples is sufficient to interpolate the smoothly changing measured expectation values. This emulates a real variational algorithm where θ can be estimated to arbitrary precision by increasing the number of repetitions to suppress statistical fluctuations [27]. Fig. 7.5c shows the partial tomography result after normalization of the visibility window. The data demonstrates high-quality phase control in the quantum circuits. The deviations in the odd parity expectation values indicate correlations in the readout of the two qubits [28]. Fig. 7.5d shows the energy curves of the H_2 molecule from both theory [29] and the VQE experiment. We observe a minimum energy at around 0.72 Å, and an error of ~ 20 mHa at the theoretical bond length 0.7414 Å, mainly attributed to slow drift in the readout parameters. This accuracy matches the results obtained using superconducting and trapped ion qubits with comparable gate fidelities [27, 30].

7.6. CONCLUSION

The two-qubit gate with fidelity above 99.5% and single-qubit gate fidelities in the two-qubit gate space above 99% on average, place semiconductor spin qubit logic at the error threshold of the surface code. Recently, a two-qubit operation between nuclear spin qubits in silicon, mediated by an electron spin qubit, has been demonstrated to surpass 99% fidelity as well, further highlighting that semiconductor spin qubits offer precise two-qubit logic [31]. Independent studies have shown spin qubit readout with a fidelity above 98% in only a few μs [32], with further improvements underway [33]. Combining high-fidelity initialization, readout, and control into a demonstration of fault-tolerance poses several key challenges to be overcome. First, sufficiently large and reliable quantum dot arrays must be constructed, with good connectivity between the qubits. Second, the fidelities achieved in small-scale systems must be maintained across such larger systems, which will require reducing idling and crosstalk errors. The same advances will allow us to implement more sophisticated algorithms in the NISQ era, such as solving energies involving excited states of more complex molecules.

7.7. APPENDICES

7.7.1. MEASUREMENT SETUP

The measurement setup and device are similar to the one used in Ref. [6]. We summarize a few key points and all the differences here. The gates LP, RP, and B are connected to arbitrary waveform generators (AWGs, Tektronix 5014C) via coaxial cables. The position in the charge stability diagram of the quantum dots is controlled by voltage pulses applied on LP and RP. Linear combinations of the voltage pulses on B, LP and RP are used to control the exchange coupling between the two qubits at the symmetry point. The compensation coefficients are: $v_{LP}/v_B = -0.081$, $v_{RP}/v_B = -0.104$. A vector signal generator (VSG, Keysight E8267D) is connected to gate MW and sends frequency-multiplexed microwave bursts (not necessarily time-multiplexed) to implement electric-dipole spin res-

onance (EDSR). The VSG has two I/Q input channels, receiving I/Q modulation pulses from two channels of an AWG. I/Q modulation is used to control the frequency, phase, and length of the microwave bursts. The current signal of the sensing quantum dot is converted to a voltage signal and recorded by a digitizer card (Spectrum M4i.44), and then converted into 0 or 1 by comparing it to a threshold value.

Two differences between the present setup and the one in Ref. [6] are that 1) the programmable mechanical switch is configured such that gate MW is always connected to the VSG, and not to the cryo-CMOS control chip; 2) a second AWG of the same model is connected to gate B with its clock synchronized with the first AWG.

7.7.2. GATE CALIBRATION

In the gate set used in this work, $\{I, X_{Q1}, Y_{Q1}, X_{Q2}, Y_{Q2}, \mathrm{CZ}\}$, the duration of the I gate and the CZ gate are set to 100 ns, and we calibrate and keep the amplitudes of the single-qubit drives fixed and in the linear response regime, where Rabi frequency is linearly dependent on the driving amplitude. The envelope of the single-qubit gates are shaped following a "tukey" window, as it allows adiabatic single-qubit gates with relatively small amplitudes, thus avoids distortion caused by nonlinear response. The general tukey window of length t_p is given by

$$W(t,r) = \begin{cases} \frac{1}{2}\left[1-\cos\left(\frac{2\pi t}{r t_p}\right)\right] & 0 \le t \le \frac{r t_p}{2} \\ 1 & \frac{r t_p}{2} < t < t_p - \frac{r t_p}{2} \\ \frac{1}{2}\left[1-\cos\left(\frac{2\pi (t_p - t)}{r t_p}\right)\right] & t_p - \frac{r t_p}{2} \le t \le t_p, \end{cases} \tag{7.1}$$

where $r = 0.5$ for our pulses. Apart from these fixed parameters, there are 11 free parameters that must be calibrated: single-qubit frequencies f_{Q1} and f_{Q2}, burst lengths for single-qubit gates t_{XY1} and t_{XY2}, phase shifts caused by single-qubit gates on the addressed qubit itself ϕ_{11} and ϕ_{22}, phase shifts caused by single-qubit gates on the unaddressed "victim qubit" ϕ_{12} and ϕ_{21} (ϕ_{12} is the phase shift on Q1 induced by a gate on Q2 and similar for ϕ_{21}), the peak amplitude of the CZ gate A_{v_B}, and phase shifts caused by the gate voltage pulses used for CZ gate on the qubits θ_1 and θ_2 (in addition, we absorb into θ_1 and θ_2 the 90 degree phase shifts needed to transform $\mathrm{diag}(1, i, i, 1)$ into $\mathrm{diag}(1, 1, 1, -1)$).

For single-qubit gates, f_{Q1} and f_{Q2} are calibrated by standard Ramsey sequences, which are automatically executed every two hours, at the beginning and the middle (after 100 times average of each sequence) of the GST experiment. The EDSR burst times t_{XY1} and t_{XY2} are initially calibrated by an AllXY calibration protocol [34]. The phases ϕ_{11}, ϕ_{12}, ϕ_{21}, and ϕ_{22} are initially calibrated by measuring the phase shift of the victim qubit (Q1 for ϕ_{11} and ϕ_{21}; Q2 for ϕ_{22} and ϕ_{12}) in a Ramsey sequence interleaved by a pair of $[X_{Qi}, -X_{Qi}]$ gates on the addressed qubit (Q1 for ϕ_{11} and ϕ_{12}; Q2 for ϕ_{22} and ϕ_{21}) (see 7.7.2).

The optimal pulse design presented in Fig. 7.3 gives a rough guidance of the pulse amplitude A_{v_B}. In a more precise calibration of the CZ gate, an optional π-rotation is applied to the control qubit (e.g. Q1) to prepare it into the $|0\rangle$ or $|1\rangle$ state, followed by a Ramsey sequence on the target qubit (Q2) interleaved by an exchange pulse. The amplitude is precisely tuned to bring Q2 completely out of phase (by 180 degree) between the two

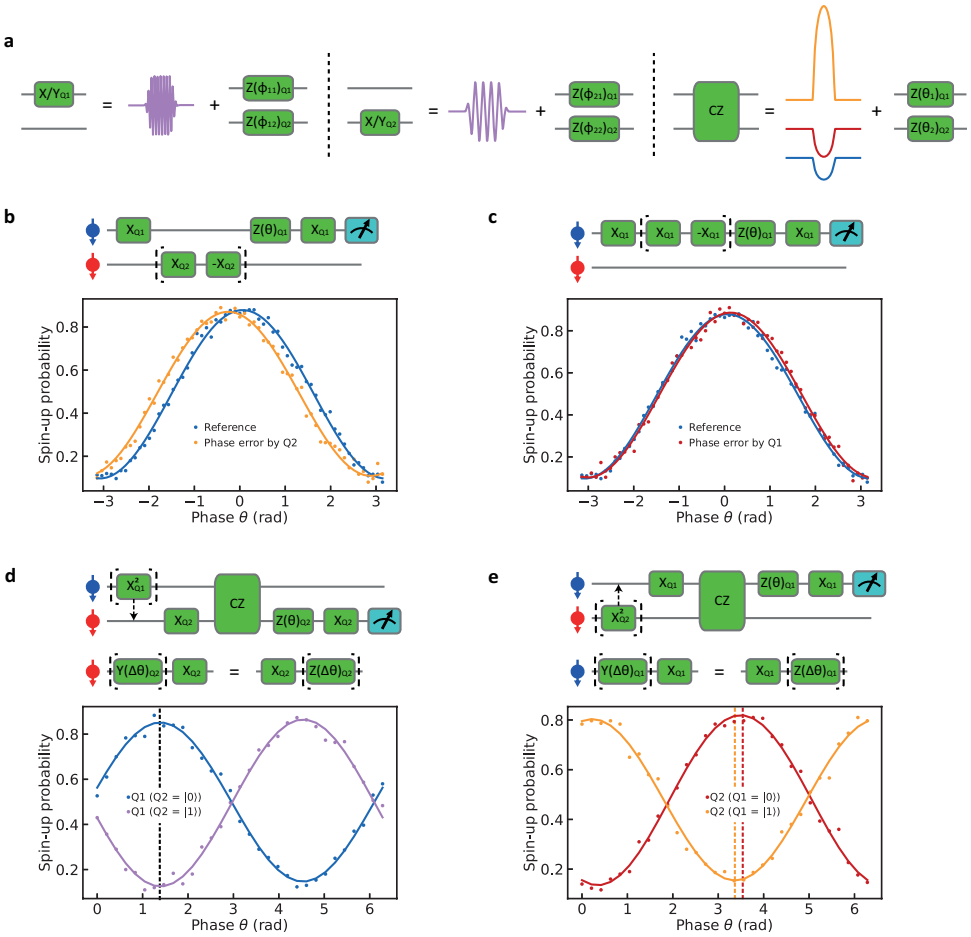

Fig. 7.6: Initial gate calibrations. a. Decomposition of single- and two-qubit gates. After each microwave burst for single-qubit rotations, a corresponding phase correction is applied to each qubit. The CZ gate is implemented by a barrier voltage pulse on gate B (orange) and negative compensation pulses on gates LP (blue) and RP (red), with the same shape as the barrier pulse. Single-qubit phase corrections are then applied on each qubit to compensate the frequency detuning induced by electron movement in the magnetic field gradient. **b-c.** Calibration of phase corrections on Q1 induced by a single-qubit gate applied on Q2 (ϕ_{21}, **b**) and on Q1 (ϕ_{11}, **c**). A relative phase shift, $2\phi_{21}$ ($2\phi_{11}$), is determined by interleaving the target gate (a $\pi/2$ rotation) and its inverse (a $-\pi/2$ rotation) on Q2 (Q1) in a Ramsey interference sequence. **d-e.** Calibration of phase corrections on each qubit after the CZ gate, using Q1 (**d**) and Q2 (**e**) as the control-qubit respectively. When the amplitude of the barrier pulse is perfectly calibrated, the two curves in each experiment should be out of phase by 180 degree. However, when the barrier pulse amplitude is calibrated such that one of the two experiments shows a 180 degree phase difference (**d**), the phase difference in the other calibration experiment always deviates by a few degrees. One possible explanation is that the optional π rotation applied to the control-qubit induces a small off-resonance rotation on the other qubit, causing an additional phase on the target qubit to appear in the measurement due to the commutation relation of the Pauli operators.

measurements (see 7.7.2). The phase θ_2 is determined such that the phase of Q2 changes by zero (π) when Q1 is in the state $|0\rangle$ ($|1\rangle$), corresponding to the CZ = diag$(1,1,1,-1)$ in the standard basis. The same measurement is then performed again with the Q2 as the control qubit and Q1 as the target qubit to determine θ_1 [14].

In such a "conventional" calibration procedure of the CZ gate, we notice that the two qubits experience different conditional phases (see 7.7.2). We believe that this effect is caused by off-resonant driving from the optional π-rotation on the control qubit (Fig. 7.6). Similar effects can also affect the calibration of the phase crosstalk from single-qubit gates.

This motivates us to use the results from GST as feedback to adjust the gate parameters (Fig. 7.7). The error generators not only describe the total errors of the gates, but also distinguish Hamiltonian errors (coherent errors) from stochastic errors (incoherent errors). We use the information on 7 different Hamiltonian errors (IX, IY, XI, YI, ZI, IZ and ZZ) of each gate, to correct all 11 gate parameters (see 7.7.2), except f_{Q1} and f_{Q2}, for which calibrations using standard Ramsey sequences are sufficient. For single-qubit gates, t_{XY1} and t_{XY2} are adjusted according to the IX, IY, XI and YI errors. The phases ϕ_{11}, ϕ_{12}, ϕ_{21}, and ϕ_{22} are adjusted according to the ZI and IZ errors. For the CZ gate, θ_1 and θ_2 are adjusted according to the ZI and IZ errors, and A_{v_B} is adjusted according to the ZZ error. The adjusted gates are then used in a new GST experiment.

7.7.3. THEORETICAL MODEL

In this section we describe the theoretical model used for the fitting, the pulse optimization, and the numerical simulations. The dynamics of two electron spins in the $(1,1)$ charge configuration can be well-described by an extended Heisenberg model [10]

$$H = g\mu_B \vec{B}_1 \cdot \vec{S}_1 + g\mu_B \vec{B}_2 \cdot \vec{S}_2 + hJ(\vec{S}_1 \cdot \vec{S}_2 - \frac{1}{4}), \tag{7.2}$$

with $\vec{S}_j = (X_j, Y_j, Z_j)^T/2$, where X_j, Y_j, Z_j are the single-qubit Pauli-matrices acting on spin $j = 1,2$, μ_B the Bohr's magneton, $g \approx 2$ the g-factor in silicon, and h is the Planck constant. The first and second term describe the interaction of the electron spin in dot 1 and dot 2 with the magnetic fields $\vec{B}_j = (B_{x,j}, 0, B_{z,j})^T$ originating from the externally applied field and the micromagnet. The transverse components $B_{x,j}$ induce spin-flips, thus, single-qubit gates if modulated resonantly via EDSR. For later convenience we define the resonance frequencies by $hf_{Q1} = g\mu_B B_{z,1}$ and $hf_{Q2} = g\mu_B B_{z,2}$, and the energy difference between the qubits $\Delta E_z = g\mu_B(B_{z,2} - B_{z,1})$. The last term in the Hamiltonian of Eq. (7.2) describes the exchange interaction J between the spins in neighboring dots. The exchange interaction originates from the overlap of the wave-functions through virtual tunneling events and is in general a non-linear function of the applied barrier voltage v_B. We note that v_B determines the compensation pulses on LP and RP for virtual barrier control. We model J as an exponential function [22, 23]

$$J(v_B) = J_{\text{res}} e^{2\alpha v_B}, \tag{7.3}$$

where $J_{\text{res}} \approx 20-100$ kHz is the residual exchange interaction during idle and single-qubit operations and α is the lever arm. In general the magnetic fields $\vec{B}_j$ depend on the exact position of the electron. We include this in our model $B_{z,j} \rightarrow B_{z,j}(v_B) = B_{z,j}(0) + \beta_j v_B^{\gamma}$,

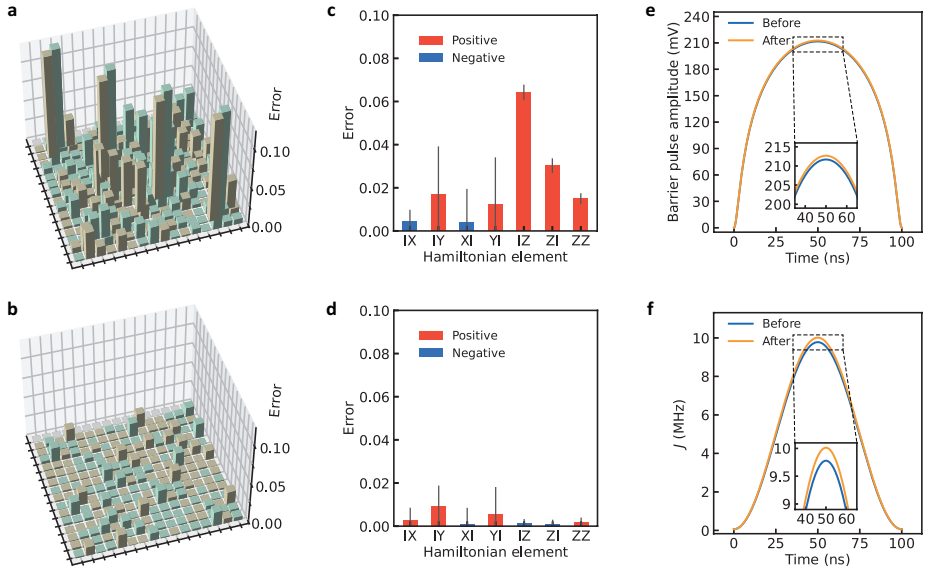

Fig. 7.7: Pulse optimization. a-b. Full error generators for (**a**) a CZ gate calibrated by conventional Ramsey sequences and (**b**) after improving the calibration using the information extracted from **a**, resulting in fidelities of 97.86% and 99.65%, respectively. **c-d.** Seven Hamiltonian errors (IX, IY, XI, YI, IZ, ZI and ZZ) extracted from the error generators shown in **a** (**c**) and **b** (**d**). Due to the crosstalk-induced additional phases shown in 7.7.2, errors IZ, ZI and ZZ occur systematically in conventional calibrations. Error bars indicate the 2σ confidence intervals computed using the Hessian of the loglikelihood function. **e-f.** Shapes of the barrier pulses (**e**) and their corresponding J envelopes (**f**) for a CZ gate before and after being corrected by GST. Since the Hamiltonian to generate a CZ gate is $H = (II + IZ + ZI - ZZ)/2$, the positive ZZ error shown in **c** is corrected by increasing the amplitude of the pulse. The IZ and ZI errors are corrected by decreasing the phase shifts θ_1 and θ_2 after the CZ gate. Hamiltonian errors in single-qubit gates are corrected similarly. The presented results in **b** and **d** are achieved in four loops of correction, with each loop correcting the parameters by ~ 70% of the measured deviation.

where β_j accounts for the impact of the barrier voltage on the resonance frequency of qubit j. The transition energies described in the main text are now given by diagonalizing Hamiltonian from Eq. (7.2) and computing the energy difference between the eigenstates corresponding to the computational basis states $\{|00\rangle, |01\rangle, |10\rangle, |11\rangle\}$ [35]. We have

$$hf_{\mathrm{Q1\ (Q2=\,|0\rangle)}} = \mathcal{E}(|10\rangle) - \mathcal{E}(|00\rangle), \tag{7.4}$$

$$hf_{\mathrm{Q1\ (Q2=\,|1\rangle)}} = \mathcal{E}(|11\rangle) - \mathcal{E}(|01\rangle), \tag{7.5}$$

$$hf_{\mathrm{Q2\ (Q1=\,|0\rangle)}} = \mathcal{E}(|01\rangle) - \mathcal{E}(|00\rangle), \tag{7.6}$$

$$hf_{\mathrm{Q2\ (Q1=\,|1\rangle)}} = \mathcal{E}(|11\rangle) - \mathcal{E}(|10\rangle), \tag{7.7}$$

where $\mathcal{E}(|\xi\rangle)$ denotes the eigenenergy of eigenstate $|\xi\rangle$ and $|0\rangle = |\downarrow\rangle$ is defined by the magnetic field direction.

In the presence of noise, qubits start to lose information. In silicon, charge noise and nuclear noise are the dominating noise sources. In the absence of two-qubit coupling and correlated charge noise, both qubits decohere largely independently of each other, giving rise to a decoherence time set by the interaction with the nuclear spins and charge noise coupling to the qubit via intrinsic and artificial (via the inhomogeneous magnetic field) spin-orbit interaction. We describe this effect by $f_{Q1} \to f_{Q1} + \delta f_{Q1}$ and $f_{Q2} \to f_{Q2} + \delta f_{Q2}$, where δf_{Q1} and δf_{Q2} are the single-qubit frequency fluctuations. Charge noise additionally can affect both qubits via correlated frequency shifts and the exchange interaction through the barrier voltage, which we model as $v_B \to v_B + \delta v_B$. In the presence of finite exchange coupling one can define four distinct pure dephasing times, each corresponding to the dephasing of a single qubit with the other qubit in a specific basis state. In a quasistatic approximation the four dephasing times are then given by

$$T_2^\star(\mathrm{Q1\ (Q2=\,|0\rangle)}) = \frac{1}{\sqrt{2}\pi\sqrt{\left[\frac{d\left(hf_{\mathrm{Q1\ (Q2=\,|0\rangle)}}\right)}{dv_B}\right]^2\delta v_B^2 + \left[\frac{d\left(hf_{\mathrm{Q1\ (Q2=\,|0\rangle)}}\right)}{dhf_{Q1}}\right]^2\delta f_{Q1}^2 + \left[\frac{d\left(hf_{\mathrm{Q1\ (Q2=\,|0\rangle)}}\right)}{dhf_{Q2}}\right]^2\delta f_{Q2}^2}}, \tag{7.8}$$

$$T_2^\star(\mathrm{Q1\ (Q2=\,|1\rangle)}) = \frac{1}{\sqrt{2}\pi\sqrt{\left[\frac{d\left(hf_{\mathrm{Q1\ (Q2=\,|1\rangle)}}\right)}{dv_B}\right]^2\delta v_B^2 + \left[\frac{d\left(hf_{\mathrm{Q1\ (Q2=\,|1\rangle)}}\right)}{dhf_{Q1}}\right]^2\delta f_{Q1}^2 + \left[\frac{d\left(hf_{\mathrm{Q1\ (Q2=\,|1\rangle)}}\right)}{dhf_{Q2}}\right]^2\delta f_{Q2}^2}}, \tag{7.9}$$

$$T_2^\star(\mathrm{Q2\ (Q1=\,|0\rangle)}) = \frac{1}{\sqrt{2}\pi\sqrt{\left[\frac{d\left(hf_{\mathrm{Q2\ (Q1=\,|0\rangle)}}\right)}{dv_B}\right]^2\delta v_B^2 + \left[\frac{d\left(hf_{\mathrm{Q2\ (Q1=\,|0\rangle)}}\right)}{dhf_{Q1}}\right]^2\delta f_{Q1}^2 + \left[\frac{d\left(hf_{\mathrm{Q2\ (Q1=\,|0\rangle)}}\right)}{dhf_{Q2}}\right]^2\delta f_{Q2}^2}}, \tag{7.10}$$

$$T_2^\star(\mathrm{Q2\ (Q1=\,|1\rangle)}) = \frac{1}{\sqrt{2}\pi\sqrt{\left[\frac{d\left(hf_{\mathrm{Q2\ (Q1=\,|1\rangle)}}\right)}{dv_B}\right]^2\delta v_B^2 + \left[\frac{d\left(hf_{\mathrm{Q2\ (Q1=\,|1\rangle)}}\right)}{dhf_{Q1}}\right]^2\delta f_{Q1}^2 + \left[\frac{d\left(hf_{\mathrm{Q2\ (Q1=\,|1\rangle)}}\right)}{dhf_{Q2}}\right]^2\delta f_{Q2}^2}}. \tag{7.11}$$

7.7.4. FITTING QUBIT FREQUENCIES AND DEPHASING TIMES

The transition energies Eqs. (7.4)-(7.7) are fitted simultaneously to the measured results from the Ramsey experiment (see Fig. 7.3a). For the fitting we use the `NonLinearModelFit` function from the software Mathematica with the least square method. The best fits yield the following parameters $\alpha = 12.1 \pm 0.05\,\mathrm{V}^{-1}$, $\beta_1 = -2.91 \pm 0.11\,\mathrm{MHz/V}^{\gamma}$, $\beta_2 = 67.2 \pm 0.63\,\mathrm{MHz/V}^{\gamma}$, and $\gamma = 1.20 \pm 0.01$, and $J_{\mathrm{res}} = 58.8 \pm 1.8\,\mathrm{kHz}$.

The dephasing times Eqs. (7.8)-(7.11) are fitted simultaneously to the measured results from the Ramsey experiment (see Fig. 7.3c) using the same method. The best fits yield the following parameters $\delta\upsilon_B = 0.40 \pm 0.01\,\mathrm{mV}$, $\delta f_{Q1} = 11 \pm 0.1\,\mathrm{kHz}$, and $\delta f_{Q2} = 24 \pm 0.7\,\mathrm{kHz}$.

7.7.5. NUMERICAL SIMULATIONS

For all numerical simulations, we solve the time-dependent Schrödinger equation

$$i\hbar \frac{d}{dt}\big|\psi(t)\big\rangle = H\big|\psi(t)\big\rangle \tag{7.12}$$

and iteratively compute the unitary propagator according to

$$U(t+\Delta t) = e^{-\frac{i}{\hbar}H(t+\Delta t)}U(t), \tag{7.13}$$

where $\hbar = h/(2\pi)$ is the reduced Planck constant. Here, $H(t+\Delta t)$ is discretized into N segments of length Δt such that $H(t)$ is constant in the time-interval $[t, t+\Delta t]$. All simulations are performed in the rotating frame of the external magnetic field $(B_{z,1} + B_{z,2})/2$ and neglecting the counter-rotating terms, making the so-called rotating wave approximation (RWA). This allows us to chose $\Delta t = 10\,\mathrm{ps}$ as a sufficiently small time step.

For the noise simulations, we included classical fluctuations of $f_{Q1} \to f_{Q1} + \delta f_{Q1}$, $f_{Q2} \to f_{Q2} + \delta f_{Q2}$, and $\upsilon_B \to \upsilon_B + \delta\upsilon_B$. We assume the noise coupling to the resonance frequencies δf_{Q1} and δf_{Q2} to be quasistatic and assume $1/f$ noise for υ_B which we describe by its spectral density $S_{\upsilon_B}(\omega) = \delta\upsilon_B/\omega$, where ω is the angular frequency. To compute time traces of the fluctuation we use the approach introduced in Refs. [36, 37] to generate time-correlated time traces. The fluctuations are discretized into N segments with time Δt such that $\delta\upsilon_B(t)$ is constant in the time interval $[t, t+\Delta t)$, with the same Δt as above. Consequently, fluctuations which are faster than $f_{\max} = \frac{1}{\Delta t}$ are truncated.

7.7.6. CZ GATE

We realize a universal CZ = diag$(1,1,1,-1)$ gate by adiabatically pulsing the exchange interaction using a carefully designed pulse shape. Starting from Eq. (7.2), the full dynamics can be projected on the odd-parity space spanned by $|01\rangle$ and $|10\rangle$. The entangling exchange gate is reduced in this subspace to a global phase shift thus the goal is to minimize any dynamics inside the subspace. Introducing a new set of Pauli operators in this subspace $\sigma_x = |01\rangle\langle 10| + |10\rangle\langle 01|$, $\sigma_y = -i\,|01\rangle\langle 10| + i\,|10\rangle\langle 01|$, and $\sigma_z = |01\rangle\langle 01| - |10\rangle\langle 10|$, we find

$$H_{\mathrm{sub}}(t) = \frac{1}{2}\big(-hJ(\upsilon_B(t)) + \Delta E_z\,\sigma_z + hJ(\upsilon_B(t))\,\sigma_x\big). \tag{7.14}$$

In order to investigate the adiabatic behaviour, it is convenient to switch into the adiabatic frame defined by $U_{\text{ad}} = e^{-\frac{i}{2}\tan^{-1}\left(\frac{hJ(v_B(t))}{\Delta E_z}\right)\sigma_y}$. The Hamiltonian accordingly transforms as

$$H_{\text{ad}} = U_{\text{ad}}^{\dagger}(t)H_{\text{sub}}(t)U_{\text{ad}}(t) - i\hbar U_{\text{ad}}^{\dagger}(t)\dot{U}_{\text{ad}}(t) \tag{7.15}$$

$$\approx \frac{1}{2}\Big(-hJ(v_B(t)) + \Delta E_z\sigma_z - \frac{h^2\dot{J}}{2\pi\Delta E_z}\sigma_y\Big), \tag{7.16}$$

where the first term is unaffected and describes the global phase accumulation due to the exchange interaction, the second term describes the single-qubit phase accumulations, and the last term $f(t) = h^2\dot{J}/(4\pi\Delta E_z)$ describes the diabatic deviation proportional to the derivative of the exchange pulse. From Eq. (7.15) to Eq. (7.16) we assumed a constant $\Delta E_z(t) \approx \Delta E_z$, and $hJ(t) \ll \Delta E_z$. The transition probability from state $|\uparrow\downarrow\rangle$ to $|\downarrow\uparrow\rangle$ using a pulse of length t_p is then given by [25]

$$P_{|\uparrow\downarrow\rangle\to|\downarrow\uparrow\rangle} \approx \left|\int_0^{t_p} f(t)e^{-\frac{i}{\hbar}\Delta E_z t}\,dt\right|^2 \tag{7.17}$$

$$\propto S_{\text{s}}\big(f(t)\big). \tag{7.18}$$

From the first to the second line we identify the integral by the (short time-scale) Fourier transform, allowing us to describe the spin-flip error probability by the energy spectral density (ESD) S_{s} of the input signal $f(t)$. Minimizing such errors is therefore identical to minimizing the ESD of a pulse, a well-known and solved problem from classical signal processing and statistics. Optimal shapes are commonly referred to as window functions $W(t)$ due to their property to restrict the spectral resolution of signals. A high-fidelity exchange pulse is consequently given by $J(0) = J(t_p)$ and

$$\int_0^{t_p} dt\, J(v_B(t)) = 1/4, \tag{7.19}$$

while setting $J(t) = A_{v_B}W(t)J_{\text{res}}$ [25], with a scaling factor A_{v_B} that is to be determined. In this work, we have chosen the cosine window

$$W(t) = \frac{1}{2}\left[1 - \cos\left(\frac{2\pi t}{t_p}\right)\right], \tag{7.20}$$

from signal processing which has a high spectral resolution. The amplitude A_{v_B} follows from condition Eq. (7.19). For a pulse length of $t_p = 100\,\text{ns}$ and a cosine pulse shape we find $A_{v_B}J_{\text{res}} = 10.06\,\text{MHz}$. As explained in the main text, due to the exponential voltage-exchange relation the target pulse shape for J(t) must be converted to a barrier gate pulse, following [38]

$$v_B(t) = \frac{1}{2\alpha}\log\big(A_{v_B}W(t)\big). \tag{7.21}$$

Our numerical simulations predict an average gate infidelity $1 - F_{\text{gate}} < 10^{-6}$ without noise and $1 - F = 0.22 \times 10^{-3}$ with the inclusion of noise through the fluctuations δf_{Q1}, δf_{Q2}, and δv_B discussed in section 7.7.5. The measured PTMs reveal significantly higher rates of incoherent errors, which we attribute to drifts in the barrier voltage on a timescale much longer than the timescale on which δf_{Q1}, δf_{Q2}, and δv_B were determined.

7.7.7. GATE SET TOMOGRAPHY ANALYSIS

We designed a gate set tomography (GST) experiment using the gate set $\{I,\ X_{Q1},\ Y_{Q1},\ X_{Q2},\ Y_{Q2},\ \mathrm{CZ}\}$, where I is a 100 ns idle gate, X_{Q1} (Y_{Q1}) and X_{Q2} (Y_{Q2}) are single qubit $\pi/2$ gates with rotation axis $\hat{x}$ ($\hat{y}$) on Q1 and Q2, with durations of 150 ns and 200 ns respectively, and $\mathrm{CZ} = \mathrm{diag}(1,1,1,-1)$. A classic two-qubit GST experiment consists of a set of germs designed to amplify all types of error in the gate set when repeated, and a set of 36 fiducials composed by the 11 elementary operations $\{$*null*, X_{Q1}, $X_{Q1}X_{Q1}$, $X_{Q1}X_{Q1}X_{Q1}$, Y_{Q1}, $Y_{Q1}Y_{Q1}Y_{Q1}$, X_{Q2}, $X_{Q2}X_{Q2}$, $X_{Q2}X_{Q2}X_{Q2}$, Y_{Q2}, $Y_{Q2}Y_{Q2}Y_{Q2}\}$ required to do quantum process tomography of the germs [39]. We use a set of 16 germs $\{I,\ X_{Q1},\ Y_{Q1},\ X_{Q2},\ Y_{Q2},\ \mathrm{CZ},\ X_{Q1}Y_{Q1},\ X_{Q2}Y_{Q2},\ X_{Q1}X_{Q1}Y_{Q1},\ X_{Q2}X_{Q2}Y_{Q2},\ X_{Q2}Y_{Q2}\mathrm{CZ},\ \mathrm{CZ}X_{Q2}X_{Q1}X_{Q1},\ X_{Q1}X_{Q2}Y_{Q2}X_{Q1}Y_{Q2}Y_{Q1},\ X_{Q1}Y_{Q2}X_{Q2}Y_{Q1}X_{Q2}X_{Q2},\ \mathrm{CZ}X_{Q2}Y_{Q1}\mathrm{CZ}Y_{Q2}X_{Q1},\ Y_{Q1}X_{Q1}Y_{Q2}X_{Q1}$-$X_{Q2}X_{Q1}Y_{Q1}Y_{Q2}\}$ [26]. Note, that the *null* gate is the instruction for doing nothing in zero time, different from the idle gate. Simple errors such as errors in the rotation angle of a particular gate can be amplified by simply repeating the same gate. More complicated errors such as tilts in rotation axes can only be amplified by a combination of different gates. The germs and fiducials are then compiled into GST sequences such that each sequence consists of two fiducials interleaved by a single germ or power of germs (as illustrated in Fig. 7.2a of the main text) [26]. The GST sequences are classified by their germ powers into lengths $L = 1,2,4,8,16\cdots$, where a sequence of length n consists of n gates plus the fiducial gates. We note that the sequences used in GST are shorter than the sequences involved in other methods to self-consistently estimate the gate performance, such as randomized benchmarking. As a result, GST suffers less from drift in qubit frequencies and readout windows induced by long sequences of microwave bursts.

After the execution of all sequences a maximum-likelihood estimation (MLE) is performed to estimate the process matrices of each gate in the gate set and the SPAM probabilities. We use the open source `pyGSTi` python package [40, 41] to perform the MLE, as well as to design an optimized GST experiment by eliminating redundant circuits, and to provide statistical error bars by computing all involved Hessians. The circuit optimization allows us to perform GST with a maximum sequence length $L_{\max} = 16$ using 1685 different sequences in total. The `pyGSTi` package quantifies the Markovian-model violation of the experimental data counting the number of standard deviations exceeding their expectation values under the χ^2 hypothesis [41]. This model violation is internally translated into a more accessible goodness ratio from $0-5$ with 5 being the best [40], where we get a 4 out of 5 rating indicating remarkably small deviations from expected results. The total number of standard deviations exceeding the expected results for each L, as well as the contribution of each sequence to this number, can be found in the `pyGSTi` report, along with the supporting data.

From the gate set tomography experiment, we have extracted the Pauli transfer matrix (PTM) $\mathcal{M}_{\mathrm{exp}}$ describing each gate in our gate set $\{I, X_{Q1}, Y_{Q1}, X_{Q2}, Y_{Q2}, \mathrm{CZ}\}$ (Fig. 7.8). The PTM is isomorphically related to the conventionally used χ-matrix describing a quantum process. The experimentally measured PTMs can be used to predict the fidelities of quantum circuits (Fig. 7.9). A completely positive trace-preserving (CPTP) two-qubit PTM has 240 parameters describing the process. To get insight in the errors of the gates in the experiment, we first compute the error in the PTM given by $E = \mathcal{M}_{\mathrm{exp}}\mathcal{M}_{\mathrm{ideal}}^{-1}$, where we have adapted the convention to add the error after the ideal gate. The average

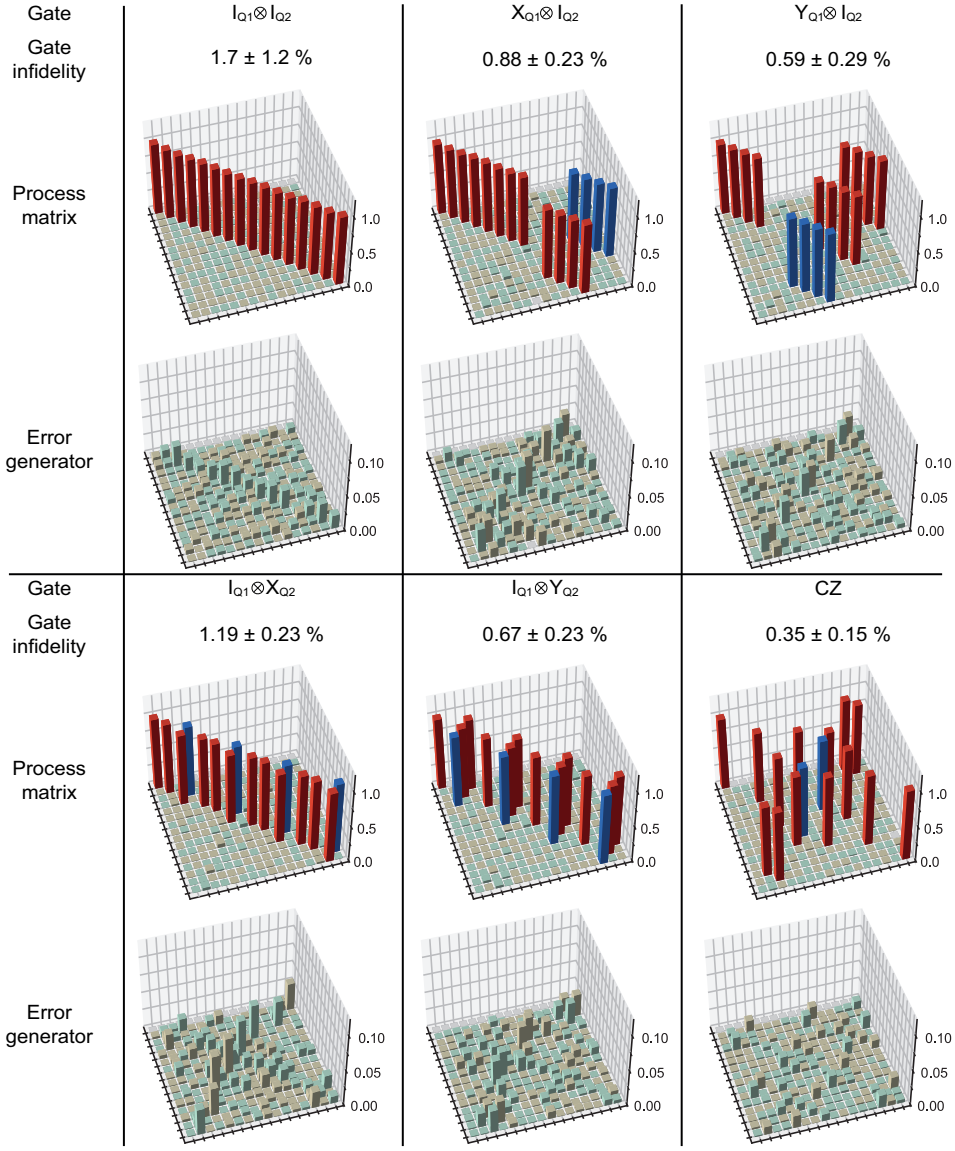

Fig. 7.8: Two-qubit processes. Average gate infidelities, process matrices (PTMs), and error generators of the 6 quantum gates in the chosen gate set. These results are analyzed by the `pyGSTi` package using maximum-likelihood estimation.

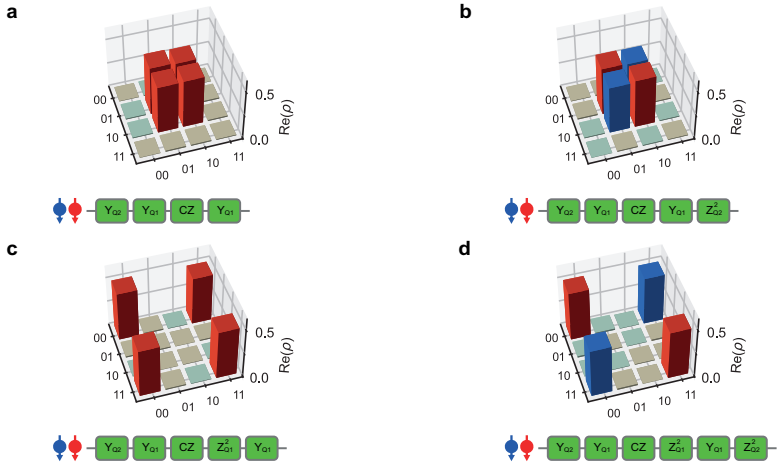

Fig. 7.9: Bell states predicted from the quantum processes. Top panels show the real part of the reconstructed density matrices of the four Bell states $|\Psi^+\rangle = (|01\rangle + |10\rangle)/\sqrt{2}$ (**a**), $|\Psi^-\rangle = (|01\rangle - |10\rangle)/\sqrt{2}$ (**b**), $|\Phi^+\rangle = (|00\rangle + |11\rangle)/\sqrt{2}$ (**c**), $|\Phi^-\rangle = (|00\rangle - |11\rangle)/\sqrt{2}$ (**d**). The color code is the same as in Fig. 7.4. Bottom panels show the quantum circuit used to reconstruct the Bell states. Z^2_{Qi} is a virtual π-rotation around the $\hat{z}$ axis on the i-th qubit, which is executed by a phase update on the microwave reference clock of the qubit and therefore is error-free. We numerically estimate the state fidelities to be 98.42% for $|\Psi^+\rangle$ and $|\Psi^-\rangle$ state, and 97.75% for $|\Phi^+\rangle$ and $|\Phi^-\rangle$ state.

gate fidelity is then conveniently given by

$$F_{\text{gate}} = \frac{\text{Tr}(\mathcal{M}^{-1}_{\text{exp}}\mathcal{M}_{\text{ideal}}) + d}{d(d+1)}. \tag{7.22}$$

It is related to the entanglement fidelity via $1 - F_{\text{ent}} = \frac{d+1}{d}(1 - F_{\text{gate}})$ [42], where d is the dimension of the two-qubit Hilbert space. While the PTM $\mathcal{M}$ perfectly describes the errors, it is more intuitive to analyze the corresponding error generator $\mathcal{L} = \log(E)$ of the process [21]. The error generator $\mathcal{L}$ relates to the error PTM E in a similar way as a Hamiltonian H relates to a unitary operation $U = e^{-iH}$. The error generator can be separated into several blocks. A full discussion about the error generator can be found in Ref. [21]. In this work, we have used the error generator to distinguish the dynamics originating from coherent Hamiltonian errors which can be corrected by adjusting gate parameters (see 7.7.2), and from noisy/stochastic dynamics which cannot be corrected easily. The coherent errors can be extracted by projecting $\mathcal{L}$ onto the 4×4-dimensional Hamiltonian space H. In the Hilbert-Schmidt space, the Hamiltonian projection is given by [21]

$$H_{mn} = -\frac{i}{d^2}\text{Tr}\left[\left(P_m^T \otimes P_n^T \otimes \mathbf{1}_d - \mathbf{1}_d \otimes P_m \otimes P_n\right)\mathcal{L}_{\text{sup}}\right], \tag{7.23}$$

where $\mathcal{L}_{\text{sup}}$ is the error generator in Liouville superoperator form, $P_m \in I, X, Y, Z$ are the extended Pauli matrices with $m, n = 0, 1, 2, 3$, $\mathbf{1}_d$ is the d-dimensional Identity matrix, and $d = 4$ is the dimension of the two-qubit Hilbert space. To improve the calibration of

our gate set, we use the information of 7 different Hamiltonian errors (IX, IY, XI, YI, ZI, IZ and ZZ). To estimate coherent Hamiltonian errors and incoherent stochastic errors, two new metrics are considered [21]: the Jamiolkowski probability

$$\epsilon_J(\mathcal{L}) = -\mathrm{Tr}(\rho_J(\mathcal{L})\,|\Psi\rangle\langle\Psi|), \tag{7.24}$$

which describes the amount of incoherent error in the process, and the Jamiolkowski amplitude

$$\theta_J(\mathcal{L}) = ||(1-|\Psi\rangle\langle\Psi|)\rho_J(\mathcal{L})\,|\Psi\rangle\,||_2, \tag{7.25}$$

which approximately describes the amount of coherent Hamiltonian errors (Table. 7.1). Here, $\rho_J(\mathcal{L}) = (\mathcal{L}\otimes\mathbf{1}_{d^2})[|\Psi\rangle\langle\Psi|]$ is the Jamiolkowski state and $|\Psi\rangle$ is a maximally entangling four-qubit state which originates from the relation of quantum processes to states in a Hilbert space twice the dimension via the Choi-Jamiolkowski isomorphism [43]. For small errors, the average gate infidelity can be approximated by [21]

$$1-F_{\mathrm{gate}} = \frac{d}{d+1}\left[\epsilon_J(\mathcal{L}) + \theta_J(\mathcal{L})^2\right]. \tag{7.26}$$

	$1-F_{\mathrm{gate}}$	$1-F_{\mathrm{sub}}$	ϵ_J	θ_J	D	$\|\|\cdot\|\|_\diamond$
I	0.017 ± 0.012	Q1: 0.0075 ± 0.0033 Q2: 0.0111 ± 0.0039	0.021	0.0097	0.024 ± 0.015	0.038 ± 0.019
X_{Q1}	0.0088 ± 0.0023	0.00320 ± 0.00073	0.010	0.027	0.032 ± 0.022	0.047 ± 0.035
Y_{Q1}	0.0059 ± 0.0029	0.0027 ± 0.0057	0.0069	0.022	0.0256 ± 0.0073	0.034 ± 0.022
X_{Q2}	0.0119 ± 0.0023	0.0039 ± 0.0068	0.014	0.028	0.035 ± 0.030	0.044 ± 0.041
Y_{Q2}	0.0067 ± 0.0023	0.00131 ± 0.00025	0.0079	0.022	0.0265 ± 0.0080	0.034 ± 0.014
CZ	0.0035 ± 0.0015	–	0.0042	0.016	0.018 ± 0.014	0.023 ± 0.010

Table 7.1: Gate metrics. Detailed overview of important metrics of the gate set [I, X_{Q1}, Y_{Q1}, X_{Q2}, Y_{Q2}, CZ]: the average gate fidelity F_{gate} (see Eq. (7.22)) and the fidelity reduced to the single-qubit subspace (see Eq. (7.27)), the Jamiolkowski probability ϵ_J (see Eq. (7.24)), Jamiolkowski amplitude θ_J (see Eq. (7.25)), the trace distance $D(\mathcal{M}_{\mathrm{ideal}},\mathcal{M}_{\mathrm{exp}}) = ||\mathcal{M}_{\mathrm{ideal}}-\mathcal{M}_{\mathrm{exp}}||_1/2$, and the diamond norm $||\mathcal{M}_{\mathrm{ideal}},\mathcal{M}_{\mathrm{exp}}||_\diamond = \max_\rho ||(\mathcal{M}_{\mathrm{ideal}}\otimes\mathbf{1}_{d^2})\rho-(\mathcal{M}_{\mathrm{exp}}\otimes\mathbf{1}_{d^2})\rho||_1/2$.

For a comparison of the performance of the single-qubit gates with previous experiments reporting single-qubit gate fidelities, we compute the fidelities projected to the single-qubit space from the PTMs or the error generators. In Fig. 7.2 and Fig. 7.10, single-qubit gate fidelities are estimated by projecting the PTMs onto corresponding subspace. Let $\mathcal{P}_j$ be the projector on the subspace of qubit j then the fidelity is given by

$$F_{\mathrm{sub}} = \frac{\mathrm{Tr}(\mathcal{P}_j\mathcal{M}_{\mathrm{exp}}^{-1}\mathcal{P}_j\mathcal{M}_{\mathrm{ideal}}) + (d/2)}{(d/2)((d/2)+1)}. \tag{7.27}$$

Error bars for the fidelity projected to the subspace are computed using standard error propagation of the confidence intervals of $\mathcal{M}_{\mathrm{exp}}$ provided by the `pyGSTi` package. A more optimistic estimation for the fidelities in the single-qubit subspace is given by projecting the error generators instead of the PTMs.

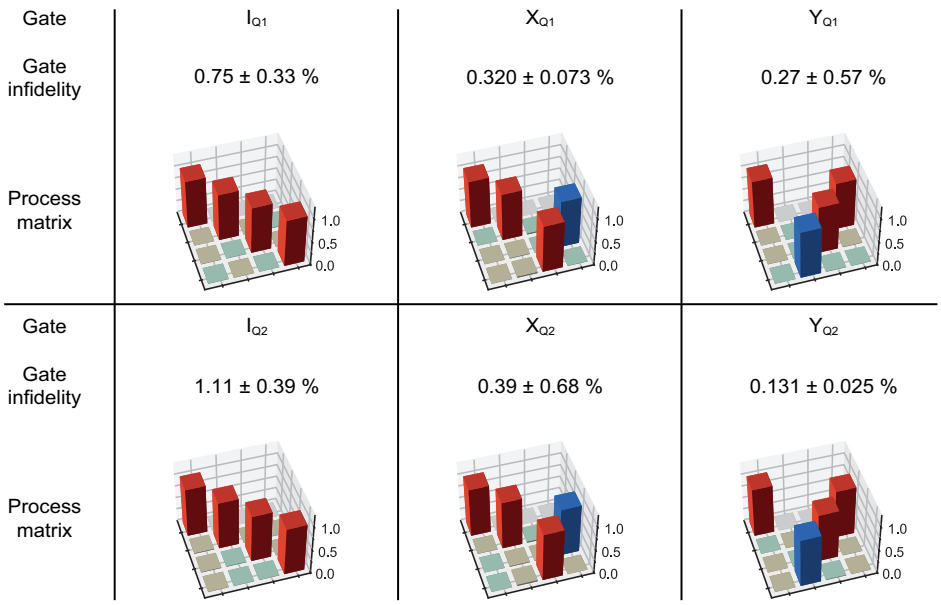

Fig. 7.10: Single-qubit processes. Average gate infidelities and process matrices (PTMs) of the identity gates (idle gates) and single-qubit X/Y gates in the subspace of the individual qubits. The individual PTMs are calculated from the PTMs in the two-qubit space.

7

7.7.8. VARIATIONAL QUANTUM EIGENSOLVER

We follow the approach of Ref. [27] to using the variational quantum eigensolver (VQE) algorithm to compute the ground state energy of molecular hydrogen, after mapping this state onto the state of two qubits. We include this information here for completeness. The Hamiltonian of a molecular system in atomic units is

$$H = -\sum_i \frac{\nabla^2_{\vec{R}_i}}{2M_i} - \sum_j \frac{\nabla^2_{\vec{r}_j}}{2} - \sum_{i,j} \frac{Q_i}{|\vec{R}_i - \vec{r}_j|} + \sum_{i,j>i} \frac{Q_i Q_j}{|\vec{R}_i - \vec{R}_j|} + \sum_{i,j>i} \frac{1}{|\vec{r}_i - \vec{r}_j|}, \tag{7.28}$$

where $\vec{R}_i$, M_i and Q_i are the position, mass and charge of the i-th nuclei, and $\vec{r}_j$ is the position of the j-th electron. The first two sums describe the kinetic energies of the nuclei and electrons, respectively. The last three sums describe the Coulomb repulsion between nuclei and electrons, nuclei and nuclei, and electrons and electrons, respectively. As we are primarily interested in the electronic structure of the molecule, and nuclear masses are a few orders of magnitude larger than the electron masses, the nuclei are treated as static point charges under the Born-Oppenheimer approximation. Conse-

quentially, the electronic Hamiltonian can be simplified to

$$H_e = -\sum_i \frac{\nabla^2_{\vec{r}_i}}{2} - \sum_{i,j} \frac{Q_i}{\left|\vec{R}_i - \vec{r}_j\right|} + \sum_{i,j>i} \frac{1}{\left|\vec{r}_i - \vec{r}_j\right|}. \tag{7.29}$$

Switching into the second-quantization representation, described by fermionic creation and annihilation operators, $a_p^\dagger$ and a_q, acting on a finite basis, the Hamiltonian becomes

$$H_e = \sum_{pq} h_{pq} a_p^\dagger a_q + \sum_{pqrs} h_{pqrs} a_p^\dagger a_q^\dagger a_r a_s, \tag{7.30}$$

where p, q, r, and s label the corresponding basis states. The anti-symmetry under exchange is retained through the anti-commutation relation of the operators. The weights of the two sums are given by the integrals

$$h_{pq} = \int d\vec{\sigma} \psi_p^*(\vec{\sigma}) (\frac{\nabla^2_{\vec{r}_i}}{2} - \sum_i \frac{Q_i}{\left|\vec{R}_i - \vec{r}\right|}) \psi_q(\vec{\sigma}), \tag{7.31}$$

$$h_{pqrs} = \int d\vec{\sigma}_1 d\vec{\sigma}_2 \frac{\psi_p^*(\vec{\sigma}_1)\psi_q^*(\vec{\sigma}_2)\psi_s(\vec{\sigma}_1)\psi_r(\vec{\sigma}_2)}{|\vec{r}_1 - \vec{r}_2|}, \tag{7.32}$$

where $\vec{\sigma}_i = (\vec{r}_i, s_i)$ is a multi-index describing the position $\vec{r}_i$ and the spin s_i of electron i. Such a second-quantized molecular Hamiltonian can be mapped onto qubits using the Jordan-Wigner (JW) or the Bravyi-Kitaev (BK) transformation [44]. The JW transformation directly encodes the occupation number (0 or 1) of the i-th spin-orbital into the state ($|0\rangle$ or $|1\rangle$) of the i-th qubit. The number of qubits required after JW transformation is thus the same as the number of spin-orbitals that are of interest. The BK transformation, on the other hand, encodes the information in both the occupation number and parities – whether there is an even or odd occupation in a subset of spin-orbitals.

Taking molecular hydrogen in the Hartree-Fock basis as an example, we are interested in investigating the bonding ($|O_1\uparrow\rangle$, $|O_1\downarrow\rangle$) and the anti-bonding orbital state ($|O_2\uparrow\rangle$, $|O_2\downarrow\rangle$). The initial guess of the solution is the Hartree-Fock (HF) state in which both electrons occupy the $|O_1\rangle$ orbital. The JW transformation encodes the HF initial state as $|1100\rangle$, representing $\left|N_{O_1\downarrow} N_{O_1\uparrow} N_{O_2\downarrow} N_{O_2\uparrow}\right\rangle$ from left to right, where $N_{O_i S}$ is the occupation of the $O_i S$ spin-orbital with $S = \uparrow, \downarrow$. The BK transformation encodes the HF initial state as $|1000\rangle$, where the first and the third qubit (counting from the right) encode the occupation number of the first and third spin-orbital ($N_{O_1\uparrow} = 1$ and $N_{O_2\uparrow} = 0$), the second qubit encodes the parity of the first two spin-orbitals (($N_{O_1\uparrow} + N_{O_1\downarrow}$) mod 2 = 0), and the fourth qubit encodes the parity of all four spin-orbitals (($N_{O_1\uparrow} + N_{O_1\downarrow} + N_{O_2\uparrow} + N_{O_2\downarrow}$) mod 2 = 0). With the standard transformation rules for fermionic creation and annihilation

operators, the system Hamiltonian becomes a four-qubit Hamiltonian

$$\begin{aligned} H_{JW} = {} & g_0 I + g_1 Z_1 + g_2 Z_2 + g_3 Z_3 + g_4 Z_4 \\ & + g_5 Z_1 Z_2 + g_6 Z_1 Z_3 + g_7 Z_1 Z_4 \\ & + g_8 Z_2 Z_3 + g_9 Z_2 Z_4 + g_{10} Z_3 Z_4 \\ & + g_{11} Y_1 X_2 X_3 Y_4 + g_{12} Y_1 Y_2 X_3 X_4 \\ & + g_{13} X_1 X_2 Y_3 Y_4 + g_{14} X_1 Y_2 Y_3 X_4, \end{aligned} \tag{7.33}$$

$$\begin{aligned} H_{BK} = {} & g_0 I + g_1 Z_1 + g_2 Z_2 + g_3 Z_3 \\ & + g_4 Z_1 Z_2 + g_5 Z_1 Z_3 + g_6 Z_2 Z_4 \\ & + g_7 Z_1 Z_2 Z_3 + g_8 Z_1 Z_3 Z_4 + g_9 Z_2 Z_3 Z_4 \\ & + g_{10} Z_1 Z_2 Z_3 Z_4 + g_{11} X_1 Z_2 X_3 \\ & + g_{12} Y_1 Z_2 Y_3 + g_{13} X_1 Z_2 X_3 Z_4 + g_{14} Y_1 Z_2 Y_3 Z_4. \end{aligned} \tag{7.34}$$

The subscripts are used to label the qubits. We see that due to the symmetry of the represented system in H_{BK}, qubit 2 and qubit 4 are never flipped, allowing us to reduce the dimension of the Hamiltonian to

$$\begin{aligned} H_{BK}^{\text{reduced}} &= h_0 I + h_1 Z_1 + h_2 Z_2 + h_3 Z_1 Z_2 \\ &\quad + h_4 X_1 X_2 + h_5 Y_1 Y_2 \\ &= h_0 + h_1 ZI + h_2 IZ + h_3 ZZ \\ &\quad + h_4 XX + h_5 YY, \end{aligned} \tag{7.35}$$

where qubit 1 has been relabeled as qubit 2 and qubit 3 has been relabeled as qubit 1. The HF initial state is therefore reduced to $|01\rangle$, and the Hamiltonian is rephrased to be consistent with the partial tomography expression in Fig. 7.5. This reduced representation requires only two qubits to simulate the hydrogen molecule. We emphasize that such a reduction of the BK Hamiltonian is not a special case for H_2 molecule but is connected to symmetry considerations to reduce the complexity of systems, in a scalable way.

VQE is a method to compute the ground state energy of the Hamiltonian. The total energy can be directly calculated by measuring the expectation value of each Hamiltonian term. This can be done easily by partial quantum state tomography. All the expectation values are then added up with a set of weights (h_0 through h_5). The weights are only functions of the internuclear separation (R) and can be computed efficiently by a classical computer. Here we use the `OpenFermion` python package to compute these weights [29].

The main task of the quantum processor is then to encode the molecular spin-orbital state into the qubits. The starting point is the HF initial state, which is believed to largely overlap with the actual ground state. In order to find the actual ground state, the initial state needs to be "parameterized" into an ansatz to explore a subspace of all possible states. We apply the unitary coupled cluster (UCC) theory to the parameterized ansatz state, which is used to describe many-body systems and cannot be efficiently executed

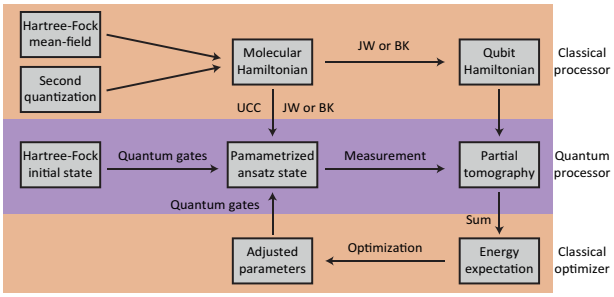

Fig. 7.11: Workflow of the VQE algorithm. The qubit Hamiltonian is typically transformed from the molecular Hamiltonian by JW transformation or BK transformation by a classical processor. A HF initial state is encoded into the qubit states according to JW or BK transformation, and then transformed by the quantum processor into a parameterized ansatz state by considering single- and double-excitation in the molecule using unitary coupled cluster (UCC) theory. The expectation value of each individual Hamiltonian term is directly measured by partial state tomography. The expectation of the total energy is then calculated by weighted sum of the individual expectations. The result is fed into a classical optimizer, which suggests a new parameterized ansatz state for the next run. This process is iterated until the expectation of the total energy converges.

on a classical computer [45]. The UCC operator has a format

$$U_{UCC}(\vec{\theta}) = e^{\sum_n (T_n(\vec{\theta}) - T_n^\dagger(\vec{\theta}))}, \tag{7.36}$$

with

$$T_1(\vec{\theta}) = \sum_{m,i} \vec{\theta}_i^m a_m^\dagger a_i, \tag{7.37}$$

$$T_2(\vec{\theta}) = \sum_{m,n,i,j} \vec{\theta}_{i,j}^{m,n} a_m^\dagger a_n^\dagger a_i a_j \tag{7.38}$$

representing single-excitation and double-excitation of the electrons. The indices i, j label the occupied spin-orbitals and m, n are the labels of the unoccupied spin-orbitals. The vector $\vec{\theta}$ is the set of all parameters to optimize. In the case of a H_2 molecule, the UCC operator is transformed into a qubit operator as

$$U_{UCC}^{BK}(\vec{\theta}) = e^{-i\theta XY}, \tag{7.39}$$

where θ is a single parameter to variationally optimize.

REFERENCES

[1] M. A. Nielsen and I. L. Chuang, *Quantum Computation and Quantum Information: 10th Anniversary Edition* (Cambridge University Press, 2011).

[2] J. Preskill, *Quantum Computing in the NISQ era and beyond,* Quantum **2**, 79 (2018).

[3] D. A. Lidar and T. A. Brun, *Quantum error correction* (Cambridge university press, 2013).

[4] R. Raussendorf and J. Harrington, *Fault-tolerant quantum computation with high threshold in two dimensions,* Phys. Rev. Lett. **98**, 190504 (2007).

[5] A. G. Fowler, M. Mariantoni, J. M. Martinis, and A. N. Cleland, *Surface codes: Towards practical large-scale quantum computation,* Phys. Rev. A **86**, 032324 (2012).

[6] X. Xue, B. Patra, J. P. G. van Dijk, N. Samkharadze, S. Subramanian, A. Corna, B. Paquelet Wuetz, C. Jeon, F. Sheikh, E. Juarez-Hernandez, B. P. Esparza, H. Rampurawala, B. Carlton, S. Ravikumar, C. Nieva, S. Kim, H.-J. Lee, A. Sammak, G. Scappucci, M. Veldhorst, F. Sebastiano, M. Babaie, S. Pellerano, E. Charbon, and L. M. K. Vandersypen, *CMOS-based cryogenic control of silicon quantum circuits,* Nature **593**, 205 (2021).

[7] J. M. Elzerman, R. Hanson, L. H. Willems van Beveren, B. Witkamp, L. M. K. Vandersypen, and L. P. Kouwenhoven, *Single-shot read-out of an individual electron spin in a quantum dot,* Nature **430**, 431 (2004).

[8] M. Pioro-Ladrière, T. Obata, Y. Tokura, Y.-S. Shin, T. Kubo, K. Yoshida, T. Taniyama, and S. Tarucha, *Electrically driven single-electron spin resonance in a slanting zeeman field,* Nature Physics **4**, 776 (2008).

[9] L. M. K. Vandersypen and I. L. Chuang, *NMR techniques for quantum control and computation,* Rev. Mod. Phys. **76**, 1037 (2005).

[10] D. Loss and D. P. DiVincenzo, *Quantum computation with quantum dots,* Phys. Rev. A **57**, 120 (1998).

[11] J. R. Petta, A. C. Johnson, J. M. Taylor, E. A. Laird, A. Yacoby, M. D. Lukin, C. M. Marcus, M. P. Hanson, and A. C. Gossard, *Coherent Manipulation of Coupled Electron Spins in Semiconductor Quantum Dots,* Science **309**, 2180 (2005).

[12] T. Meunier, V. E. Calado, and L. M. K. Vandersypen, *Efficient controlled-phase gate for single-spin qubits in quantum dots,* Phys. Rev. B **83**, 121403 (2011).

[13] M. Veldhorst, C. H. Yang, J. C. C. Hwang, W. Huang, J. P. Dehollain, J. T. Muhonen, S. Simmons, A. Laucht, F. E. Hudson, K. M. Itoh, A. Morello, and A. S. Dzurak, *A two-qubit logic gate in silicon,* Nature **526**, 410 (2015).

[14] T. F. Watson, S. G. J. Philips, E. Kawakami, D. R. Ward, P. Scarlino, M. Veldhorst, D. E. Savage, M. G. Lagally, M. Friesen, S. N. Coppersmith, M. A. Eriksson, and L. M. K. Vandersypen, *A programmable two-qubit quantum processor in silicon,* Nature **555**, 633 (2018).

[15] F. Martins, F. K. Malinowski, P. D. Nissen, E. Barnes, S. Fallahi, G. C. Gardner, M. J. Manfra, C. M. Marcus, and F. Kuemmeth, *Noise Suppression Using Symmetric Exchange Gates in Spin Qubits,* Phys. Rev. Lett. **116**, 116801 (2016).

[16] M. D. Reed, B. M. Maune, R. W. Andrews, M. G. Borselli, K. Eng, M. P. Jura, A. A. Kiselev, T. D. Ladd, S. T. Merkel, I. Milosavljevic, E. J. Pritchett, M. T. Rakher, R. S. Ross, A. E. Schmitz, A. Smith, J. A. Wright, M. F. Gyure, and A. T. Hunter, *Reduced*

Sensitivity to Charge Noise in Semiconductor Spin Qubits via Symmetric Operation, Phys. Rev. Lett. **116**, 110402 (2016).

[17] R. Blume-Kohout, J. K. Gamble, E. Nielsen, K. Rudinger, J. Mizrahi, K. Fortier, and P. Maunz, *Demonstration of qubit operations below a rigorous fault tolerance threshold with gate set tomography,* Nature Communications **8**, 14485 (2017).

[18] E. Magesan, J. M. Gambetta, and J. Emerson, *Characterizing quantum gates via randomized benchmarking,* Phys. Rev. A **85**, 042311 (2012).

[19] J. P. Dehollain, J. T. Muhonen, R. Blume-Kohout, K. M. Rudinger, J. K. Gamble, E. Nielsen, A. Laucht, S. Simmons, R. Kalra, A. S. Dzurak, and A. Morello, *Optimization of a solid-state electron spin qubit using gate set tomography,* New J. Phys. **18**, 103018 (2016).

[20] G. A. White, C. D. Hill, and L. C. Hollenberg, *Performance optimization for drift-robust fidelity improvement of two-qubit gates,* Phys. Rev. Applied **15**, 014023 (2021).

[21] R. Blume-Kohout, M. P. da Silva, E. Nielsen, T. Proctor, K. Rudinger, M. Sarovar, and K. Young, *A taxonomy of small Markovian errors,* arXiv:2103.01928 (2021).

[22] P. Cerfontaine, R. Otten, M. A. Wolfe, P. Bethke, and H. Bluhm, *High-fidelity gate set for exchange-coupled singlet-triplet qubits,* Phys. Rev. B **101**, 155311 (2020).

[23] A. Pan, T. E. Keating, M. F. Gyure, E. J. Pritchett, S. Quinn, R. S. Ross, T. D. Ladd, and J. Kerckhoff, *Resonant exchange operation in triple-quantum-dot qubits for spin–photon transduction,* Quantum Sci. Technol. **5**, 034005 (2020).

[24] D. M. Zajac, A. J. Sigillito, M. Russ, F. Borjans, J. M. Taylor, G. Burkard, and J. R. Petta, *Resonantly driven cnot gate for electron spins,* Science **359**, 439 (2017).

[25] J. M. Martinis and M. R. Geller, *Fast adiabatic qubit gates using only σ_z control,* Phys. Rev. A **90**, 022307 (2014).

[26] E. Nielsen, J. K. Gamble, K. Rudinger, T. Scholten, K. Young, and R. Blume-Kohout, *Gate set tomography,* arXiv:2009.07301 (2020).

[27] C. Hempel, C. Maier, J. Romero, J. McClean, T. Monz, H. Shen, P. Jurcevic, B. P. Lanyon, P. Love, R. Babbush, A. Aspuru-Guzik, R. Blatt, and C. F. Roos, *Quantum chemistry calculations on a trapped-ion quantum simulator,* Phys. Rev. X **8**, 031022 (2018).

[28] J. M. Chow, L. DiCarlo, J. M. Gambetta, A. Nunnenkamp, L. S. Bishop, L. Frunzio, M. H. Devoret, S. M. Girvin, and R. J. Schoelkopf, *Detecting highly entangled states with a joint qubit readout,* Phys. Rev. A **81**, 062325 (2010).

[29] J. R. McClean, N. C. Rubin, K. J. Sung, I. D. Kivlichan, X. Bonet-Monroig, Y. Cao, C. Dai, E. S. Fried, C. Gidney, B. Gimby, P. Gokhale, T. Häner, T. Hardikar, V. Havlicek, O. Higgott, C. Huang, J. Izaac, Z. Jiang, X. Liu, S. McArdle, M. Neeley, T. O'Brien,

B. O'Gorman, I. Ozfidan, M. D. Radin, J. Romero, N. P. D. Sawaya, B. Senjean, K. Setia, S. Sim, D. S. Steiger, M. Steudtner, Q. Sun, W. Sun, D. Wang, F. Zhang, and R. Babbush, *OpenFermion: the electronic structure package for quantum computers,* Quantum Sci. Technol. **5**, 034014 (2020).

[30] M. Ganzhorn, D. Egger, P. Barkoutsos, P. Ollitrault, G. Salis, N. Moll, M. Roth, A. Fuhrer, P. Mueller, S. Woerner, I. Tavernelli, and S. Filipp, *Gate-efficient simulation of molecular eigenstates on a quantum computer,* Phys. Rev. Applied **11**, 044092 (2019).

[31] M. T. Mądzik, S. Asaad, A. Youssry, B. Joecker, K. M. Rudinger, E. Nielsen, K. C. Young, T. J. Proctor, A. D. Baczewski, A. Laucht, V. Schmitt, F. E. Hudson, K. M. Itoh, A. M. Jakob, B. C. Johnson, D. N. Jamieson, A. S. Dzurak, C. Ferrie, R. Blume-Kohout, and A. Morello, *Precision tomography of a three-qubit electron-nuclear quantum processor in silicon,* arXiv:2106.03082 (2021).

[32] G. Zheng, N. Samkharadze, M. L. Noordam, N. Kalhor, D. Brousse, A. Sammak, G. Scappucci, and L. M. K. Vandersypen, *Rapid gate-based spin read-out in silicon using an on-chip resonator,* Nature Nanotechnology **14**, 742 (2019).

[33] S. Schaal, I. Ahmed, J. A. Haigh, L. Hutin, B. Bertrand, S. Barraud, M. Vinet, C.-M. Lee, N. Stelmashenko, J. W. A. Robinson, J. Y. Qiu, S. Hacohen-Gourgy, I. Siddiqi, M. F. Gonzalez-Zalba, and J. J. L. Morton, *Fast gate-based readout of silicon quantum dots using josephson parametric amplification,* Phys. Rev. Lett. **124**, 067701 (2020).

[34] M. Reed, *Entanglement and Quantum Error Correction with Superconducting Qubits,* PhD Thesis, Yale Univ. (2013).

[35] M. Russ, D. M. Zajac, A. J. Sigillito, F. Borjans, J. M. Taylor, J. R. Petta, and G. Burkard, *High-fidelity quantum gates in Si/SiGe double quantum dots,* Phys. Rev. B **97**, 085421 (2018).

[36] Y.-C. Yang, S. N. Coppersmith, and M. Friesen, *Achieving high-fidelity single-qubit gates in a strongly driven charge qubit with 1/f charge noise,* npj Quantum Information **5**, 12 (2019).

[37] J. V. Koski, A. J. Landig, M. Russ, J. C. Abadillo-Uriel, P. Scarlino, B. Kratochwil, C. Reichl, W. Wegscheider, G. Burkard, M. Friesen, S. N. Coppersmith, A. Wallraff, K. Ensslin, and T. Ihn, *Strong photon coupling to the quadrupole moment of an electron in a solid-state qubit,* Nature Physics **16**, 642 (2020).

[38] M. Russ, S. Philips, X. Xue, and L. M. K. Vandersypen, *The path to high fidelity multi-qubit gates for quantum dot spin qubits,* Unpublished (2021).

[39] D. Greenbaum, *Introduction to Quantum Gate Set Tomography,* arXiv:1509.02921 (2015).

[40] E. Nielsen, R. J. Blume-Kohout, K. M. Rudinger, T. J. Proctor, L. Saldyt, and USDOE, *Python GST Implementation (PyGSTi) v. 0.9*, Tech. Rep. PyGSTi (Sandia National Lab. (SNL-NM), Albuquerque, NM (United States), 2019).

[41] E. Nielsen, K. Rudinger, T. Proctor, A. Russo, K. Young, and R. Blume-Kohout, *Probing quantum processor performance with pyGSTi,* Quantum Sci. Technol. **5**, 044002 (2020).

[42] A. G. White, A. Gilchrist, G. J. Pryde, J. L. O'Brien, M. J. Bremner, and N. K. Langford, *Measuring two-qubit gates,* J. Opt. Soc. Am. B **24**, 172 (2007).

[43] A. Jamiolkowski, *Linear transformations which preserve trace and positive semidefiniteness of operators,* Reports on Mathematical Physics **3**, 275 (1972).

[44] S. McArdle, S. Endo, A. Aspuru-Guzik, S. C. Benjamin, and X. Yuan, *Quantum computational chemistry,* Rev. Mod. Phys. **92**, 015003 (2020).

[45] A. G. Taube and R. J. Bartlett, *New perspectives on unitary coupled-cluster theory,* International Journal of Quantum Chemistry **106**, 3393 (2006).

8

CMOS-BASED CRYOGENIC CONTROL OF SILICON QUANTUM CIRCUITS

The most promising quantum algorithms require quantum processors hosting millions of quantum bits when targeting practical applications. A major challenge towards large-scale quantum computation is the interconnect complexity. In current solid-state qubit implementations, a major bottleneck appears between the quantum chip in a dilution refrigerator and the room temperature electronics. Advanced lithography supports the fabrication of both control electronics and qubits in silicon with CMOS compatible technology. When the electronics are designed to operate at cryogenic temperatures, it can thus ultimately be integrated with the qubits on the same die or package, overcoming the wiring bottleneck. Here we report a cryogenic CMOS control chip operating at 3 K, which outputs tailored microwave bursts to drive silicon quantum bits cooled to 20 mK. We first benchmark the control chip and find electrical performance consistent with 99.99% fidelity qubit operations, assuming ideal qubits. Next, we use it to coherently control actual qubits encoded in the spin of single electrons confined in silicon quantum dots and find that the cryogenic control chip achieves the same fidelity as commercial instruments at room temperature. Furthermore, we highlight the extensive capabilities of the control chip by programming a number of benchmarking protocols as well as the Deutsch-Josza algorithm on a two-qubit quantum processor. These results open up the path towards a fully integrated, scalable silicon-based quantum computer.

This chapter has been published in Nature **593**, 205–210 (2021).

8.1. INTRODUCTION

A practical quantum computer comprises two main building blocks – a quantum processor with millions of qubits and classical instrumentation to generate control signals (input) and to process readout signals (output) [1, 2]. A standard setup for semiconducting or superconducting qubits has the qubits operating in a dilution refrigerator at ~ 20 mK, while bulky microwave vector sources and arbitrary waveform generators are placed at room temperature and connected to the qubits via long cables and attenuators (Fig. 8.1a, left). This approach has recently enabled an experimental demonstration of the advantage of quantum computing over classical computing in a random circuit sampling experiment, that utilizes a superconducting quantum processor consisting of 53 qubits [3]. This system requires more than 200 coaxial control lines from room temperature to the quantum chip operated below 20 mK. This brute-force approach to reach higher qubit numbers will soon hit its limits.

A promising path forward is to bring the control electronics close to the quantum chip, at cryogenic temperatures. While important steps in this direction have been taken [4–13], high-fidelity multi-qubit control and a universal gate set remain to be demonstrated using cryogenic controllers. A central challenge is that the power dissipation of the control electronics easily surpasses the typical cooling power of 10 μW available at 20 mK [14, 15]. Since silicon spin qubits can be operated and measured above 1 K [16–18], they are well-positioned for overcoming the wiring bottleneck by on-die or on-package co-integration with classical electronics (Fig. 8.1a, right) at a temperature of 1-3 K, where the cooling power is orders of magnitude higher than at mK temperatures.

A cryogenic quantum controller for practical quantum information processing must meet multiple criteria: a form factor compatible with integration in a cryogenic refrigerator; frequency multiplexing to facilitate scalability; low power consumption within the limit of refrigerator cooling power; sufficiently high output power to enable fast operations compared to the qubit coherence times; high signal-to-noise ratio (SNR) and spurious-free-dynamic-range (SFDR) for high-fidelity control; the ability to generate tailored pulse shapes and perform a universal set of quantum operations; an integrated instruction set memory for the efficient execution of complex algorithms. All these requirements can be met by commercial CMOS circuits designed to operate at a few K.

In this work, we utilize a quantum control chip operating at 3 K (cryo-controller, named Horse Ridge) and fabricated in Intel 22 nm-FinFET low-power CMOS technology [5] to coherently control two electron spin qubits in a silicon double quantum dot. In order to benchmark the limits of the controller, we keep the qubits at ~ 20 mK, where they are most coherent and the non-idealities of the control chip can be assessed best (Fig. 8.1a, middle). Extensive electrical characterization and benchmarking using the quantum processor show that the cryo-controller meets all the above criteria.

8.2. DEVICE AND SETUP

The specifications for the cryo-controller derive from the demands on the qubit control. Here we target qubits that can be resonantly controlled with drive frequencies in the 2-20 GHz band, covering the typical resonance frequencies of both superconducting and spin qubits [4, 16, 20–22]. The cryo-controller has four output ports, each with up to 32

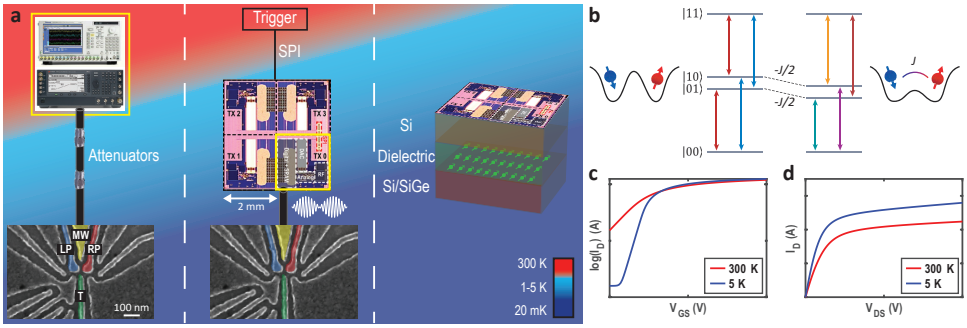

Fig. 8.1: The cryogenic quantum control system. a. Three stages of development of the control system towards full integration. From left to right: room temperature instruments connected to qubits via coax lines and attenuators; cryo-controller placed at 1-5 K directly connected to the qubits and triggered from room temperature using a serial peripheral interface (SPI), which leaves the wiring from 1-5 K to the qubit sample unaltered, but brings a significant reduction in the wire count from room temperature to 1-5 K when targeting many qubits; a future perspective of fully integrated control electronics and qubits on the same package/die, eliminating dense wiring all the way down to the package/die (note that we do not envision one transmitter above every qubit, so the qubit and transmitter form factor can be different [1, 19]). Two single electron spins used as qubits are located underneath gates LP (blue) and RP (red), as shown in the SEM image. Multiplexed microwave signals are sent to gate MW (yellow) to control both qubits. Gate T (green) is used to tune the coupling between the qubits. **b.** Energy level diagram without (left) and with (right) exchange coupling (J). The resonance frequency of each qubit depends on the other qubit only when the coupling is on (low tunnel barrier between the dots). **c, d.** FinFET NMOS device characteristics at room temperature versus 5 K (temperature of the sample holder): drain current (I_D) versus gate-source voltage (V_{GS}) at drain-source voltage V_{DS} = 1 V (**c**) and I_D versus V_{DS} at V_{GS} = 0.4 V(**d**).

frequency-multiplexed tones. Since the controller must dissipate minimal power and have a small form factor, we analyze in detail the signal specifications that are sufficient to achieve a 99.99% gate fidelity [23]. Among other performance metrics, the most stringent ones dominating the architecture and power consumption of the controller are the SNR (> 48 dB) and SFDR (> 44 dB) for frequency-multiplexed control [23].

Further challenges arise in designing complex CMOS circuits at deep cryogenic temperatures. Key device characteristics such as the threshold voltage (V_{th}) and mobility (μ) increase compared to room temperature, as seen in Fig. 8.1c, d [24]. Moreover, the degradation of active device matching [25] and the improvement of the quality factor of on-chip passive components [26], necessitate careful characterization and modeling for circuits operated at cryogenic temperatures.

As a benchmark of performance, we use the cryo-controller to coherently control a two-qubit quantum processor. The quantum processor is made of a double quantum dot (DQD) electrostatically confined in an undoped ^{28}Si/SiGe heterostructure. By tuning the voltage on plunger gates LP and RP, two single electrons are locally accumulated underneath each gate, shown in blue and red in the scanning electron microscope (SEM) image in Fig. 8.1a. By applying an external magnetic field of 380 mT, combined with the longitudinal magnetic field induced by a micro-magnet on top of the DQD, we can encode the qubit states into the Zeeman split states of the two electrons, where spin-up is used as $|1\rangle$ and spin-down is used as $|0\rangle$. The resonance frequencies of Qubit 1 (Q_1, underneath gate LP) and Qubit 2 (Q_2, underneath gate RP) are 13.62 GHz and

13.51 GHz, respectively. Rotations around the $\hat{x}$ and $\hat{y}$ axes are implemented by sending microwave bursts with the microwave phase controlling the rotation axis, e.g. an in-phase (quadrature) microwave burst implements a rotation about $\hat{x}$ ($\hat{y}$). The microwave bursts are applied to gate MW, which drives electric-dipole spin resonance (EDSR) enabled by the transverse magnetic field gradient from the micro-magnet [27], while the rotation around the $\hat{z}$ axis (phase control) is achieved by changing the reference phase in the cryo-controller, which adds a phase shift to all the subsequent bursts [28]. The two-qubit interaction is mediated by the exchange coupling (J) between the two spins [29], controlled by gate T. Its effect here is to shift the anti-parallel spin states down in energy [30]. As a result, the resonance frequency of each qubit now depends on the state of the other qubit, allowing conditional operations on each qubit via narrow-band microwave bursts [21, 22] (Fig. 8.1b). The corresponding four different frequencies can be individually addressed using frequency multiplexing. Both qubits are read out in single-shot mode [31].

8.3. THE CRYOGENIC CONTROL CHIP

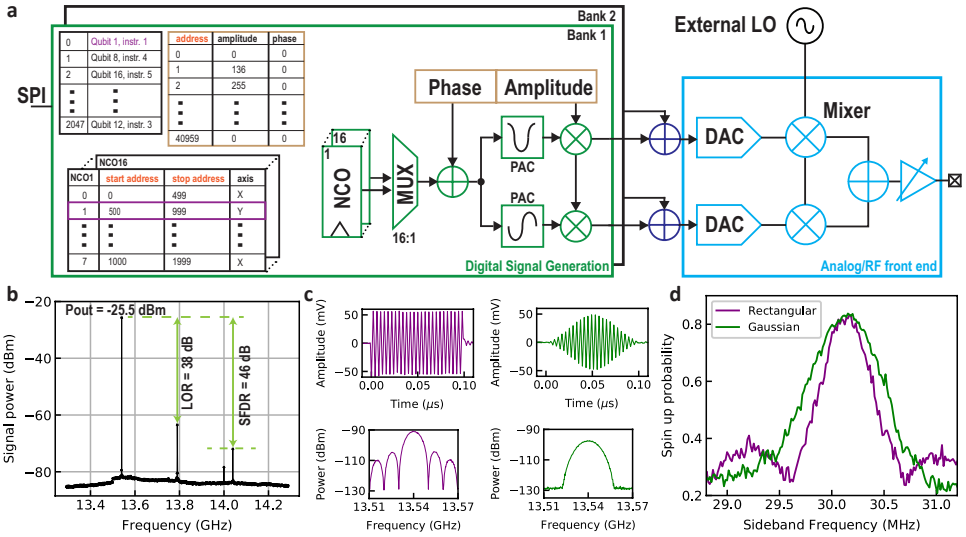

Fig. 8.2: The Horse Ridge cryogenic controller characterized at 3 K. a. System-level representation showing the digital signal generation and analog/RF front end of the cryo-controller, programmable via the SPI. **b.** Continuous-wave output spectrum from the cryo-controller at 13.54 GHz using only Bank 1 (for both banks refer to 8.6.3), showing the main output tone, LO rejection ratio (LOR) and SFDR limited by the image tone. **c.** Rectangular (purple) and Gaussian (green) shaped bursts before up-conversion (baseband signal) and the corresponding spectra after up-conversion. **d.** Qubit response for different burst envelopes, obtained when sweeping the NCO frequency around the qubit resonance across a span of ~ 3 MHz with a resolution of 15 KHz.

Fig. 8.2 shows the system-level architecture of one transmitter module (TX) in the cryo-controller, which consists of a digital signal generation unit with an analog/RF front-end. At the core of the digital signal generation, a numerically controlled oscillator (NCO)

outputs a sequence of bit strings every clock period [32]. This bit string encodes a phase that is intended to track the reference phase of one particular qubit. The output of 16 NCOs is multiplexed and fed to a phase-to-amplitude converter (PAC) implemented as hard-wired look-up table, to generate a sinusoidal (in-phase) and cosinusoidal (quadrature) signal. The NCO phases are constructed via a phase accumulator, which increments the phase in steps determined by a digital frequency tuning word (FTW). The 22-bit (N) FTWs in combination with the 1 GHz clock frequency (f_s) of the phase accumulator gives a frequency resolution of ~ 234 Hz, i.e. $f_s/2^N$.

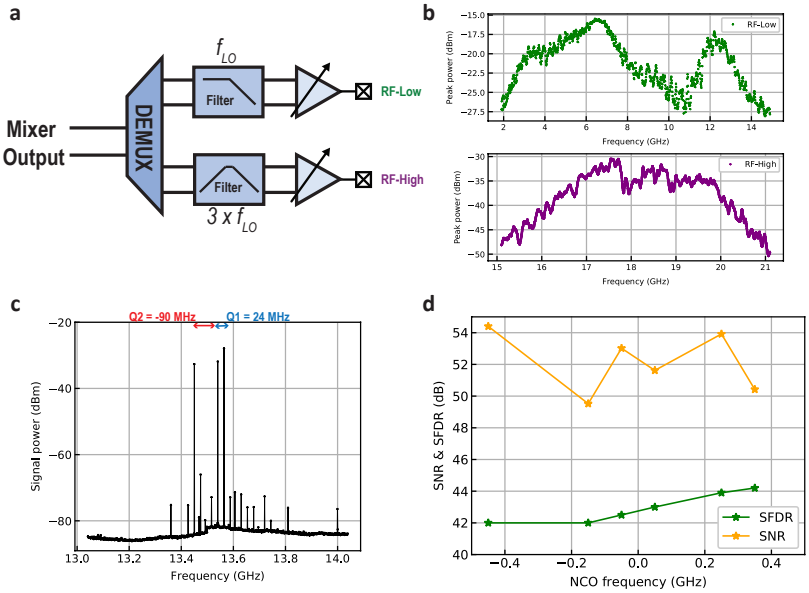

Fig. 8.3: Detailed electrical characterization of the cryo-controller. a. Schematics of the output driver (see 8.6.3 for the complete version) showing the two different RF outputs which use the same external LO to generate two different frequencies i.e. a 1 GHz band around f_{LO} or a 1 GHz band around $3 \times f_{LO}$ by selecting the RF-Low or RF-High path respectively. RF-High uses the third harmonic output of the mixer to generate the tone around $3 \times f_{LO}$. **b.** Peak output power versus frequency generated using the RF-Low and RF-High path respectively, as reported in [5]. The output power can be lowered by up to 40 dB below the peak power in the entire frequency range e.g. at 6 GHz the amplitude range is from -56 dBm to -16 dBm. **c.** Two-tone output spectrum of the cryo-controller used in the simultaneous Rabi oscillation experiment. **d.** SNR and SFDR of the cryo-controller at various NCO frequencies around 13.54 GHz.

The sine and cosine signals are amplitude and phase modulated using the envelope memory (orange box) containing up to 40960 points, each specifying an amplitude and phase value. An instruction table memory can store up to 8 different instructions per qubit/NCO by referring to start and stop addresses in the envelope memory. Finally, these instructions are listed in the instruction list to execute up to 2048 instructions from multiple instruction tables, initiated by a single external trigger, and acting sequentially on up to 16 qubits. The output of two such banks, each generating a digital signal, are summed to simultaneously control two qubits, consequently increasing the number of supported (uncoupled) qubits from 16 to 32 per TX module.

The generated digital signals are translated to the analog domain using 1GS/s 10-bit current-steering digital-to-analog converters (DAC), low pass filtered with an adjustable bandwidth to remove the sampling replicas and upconverted to the required qubit frequency using an I/Q mixer and an external local oscillator (LO). Finally, an output driver is incorporated to produce the required voltage amplitude (through a tunable gain of 40 dB) in the frequency range of 2 to 20 GHz, while driving the 50 Ω coaxial cable connecting to the qubits. Such a wide frequency and output power range allows the control of various solid-state qubits such as spin qubits and superconducting qubits. The controller dissipates 384 mW with all the NCOs simultaneously operating at a clock frequency of 1 GHz (Digital Signal Generation: 330 mW, Analog/RF front-end: 54 mW) (see 8.6.3). This architecture is replicated 4 times in a die area of 16 mm^2 (TX0-TX3 in Fig. 8.1) with an ability to control up to 4 × 32 frequency multiplexed qubits.

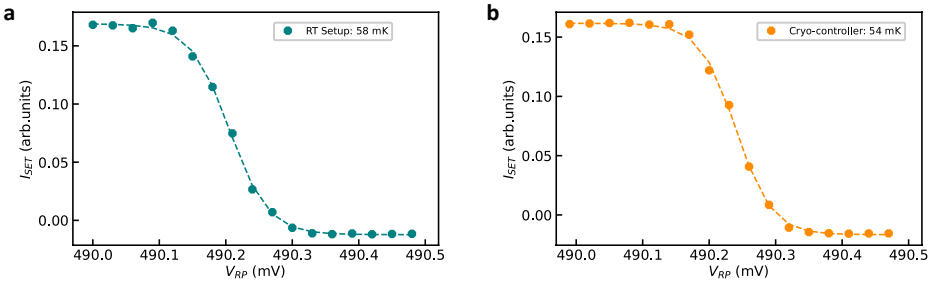

Fig. 8.4: Electron temperature measured at different configurations. SET current signal (I_{SET}) as a function of RP voltage (V_{RP}) measured at the charge transition between (1,0) and (1,1) when the quantum device is connected to the VSG (**a**) and to the cryo-controller (**b**) (at zero magnetic field). The electron temperatures are extracted by fitting the curves with the Fermi-Dirac distribution, with a lever arm of 0.172 eV/V. The measurements indicate that the output noise of the cryo-controller does not affect the electron temperature more than the noise from the RT setup reduced by 6 dB at the 3 K plate.

The purity of the generated signal can be quantified using the output signal spectrum shown in Fig. 8.2b. The generated signal has an SFDR of 46 dB at 13.54 GHz in a 1 GHz bandwidth, excluding the residual LO leakage (Fig. 8.3 for a two-tone test). The noise floor is flat across the 1 GHz bandwidth, and the cryo-controller leaves the electron temperature of the quantum device unaffected (Fig. 8.4). The SNR is 48 dB when integrating over 25 MHz, corresponding to the targeted maximum qubit Rabi frequency. Along with the low quantization noise and frequency noise, the output signal quality is predicted to achieve a single-qubit gate fidelity of 99.99%, assuming ideal qubits [23]. The amplitude and phase modulation capabilities of the controller allow the chip to generate arbitrary waveforms to precisely shape the spectral content of the pulse used to manipulate the qubits, as shown in Fig. 8.2c. In illustration, Fig. 8.2d shows the response of Q_2 to a microwave burst with rectangular versus Gaussian envelope, both calibrated to invert the qubit state when the drive is on-resonance with the qubit.

8.4. SINGLE- AND TWO-QUBIT LOGIC

Next, we test the functionality of the cryo-controller for controlling uncoupled qubits. The LO frequency is set to 13.54 GHz. Q_1 is then offset from the LO by 24 MHz and Q_2 by

-90 MHz. The qubit resonances are found by sweeping one single-sideband tone generated by one NCO (Fig. 8.5a), using the 22-bit FTW. Then we use one NCO from each bank to generate two tones on resonance with the two qubits and drive simultaneous Rabi oscillations on both qubits (Fig. 8.5b). Here a 5 μs rectangular envelope is uploaded to the envelope memory, and saved as an instruction. The duration of the microwave burst is swept by updating the start or stop address of this instruction.

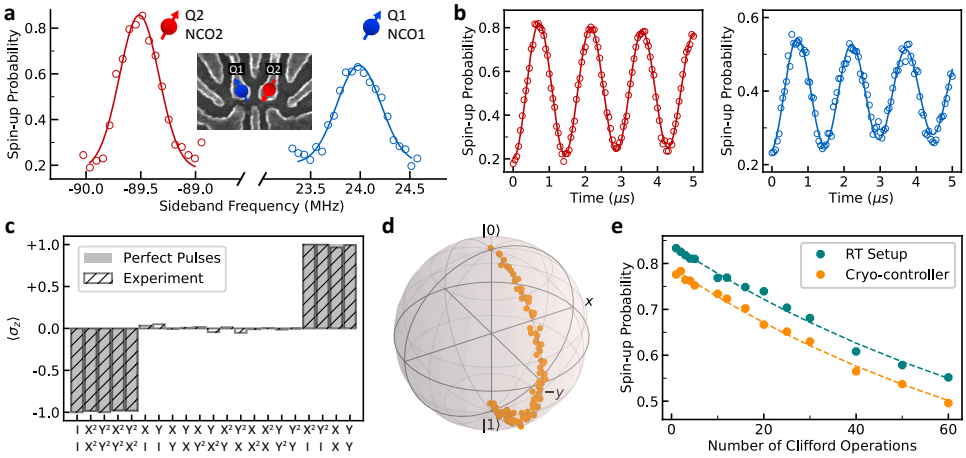

Fig. 8.5: Frequency-multiplexed qubit control and fidelity benchmarks with the cryo-controller a. Spectra showing the qubit resonances. Inset: SEM image indicating the qubits' positions. **b.** Frequency-multiplexed control producing simultaneous Rabi oscillations of Q_2 (left) and Q_1 (right). The decay arises mainly from the residual coupling between the two qubits (see 8.6.6 for Rabi oscillations in individual driving mode). **c.** $\langle\sigma_z\rangle$ of Q_2 measured after an AllXY sequence consisting of 21 different pairs of gates, each listed vertically on the X-axis. The output power is calibrated to achieve a $\sim$ 1 MHz Rabi frequency (the same applies to the QST and RB experiments). The visibility is normalized by removing the readout error (see 8.6.5). **d.** Trajectory of the state of Q_2 under an X^2 gate reconstructed by QST. Orange data points indicate the qubit state after incrementing microwave burst times. **e.** Randomized benchmarking of Q_2 performed by the cryo-controller and the room temperature setup. We offset the orange data points by -0.05 along the Y-axis to facilitate comparison of the two traces.

The pulses for single-qubit rotations are precisely calibrated using the AllXY sequence [33]. In the AllXY experiment, 21 different pairs of single-qubit gates from the set $\{I, X, Y, X^2, Y^2\}$ are applied to a qubit initialized to $|0\rangle$. Here I is the identity operation, X and Y are $\pi/2$ rotations around the $\hat{x}$ and $\hat{y}$ axis respectively, and X^2 and Y^2 are π rotations. The final state $\hat{z}$-projection $\langle\sigma_z\rangle$ takes values from $\{-1, 0, +1\}$ under perfect operations (shown as the gray shaded areas in Fig. 8.5c). Any miscalibration in the amplitude, frequency or phase of the pulse results in deviations from the ideal outcome (hatched bars in Fig. 8.5c). In addition, we reconstruct the trajectory of an X^2 gate by performing quantum-state tomography (QST) [34] at incremental burst times of a rectangular microwave signal (Fig. 8.5d), which shows an average state fidelity of 97.92%. Here the infidelity comes from the error during the operation as well as the errors in the initialization and readout of the qubit (see 8.6.5). The AllXY and QST results indicate that the single-qubit gate set is well calibrated, offering a good starting point for benchmarking the gate fidelity.

The gate fidelity is a crucial metric to express the performance of a quantum processor and its classical controller. We use single-qubit randomized benchmarking (RB) [35, 36] to compare the performance of the cryo-controller with the conventional room temperature (RT) setup, which consists of an arbitrary waveform generator (Tektronix 5014C) and a vector signal generator (Keysight E8267D). A programmable mechanical microwave switch placed at the 3 K plate allows to conveniently alternate between the cryo-controller and the RT setup. In the RB experiment, sequences of increasing numbers of randomly selected Clifford operations are applied to the qubit (Q_2), followed by a final Clifford operation that returns the qubit to its initial state in the ideal case. For each data point in Fig. 8.5e, 32 different sequences are randomly sampled and each is repeated 200 times. Envelopes of all gates to be used are uploaded to the envelope memory, and saved as instructions. The random sequences are constructed by updating the instruction list. The instructions in the list are executed sequentially after an external trigger via the SPI in Fig. 8.2a is received. Exactly the same random sequences are used in an RB experiment using the RT setup. We find an average single-qubit gate fidelity of $99.71 \pm 0.03\%$ with the RT setup and $99.69 \pm 0.02\%$ with the cryo-controller. The fidelities are consistently identical within the error bars and well above the threshold for fault-tolerance [37], with the infidelity limited by the qubit. These experiments demonstrate the high signal quality from the cryo-controller as well as its capability of generating complex sequences.

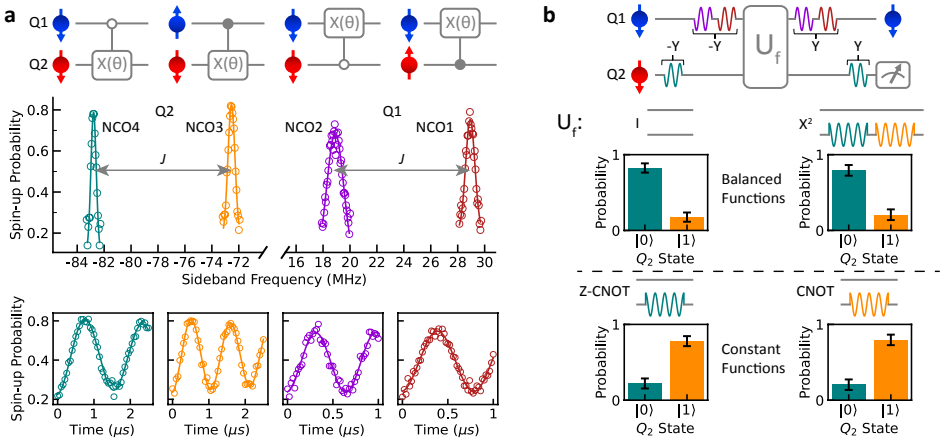

Fig. 8.6: Programming a quantum processor with the cryo-controller. a. Two-qubit logic with the cryo-controller. The middle panel shows the spectra of two qubits obtained using the cryo-controller with the exchange coupling (J) between the qubits turned on. Selective excitation of each of the four resonances can be used for implementing various two-qubit controlled-rotation gates, shown in the upper panel. The lower panels (shared Y-axis labels) show the Rabi oscillations at each frequency. **b.** (Top) Pulse sequences of the Deutsch–Josza algorithm programmed into the cryo-controller and (Bottom) measured probabilities of the output qubit state (Q_2) after running the algorithm. A constant function is composed of either a $CNOT$ or a Z-$CNOT$ gate, which consists of a $CROT$ gate on Q_2 and a phase correction on Q_1 (not plotted). Only the lower frequency (green branch, Z-$CROT$) is used for the $-Y$ and Y gate on Q_2 because Q_1 (ideally) starts from and ends up in $|0\rangle$. Error bars are standard deviations of the measured probability data. The visibility of Q_2 is normalized by removing the readout error. Empirically, we attribute the remaining errors mostly to charge noise in the presence of a finite J (see 8.6.6).

To further test the programmability of the cryo-controller, we use it to implement

two-qubit logic in the quantum processor. Taking advantage of the frequency shift of each qubit conditional on the state of the other qubit (Fig. 8.1b), we use controlled-rotation ($CROT$) gates as the native two-qubit gates. These are achieved by frequency selective addressing [21, 22], thus demanding 2 NCOs per qubit. A π-rotation at the higher or lower frequency implements the canonical controlled-NOT ($CNOT$) gate or the zero-controlled-NOT (Z-$CNOT$) gate respectively, up to a single-qubit $\pi/2$ $\hat{z}$-rotation on the control qubit. Due to cross-talk, an additional phase correction in the form of a $\hat{z}$-rotation is needed. All $\hat{z}$ rotations are implemented by updating the reference phase of the NCO (see 8.6.3). Single-qubit gates are implemented by addressing both frequencies of the same qubit sequentially. Making use of four NCOs, we program the cryo-controller to run the two-qubit Deutsch–Josza algorithm, which determines whether a function gives constant or balanced outcomes [38]. The two constant (balanced) functions that map one input bit on one output bit are implemented by the $CNOT$ and Z-$CNOT$ (I and X^2) operations. Here, we choose Q_1 to be the output qubit and Q_2 to be the input qubit. Fig. 8.6b shows the pulse sequence and the measurement results, where the constant (balanced) functions lead to a high probability of 78% - 80% (79% - 82%) for measuring the data qubit as $|1\rangle$ ($|0\rangle$), as expected. This experiment highlights the ability to program the cryo-controller with arbitrary sequences of operations.

The cryo-controller allows for much more complex sequences, containing up to 2048 instructions for each of the four transmitters. Each instruction defines a microwave burst at one of 32 independent frequencies with an amplitude and phase profile that can be arbitrarily shaped. The cryo-controller can be conveniently embedded in existing micro-architectures and programmed via standard QASM variants [39]. This quantum-classical architecture can thus be directly applied to multi-qubit algorithms and noisy intermediate-scale quantum devices [40].

8.5. CONCLUSION

The versatile programmability combined with the signal quality allowing up to 99.99% gate fidelities, the footprint of just 4 mm^2, the power consumption of 384 mW, the ability to integrate multiple transmitters on one die, and operation at 3 K, highlight the promise of cryo-controllers to address key challenges in building a large-scale quantum computer. Optimized design of cryogenic CMOS circuits, e.g. the use of a narrower frequency band, can substantially reduce the power consumption (see 8.6.3) and make it possible to work at 1 K or even lower temperatures. Furthermore, FinFET quantum dots have been developed that are fully compatible with CMOS processing [41] and increased operating temperatures ($\sim$ 1 K) of spin qubits show only a modest reduction in coherence times [16, 17]. These advances imply it may be possible to fully integrate the quantum processor with the classical controller on-chip or by flip-chip technology, lifting a major roadblock in scaling.

8.6. APPENDICES

8.6.1. SETUP IN DILUTION REFRIGERATOR

The real setup in the dilution refrigerator is shown in Fig. 8.7.

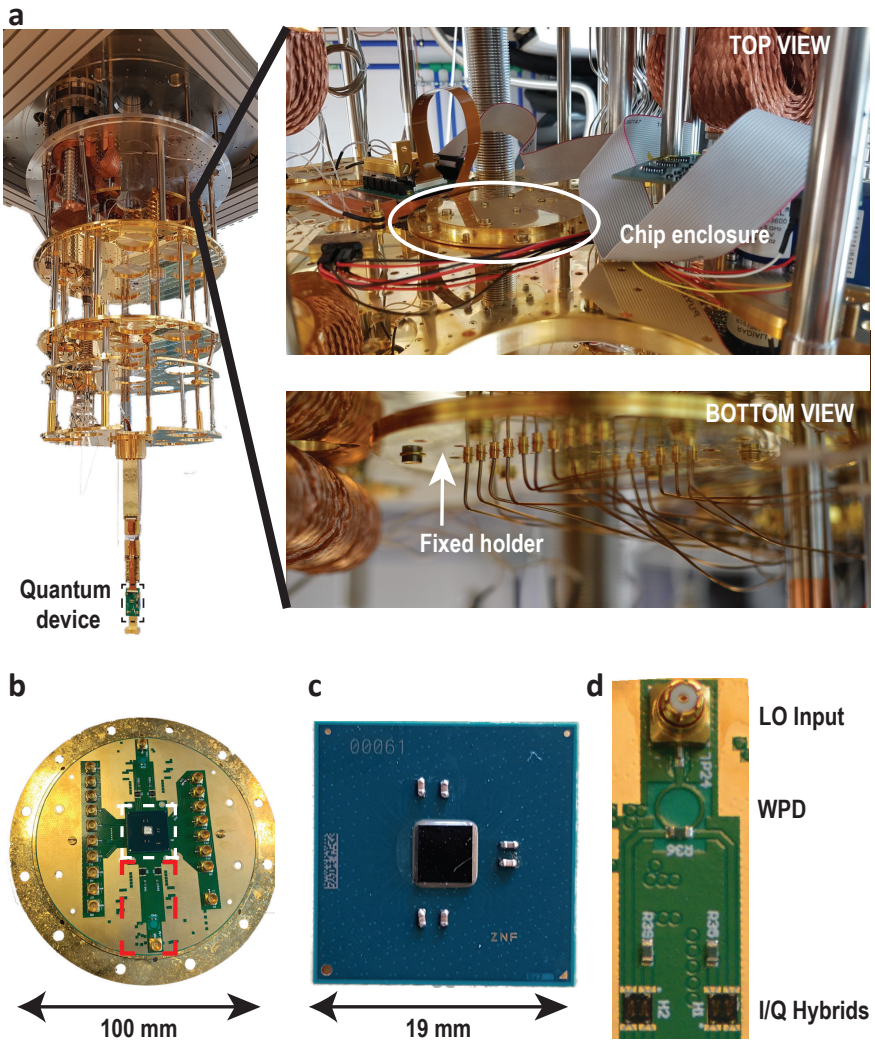

Fig. 8.7: Dilution refrigerator setup a. Location of the cryo-controller and the quantum device inside the dilution refrigerator (left). Top view and bottom view of the 3 K plate showing the mounted chip enclosure and the fixed holder for the enclosure respectively (right). **b.** Top view of the gold-plated annealed copper enclosure (without the lid) which is used to mount and thermalize the cryo-controller. **c.** Ball-grid-array(BGA)-324 package hosting the cryo-controller chip with on-package decoupling capacitors (highlighted as white box in **b**). **d.** The Wilkinson power divider (WPD) splits the input LO power into two equal paths with half power in each implemented on a PCB. Discrete I/Q hybrids create the in-phase and quadrature phase component of the input LO are wire-bonded on the PCB for LO distribution between the different transmitters inside the cryo-controller (highlighted as red box in **b**).

8.6.2. PROGRAMMING THE CRYO-CONTROLLER

The setup contains a field-programmable gate array (FPGA) that configures the cryo-controller (e.g. FTW), programs the various memories inside the cryo-controller (e.g. envelope memories, instruction tables and instruction lists), and controls the start of the execution of the instruction list. The FPGA is connected to the host PC, which sends the data that needs to be uploaded to the cryo-controller over the SPI. The instruction list integrated in the cryo-controller does not support classical instructions that allow for e.g. branching or wait statements, as required for performing certain qubit experiments and for synchronization with other equipment. Therefore, switching between different instruction lists and synchronization with the rest of the equipment, is controlled by two trigger lines from the AWG to the FPGA. The application of the *execute* trigger starts the execution of the instruction list that is programmed in the cryo-controller, for performing repeated measurements. The application of the *sweep* trigger loads the next instruction list from the FPGA SRAM into the cryo-controller's instruction list.

8.6.3. CIRCUIT DETAIL AND POWER BUDGET

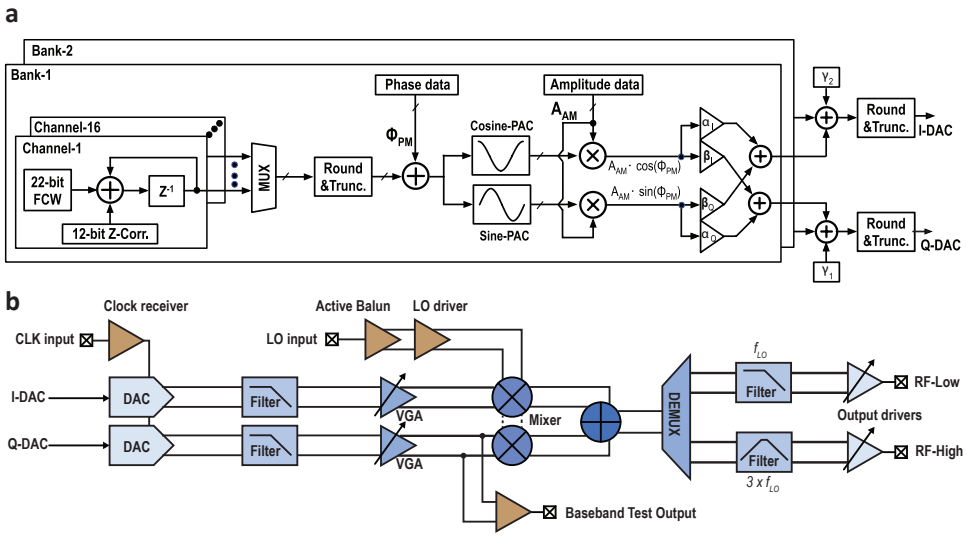

Fig. 8.8: Detailed cryo-controller schematic a. Detailed representation of the digital circuitry. **b.** Detailed system-level schematic of the analog circuity inside the controller.

A detailed schematic of the cryo-controller is given in Fig. 8.8. All memory blocks except NCO phase update registers ((to perform phase corrections: 'Z-corr' in Fig. 8.8) are implemented using SRAM. The high power consumption of the digital circuitry of the cryo-controller (Fig. 8.9) is caused due to the lack of clock gating in registers, thus causing them to continuously operate instead of just during the read/write cycle. This could easily be reduced by further optimizations (e.g. by replacing more registers with SRAM memory and by adding clock gating), that were not yet included in the first gen-

eration cryo-controller. Based on the Cadence simulation with clock-gating, the power consumption of the digital circuitry should be lower than 40 mW instead of 330 mW in the current design. Migrating to a finer technology node would result in further substantial power savings [23].

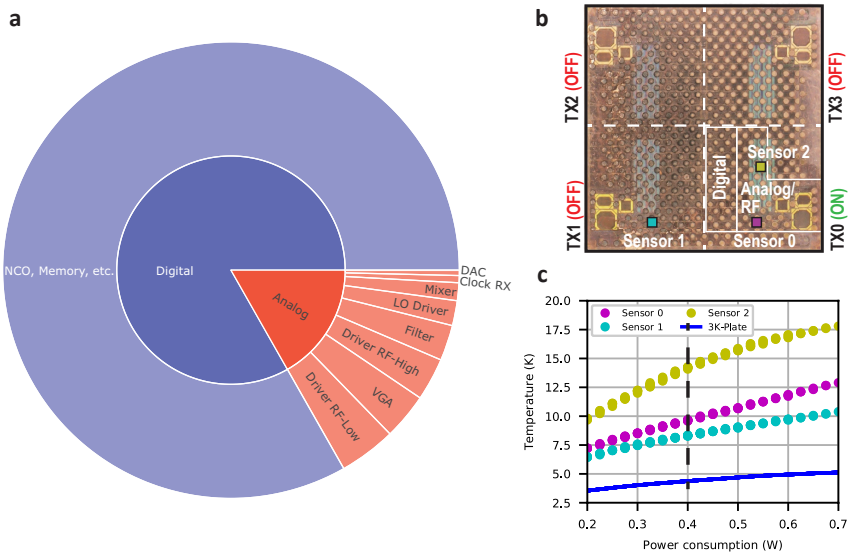

Fig. 8.9: Power consumption and self-heating of the cryo-controller. a. Power consumption pie chart showing the contribution of the digital and analog circuits in the cryo-controller. The power-consumption breakdown of individual circuit blocks are shown for the analog circuits. The digital circuits use a 0.7 V supply and the analog circuits use a 1 V supply. **b.** Chip micrograph showing the on-chip bumps used as I/Os. The locations of on-chip temperature sensing diodes and the analog and digital circuitry (in TX0) are highlighted. **c.** The measured on-chip and 3 K plate temperature using different sensors versus the power consumption of TX0, as reported in [5]. The power consumption is varied by changing the clock frequency of the chip. The nominal operating point for the work presented here and corresponding temperatures are highlighted with a dashed vertical line. All the other transmitters (TX1, TX2, TX3) are switched OFF in this measurement.

Moreover, this chip was designed to address both transmons and spin qubits and hence an ultra-wide output frequency range was supported i.e. 2 to 20 GHz with an LO frequency of 2.5 to 14.5 GHz, using both fundamental and third harmonic outputs (Fig. 8.3.b). Once the qubit frequency is fixed within a few GHz range, the power consumption of the analog circuitry can be significantly reduced to limit the power consumption to ~ 20 mW instead of 54 mW. In the current architecture (see 8.6.3 and Ref. [5]), such power savings can be achieved by: (1) Eliminating the output drivers and compensating the gain loss by increasing the matching network impedance transformation, as allowed by the reduced frequency range, which also results in a higher mixer load and consequently lower VGA bias current (2) Replacing the folded-current topology of the anti-aliasing filter with a stacked topology. (3) Replacing the active balun before the LO drivers with a passive matching network. Further power savings could be achieved by architecture improvements, e.g. by replacing the gm-C filter with a passive filter, thus

eliminating the power consumption of the filter [23]. Moreover, the integration of a PLL can eliminate I/Q active baluns completely.

8.6.4. QUBIT READOUT

The readout scheme has described in Chapter 2. We summarize it as follows. After each operation sequence, Q_2 is measured by spin-selective tunneling to the electron reservoir, where a spin-up ($|1\rangle$) electron can tunnel out and a spin-down ($|0\rangle$) electron is blockaded from tunneling out. Such a spin-to-charge conversion changes the charge occupancy in the quantum dot conditional on the spin state. This in turn changes the current signal in an adjacent capacitively coupled single-electron-transistor (SET). Single-shot readout of the qubit state can be done by thresholding the current signal through the SET [31]. The post-measurement state in this readout protocol is the $|0\rangle$ state, serving as reinitialization. Q_1 is tuned to be only weakly coupled to the SET, which serves as the electron reservoir for Q_1. This is to minimize the back-action from the SET, but also makes it less efficient to readout Q_1 by spin-selective tunneling to the SET. Therefore, with Q_2 reinitialized, a *CROT* gate is applied to map the state of Q_1 onto Q_2. Then Q_1 is readout by measuring Q_2 again [31]. The readout fidelity of Q_2 is mainly limited by the thermal broadening of the electron reservoir, and the readout fidelity of Q_1 is limited by both the error in the *CROT* gate and in the readout of Q_2. Thus the readout visibility of Q_1 is lower than Q_2. Alternatively, Q_1 could have been read out by shuttling the electron to the location of Q_2 after emptying the dot hosting Q_2. We here chose to map the state of Q_1 onto that of Q_2 using a *CROT* gate, since this reduces charging effects on the bias-tees on the PCB. The *CROT* gate used here is also executed by the cryo-controller.

8.6.5. READOUT ERROR REMOVAL

In the AllXY experiments and in the implementation of the Deutsch-Jozsa algorithm, the readout probabilities of Q_2 are normalized with calibrated readout fidelities $(F_{|0\rangle}, F_{|1\rangle})$. After preparing Q_2 in $|0\rangle$, $F_{|0\rangle}$ can be calibrated directly through the measured spin-down probability, and $F_{|1\rangle}$ is calibrated through the measured spin-up probability after a spin-flip operation (the spin-flip fidelity is above 99%). Based on the measured state probabilities in the AllXY and Deutsch-Jozsa experiments, $\mathbf{P^M} = (P^M_{|0\rangle}, P^M_{|1\rangle})^T$, the actual state probabilities $(P_{|0\rangle}, P_{|1\rangle})$ can be reconstructed by $\mathbf{P} = \mathbf{F}^{-1}\mathbf{P^M}$, where

$$\mathbf{F} = \begin{pmatrix} F_{|0\rangle} & 1-F_{|1\rangle} \\ 1-F_{|0\rangle} & F_{|1\rangle} \end{pmatrix}. \tag{8.1}$$

8.6.6. ERROR SOURCES

In the simultaneous Rabi oscillation experiment (Fig.8.5), we attribute the visible decays in both curves to the residual exchange coupling between the two qubits. Simultaneous Rabi oscillations recorded (in this case using the RT setup) over larger numbers of oscillations show beating patterns. These patterns are well reproduced by numerical models of the spin evolution in the presence of a finite residual exchange coupling. Such a beating effect looks like a decay in the beginning. It is absent in the individually driven

Rabi oscillation (Fig. 8.10). In the two-qubit experiments shown in Fig. 8.6, the decay in the controlled-rotation Rabi oscillations and the finite visibilities in the Deutsch-Jozsa algorithm are largely attributed to charge noise. With the exchange coupling turned on, as needed for two-qubit gates, the energy levels are much more sensitive to charge noise.

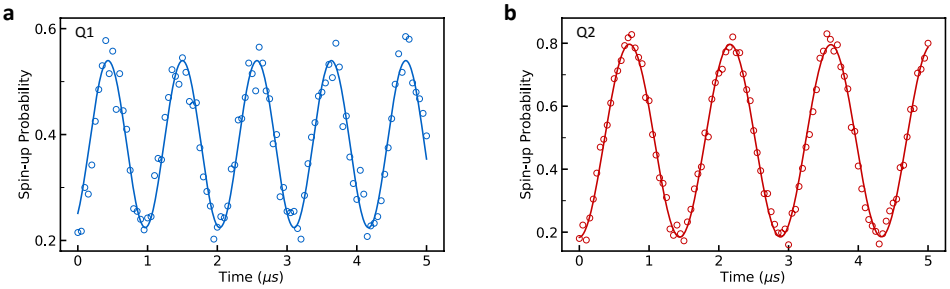

Fig. 8.10: Rabi oscillations of qubits individually driven by the cryo-controller. The output frequency of two NCOs are set to the frequencies of Q_1 and Q_2 respectively, but only one NCO is active each time. Using the same method as described in the main text, Rabi oscillations of Q_1 (**a**) and Q_2 (**b**) are measured individually. Compared to the simultaneous Rabi oscillations shown in Fig. 8.5.b, the decay is much slower in the individual driving experiments.

8.6.7. QUANTUM STATE TOMOGRAPHY

In the QST experiment, the qubit state is measured by projecting it onto the $(-\hat{z}, +\hat{x}, -\hat{y}, +\hat{z})$ axes. The projection on the $-\hat{z}$ axis is measured by direct readout of the spin state, while the projections on other axes are measured by applying a X, Y, or X^2 gate, which are calibrated by the AllXY experiment, before the readout. The trajectory of the qubit state in the course of a X^2 gate can be reconstructed by performing QST at incremental burst times of a rectangular microwave signal (Fig.8.5.c.), with each measurement repeated 1,000 times. To visualize the qubit state in the Bloch sphere, we remove the readout error from the data. Since error removal can lead to unphysical states such as data points outside the Bloch sphere, a maximum likelihood estimation is implemented to find the closest physical state of the qubit [34]. The ideal quantum state at each burst time can be predicted using the Rabi frequency fitted from experimental data. We then calculate the quantum state fidelities at each burst time and obtain an average state fidelity of 97.92%. The difference between this number and the fidelity obtained from randomized benchmarking is mostly from residual state preparation and measurement (SPAM) error after imperfect readout error removal.

REFERENCES

[1] L. M. K. Vandersypen, H. Bluhm, J. S. Clarke, A. S. Dzurak, R. Ishihara, A. Morello, D. J. Reilly, L. R. Schreiber, and M. Veldhorst, *Interfacing spin qubits in quantum dots and donors–hot, dense, and coherent,* npj Quantum Information **3**, 34 (2017).

[2] R. Van Meter and C. Horsman, *A blueprint for building a quantum computer,* Communications of the ACM **56**, 84 (2013).

[3] F. Arute, K. Arya, R. Babbush, D. Bacon, J. C. Bardin, R. Barends, R. Biswas, S. Boixo, F. G. Brandao, D. A. Buell, *et al.*, *Quantum supremacy using a programmable superconducting processor,* Nature **574**, 505 (2019).

[4] J. C. Bardin, E. Jeffrey, E. Lucero, T. Huang, S. Das, D. T. Sank, O. Naaman, A. E. Megrant, R. Barends, T. White, *et al.*, *Design and Characterization of a 28-nm Bulk-CMOS Cryogenic Quantum Controller Dissipating Less Than 2 mW at 3 K,* IEEE Journal of Solid-State Circuits **54**, 3043 (2019).

[5] B. Patra, J. P. van Dijk, S. Subramanian, A. Corna, X. Xue, C. Jeon, F. Sheikh, E. Juarez-Hernandez, B. P. Esparza, H. Rampurawala, *et al.*, *A Scalable Cryo-CMOS 2-to-20GHz Digitally Intensive Controller for 4× 32 Frequency Multiplexed Spin Qubits/Transmons in 22nm FinFET Technology for Quantum Computers,* in *2020 IEEE International Solid-State Circuits Conference-(ISSCC)* (IEEE, 2020) pp. 304–306.

[6] L. Le Guevel, G. Billiot, X. Jehl, S. De Franceschi, M. Zurita, Y. Thonnart, M. Vinet, M. Sanquer, R. Maurand, A. G. Jansen, *et al.*, *A 110mK 295μW 28nm FDSOI CMOS Quantum Integrated Circuit with a 2.8 GHz Excitation and nA Current Sensing of an On-Chip Double Quantum Dot,* in *2020 IEEE International Solid-State Circuits Conference-(ISSCC)* (IEEE, 2020) pp. 306–308.

[7] S. Bonen, U. Alakusu, Y. Duan, M. Gong, M. Dadash, L. Lucci, D. Daughton, G. Adam, S. Iordănescu, M. Păşteanu, *et al.*, *Cryogenic characterization of 22-nm FDSOI CMOS technology for quantum computing ICs,* IEEE Electron Device Letters **40**, 127 (2018).

[8] A. Esmailiyan, H. Wang, M. Asker, E. Koskin, D. Leipold, I. Bashir, K. Xu, A. Koziol, E. Blokhina, and R. B. Staszewski, *A Fully Integrated DAC for CMOS Position-Based Charge Qubits with Single-Electron Detector Loopback Testing,* IEEE Solid-State Circuits Letters (2020).

[9] S. R. Ekanayake, T. Lehmann, A. S. Dzurak, R. G. Clark, and A. Brawley, *Characterization of SOS-CMOS FETs at low temperatures for the design of integrated circuits for quantum bit control and readout,* IEEE Transactions on Electron Devices **57**, 539 (2010).

[10] O. Mukhanov, A. Kirichenko, C. Howington, J. Walter, M. Hutchings, I. Vernik, D. Yohannes, K. Dodge, A. Ballard, B. Plourde, *et al.*, *Scalable Quantum Computing Infrastructure Based on Superconducting Electronics,* in *2019 IEEE International Electron Devices Meeting (IEDM)* (IEEE, 2019) pp. 31–2.

[11] B. Patra, R. M. Incandela, J. P. Van Dijk, H. A. Homulle, L. Song, M. Shahmohammadi, R. B. Staszewski, A. Vladimirescu, M. Babaie, F. Sebastiano, *et al.*, *Cryo-CMOS circuits and systems for quantum computing applications,* IEEE Journal of Solid-State Circuits **53**, 309 (2018).

[12] S. Pauka, K. Das, R. Kalra, A. Moini, Y. Yang, M. Trainer, A. Bousquet, C. Cantaloube, N. Dick, G. Gardner, *et al.*, *A cryogenic interface for controlling many qubits,* arXiv:1912.01299 (2019).

[13] Y. Xu, F. Unseld, A. Corna, A. Zwerver, A. Sammak, D. Brousse, N. Samkharadze, S. Amitonov, M. Veldhorst, G. Scappucci, *et al.*, *On-chip integration of Si/SiGe-based quantum dots and switched-capacitor circuits,* Applied Physics Letters **117**, 144002 (2020).

[14] G. Batey, A. Matthews, and M. Patton, *A new ultra-low-temperature cryogen-free experimental platform,* in *Journal of Physics: Conference Series*, Vol. 568 (2014) p. 032014.

[15] M. Green, *The cost of coolers for cooling superconducting devices at temperatures at 4.2 K, 20 K, 40 K and 77 K,* in *IOP Conference Series: Materials Science and Engineering*, Vol. 101 (IOP Publishing, 2015) p. 012001.

[16] L. Petit, H. Eenink, M. Russ, W. Lawrie, N. Hendrickx, S. Philips, J. Clarke, L. Vandersypen, and M. Veldhorst, *Universal quantum logic in hot silicon qubits,* Nature **580**, 355 (2020).

[17] C. H. Yang, R. Leon, J. Hwang, A. Saraiva, T. Tanttu, W. Huang, J. C. Lemyre, K. W. Chan, K. Tan, F. E. Hudson, *et al.*, *Operation of a silicon quantum processor unit cell above one kelvin,* Nature **580**, 350 (2020).

[18] M. Urdampilleta, D. J. Niegemann, E. Chanrion, B. Jadot, C. Spence, P.-A. Mortemousque, C. Bäuerle, L. Hutin, B. Bertrand, S. Barraud, *et al.*, *Gate-based high fidelity spin readout in a CMOS device,* Nature Nanotechnology , 1 (2019).

[19] J. M. Boter, J. P. Dehollain, J. P. van Dijk, T. Hensgens, R. Versluis, J. S. Clarke, M. Veldhorst, F. Sebastiano, and L. M. Vandersypen, *A sparse spin qubit array with integrated control electronics,* in *2019 IEEE International Electron Devices Meeting (IEDM)* (IEEE, 2019) pp. 31–4.

[20] T. F. Watson, S. G. J. Philips, E. Kawakami, D. R. Ward, P. Scarlino, M. Veldhorst, D. E. Savage, M. G. Lagally, M. Friesen, S. N. Coppersmith, M. A. Eriksson, and L. M. K. Vandersypen, *A programmable two-qubit quantum processor in silicon,* Nature **555**, 633 (2018).

[21] D. M. Zajac, A. J. Sigillito, M. Russ, F. Borjans, J. M. Taylor, G. Burkard, and J. R. Petta, *Resonantly driven cnot gate for electron spins,* Science **359**, 439 (2017).

[22] W. Huang, C. Yang, K. Chan, T. Tanttu, B. Hensen, R. Leon, M. Fogarty, J. Hwang, F. Hudson, K. M. Itoh, A. Morello, A. Laucht, and A. S. Dzurak, *Fidelity benchmarks for two-qubit gates in silicon,* Nature **569**, 532 (2019).

[23] J. P. van Dijk, B. Patra, S. Pellerano, E. Charbon, F. Sebastiano, and M. Babaie, *Designing a DDS-based SoC for high-fidelity multi-qubit control,* IEEE Transactions on Circuits and Systems I: Regular Papers **67**, 5380 (2020).

[24] A. Beckers, F. Jazaeri, and C. Enz, *Characterization and modeling of 28-nm bulk CMOS technology down to 4.2 K,* IEEE Journal of the Electron Devices Society **6**, 1007 (2018).

[25] P. A. T Hart, M. Babaie, E. Charbon, A. Vladimirescu, and F. Sebastiano, *Subthreshold Mismatch in Nanometer CMOS at Cryogenic Temperatures,* IEEE Journal of the Electron Devices Society **8**, 797 (2020).

[26] B. Patra, M. Mehrpoo, A. Ruffino, F. Sebastiano, E. Charbon, and M. Babaie, *Characterization and analysis of on-chip microwave passive components at cryogenic temperatures,* IEEE Journal of the Electron Devices Society **8**, 448 (2020).

[27] M. Pioro-Ladrière, T. Obata, Y. Tokura, Y.-S. Shin, T. Kubo, K. Yoshida, T. Taniyama, and S. Tarucha, *Electrically driven single-electron spin resonance in a slanting zeeman field,* Nature Physics **4**, 776 (2008).

[28] L. M. K. Vandersypen and I. L. Chuang, *NMR techniques for quantum control and computation,* Rev. Mod. Phys. **76**, 1037 (2005).

[29] J. R. Petta, A. C. Johnson, J. M. Taylor, E. A. Laird, A. Yacoby, M. D. Lukin, C. M. Marcus, M. P. Hanson, and A. C. Gossard, *Coherent manipulation of coupled electron spins in semiconductor quantum dots,* Science **309**, 2180 (2005).

[30] T. Meunier, V. E. Calado, and L. M. K. Vandersypen, *Efficient controlled-phase gate for single-spin qubits in quantum dots,* Phys. Rev. B **83**, 121403 (2011).

[31] X. Xue, B. D'Anjou, T. F. Watson, D. R. Ward, D. E. Savage, M. G. Lagally, M. Friesen, S. N. Coppersmith, M. A. Eriksson, W. A. Coish, *et al., Repetitive quantum nondemolition measurement and soft decoding of a silicon spin qubit,* Phys. Rev. X **10**, 021006 (2020).

[32] P. Saul and M. Mudd, *A direct digital synthesizer with 100-MHz output capability,* IEEE journal of solid-state circuits **23**, 819 (1988).

[33] M. Reed, *Entanglement and Quantum Error Correction with Superconducting Qubits,* PhD Thesis, Yale Univ. (2013).

[34] J. B. Altepeter, E. R. Jeffrey, and P. G. Kwiat, *Photonic state tomography,* Advances in Atomic, Molecular, and Optical Physics **52**, 105 (2005).

[35] E. Knill, D. Leibfried, R. Reichle, J. Britton, R. B. Blakestad, J. D. Jost, C. Langer, R. Ozeri, S. Seidelin, and D. J. Wineland, *Randomized benchmarking of quantum gates,* Phys. Rev. A **77**, 012307 (2008).

[36] E. Magesan, J. M. Gambetta, and J. Emerson, *Characterizing quantum gates via randomized benchmarking,* Phys. Rev. A **85**, 042311 (2012).

[37] A. G. Fowler, M. Mariantoni, J. M. Martinis, and A. N. Cleland, *Surface codes: Towards practical large-scale quantum computation,* Phys. Rev. A **86**, 032324 (2012).

[38] D. Deutsch and R. Jozsa, *Rapid solution of problems by quantum computation,* Proceedings of the Royal Society of London. Series A: Mathematical and Physical Sciences **439**, 553 (1992).

[39] K. M. Svore, A. V. Aho, A. W. Cross, I. Chuang, and I. L. Markov, *A layered software architecture for quantum computing design tools,* Computer **39**, 74 (2006).

[40] J. Preskill, *Quantum computing in the NISQ era and beyond,* Quantum **2**, 79 (2018).

[41] R. Pillarisetty, N. Thomas, H. George, K. Singh, J. Roberts, L. Lampert, P. Amin, T. Watson, G. Zheng, J. Torres, *et al., Qubit device integration using advanced semiconductor manufacturing process technology,* in *2018 IEEE International Electron Devices Meeting (IEDM)* (IEEE, 2018) pp. 6–3.

9

CONCLUSION AND OUTLOOK

9.1. CONCLUSION

A fault-tolerant quantum computer needs to be built on logical qubits, with each of them containing a certain number of physical qubits in order to correct errors in real time [1]. We anticipate a few challenges on the way: operating quantum logic at high gate fidelities; reading out the physical qubit states using fast and high-fidelity quantum nondemolition measurements; understanding and precisely characterizing noise correlations and crosstalk errors; achieving large-scale quantum control by reducing the interconnect complexity between quantum processors and classical control units. In this dissertation, I have discussed the milestones that we have reached towards the final grand goal. Importantly, we have quantitatively benchmarked the performance of silicon quantum processors on the above-mentioned aspects.

9.1.1. HIGH-FIDELITY QUANTUM LOGIC

Quantum logic fidelities of spin qubits are studied in **Chapter 3** and **Chapter 7**, using a natural silicon device and an isotopically purified silicon (^{28}Si/SiGe) device respectively. The two-qubit CPhase gate is the main focus in both works. We have made significant improvement in the latter work where the CPhase gate fidelity is higher than 99.5%, well above the threshold for surface code [2]. These works together broke perhaps the biggest barrier for spin qubits – demonstrating a high-fidelity two-qubit gate.

NATURAL SILICON DEVICE

In **Chapter 3**, a two-qubit system in a natural silicon device is completely benchmarked using randomized benchmarking (RB).

- Individually performed single-qubit RB experiments show that single-qubit gate fidelities are around 99% when the other qubit is idle. These numbers decrease to 98.8% for qubit 1 and to 96.9% for qubit 2 in simultaneous RB, with additional errors coming from the crosstalk between single-qubit gates.

- The fidelity of the CPhase gate is estimated to be 92% by character randomized benchmarking. The dominating errors include nuclear spin noise from the ^{29}Si atoms, charge noise which couples to the energy detuning between the quantum dots, and Hamiltonian errors from imperfect adiabaticity in the pulses.

- An improved RB approach, namely character randomized benchmarking (CRB), is proposed and applied to the two-qubit system. Compared to conventional two-qubit RB, CRB is capable for benchmarking the two-qubit system more efficiently, and it naturally separates the three noise channels, i.e. two single-qubit noise channels and a two-qubit correlated noise channel. This approach can reliably characterize not only gate fidelities but also the correlated errors between qubits, all from one single execution.

PURIFIED SILICON DEVICE

In **Chapter 7**, a two-qubit system in an isotopically purified silicon device is completely benchmarked using gate set tomography (GST).

- The exchange interaction between the two spins is precisely calibrated at the "symmetry point" using only barrier control, which is more robust against charge noise compared to the detuning control [3, 4]. The pulse of the CPhase gate is shaped for adiabatic control and thus reduces the Hamiltonian errors.

- GST is utilized to characterize the process matrices and to diagnose the errors of all single- and two-qubit gates used in the two-qubit state space. The gate parameters are adjusted using this information to further correct the residual Hamiltonian errors.

- After optimization, the fidelity of a CPhase gate reaches >99.5%, well above the commonly referred 99% threshold for quantum error correction. Numerical simulations based on a realistic noise model indicate that the achieved fidelity is not limited by coherence yet, meaning that it is possible to further boost the fidelity by more advanced Hamiltonian engineering.

9.1.2. NOISE CORRELATIONS AND CROSSTALK

We study the spatial noise correlations and crosstalk errors between nearby qubits in **Chapter 4** and **Chapter 5**. These errors are considered as major bottlenecks for scaling. Correlated noise can actually be useful in many occasions if they are precisely characterized, e.g. quantum algorithms can be designed into a decoherence-free subspace; the error on a qubit can be corrected by only measuring the error on a correlated ancilla qubit. For spin qubits, correlated noise is expected to mostly come from charge noise, whereas the hyperfine interaction is believed to be only a local effect. Different from correlated noise, crosstalk errors are mostly harmful to quantum operations and must be mitigated from the source. Most crosstalk errors directly come from the control signals. They can result in unintentional qubit rotations or decoherence. A deeper understanding of these crosstalk effects will help to compensate them via improving the experimental setup.

SPATIAL NOISE CORRELATIONS

Spatial noise correlations between two idle spin qubits in a natural silicon device are studied in **Chapter 4**.

- Noise correlations are quantified by the coherence times measured in two different decoherence-free subspaces (DFSs). These DFSs are spanned by Bell states with parallel spins and anti-parallel spin states respectively, and thus they are only sensitive to either correlated errors (parallel Bell state) or anti-correlated errors (anti-parallel Bell state).

- A small spatial correlation factor of ~ 0.31 in low-frequency noise is observed, while correlations of noise at higher frequency are absent. The observed small correlation can be explained by a combination of noise from remote charge fluctuators which has different noise amplitudes on the two spins, and the nuclear spin noise which typically has only local effect.

CROSSTALK IN SINGLE-QUBIT OPERATIONS

Chapter 5 presents the microscopic origin of the nonlinear response in EDSR and the consequential crosstalk effects in simultaneously driven spin qubits in a purified silicon device.

- The electric dipole moment in Si/SiGe quantum dots comes from hybridized valley-orbit states, which is the major mechanism for EDSR. The anharmonicity in the valley-orbitals can give rise to the nonlinear dependence of the Rabi frequency on the amplitude of the driving signals.
- The nonlinear response in EDSR leads to an undesired distortion of driving signals under large oscillating electric fields. This forms a crosstalk channel between qubits being simultaneously driven, and is observed from a reduced Rabi frequency of each qubit compared to that measured in the individual driving mode.

9.1.3. QUANTUM NONDEMOLITION MEASUREMENT

In error correction codes, the errors of a data qubit needs to be detected via quantum nondemolition measurement using adjacent ancilla qubits [1]. In **Chapter 6**, QND measurement of a spin qubit is studied in silicon quantum dots, with a second spin qubit used as the readout ancilla.

- High-fidelity measurement of a spin qubit in silicon is achieved by repetitively executing QND measurements. Each QND loop consists of two steps: mapping the data qubit state to the ancilla using a two-qubit CROT gate and then measuring the ancilla state using spin-selective tunnelling. The total measurement fidelity is enhanced from 75% in a single QND measurement to 95% for 15 QND repetitions.
- An improved signal processing method – soft decoding, which makes use of the analog information in the readout signal, is studied and compared with the conventional threshold method. When the readout errors are limited by Gaussian noise, soft decoding can significantly reduce the number of QND measurements required to achieve a certain readout fidelity. This method will be advantageous in scenarios where the signal-to-noise ratio (SNR) is low, such as gate-based readout, and readout at elevated temperatures.

9.1.4. SCALABLE CRYOGENIC CONTROL

A scalable solution to the interconnect bottleneck of a quantum computer would be the so-called quantum integrated circuit [5]. In **Chapter 8**, a milestone is achieved by placing a CMOS control chip (cryo-controller) at cryogenic temperature and using it to implement universal two-qubit operations. The capability of this chip is tested in various experiments. Importantly, it is verified that the control fidelity of the cryo-controller matches that reached using the state-of-art commercial instrumentation at room temperature.

- The cryo-controller is fabricated in Intel 22 nm-FinFET low-power CMOS technology [6]. It is operated at 3 K and outputs tailored microwave bursts to coherently control spin qubits in a silicon chip which is cooled to ~ 20 mK.

- Extensive electrical characterizations show that the design of this cryo-controller allows up to 99.99% single-qubit gate fidelity. A fidelity of 99.7% is consistently obtained from randomized benchmarking of a real spin qubit using both the cryo-controller and the commercial control instruments.

- The versatile programmability, the small footprint, and the low power consumption of the cryo-controller, show that the wiring bottleneck of a quantum computer can be potentially solved by the co-integration of such cryo-controllers with quantum processors on the same die/package.

9.2. OUTLOOK

While we believe that a few crucial steps towards a real silicon quantum computer have been made via the works presented in this dissertation, new challenges keep showing up. We now discuss a few well-know but not yet addressed problems: the heating problem, the crosstalk in EDSR, and a scalable architecture with micromagnets.

9.2.1. HEATING PROBLEMS

Microwave bursts used for single-qubit rotations can cause local heating effects on the quantum dots. We first clarify that we here use the term "heating" since the observed behavior shows similarities to what would be observed for thermal heating, but we are not certain that an actual temperature increase of the sample underlies the observations. For this reason, effects such as the Stark shift or any other type of instantaneous parameter change are not considered as heating effects. A heating effect is built up smoothly, and reaches an equilibrium stage after a certain burst duration. Once the microwave burst is turned off, the effect gradually disappears. This makes the heating effect generally time-dependent within a quantum circuit, and thus it can cause non-Markovian errors in benchmarking experiments [7]. In addition, the impact is typically dependent on the power or amplitude of the microwave pulses.

Three well-known consequences of heating are the thermal broadening of the electron reservoir and the charge sensor, the modulation of the qubit parameters especially the qubit frequencies, and faster decoherence of the qubit states. Solving the first problem is perhaps of less urgency, as the reservoir and the sensor are mainly used for qubit readout, whereas the recently developed gate-based readout technique can be implemented without theses components [8–11]. In contrast, the modulation of the qubit parameters and the heating-induced decoherence are harder to circumvent. While the parameter modulations might be compensated coherently by Hamiltonian engineering, the feature of time-dependence, and more importantly, device-dependence make it rather complicated to calibrate.

Fig. 9.1 shows an example of the frequency shift induced by microwave heating, observed in a ^{28}Si/SiGe device that has been used for the works in Chapter 5, 7 and 8. In this experiment, an off-resonance burst which is far detuned from the qubit (Q2) frequency is applied, followed by a pre-calibrated π-rotation pulse (X_{180}). We observe both a frequency shift of the qubit as well as a decrease in the visibility of the readout signal. The frequency shift behaves as a clear heating-like effect, and it approaches thermal equilibrium after $\sim 50\,\mu$s. To verify the feature of heating, we perform another experiment to

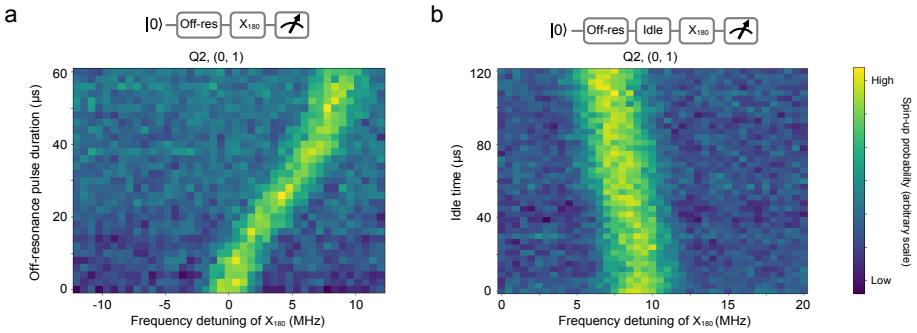

Fig. 9.1: a. Frequency shift as a function of the burst time of an off-resonance pulse, which is generated at the same power as the X_{180} gate, and is detuned from the qubit freqeuency by -80 MHz. The horizontal axis shows the frequency detuning of the X_{180} gate with respect to its pre-calibrated frequency, which is roughly at the qubit frequency. The vertical axis is the total duration of the off-resonance burst. **b.** Frequency shift as a function of the idle time between a 60 μs off-resonance burst and the X_{180} gate, which is shown on the vertical axis. To eliminate the possibility that crosstalk from the other qubit plays a role, the double dot is set to (0,1) charge configuration in these experiments.

test the "cooling" effect. Now the off-resonance pulse is fixed at 60 μs to make the qubit start from the equilibrium state, and we vary the waiting time before the X_{180} gate. The result shows that the qubit frequency slowly shifts backwards, just like a cooling process.

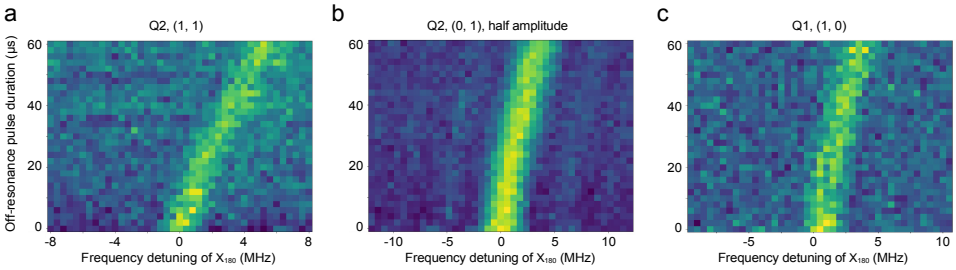

Fig. 9.2: a. Frequency shift of Q2 with a second qubit (Q1) present in the measurement. Q1's frequency is detuned from Q2 by ~ +100 MHz and thus it's not affected by the off-resonance pulse. **b.** Frequency shift of Q2 with the off-resonance pulse amplitude set to half of the X_{180} pulse amplitude. **c.** Frequency shift of Q1 measured in the absence of Q2.

To further investigate this effect, we perform a few similar heating tests under different conditions. First, the same experiment as in Fig 9.1a is performed on Q2 but with the second quantum dot loaded with one electron. a similar frequency shift is observed, while the saturation effect is not seen in the measurement window. The difference might be related to additional crosstalk or capacitive coupling between the two qubits. Second, we perform the same measurement on Q2 in the (0,1) charge configuration but with the amplitude of the off-resonance pulse lowerd by half. We see that the frequency shift is roughly reduced by half, and the saturation is still far from reach in 60 μs. This well verifies the heating hypothesis. Third, we execute the heating test on Q1 in the (1,0) charge configuration, and have observed a smaller heating effect. Note that the

frequency shift of Q1 cannot be directly compared to Q2, because it has a different frequency and thus the microwave power delivered to the sample is different, due to the frequency-dependent attenuation in the control lines.

There have been several heating mechanisms proposed, including local lattice heating, rectifications in quantum dot confinement, charging and discharging in the heterostructure or off-chip electronic components [7, 12]. Although the heating effect is frequently observed in experiments, till now almost all attempts to quantitatively explain it have failed. Addressing the heating problem is certainly an important step in future spin qubit research.

9.2.2. REDUCING CROSSTALK

Whereas heating effects can be a form of crosstalk, in this section we use the term crosstalk to refer to effects that occur instantaneously. The errors directly originating from crosstalk are typically coherent Hamiltonian errors, such as unintentional rotations of nearby qubits and phase changes induced by AC-Starks shift. However, decoherence errors can be indirectly caused by crosstalk effect as it often affects the qubits' coupling strength to environmental noise. We have observed several different types of crosstalk in the two devices discussed in this thesis.

In the natural silicon device, an unexpected frequency shift of Q2 by $\sim +2$ MHz is induced by the driving pulses for Q1 [13]. Different from the heating effect reported in 9.2.1, the frequency shift discussed here happens instantaneously. Meanwhile, the coherence time of Q2 is notably reduced while applying a far-detuned pulse simultaneously. This is observed from an enhanced decay in the Rabi oscillation of Q2 while driving Q1 in parallel, and it results in a significantly fidelity drop in simultaneous randomized benchmarking [14]. It's worth mentioning that such effect is asymmetric as we haven't observed any noticeable effect on Q1 from the driving of Q2.

In the ^{28}Si/SiGe device, an amplitude modulation effect is found, which has been discussed in the conclusion. In brief, in the simultaneous Rabi oscillation experiment, the Rabi frequency of any one of the two qubits decreases compared to its Rabi frequency when being driven alone. The decrease in Rabi frequency is dependent on the amplitude of the driving burst for the other qubit. Generally speaking, the higher the driving amplitude for the other qubit, the slower the Rabi oscillation of the target qubit. In contrast to the asymmetry of the crosstalk effect in the natural silicon device, the amplitude modulation here is present in both qubits.

In Chapter 5, we have discussed a possible interpretation of the amplitude modulation effect from a perspective of a microscopic rectification effect. Although lacking a comprehensive modelling, we think that the crosstalk observed in the natural silicon device can also be explained by the same mechanism: the frequency shift of Q2 possibly arises from an average shift of its spatial wavefunction in an asymmetric confinement potential; the enhanced decoherence can be induced by the electric noise that couples to Q2 via the large longitudinal field gradient.

These observations actually unveil a commonly ignored difference between ESR and EDSR: in ESR, the crosstalk is simply described by the response of the spin degree of freedom to an oscillating magnetic field at a different frequency, and the response becomes weaker for farther detuned oscillating fields; whereas in EDSR, an additional ef-

fect comes from the charge degree of freedom, which always strongly responds to any oscillating electric field, no matter what frequency it has. Similar crosstalk effect has actually been studied in the static biasing voltage on the metallic gates, and a well-know solution is the so-called "virtual gate" [15, 16]. Inspired by the applications of static virtual gates, we here propose "virtual EDSR gates", in which EDSR is executed on a target qubit with high-selectivity via simultaneously pulsing on different gates in a quantum dot array. By carefully offsetting the phases of the signals applied to different gates, the spatial wavefunctions of unaddressed qubits could be stabilized.

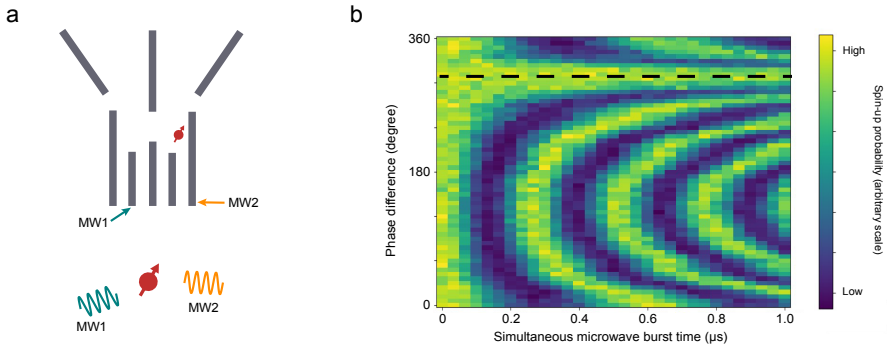

Fig. 9.3: a. Two vector signal generators (VSGs) are used to send microwave pulses to MW1 and MW2 to resonantly control the same qubit. The output signals are at 6.2 dBm and 5.0 dBm respectively. The two VSGs are synchronized by the same clock. **b.** Rabi oscillation as a function of the phase difference between the two microwave bursts. Note that the phase difference here is determined by both the difference in the distance between the VSGs and the qubit, and the random initial phases of the local oscillators in the VSGs.

As a first attempt of a virtual EDSR gate, we use two different gates (MW1 and MW2) in the natural silicon device to control one qubit (Fig. 9.3a). The powers of the two microwave bursts are individually calibrated to achieve the same Rabi frequency (~ 2 MHz). We then perform Rabi oscillation experiments on the qubit using combined driving. The qubit is prepared to the $|1\rangle$ state, followed by parallel microwave bursts sent to MW1 and MW2 gates of incremental duration. In addition, we sweep the phase difference between the two signals. From the pattern shown in Fig. 9.3b, we observe that the Rabi oscillation varies from being enhanced to being suppressed. An interesting phenomena happens at a particular phase difference that the the qubit is not driven at all and is stabilized at the $|1\rangle$ state. This shows that it is possible to stabilize the spatial wavefunction of a qubit via virtual EDSR gates to mitigate crosstalk errors.

The virtual EDSR gate has many potential applications. One can design a device such that the qubit can be driven in different directions (Fig. 9.4a). Using combined driving signals from two perpendicular gates, the spatial wavefunciton can oscillate in all different ways, including linear oscillations in arbitrary directions and even circular oscillations. By studying the relation between the Rabi frequency and the linear oscillation direction, we can extract more microscopic details in the quantum dot such as the shape of the confinement potential and the valley dipole orientation. If the transverse magnetic field gradient can be engineered in both the $\hat{x}$ and $\hat{y}$ directions, circular oscillating driving fields can be produced natively, such that the Bloch-Siegert shift can

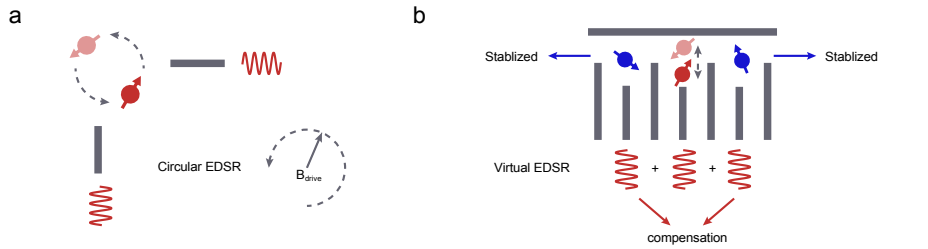

Fig. 9.4: a. Combining the microwave driving signals from two perpendicular gates, various types of spatial wavefunction oscillation can be realized. **b.** Virtual EDS gate applied in a linear qubit array to selectively address a targeted qubit while stabilizing the other ones.

be avoided [17]. Another useful application of the virtual EDSR gate is to implement it in a dense linear qubit array (Fig. 9.4b). The advantage is that the unadressed qubits are spatially stabilized and thus are less susceptible to local noise. In addition, as the addressability is given by the virtual gate, there is no need to specifically engineer the longitudinal magnetic field gradient which eases the design of the micromagnet.

9.2.3. SCALABLE DESIGN

The small footprints of spin qubits and their similarities to conventional CMOS transistors place them in a good position for scaling. However, the elephant in the room is the complexity in controlling a dense qubit array. First, the wiring issue has been proposed to be solved in various approaches [18–20], but these methods require either high material uniformity and complicated manufacturing, or sacrificing the footprint advantage of quantum dots. Second, each qubit in a dense array must be individually addressable. This not only puts a very high bar on reducing crosstalk and residual coupling, but also requires the qubits to be well separated from either in frequency or in space. To keep the qubits relatively dense, micromagnets remain the best solution. Here I propose a modular architecture with symmetric micromagnet design, which is compatible with both operating local registers and shuttling electrons between distant registers.

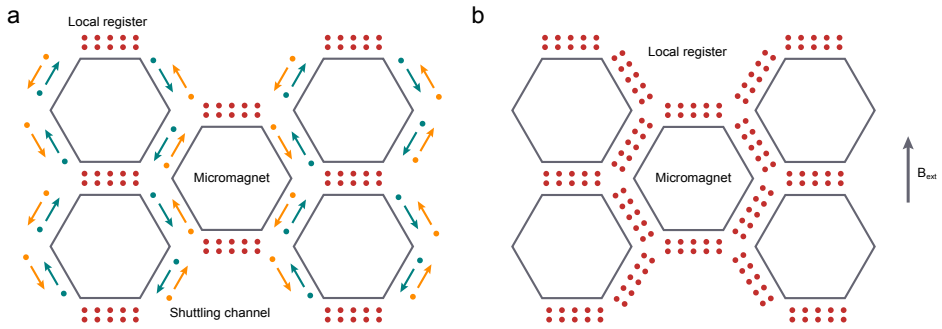

Fig. 9.5: a. A quantum processor architecture with sparse local registers. Each local register is a bilinear quantum dot array, and they are connected via shuttle channels. **b.** A similar architecture with densely placed local registers.

In the proposed architecture, I anticipate hexagonal-shaped micromagnets placed periodically on top of a sample. The local registers are bilinear arrays of quantum dots. Such a choice is for two reasons: bilinear arrays can be easily addressed without stacking many gate layers or multiplexing the control wires; modern micromagnet designs are only suitable for controlling linear qubit arrays. In this design, the micromagnets are patterned symmetrically, and thus there is no specifically engineered longitudinal magnetic field gradient. The addressability of the qubits is guaranteed by virtual EDSR gates. Fig. 9.5 shows two example architectures. The horizontally oriented arrays are used as local registers in both cases, while the arrays along the tilted edges of the micromagnets can be used either for dedicated shuttle channels, or simply for more local registers. The symmetric and periodic micromagnet design allows the shuttle channel or tilted local registers to be placed in proximity to the position with zero transverse magnetic field, which is the so-called "sweet spot".

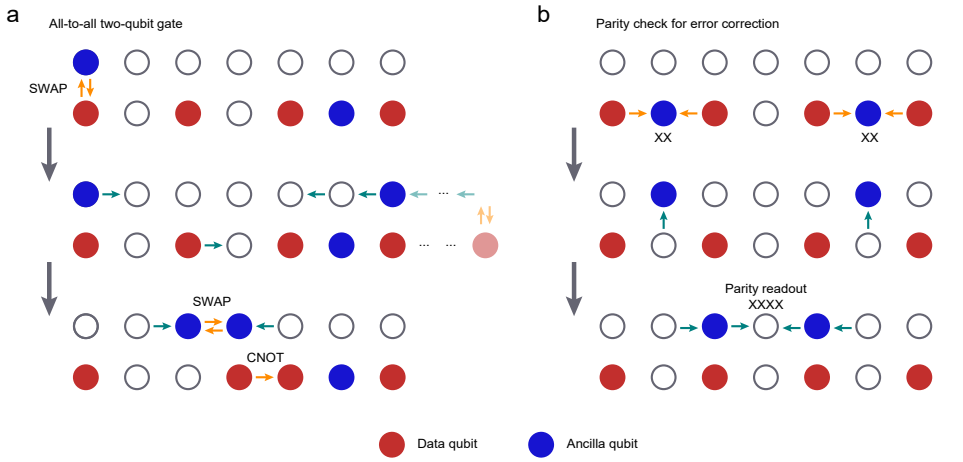

Fig. 9.6: a. All-to-all two-qubit gates. A two-qubit gate between remote data qubits, e.g. a SWAP gate, is executed by first performing two-qubit gates between the data qubits and their ancilla qubits, followed by shuttling the ancilla qubits to the middle and performing a two-qubit gate between them. For the two-qubit gate between neighbor qubits, e.g. a CNOT gate, it can be simply implemented after shuttling a data qubit towards the other one. **b.** Surface code implementation in a local register. In the example of a ⟨XXXX⟩ measurement, two ancilla qubits are first used to map the ⟨XX⟩ value of two data qubit pairs. Then the two ancilla qubits are shuttled to the middle for a parity measurement.

Next, I give my thoughts on the operation of a local register. I propose the data qubits to be placed in one of the two linear arrays, and they sparsely occupy every other quantum dot. Every two data qubits directly communicate with one ancilla qubit in between. The second array is left empty and is used as a shuttle channel within the local register. The first advantage of this design is that it suits well the existing micromagnet design. The sweet spot in the magnetic field gradient is typically a very narrow area that can only fit a single linear array, which accommodates all data qubits and all EDSR operations. The second advantage is that the dedicated shuttle channel for the ancilla qubits allows all-to-all connectivity. This not only allows for two-qubit gates between any pair of data qubits, but also makes it possible to implement the surface code equivalently to

a two-dimensional qubit array (Fig. 9.6), which is known to have a looser error threshold than the one-dimensional implementation [2]. Moreover, because the data qubits are sparsely placed and the ancilla qubits will sit in the top row during the manipulation of the data qubits, the residual exchange coupling and the crosstalk between them can be efficiently suppressed.

REFERENCES

[1] M. H. Devoret and R. J. Schoelkopf, *Superconducting circuits for quantum information: an outlook,* Science **339**, 1169 (2013).

[2] A. G. Fowler, M. Mariantoni, J. M. Martinis, and A. N. Cleland, *Surface codes: Towards practical large-scale quantum computation,* Phys. Rev. A **86**, 032324 (2012).

[3] M. Reed, B. Maune, R. Andrews, M. Borselli, K. Eng, M. Jura, A. Kiselev, T. Ladd, S. Merkel, I. Milosavljevic, *et al.*, *Reduced sensitivity to charge noise in semiconductor spin qubits via symmetric operation,* Phys. Rev. Lett. **116**, 110402 (2016).

[4] F. Martins, F. K. Malinowski, P. D. Nissen, E. Barnes, S. Fallahi, G. C. Gardner, M. J. Manfra, C. M. Marcus, and F. Kuemmeth, *Noise suppression using symmetric exchange gates in spin qubits,* Phys. Rev. Lett. **116**, 116801 (2016).

[5] L. M. K. Vandersypen, H. Bluhm, J. S. Clarke, A. S. Dzurak, R. Ishihara, A. Morello, D. J. Reilly, L. R. Schreiber, and M. Veldhorst, *Interfacing spin qubits in quantum dots and donors–hot, dense, and coherent,* npj Quantum Information **3**, 34 (2017).

[6] B. Patra, M. Mehrpoo, A. Ruffino, F. Sebastiano, E. Charbon, and M. Babaie, *Characterization and analysis of on-chip microwave passive components at cryogenic temperatures,* IEEE Journal of the Electron Devices Society **8**, 448 (2020).

[7] E. Kawakami, T. Jullien, P. Scarlino, D. R. Ward, D. E. Savage, M. G. Lagally, V. V. Dobrovitski, M. Friesen, S. N. Coppersmith, M. A. Eriksson, *et al.*, *Gate fidelity and coherence of an electron spin in an si/sige quantum dot with micromagnet,* Proceedings of the National Academy of Sciences **113**, 11738 (2016).

[8] P. Pakkiam, A. V. Timofeev, M. G. House, M. R. Hogg, T. Kobayashi, M. Koch, S. Rogge, and M. Y. Simmons, *Single-shot single-gate rf spin readout in silicon,* Phys. Rev. X **8**, 041032 (2018).

[9] A. West, B. Hensen, A. Jouan, T. Tanttu, C.-H. Yang, A. Rossi, M. F. Gonzalez-Zalba, F. Hudson, A. Morello, D. J. Reilly, and A. S. Dzurak, *Gate-based single-shot readout of spins in silicon,* Nature Nanotechnology **14**, 437 (2019).

[10] M. Urdampilleta, D. J. Niegemann, E. Chanrion, B. Jadot, C. Spence, P.-A. Mortemousque, C. Bäuerle, L. Hutin, B. Bertrand, S. Barraud, *et al.*, *Gate-based high fidelity spin readout in a CMOS device,* Nature Nanotechnology , 1 (2019).

[11] G. Zheng, N. Samkharadze, M. L. Noordam, N. Kalhor, D. Brousse, A. Sammak, G. Scappucci, and L. M. K. Vandersypen, *Rapid gate-based spin read-out in silicon using an on-chip resonator,* Nature Nanotechnology **14**, 742 (2019).

[12] K. Takeda, J. Yoneda, T. Otsuka, T. Nakajima, M. Delbecq, G. Allison, Y. Hoshi, N. Usami, K. Itoh, S. Oda, *et al.*, *Optimized electrical control of a Si/SiGe spin qubit in the presence of an induced frequency shift,* npj Quantum Information **4**, 1 (2018).

[13] T. F. Watson, S. G. J. Philips, E. Kawakami, D. R. Ward, P. Scarlino, M. Veldhorst, D. E. Savage, M. G. Lagally, M. Friesen, S. N. Coppersmith, M. A. Eriksson, and L. M. K. Vandersypen, *A programmable two-qubit quantum processor in silicon,* Nature **555**, 633 (2018).

[14] X. Xue, T. F. Watson, J. Helsen, D. R. Ward, D. E. Savage, M. G. Lagally, S. N. Coppersmith, M. A. Eriksson, S. Wehner, and L. M. K. Vandersypen, *Benchmarking gate fidelities in a* Si/SiGe *two-qubit device,* Phys. Rev. X **9**, 021011 (2019).

[15] T. Hensgens, T. Fujita, L. Janssen, X. Li, C. Van Diepen, C. Reichl, W. Wegscheider, S. D. Sarma, and L. M. Vandersypen, *Quantum simulation of a Fermi–Hubbard model using a semiconductor quantum dot array,* Nature **548**, 70 (2017).

[16] C. Volk, A.-M. J. Zwerver, U. Mukhopadhyay, P. T. Eendebak, C. J. van Diepen, J. P. Dehollain, T. Hensgens, T. Fujita, C. Reichl, W. Wegscheider, *et al.*, *Loading a quantum-dot based "Qubyte" register,* npj Quantum Information **5**, 1 (2019).

[17] F. Bloch and A. Siegert, *Magnetic resonance for nonrotating fields,* Phys. Rev. **57**, 522 (1940).

[18] M. Veldhorst, H. Eenink, C.-H. Yang, and A. S. Dzurak, *Silicon CMOS architecture for a spin-based quantum computer,* Nature communications **8**, 1 (2017).

[19] R. Li, L. Petit, D. P. Franke, J. P. Dehollain, J. Helsen, M. Steudtner, N. K. Thomas, Z. R. Yoscovits, K. J. Singh, S. Wehner, *et al.*, *A crossbar network for silicon quantum dot qubits,* Science Advances **4**, eaar3960 (2018).

[20] J. M. Boter, J. P. Dehollain, J. P. van Dijk, T. Hensgens, R. Versluis, J. S. Clarke, M. Veldhorst, F. Sebastiano, and L. M. Vandersypen, *A sparse spin qubit array with integrated control electronics,* in *2019 IEEE International Electron Devices Meeting (IEDM)* (IEEE, 2019) pp. 31–4.

ACKNOWLEDGEMENTS

During my time at QuTech, there are many friends and colleagues to whom I sincerely want to say thanks. I'd like to take this opportunity to recall those nice days. However, if you find your name missing, let me know and I will post an author correction note.

Lieven, when I approached you for a PhD position, I was actually lost in the dark and didn't know if I should continue in science. Your offer changed everything and started a new chapter in my life. From those inspiring discussions, and those unpleasant arguments, you have shown me not only how to be a great scientist, but also how to be a great leader. With all the skills I learned from you, there is no doubt that my team in the future will outperform yours:). Seriously, I cannot express how proud I am when saying that I'm from the Vandersypen lab at the beginning of each conference talk.

Tom, it's such a great pleasure to work with you. Almost everything I know about measurement came from you. Even after you left, I still wanted to find you when I had a problem. I couldn't imagine how I can achieve all the nice results without you. **Nodar** and **Max**, thank you for being my paranymphs and for accompanying me towards the destination. **Nodar**, it must be very stressful to work with me, especially when I feel stressed. I know it could be easier for you to go for someone else but you never did that. It's crazy that we celebrated the high-fidelity two-qubit gate even two years before we actually obtained the result, but now it's time for a real celebration. **Max**, it is incredible to have a theorist like you in our team. I remember I was trying so hard to convince you to join after your interview, but I didn't expect our collaboration would work out so perfectly. I definitely look forward to working with you more in future.

Guoji, I started saving lots of money somehow since I moved into QCLab2, and it stopped since you left because there's no one telling me where to find free food anymore. My bro, I'll see you soon in the next conference. **Udi**, the foodies group was dismissed because of your leave! You've been gone for more than two years but I still feel you were around yesterday. **Sjaak**, our daily discussion started since we were in the wet fridge neighborhood. I'll never forget our days with coffee, sushi, and sometimes physics. Oh, I should congratulate you for publishing the third PRX in our group:P. **Anne-Marije**, you are amazing not only for handling so many different projects, but also for being the catalyst in the team. Those activities wouldn't be that enjoyable without you. **Stephan**, you are such a smart guy with lots of innovations everyday. I believe everyone can learn a lot from your six-qubit experiment. **Brian**, the giant white board in my office witnessed the sparks from our brainstorms. Don't forget our bet on the applications of quantum computers in ten years. I'll reserve a nice restaurant for you to treat me! **Brennan** and **Jurgen**, working with the young generation like you makes me excited, but more importantly, I have learned a lot from you. **Brennan**, I won't try to tell you how to succeed in research because I know you will simply do better. **Jurgen**, you are a great experimentalist and you will be greater if you learn how to release your pressure just a little bit. **Jelmer**, I'll never forget the liquorices from you which I couldn't finish... **Tobias**, thanks for not

abandoning the old fridge and keeping it healthy. Thank you both for making me not alone in F006. **Bishnu** and **Jeroen**, your patience, your carefulness, and your efficiency were the best lessons for me. I'm glad that we published the paper in a "real journal":). **Andrea**, thanks for your effort in Big Whoop. That's where amazing happens.

Patrick, my super knowledgeable office mate, I miss all the "fights" we had because we only fought for physics! **Sergey**, we always share hotel rooms. I wish we can visit Sydney together again, but I might need a working device in order to go there? **Tzu-Kan**, look forward to visiting you and your group in Taiwan and please, cover my expenses:). **Alice**, it's not easy but I'm glad to see your project finally worked out. **Mateusz**, you are a special one because of our back-to-back publications and that beautiful cover. Good luck at Intel. **Pablo**, the best way to kill time is talking to you about physics and Chinese. 但是相比于中文, 你好像更擅长物理... **Oriol**, take care of Big Whoop. This fridge needs to be fed with a Nature every year:). **Florian**, good to see your devices start to work. You will get great rewards. **Eline**, **Maxim**, **Xin**, **Liza**, glad to have you join us. Wish you success in the next few years. **Rick**, leave me enough candies before you leave. **Christian**, you are the most chill person and I miss those hours in TPKV. **Kostas**, I won't forget those days when we stayed late in the lab. **Haruki**, wish you all the best in Osaka. **JP**, **Toivo** and **Takafumi**, your beautiful works in GaAs motivated me to join this group and work on spin qubits. **Gabriel** and **Nima**, we shall never forget your effort in fabrications during the hard time.

Sander, **Pieter** and **Luc**, many thanks for your support in software! **Amir**, **Delphine**, **Dave** and **Larysa**, I appreciate your hard work in materials and fabrications. Thanks to **Olaf**, **Jason**, **Remco**, **Mark**, **Jelle**, **Siebe** for your kind help when there's a problem in my fridge. And thanks to the **Raymond's** and **Marijn** for spoiling us in electronics.

I appreciate the interactions with colleagues in other spin qubit groups. **Menno**, you are a genius scientist with critical opinions. I enjoy our discussions in the lab and at the lunch table, especially those sharp questions from you. **Giordano**, you are the hero behind all the achievements! Whenever there's good news, you are one of the first that I want to tell. Finger crossed for the next one. **Will**, you are always energetic, and you make me not the only one here struggling with those fidelity numbers. All the best in Copenhagen. **Roy**, thanks for your help at the beginning, when I had a hard time finding my way. **Luka**, we started talking a lot since the March meeting at Chicago. What a shame that we didn't make friends earlier! **Floor**, I still want to place you in the paragraph of Lieven's group:). Glad to see your success in Menno's team. **Davide**, **Alberto**, **Lucas**, **Mario**, **LaReine**, **Diego**, you are fantastic folks who build the base (literally) of all the success. **Luca**, **Gertjan**, **Nico**, **David**, **Marco**, you guys are phenomenal. I sometimes felt that the biggest pressure came from you instead of the outside. **Marcel**, **Hanifa**, **Chien-An**, **Valentin**, **Corentin**, **Francesco**, **Job**, **Önder**, **Tumi**, good luck with your projects and don't forget to enjoy spinning! There are many more "QuTechers" whom I enjoy spending time with. **Tim** and **Attila**, thank you for giving me green lights at my go/no-go:). **Sebastian** and **Eliska**, I appreciate the chance to know you and collide our ideas at the end of my PhD. **Niels**, **Adriaan**, **Xiang**, **Ramiro**, **Mark**, **Gerd**, **Bagas**, **Conor**, **Mohamed**, **Lingling**, **Matt**, **Jie**, **Jaap**, **Jiyin**, **Lin**, **Qing**, **Christian**, **Alessandro**, **Jake**, **Francesco**, **Yang**, **Chun-Xiao**, **Sjoerd**, **Kian**, **Arian**, **Thorsten**, **Richard**, you made QuTech such a cool and diversified place. **Di**, I'll remember those days with empty plates and exploding stom-

achs. **Filip**, thanks for your pioneer work on symmetric operation:). Many thanks to **Marja** and **Chantal** for making our life so convenient.

Collaborations form a big part of my research. I want to thank the **Wisconsin** team: **Mark** (E.), **Sue**, **Mark** (F.), **Bob**, **Vickram**, **Max**. I wouldn't be able to take off so smoothly without you. And I appreciate the chance to work with the **Intel** team and the **EWI** team, especially **Stefano**, **Sushil**, **Fabio**, **Masoud** and **Edoardo**. I also had the luxury to closely work with many more top-tier theorists inside and outside QuTech: **Jonas** and **Stephanie**, **Ben** and **Bill**, **Mahammad** and **Slava**. Thank you for being patient to explain me once and once again so I could understand 1 percent of your thoughts. I know many of my colleagues are jealous because of you!

Fabio, thank you for being my copromotor. And thanks to **Menno**, **Leo**, **Seigo**, **Guido** and **Barbara** for being in my committee. I appreciate all the inspiration and motivation I got from you. It's an honor to have you participating my defense and challenging me. This will be a memorable day.

Mom and **Dad**, thank you for always trusting my decision, no matter how stupid it might look.

Le, thank you for your support from the beginning. I know this is not an easy way, but we will find the right way.

May the force be with you, **everyone**.

CURRICULUM VITÆ

Xiao XUE

02-01-1992 Born in Zibo, China.

EDUCATION

2010–2014 BSc in Physics
University of Science and Technology of China

2014–2016 Graduate student in Quantum Information
Tsinghua University

2016–2017 Research internship in Quantum Optics
École Polytechnique Fédérale de Lausanne

2017–2022 PhD in Experimental Quantum Physics
Delft University of Technology
Thesis: Performance benchmarking of silicon quantum processors
Promotor: Prof. dr. ir. L.M.K. Vandersypen

LIST OF PUBLICATIONS

JOURNAL PUBLICATIONS AND PREPRINTS

9. *Nonlinear Response and Crosstalk of Strongly Driven Silicon Spin Qubits*
B. Undseth*, **X. Xue***, M. Mehmandoost, M. Russ, N. Samkharadze, A. Sammak, V. V. Dobrovitski, G. Scappucci, L. M. K. Vandersypen
arXiv:2205.04905 (2022).

8. *Quantum logic with spin qubits crossing the surface code threshold (**Cover**)*
X. Xue, M. Russ, N. Samkharadze, B. Undseth, A. Sammak, G. Scappucci, L. M. K. Vandersypen
Nature **601**, 343–347 (2022).

7. *Atomic fluctuations lifting the energy degeneracy in Si/SiGe quantum dots*
B. Paquelet Wuetz, M. P. Losert, S. Koelling, L. E. A. Stehouwer, A.-M. J. Zwerver, S. G. J. Philips, M. T. Mądzik, **X. Xue**, G. Zheng, M. Lodari, S. V. Amitonov, N. Samkharadze, A. Sammak, L. M. K. Vandersypen, R. Rahman, S. N. Coppersmith, O. Moutanabbir, M. Friesen, G. Scappucci
arXiv:2112.09606 (2021).

6. *CMOS-based cryogenic control of silicon quantum circuits*
X. Xue*, B. Patra*, J. P. G. van Dijk*, S. Subramanian, N. Samkharadze, A. Corna, C. Jeon, F. Sheikh, H. Rampurawala, B. Carlton, S. Ravikumar, C. Nieva, S. Kim, H.-J. Lee, A. Sammak, G. Scappucci, M. Veldhorst, E. Charbon, S. Pellerano, M. Babaie, F. Sebastiano, L. M. K. Vandersypen
Nature **593**, 205–210 (2021).

5. *A Scalable Cryo-CMOS Controller for the Wideband Frequency-Multiplexed Control of Spin-Qubits and Transmons*
J. P. G. van Dijk, B. Patra, S. Subramanian, **X. Xue**, N. Samkharadze, A. Corna, C. Jeon, F. Sheikh, E. Juarez-Hernandez, B. P. Esparza, H. Rampurawala, B. Carlton, S. Ravikumar, C. Nieva, S. Kim, H.-J. Lee, A. Sammak, G. Scappucci, M. Veldhorst, L. M. K. Vandersypen, E. Charbon, S. Pellerano, M. Babaie, F. Sebastiano
IEEE Journal of Solid-State Circuits, **55**, 2930-2946 (2020).

4. *Repetitive Quantum Nondemolition Measurement and Soft Decoding of a Silicon Spin Qubit*
X. Xue*, B. D'Anjou*, T. F. Watson, D. R. Ward, D. E. Savage, M. G. Lagally, M. Friesen, S. N. Coppersmith, M. A. Eriksson, W. A. Coish, and L. M. K. Vandersypen
Phys. Rev. X **10**, 021006 (2020).

3. *Spatial noise correlations in a Si/SiGe two-qubit device from Bell state coherences*
J. M. Boter*, **X. Xue***, T. S. Krähenmann, T. F. Watson, V. N. Premakumar, D. R. Ward, D. E. Savage, M. G. Lagally, M. Friesen, S. N. Coppersmith, M. A. Eriksson, R. Joynt, L. M. K. Vandersypen
Phys. Rev. B **101**, 235133 (2020).

2. *Benchmarking Gate Fidelities in a Si/SiGe Two-Qubit Device*
X. Xue, T. F. Watson, J. Helsen, D. R. Ward, D. E. Savage, M. G. Lagally, S. N. Coppersmith, M. A. Eriksson, S. Wehner, L. M. K. Vandersypen
Phys. Rev. X **9**, 021011 (2019).

1. *A new class of efficient randomized benchmarking protocols*
J. Helsen, **X. Xue**, L. M.K. Vandersypen, S. Wehner
npj Quantum Information, **5**, 71 (2019).

CONFERENCE PROCEEDINGS

4. *Cryogenic CMOS for Qubit Control and Readout (**Best paper award**)*
S. Pellerano, S. Subramanian, J.-S. Park, B. Patra, T. Mladenov, **X. Xue**, L.M.K. Vandersypen, M. Babaie, E. Charbon, F. Sebastiano
2022 IEEE Custom Integrated Circuits Conference (CICC).

3. *Cryo-CMOS Interfaces for Large-Scale Quantum Computers*
F. Sebastiano, J.P.G. van Dijk, P.A. 't Hart, B. Patra, J. van Staveren, **X. Xue**, C.G. Almudever, G. Scappucci, M. Veldhorst, L.M.K. Vandersypen, A. Vladimirescu, S. Pellerano, M. Babaie, E. Charbon
2020 IEEE International Electron Devices Meeting (IEDM), 25.2.1-25.2.4 (2020).

2. *Quantum Inspire: QuTech's platform for co-development and collaboration in quantum computing*
T. Last, N. Samkharadze, P. Eendebak, R. Versluis, **X. Xue**, A. Sammak, D. Brousse, K. Loh, H. Polinder, G. Scappucci, M. Veldhorst, L. M. K. Vandersypen, K. Maturová, J. Veltin, G. Alberts
Novel Patterning Technologies for Semiconductors, MEMS/NEMS and MOEMS; 113240J (2020).

1. *A Scalable Cryo-CMOS 2-to-20GHz Digitally Intensive Controller for 4×32 Frequency Multiplexed Spin Qubits/Transmons in 22nm FinFET Technology for Quantum Computers (**Best European paper award**)*
B. Patra, J. P. G van Dijk, S. Subramanian, A. Corna, **X. Xue**, C. Jeon, F. Sheikh, E. Juarez-Hernandez, B. P. Esparza, H. Rampurawala, B. Carlton, N. Samkharadze, S. Ravikumar, C. Nieva, S. Kim, H.-J. Lee, A. Sammak, G. Scappucci, M. Veldhorst, L. M. K. Vandersypen, M. Babaie, F. Sebastiano, E. Charbon, S. Pellerano
2020 IEEE International Solid- State Circuits Conference - (ISSCC), 304-306 (2020).

PATENT

1. *Compensated microwave driven semiconductor qubits (under process)*
N. Samkharadze, **X. Xue**